

**FACULTY
OF MATHEMATICS
AND PHYSICS**
Charles University

DOCTORAL THESIS

Miroslav Halló

**Influence of velocity model uncertainty
in earthquake source inversions**

Department of Geophysics

Supervisor of the doctoral thesis: doc. RNDr. František Gallovič, Ph.D.

Study programme: Physics

Study branch: Geophysics

Prague 2018

I declare that I carried out this doctoral thesis independently, and only with the cited sources, literature and other professional sources.

I understand that my work relates to the rights and obligations under the Act No. 121/2000 Sb., the Copyright Act, as amended, in particular the fact that the Charles University has the right to conclude a license agreement on the use of this work as a school work pursuant to Section 60 subsection 1 of the Copyright Act.

In Prague 21st May, 2018

..... Miroslav Halló

First of all, I would like to thank my supervisor Dr. František Gallovič for all of his enormous support and guidance during my doctoral studies. I really appreciate your help and I enjoyed the time of cooperation with you!

Huge thank to Prof. Jiří Zahradník, Dr. Jakub Velímský, Jiří Vackář, Filip Kostka and Dr. Ľubica Valentová for many inspiring discussions and their help in variety of scientific issues. I also thank to Prof. Ondřej Čadek, Dr. Hana Čížková and ALL the teachers and students at the Department of Geophysics of Charles University for friendly atmosphere and interesting discussions from various areas of science and life. My special thank belongs to my supervisor Dr. Kimiyuki Asano at short-term research visit at Disaster Prevention Research Institute, Kyoto University, for making my stay possible and productive. Truly heartily thank belongs to my family and close friends who supported me even in desperate times. I would not be able to go so far without all of you!

Next, I would like to thankfully acknowledged all operators involved in station maintenance at K-NET, KiK-net and F-net seismograph networks operated by National Research Institute for Earth Science and Disaster Resilience. I appreciate waveform data provided by the Hellenic Unified Seismic Network operated by the Geodynamic Institute of the National Observatory of Athens, the Aristotle University of Thessaloniki, the University of Patras, co-operating certain stations jointly with the Charles University, and the University of Athens. Thank belongs also to Dr. Aitaro Kato from Earthquake Research Institute, University of Tokyo, who provided his locations of hypocenters from 2016 Kumamoto earthquake sequence.

The author was supported by Grant Agency of the Charles University project GAUK-728916 and collaborative research program 28S-02 of the Disaster Prevention Research Institute of Kyoto University. This research was also supported by Charles University grants SVV-260218, SVV-260447/2017, SVV-260447 and by the Czech Science Foundation projects 14-04372S and 18-06716J. Computational feasibility of this study was supported by The Ministry of Education, Youth and Sports from the Large Infrastructures for Research, Experimental Development and Innovations project “IT4Innovations National Supercomputing Center – LM2015070”.

Děkuji Vám

Thank you



ありがとう
ございました

Title: Influence of velocity model uncertainty in earthquake source inversions

Author: Miroslav Halló

Department: Department of Geophysics

Supervisor: doc. RNDr. František Gallovič, Ph.D., Department of Geophysics

Abstract: Earthquake ground motions originate from rupture processes on faults in Earth. Constraints on earthquake source models are important for better understanding of earthquake physics and for assessment of seismic hazard. The source models are inferred from observed waveforms by inverse modeling, which is subject to uncertainty. For large tectonic earthquakes the major source of uncertainty is an imprecise knowledge of crustal velocity model. The research topic of this Thesis is the influence of the velocity model uncertainty on the inferred source models. We perform Monte-Carlo simulations of Green's functions (GFs) in randomly perturbed velocity models to reveal the effects of the imprecise velocity model on the synthetic waveforms. Based on the knowledge gained, we derive closed-form formulas for approximate covariance functions to obtain fast and effective characterization of the GFs' uncertainty. We demonstrate that approximate covariances capture correctly the GF variability as obtained by the Monte-Carlo simulations. The proposed approximate covariance functions are massively tested on moment tensor inversions of synthetic and real data sets. In particular, Bayesian inversion tests show that the posterior probability density provides also realistic estimate of uncertainty of the moment tensors. We apply the method on the case study of foreshocks and aftershocks of the 2016 Kumamoto, Kyushu, Japan, earthquake sequence, where our assessment of the realistic uncertainties of the centroid moment tensors proved to be beneficial for interpretation of the results in seismo-tectonic framework. Further, we develop a new Bayesian parametric fault slip inversion, which accounts for the GFs' uncertainty by means of the approximate covariance functions. Our non-linear kinematic finite-extent source inversion method relies on self-adapting parametrization of slip. Performance of the slip inversion method is demonstrated on the destructive M_w 7.1 mainshock of the 2016 Kumamoto sequence. The posterior probability density is sampled by trans-dimensional Markov chain Monte-Carlo algorithm, which results into an ensemble of more than 590k possible finite source models. This allows us to inspect which features of the finite-extent source model are reliable and which are rather artifacts caused by the imprecise knowledge of the velocity model.

Keywords: earthquake source, velocity model, Green's function, Bayesian inversion, 2016 Kumamoto sequence

Název práce: Vliv neurčitosti rychlostního modelu při studiu zemětřeseného zdroje

Autor: Miroslav Halló

Katedra: Katedra geofyziky

Vedoucí disertační práce: doc. RNDr. František Gallovič, Ph.D., Katedra geofyziky

Abstrakt: Zemětřesené pohyby pozorované na zemském povrchu jsou vyvolané náhlým uvolněním napětí na tektonických zlomech v zemské kůře. Výzkum zemětřesených zdrojů je nutný pro lepší pochopení fyziky vzniku a šíření trhliny na zlomu a také pro vyhodnocení seismického ohrožení. Fyzikální modely tektonických zemětřesených zdrojů jsou získávány pomocí inverzního modelování, které je zatíženo nejistotou způsobenou nejednoznačností úlohy. U velikých tektonických zemětřesení má na nejistotu výsledku zásadní vliv neurčitost rychlostního modelu zemské kůry, jenž je předmětem tohoto výzkumu. Zde nejprve studujeme účinky nepřesného rychlostního modelu na vlnové pole pomocí Monte-Carlo simulací Greenových funkcí v náhodně perturbovaných rychlostních modelech. Na základě získaných poznatků pak odvozujeme analytické vzorce pro výpočet přibližných kovariančních funkcí, určených k rychlému a efektivnímu posouzení neurčitostí Greenových funkcí. Ukazujeme, že tyto přibližné kovarianční funkce správně zachycují variabilitu Greenových funkcí získanou z Monte-Carlo simulací. Pomocí testů na syntetických a reálných datech pak ukazujeme, že obrácená úloha na momentový tenzor v Bayesovské formulaci vede na realistický odhad nejistoty výsledku. Dále je tato metoda použita na případovou studii předtřesů a dotřesů zemětřesené sekvence v Japonské prefektuře Kumamoto z dubna 2016, kde odhad neurčitostí určených momentových tenzorů přispěl k sesmotektonické interpretaci výsledků. Dále byla vyvinuta nová Bayesovská obrácená úloha na skluz na zlomu konečných rozměrů, která zahrnuje odhad neurčitosti Greenových funkcí pomocí odvozených přibližných kovariančních funkcí. Tato nelineární kinematická obrácená úloha se opírá o adaptivní parametrizaci skluzu na zlomu. Vlastnosti této metody demonstrujeme na ničivém hlavním otřesu ze zemětřesené sekvence v Japonské prefektuře Kumamoto o magnitudu $M_w 7.1$ (otřes z 16. dubna 2016). Posteriorní hustotu pravděpodobnosti vzorkujeme pomocí trans-dimenzionálních Markovových řetězců. Výsledný soubor více než 590 tisíc možných modelů nám umožňuje prozkoumat, které modelové rysy jsou spolehlivě určené, a které jsou spíše artefakty zapříčiněné neurčitostí rychlostního modelu.

Klíčová slova: zemětřesný zdroj, rychlostní model, Greenovy funkce, Bayesovské metody, zemětřesená sekvence Kumamoto 2016

Contents

Introduction	3
Structure of the Thesis	5
1 Theoretical background	7
1.1 Kinematic representation of seismic source	7
1.1.1 Point source approximation	9
1.1.2 Finite fault source representation	12
1.1.3 Moment tensor decomposition	16
1.2 Bayesian probabilistic framework	20
1.2.1 Linear least-squares methods	22
1.2.2 Monte-Carlo methods	24
2 Fast and cheap approximation of Green’s functions uncertainty for waveform-based earthquake source inversions	29
2.1 Introduction	29
2.2 Covariance of Green’s functions	31
2.2.1 Monte-Carlo estimation	31
2.2.2 Approximate covariance function	33
2.2.3 Stationarized covariance function	36
2.2.4 Performance in capturing the GF variations	41
2.2.5 Examples of cross-covariance	43
2.3 Example of application of the approximate covariances in moment tensor inversion	47
2.3.1 Inversion method	47
2.3.2 Source inversion of synthetic data set	48
2.3.3 Moment tensor inversion of real data set	55
2.3.4 Remark on the role of the covariance matrix in the inversion	57
2.4 Conclusions	63
2.5 Unpublished supplementary material	65
2.5.1 Alternative estimation of parameter L	65
2.5.2 Inversion performance with non-DC MT	67
3 Bayesian inference and interpretation of centroid moment tensors of the 2016 Kumamoto earthquake sequence, Japan	73
3.1 Introduction	74
3.2 Methods	76
3.2.1 Problem formulation	76
3.2.2 Bayesian inference of CMT	76
3.2.3 Accounting for the uncertainty of the velocity structure . .	78
3.3 Application to the Kumamoto sequence	79
3.3.1 Data selection and processing	79
3.3.2 Velocity model	80
3.3.3 Application details	81
3.3.4 Solutions of the CMT inversion	85
3.3.5 CMTs with significant CLVD component	87

3.4	Geometry of the activated ruptures	90
3.5	Discussion	94
3.5.1	Solutions in seismotectonic framework	94
3.5.2	Complexity of activated ruptures	96
3.5.3	Comparison with routine MT catalogues	96
3.6	Conclusions	97
3.7	Unpublished supplementary material	98
3.7.1	ISO component	98
4	Bayesian self-adapting fault slip inversion with Green's functions	
	uncertainty	101
4.1	Introduction	101
4.2	Method	104
4.2.1	Rupture parametrization	104
4.2.2	Forward problem	107
4.2.3	Bayesian inference	108
4.3	Application to the mainshock of the 2016 Kumamoto sequence . .	115
4.3.1	Inversion settings	115
4.3.2	Application details	118
4.3.3	Solution of the fault slip inversion	119
4.4	Discussion and Conclusions	131
4.5	Supplementary material	133
4.5.1	Regularized Yoffe function	133
	Conclusion	135
	Bibliography	137
	List of Abbreviations	147
	List of included publications	149
A	Attachments	151
A.1	Fortran code for ACF (AXCF)	151
A.2	Fortran code for SACF (SAXCF)	153
A.3	Matlab code for ACF (AXCF)	155
A.4	Matlab code for SACF (SAXCF)	157
A.5	Tectonic cube - Earth's stress regimes	159

Introduction

Earthquake ground motions originate from rupture processes on faults in Earth. Constraints on earthquake source models are important for better understanding of earthquake physics and for seismic hazard analysis, which is particularly significant for construction engineering and disaster mitigation planning (e.g., Hutchings et al. 2017). In addition, earthquake source models serve as input for studies like analysis of the earthquake energy budget (e.g., Kanamori & Rivera 2006), dynamic stress drop analysis (e.g., Day et al. 1998), Coulomb stress modeling (e.g., King & Devès 2015), etc. Realistic estimate of the uncertainty of earthquake source models is essential for evaluation of solution quality. Strictly speaking, any interpretation of centroid moment tensor or finite-extent model requires proper assessment of their uncertainty (e.g., Sokos et al. 2015; Dettmer et al. 2014; Duputel et al. 2015).

Earthquake source models are inferred from observed waveforms by inverse modeling, which is subject to uncertainty. Synthetic waveforms required by the inverse modeling are computed using Green's functions (GFs) representing response of Earth's crust to an impulse stimulus. In the case of large tectonic earthquakes, the major source of uncertainty of the inferred source models is related to the uncertainty of the GFs due to the inaccuracy of the crustal models considered. In practical applications, the uncertainties of the inferred source parameters are typically estimated by accepting all models within a given threshold on the misfit value (e.g., Piatanesi et al. 2007; Valentine & Trampert 2012; Zahradník & Custódio 2012; Gallovič & Zahradník 2012). However, the value of such threshold is not based on a proper analysis of the underlying origin of the uncertainty. We point out that imprecise knowledge of the velocity model can lead to spurious non-double-couple components in moment tensor inversions (Zahradník et al. 2015) and artificial slip-rate peaks in slip inversions (Gallovič et al. 2015).

Earthquake source model inversions with the assessment of the solution uncertainty are usually performed in the Bayesian probabilistic framework (e.g., Yagi & Fukahata 2011; Minson et al. 2013, 2014; Dettmer et al. 2007, 2014; Duputel et al. 2014, 2015; Kubo et al. 2016a; Mustač & Tkalčić 2016; Vackář et al. 2017). In this way a prior information on the physical model is specified, which is then updated to a conditional posterior probability on model parameters affected by the observed data (e.g., Tarantola & Valette 1982; Tarantola 2005). In such framework, the assumptions on uncertainty of the observed waveforms and computed GFs can be incorporated, e.g., by means of Gaussian covariance matrices. The inferred solution is then represented by the conditional posterior probability on model parameters. The uncertainty of the inferred source model may be then assessed by analytical formulas (if possible) or by ensemble of solutions drawn from the posterior probability density.

The covariance matrix of GFs has been considered by other researchers, however a proper analysis of the GFs' uncertainty has not been done yet. In particular, Yagi & Fukahata (2011) and Minson et al. (2013) considered diagonal GF covariance matrix in their Bayesian slip inversion, treating the GF variance as an unknown parameter. Duputel et al. (2012) showed the importance of considering

the full covariance matrix of GF in the moment tensor inversion. However, in their examples they assume that the major origin of the error is due to the centroid mislocation. That study was extended by Duputel et al. (2014, 2015), who proposed to estimate the full covariance matrix approximately by considering linear relationship between the GFs and random, generally 3D, perturbations of the velocity model. However, their approach requires evaluation of sensitivity kernels, which are, in practice, very expensive to acquire. An alternative approach is represented by “empirical” estimation of the covariances from data residuals in so-called hierarchical inversions (Dettmer et al. 2007, 2014; Mustač & Tkalčić 2016). In particular, Dettmer et al. (2007, 2014) took into account the non-stationary character of the noise by scaling rows and columns of the covariance matrix by running averages of the residual waveforms.

This research is focused on the influence of uncertainty of a crustal velocity model by means of uncertainty of GFs in earthquake source inversions. We first perform Monte-Carlo simulations of GFs in randomly perturbed velocity models to reveal the effects of the imprecise velocity model on the synthetic waveforms. We derive closed-form formulas for approximate covariance functions to obtain fast and effective characterization of the GFs’ uncertainty avoiding any demanding computations (Hallo & Gallovič 2016). The proposed approximate covariance functions are tested on Bayesian moment tensor inversions of synthetic data, and bench-marked on real earthquake from Corinth Gulf, Greece. In particular, experiments with the large number of synthetic target datasets obtained by randomly perturbing velocity models reveal the effects of the imprecise velocity model on the inferred moment tensors. Inversion tests with the approximate covariance functions of GFs show that the posterior covariance matrix of model parameters provides accordant realistic estimate of the moment tensor uncertainties.

In the consecutive research, Hallo et al. (2017), we incorporated the approximate covariances into the Bayesian full-waveform centroid moment tensor inversion code package ISOLA-ObsPy (Vackář et al. 2017). The modification of the ISOLA-ObsPy with assessment of GF uncertainties was applied on foreshocks and aftershocks of the 2016 Kumamoto, Kyushu, Japan, earthquake sequence. The assessment of the uncertainties of the centroid moment tensors showed to be beneficial in terms of interpretation of the results in the seismo-tectonic framework.

Further, we developed a new Bayesian parametric fault slip inversion, which accounts for the GFs’ uncertainty again by means of the approximate covariance functions. Our non-linear finite-extent source inversion method relies on self-adapting parametrization of slip function by means of varying number of spline control points on the fault surface. The posterior probability density is then sampled by trans-dimensional Markov chain Monte Carlo algorithm. Performance of the slip inversion method is demonstrated on the destructive M_w 7.1 mainshock of the 2016 Kumamoto sequence. We infer ensemble of more than 590k possible finite source models following the posterior probability density. This allows us to inspect which features of the source model are reliable and which are rather artifacts caused by imprecise knowledge of a crustal velocity model.

Structure of the Thesis

This Thesis is divided into four Chapters, each organized in Sections. The individual Chapters are independent, though they subsequently follow and interlink each other. The Thesis contains also short Appendix with major source codes and supplementary material. The Chapters are organized as follows:

- Chapter 1 overviews the theoretical background and probabilistic techniques used in Thesis. Section 1.1 contains description of the kinematic representation of seismic sources with focus on tectonic earthquakes (point source approximation and finite-extent fault sources). Then, in Section 1.2 we overview the basic concepts of the Bayesian probabilistic framework. This Section includes Bayesian formulations of Linear Least-Squares methods and Metropolis-Hastings sampling algorithm.
- The aim of Chapter 2 (also published as Hallo & Gallovič 2016) is to introduce a simple approach to efficiently involve the uncertainty of a crustal velocity model in earthquake source inversions. After introduction in Section 2.1, we propose a simple yet efficient method (Section 2.2), which is tested on synthetic and real data (Section 2.3). This Chapter incorporates also its published electronic supplement. The Section 2.5 — “Unpublished supplementary material” includes additional unpublished results which complement the content of the Chapter.
- In Chapter 3 (also published as Hallo et al. 2017) we apply modification of the Bayesian full-waveform centroid moment tensor inversion, ISOLA-ObsPy, to foreshocks and aftershocks of the 2016 Kumamoto, Kyushu, Japan, earthquake sequence (see Section 3.1 for introduction of the 2016 Kumamoto earthquake sequence). The method in Section 3.2 is used to infer centroid moment tensors of selected earthquakes (Section 3.3). Then, we interpret the results in seismo-tectonic framework (Section 3.4) and show the advantages of the used methodology (see Section 3.5). This Chapter was conducted in co-operation with Dr. Kimiyuki Asano from the Disaster Prevention Research Institute, Kyoto University. Section 3.7 — “Unpublished supplementary material” includes additional analysis which completes the content of this Chapter.
- In Chapter 4 we propose a new Bayesian parametric fault slip inversion which accounts for GFs’ uncertainty by means of the approximate covariance functions (see Section 4.1). The newly developed method relies on self-adapting parametrization, fast direct solver, and trans-dimensional Markov chain Monte Carlo sampling algorithm (Section 4.2). The method is demonstrated on the M_w 7.1 mainshock of the 2016 Kumamoto sequence (Section 4.3).

1. Theoretical background

Here we overview theoretical background of physical and mathematical representation of seismic sources and the Bayesian inference framework used in the Thesis. The section with representation of seismic sources is based on well investigated theoretical problem in elastodynamics and classical books of seismology (e.g., Aki & Richards 2002; Kanamori & Brodsky 2004). The overview of the Bayesian framework includes the basic concepts of Tarantola (2005) necessary for Bayesian earthquake source inversions and overview of the Metropolis-Hastings algorithm (Metropolis et al. 1953; Hastings 1970).

1.1 Kinematic representation of seismic source

Seismic sources originating inside the solid Earth are connected to physical phenomena as tectonic faulting, underground explosions, volcanic intrusions, cavity collapses, etc. The most common faulting sources are associated with a fast dislocation across an underground surface (i.e. fault plane). The description of these sources is based on two different concepts. First, from the point of view of dynamic forces applied on the medium to cause the seismic source (i.e. dynamic representation); and second, by the slip or strain associated with the seismic source process (kinematic representation). The kinematic representation of seismic sources is deprived of dynamic forces actually causing the event, nevertheless its advantage is a straightforward relation with the radiated seismic waves. Here we follow the kinematic concept where the process of dislocation on a buried fault and the respective radiated wavefield are related by the representation theorem.

Let us assume volume V inside the solid Earth bounded by surface S . Displacement $\mathbf{u} = (u_1, u_2, u_3)$ at a certain point from contribution due to body force \mathbf{f} throughout V can be expressed from Betti's theorem (Aki & Richards 2002, eq. 2.35). The representation theorem reads (Aki & Richards 2002, eq. 2.41)

$$u_n(\mathbf{x}, t) = \iiint_V f_i(\boldsymbol{\xi}, t) * H_{ni}(\mathbf{x}, t; \boldsymbol{\xi}) dV(\boldsymbol{\xi}), \quad (1.1)$$

where $*$ denotes temporal convolution. Measured displacement field $u_n(\mathbf{x}, t)$ for its n -th component, at position \mathbf{x} and time t , is expressed by volumetric integral from density of the body force $f_i(\boldsymbol{\xi}, t)$ and Green's tensor $H_{ni}(\mathbf{x}, t; \boldsymbol{\xi})$. The body force is assumed at source position $\boldsymbol{\xi}$, and the Green's tensor H_{ni} for the n -th component represents the elastic response of the medium to a unit point source force acting at position $\boldsymbol{\xi}$ and in direction i with the Dirac $\delta(t)$ source time function.

Assume that volume V surrounds buried fault surface Σ of finite size, along which slip occurs. The total slip is small (cm to m) in comparison with the total fault size (tens of m to tens of km), therefore the small-strain approximation is assumed to hold and fault surface Σ itself is unchanged by the deformation. Further, let us assume that the mutual arbitrary dislocations on both sides of the surface have the same size of opposite direction, then the force corresponding to an infinitesimal surface element $d\Sigma(\boldsymbol{\xi})$ can be represented as sum of nine couples of forces (Fig. 1.1). The seismic source is then considered as force system

described by seismic moment tensor density $m_{pq}(\boldsymbol{\xi}, t)$ along the fault plane Σ . The representation theorem in Eq. (1.1) leads to (Aki & Richards 2002, eq. 3.20)

$$u_n(\mathbf{x}, t) = \iint_{\Sigma} m_{pq}(\boldsymbol{\xi}, t) * H_{np,q}(\mathbf{x}, t; \boldsymbol{\xi}) d\Sigma(\boldsymbol{\xi}). \quad (1.2)$$

Such a form of the representation theorem can be used for kinematic description of various underground seismic sources including pure-shear movements, tensile cracks, shear-tensile cracks, etc.

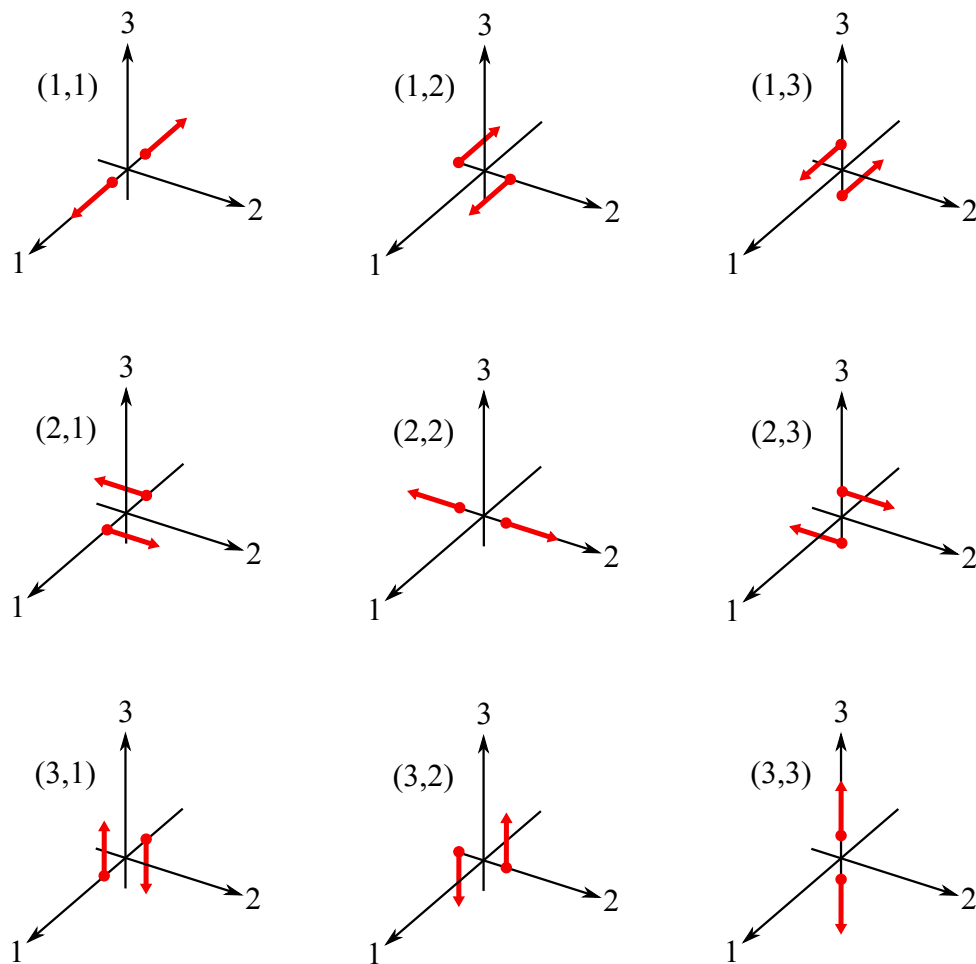


Figure 1.1: Nine possible force couples that substitute generally oriented displacement discontinuity in terms of seismic radiation (following Aki & Richards 2002, fig. 3.7).

1.1.1 Point source approximation

Here we describe approximation of seismic source representation when the size of the fault Σ is small enough with respect to the distance between the source and the receiver and only long wavelengths are considered (see Aki & Richards 2002, pp. 49–52). In this particular case the Green's functions $H_{np,q}(\mathbf{x}, t; \boldsymbol{\xi})$ do not vary significantly over the fault plane Σ and can be substituted by Green's functions with respect to an optimal point on the fault $\boldsymbol{\xi}_0$. The representation theorem from Eq. (1.2) reduces to

$$u_n(\mathbf{x}, t) = \iint_{\Sigma} m_{pq}(\boldsymbol{\xi}, t) d\Sigma(\boldsymbol{\xi}) * H_{np,q}(\mathbf{x}, t; \boldsymbol{\xi}_0). \quad (1.3)$$

Eq. (1.3) still describes a source of finite size, as $m_{pq}(\boldsymbol{\xi}, t)$ may vary over Σ in general. The integral of seismic moment tensor density over the whole fault surface can be substituted by a system of couple forces located at point $\boldsymbol{\xi}_0$ by time-dependent moment tensor $M_{pq}(t)$ as

$$u_n(\mathbf{x}, t) = M_{pq}(t) * H_{np,q}(\mathbf{x}, t; \boldsymbol{\xi}_0). \quad (1.4)$$

This is so-called point source approximation of seismic source, where contributions from different surface elements $d\Sigma$ cannot be any longer distinguished from each other. When the time dependence of the moment tensor is assumed to be the same for all its components, Eq.(1.4) reduces to

$$u_n(\mathbf{x}, t) = M_{pq}\Omega(t) * H_{np,q}(\mathbf{x}, t; \boldsymbol{\xi}_0). \quad (1.5)$$

$\Omega(t)$ is the moment time function and $M_{pq} = M_{pq}(t \rightarrow \infty)$ is the seismic moment tensor (MT). It is advantageous to define so-called source time function (STF) as the time derivative of $\dot{\Omega}(t)$. Eq. (1.5) is then modified to

$$u_n(\mathbf{x}, t) = M_{pq}\dot{\Omega}(t) * \widetilde{H}_{np,q}(\mathbf{x}, t; \boldsymbol{\xi}_0), \quad (1.6)$$

where $\widetilde{H}_{np,q}$ represents Green's function $H_{np,q}$ integrated in time. Note that

$$1 = \int_{-\infty}^{\infty} \dot{\Omega}(t) dt, \quad (1.7)$$

as denoted by hatched area in schematic Fig. 1.2a.

The rupture process is assumed to start at time t_A , then the moment time function is zero before the rupture process starts, i.e. $\Omega(t \leq t_A) = 0$. Because we assume a source of finite size, the rupture process cannot continue infinitely long and the STF converges to zero in a finite time t_B in which the process terminates, i.e. $\dot{\Omega}(t \geq t_B) = 0$. As the STF is non-zero only for the finite time interval (t_A, t_B) (see Fig. 1.2a), its source spectrum (Fourier amplitude spectrum, Fig. 1.2b) defined as

$$\dot{\Omega}_f(f) = \left| \mathcal{F}(\dot{\Omega}(t)) \right| \quad (1.8)$$

tends to a constant equal to one at low frequencies (see Aki & Richards 2002, pp. 497–516). If we also assume that the STF never changes its sign, then the source spectrum $\dot{\Omega}_f(f)$ achieve its maximum for $f = 0$ Hz. A reasonable STF model has

then constant source spectrum on low frequencies, while its high frequency content is proportional to a negative power of f . Brune (1970) defined a corner frequency f_0 as the intersection of flat low-frequency and high-frequency asymptotes of the source spectrum $\dot{\Omega}_f(f)$. The corner frequency value is dependent on source parameters, e.g., magnitude and stress drop, and its value is reciprocal to STF duration. It is higher for small-size ($M_w < 3$) earthquakes (approx. $f_0 > 1.0 \text{ Hz}$) than for mid-size ($3 \leq M_w < 6$) earthquakes (approx. $1.0 \text{ Hz} \geq f_0 > 0.2 \text{ Hz}$) or large-size ($M_w \geq 6$) earthquakes (approx. $f_0 \leq 0.2 \text{ Hz}$), as the duration of STFs for small-size earthquakes is shorter. Please consider these values of f_0 as orientative for educational purpose.

When Dirac delta function $\delta(t)$ is considered as STF, then the modeled source spectrum results in a constant equal one. This leads to low-frequency approximation, where are used only low frequencies with “flat” part of the source spectrum below the to corner frequency f_0 . The representation of the point source in low-frequency approximation is then from Eq. (1.6) as follows:

$$u_n(\mathbf{x}, t) = M_{pq} \widetilde{H}_{np,q}(\mathbf{x}, t - t_A; \boldsymbol{\xi}_0), \quad (1.9)$$

where is $M_{pq} \dot{\Omega}(t)$ from Eq. (1.6) substituted by centroid moment tensor (CMT) defined as $M_{pq} \delta(\boldsymbol{\xi} - \boldsymbol{\xi}_0) \delta(t - t_A)$. Note that $\delta(t - t_A)$ is delayed Dirac delta function by so-called centroid time t_A .

The representation of seismic source by Eq. (1.9) is especially advantageous, as it is linear form. Such linear formulation allows to effectively solve the inverse problem by least-squares method for a given possible position of CMT (e.g., Kikuchi & Kanamori 1991; Vackář et al. 2017; Hallo et al. 2017; Zahradník & Sokos 2018). Nevertheless, even more complex source models with various STFs can be described in point source approximation. For example, Zahradník & Sokos (2018) in their multiple-point MT inversion reproduce STF as a superposition of multiple triangle functions.

To conclude, the point source approximation of seismic source is effective in terms of inverse problem performance and diversity of possible source type like pure-shear movements, tensile cracks, shear-tensile cracks and implicitly also explosions (the last is not discussed in this work).

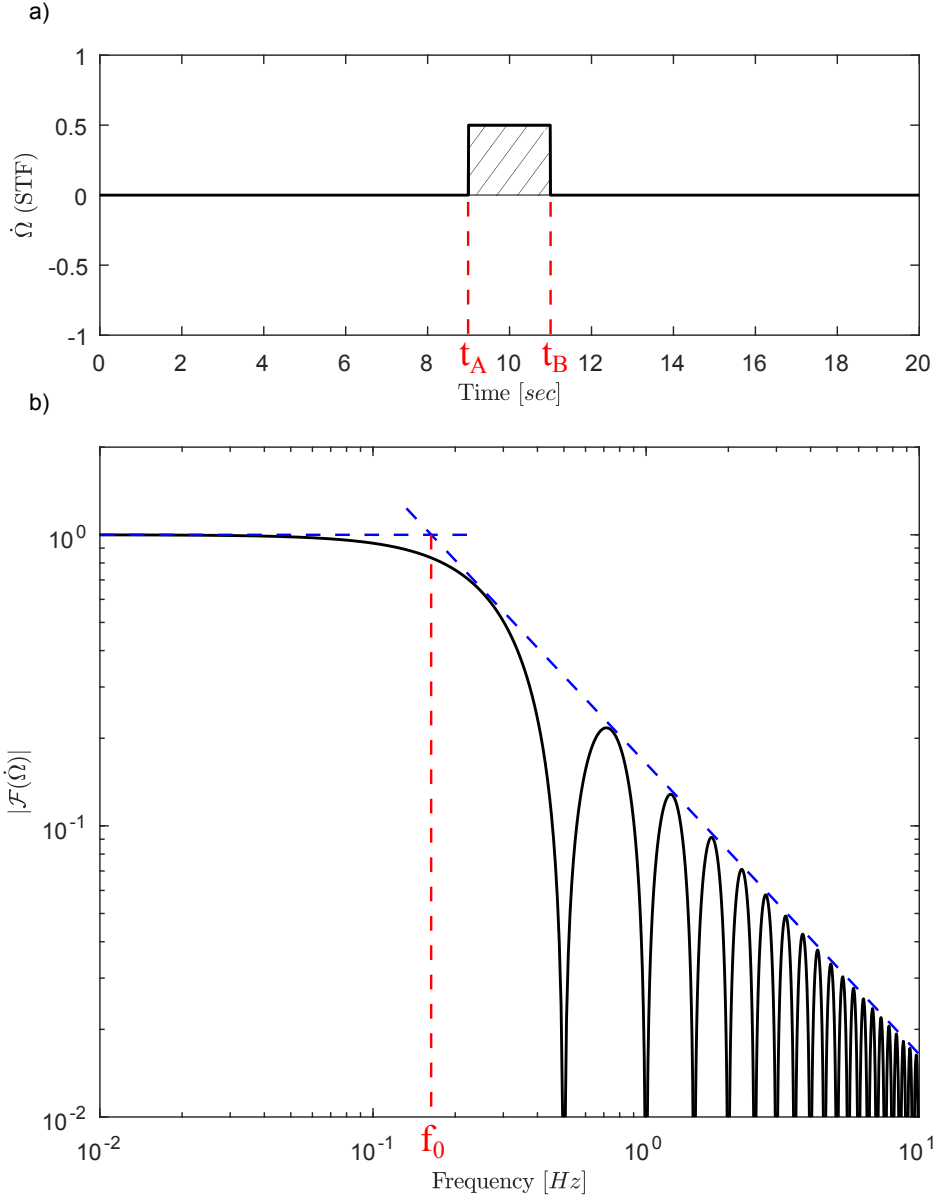


Figure 1.2: Schematic example of simple STF and its Fourier spectrum. **a)** The boxcar STF $\dot{\Omega}(t)$ of total length 2 sec with start time t_A and terminating time t_B . Note that hatched area has unit size (see Eq. (1.7)). **b)** The source spectrum $\dot{\Omega}_f(f)$ of the boxcar STF; f_0 is the source corner frequency.

1.1.2 Finite fault source representation

The tectonic earthquakes can be characterized by heterogeneous distribution of slip over the fault surface. Therefore, the seismic moment tensor density $m_{pq}(\boldsymbol{\xi}, t)$ is rather heterogeneous. Here, we describe representation of finite seismic source which account for the possible heterogeneous distribution of slip.

Let us assume a pure shear slip movement (mutual dislocations exclusively tangential to the fault surface) on the fault of finite size Σ . Then, slip corresponding to an infinitesimal surface element $d\Sigma(\boldsymbol{\xi})$ can be represented in terms of wave radiation by combination of double-couple forces oriented in slip direction $\boldsymbol{\nu}^\Sigma$ and in normal to the surface \mathbf{n}^Σ (see Fig. 1.3).

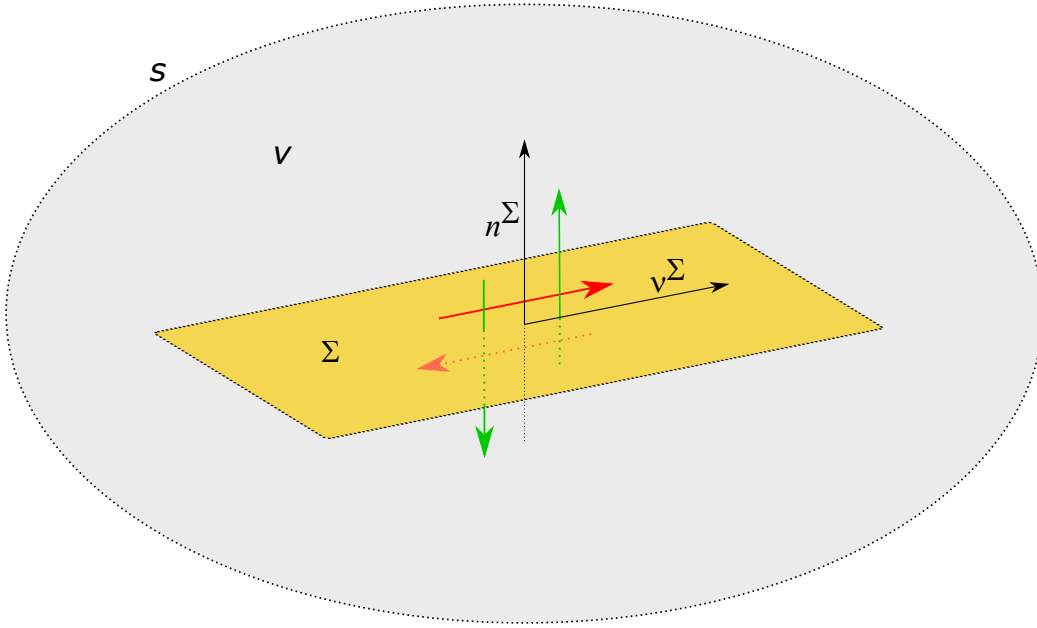


Figure 1.3: Schematic model of finite shear seismic source with depicted double-couple forces. The surface of fault Σ shown by yellow rectangle is enclosed inside elastic volume V bounded by surface S . Vectors $\boldsymbol{\nu}^\Sigma$ and \mathbf{n}^Σ depict the shear slip direction and normal to the surface, respectively. Colored arrows are the equivalent double-couple forces.

The seismic moment tensor density in Eq. (1.2) for such a source in isotropic medium reads (see Aki & Richards 2002, eq. 3.22)

$$m_{pq}(\boldsymbol{\xi}, t) = \mu(\boldsymbol{\xi}) \Delta u(\boldsymbol{\xi}, t) \left[\mathbf{n}_p^\Sigma(\boldsymbol{\xi}) \boldsymbol{\nu}_q^\Sigma(\boldsymbol{\xi}) + \mathbf{n}_q^\Sigma(\boldsymbol{\xi}) \boldsymbol{\nu}_p^\Sigma(\boldsymbol{\xi}) \right], \quad (1.10)$$

where μ is the medium rigidity and $\Delta u(\boldsymbol{\xi}, t)$ is the slip time function at fault position $\boldsymbol{\xi}$.

Putting Eq. (1.10) into Eq. (1.2) we get

$$u_n(\mathbf{x}, t) = \iint_{\Sigma} \Delta u(\boldsymbol{\xi}, t) * T_n(\mathbf{x}, t; \boldsymbol{\xi}) d\Sigma(\boldsymbol{\xi}), \quad (1.11)$$

where $T_n(\mathbf{x}, t; \boldsymbol{\xi})$ is the impulse response of the medium at point $\boldsymbol{\xi}$ defined as

$$T_n(\mathbf{x}, t; \boldsymbol{\xi}) = \mu(\boldsymbol{\xi}) \mathbf{n}_p^\Sigma(\boldsymbol{\xi}) \nu_q^\Sigma(\boldsymbol{\xi}) [H_{np,q}(\mathbf{x}, t; \boldsymbol{\xi}) + H_{nq,p}(\mathbf{x}, t; \boldsymbol{\xi})]. \quad (1.12)$$

Formula in Eq. (1.11) is the kinematic representation of finite fault source by means of source slip time functions. Further, the slip time functions are substituted by its time derivatives, i.e. slip rate function $\Delta\dot{u}(\boldsymbol{\xi}, t)$ (SRF). Eq. (1.11) is then written as

$$u_n(\mathbf{x}, t) = \iint_{\Sigma} \Delta\dot{u}(\boldsymbol{\xi}, t) * \tilde{T}_n(\mathbf{x}, t; \boldsymbol{\xi}) d\Sigma(\boldsymbol{\xi}), \quad (1.13)$$

where \tilde{T}_n represents the response of the medium T_n integrated in time.

The representation integrals in Eqs (1.11) and (1.13) relate the radiated wavefield with slip time function $\Delta u(\boldsymbol{\xi}, t)$ and slip rate function $\Delta\dot{u}(\boldsymbol{\xi}, t)$, respectively. Therefore, these functions describe the spatially heterogeneous slip history on the assumed fault plane Σ . These time functions may be generally arbitrary, but there are two conditions: **1)** as the rupture process is assumed to be dislocation with defined rupture front arrival $t_0(\boldsymbol{\xi})$, so-called rupture time, then these functions must be zero before the rupture process starts, i.e. $\Delta u(\boldsymbol{\xi}, t \leq t_0(\boldsymbol{\xi})) = 0$. **2)** because we assume a source of finite size, the rupture process cannot continue infinitely long, SRF then converges to zero in finite time ($t_0(\boldsymbol{\xi}) + \tau_R(\boldsymbol{\xi})$), i.e. $\Delta\dot{u}(\boldsymbol{\xi}, t \geq (t_0(\boldsymbol{\xi}) + \tau_R(\boldsymbol{\xi}))) = 0$. The total slip $A(\boldsymbol{\xi})$ on fault surface position $\boldsymbol{\xi}$ is then defined as

$$\begin{aligned} A(\boldsymbol{\xi}) &= \int_{-\infty}^{\infty} \Delta\dot{u}(\boldsymbol{\xi}, t) dt = \int_{t_0(\boldsymbol{\xi})}^{(t_0(\boldsymbol{\xi}) + \tau_R(\boldsymbol{\xi}))} \Delta\dot{u}(\boldsymbol{\xi}, t) dt = \\ &= \int_0^{\tau_R(\boldsymbol{\xi})} \Delta\dot{u}(\boldsymbol{\xi}, t - t_0(\boldsymbol{\xi})) dt, \end{aligned} \quad (1.14)$$

where $\tau_R(\boldsymbol{\xi})$ is so-called rise time, defined as the duration in which the total slip reaches its final value. The formula for total slip in Eq. (1.14) allows us to express SRF as

$$\Delta\dot{u}(\boldsymbol{\xi}, t) = A(\boldsymbol{\xi}) s(\boldsymbol{\xi}, t - t_0(\boldsymbol{\xi})), \quad (1.15)$$

where $s(\boldsymbol{\xi}, t - t_0(\boldsymbol{\xi}))$ describes the shape of SRF, where

$$1 = \int_0^{\tau_R(\boldsymbol{\xi})} s(\boldsymbol{\xi}, t - t_0(\boldsymbol{\xi})) dt. \quad (1.16)$$

The broad analysis of tectonic seismic sources and dynamic modeling suggests rise time $\tau_R(\boldsymbol{\xi})$ having duration of fractions of seconds to seconds. A comparison of rise time $\tau_R(\boldsymbol{\xi})$ with the duration of the propagation of the rupture along the fault plane, $\tau_\Sigma = \max(t_0(\boldsymbol{\xi})) - \min(t_0(\boldsymbol{\xi}))$, may distinguish crack-like sources where $\tau_R(\boldsymbol{\xi}) \approx \tau_\Sigma$, and pulse-like sources where $\tau_R(\boldsymbol{\xi}) < \tau_\Sigma$, but this issue is still widely discussed (e.g., Kanamori & Brodsky 2004). The particular duration and shapes of SRF (as functions of time in Eq. (1.15)) can be subject of finite

source inversion (e.g., Gallovič & Zahradník 2010; Gallovič & Ampuero 2015), or alternatively a prescribed SRF's shapes parametrized by a few parameters can be assumed (i.e. parametrized SRFs; e.g., Graves & Wald 2001; Minson et al. 2013; Dettmer et al. 2014). There are several types of SRF's shapes proposed by other researches, here we show a few examples (see Fig. 1.4).

- Delayed Dirac delta function $\delta(t - t_0(\boldsymbol{\xi}))$ (Fig. 1.4, black) can be used as the simplest case, reducing the SRF to

$$\Delta\dot{u}(\boldsymbol{\xi}, t) = A(\boldsymbol{\xi})\delta(t - t_0(\boldsymbol{\xi})). \quad (1.17)$$

The respective slip time function is the Heaviside (Fig. 1.4b) with step in rupture time $t_0(\boldsymbol{\xi})$. Then SRF is parametrized at each position on fault $\boldsymbol{\xi}$ by **two** independent parameters $A(\boldsymbol{\xi})$ and $t_0(\boldsymbol{\xi})$.

- As the shape of SRF are often used delayed boxcar or triangle functions Π_{τ_R} and \wedge_{τ_R} , respectively, and their superposition (Fig. 1.4, red and blue). Rise time $\tau_R(\boldsymbol{\xi})$ define duration of boxcar (or triangle) function, while rupture time $t_0(\boldsymbol{\xi})$ determines the time of the earliest non-zero value. When we define general boxcar and triangle functions as centered around zero time and having unit area, then SRFs reads

$$\Delta\dot{u}(\boldsymbol{\xi}, t) = A(\boldsymbol{\xi})\Pi_{\tau_R(\boldsymbol{\xi})}\left(t - t_0(\boldsymbol{\xi}) - \frac{\tau_R(\boldsymbol{\xi})}{2}\right), \quad (1.18)$$

$$\Delta\dot{u}(\boldsymbol{\xi}, t) = A(\boldsymbol{\xi})\wedge_{\tau_R(\boldsymbol{\xi})}\left(t - t_0(\boldsymbol{\xi}) - \frac{\tau_R(\boldsymbol{\xi})}{2}\right), \quad (1.19)$$

for boxcar and triangle function, respectively. Such SRFs are parametrized at each position on fault $\boldsymbol{\xi}$ by **three** independent parameters $A(\boldsymbol{\xi})$, $t_0(\boldsymbol{\xi})$ and $\tau_R(\boldsymbol{\xi})$. These functions are widely used in parametric finite fault inversions, for example Minson et al. (2013) use triangle shape of SRFs in his Bayesian finite source inversion. Moreover, even more complex shapes of SRFs can be described by their superposition, for example Kubo et al. (2016a) utilize multiple boxcar functions in his multiple-time-window Bayesian finite source inversion.

- The last example of SRF's shape is regularized Yoffe function $\Upsilon_{\tau_R}^{\tau_P}$ as introduced by Tinti et al. (2005), derived for earthquake kinematic modeling (Fig. 1.4, green). Such SRF's shape is compatible with dynamic propagation of earthquake ruptures (e.g., Bizzarri 2012), and hence, it may interlink kinematic and dynamic source parameters using appropriate scaling laws. Explicit analytical form was derived in Tinti et al. (2005) as dependent on rise time duration $\tau_R(\boldsymbol{\xi})$ and time to peak slip velocity (i.e. the duration of positive slip acceleration), called peak time $\tau_P(\boldsymbol{\xi})$. The formula for SRF using regularized Yoffe function reads

$$\Delta\dot{u}(\boldsymbol{\xi}, t) = A(\boldsymbol{\xi})\Upsilon_{\tau_R}^{\tau_P}(t - t_0(\boldsymbol{\xi})). \quad (1.20)$$

Such SRF is then parametrized at each position on fault $\boldsymbol{\xi}$ by **four** independent parameters $A(\boldsymbol{\xi})$, $t_0(\boldsymbol{\xi})$, $\tau_R(\boldsymbol{\xi})$ and $\tau_P(\boldsymbol{\xi})$.

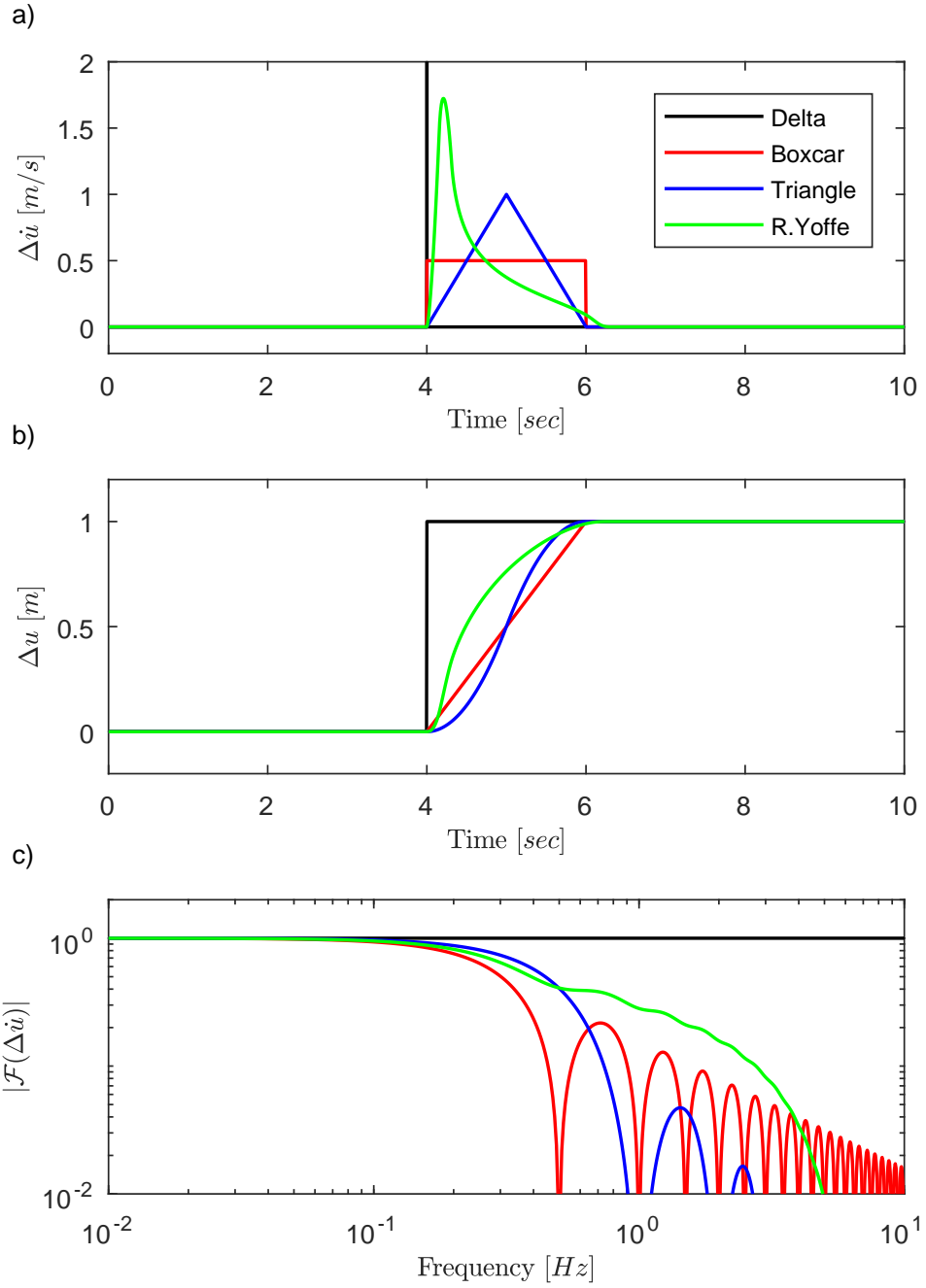


Figure 1.4: Schematic examples of slip functions of various shapes and their Fourier spectra. Each color has meaning of different shape of SRF described in text (see legend). Independent parameters defining these SRFs are the same for all shapes with $A = 1$ m, $t_0 = 4$ sec, $\tau_R = 2$ sec and $\tau_P = 0.2$ sec (unnecessary parameters are neglected). Panel **a)** show slip rate functions (SRF) $\Delta \dot{u}(t)$; panel **b)** represents their temporal integrals, i.e. slip time functions $\Delta u(t)$. **c)** Fourier amplitude spectra of the respective SRFs.

1.1.3 Moment tensor decomposition

Seismic moment tensor, MT, was introduced in Section 1.1.1 (see Eq. (1.5)) as an earthquake source model in the point source approximation. Such MT is a symmetric tensor of the second order describing nine couples of equivalent dipole forces that substitute generally oriented strain in source region in terms of seismic radiation. As the most common seismic sources originating inside the solid Earth are associated with shear faulting across an fault plane (Section 1.1.2), the most common type of MT is the double-couple (DC) source representing force equivalent of a displacement on the fault. Nevertheless, there are many examples of real seismic sources with a non-double-couple (non-DC) force equivalent as revealed by seismic wave radiation (e.g., Frohlich 1994; Miller et al. 1998). A possible type of non-DC components is an isotropic (ISO) source associated with a volumetric change in strain caused by underground explosions and implosions (e.g., Liu et al. 2018). Another types of non-DC force equivalents can be produced by volcanic intrusions (e.g., Nettles & Ekström 1998), cavity collapses (e.g., Rudajev & Šílený 1985), presence of high-pressure fluids during faulting (e.g., Vavryčuk 2011), shear faulting in anisotropic media (e.g., Vavryčuk 2005), and by shear faulting on a non-planar or complex faults (e.g., Frohlich 1994). The latter is also evident in Eq. (1.3) as the MT is an integral of the moment tensor density over the whole fault surface, which may be curved in general. Note that the non-DC force equivalents assumed in this section are not artifacts of MT inversion but real features of full MTs.

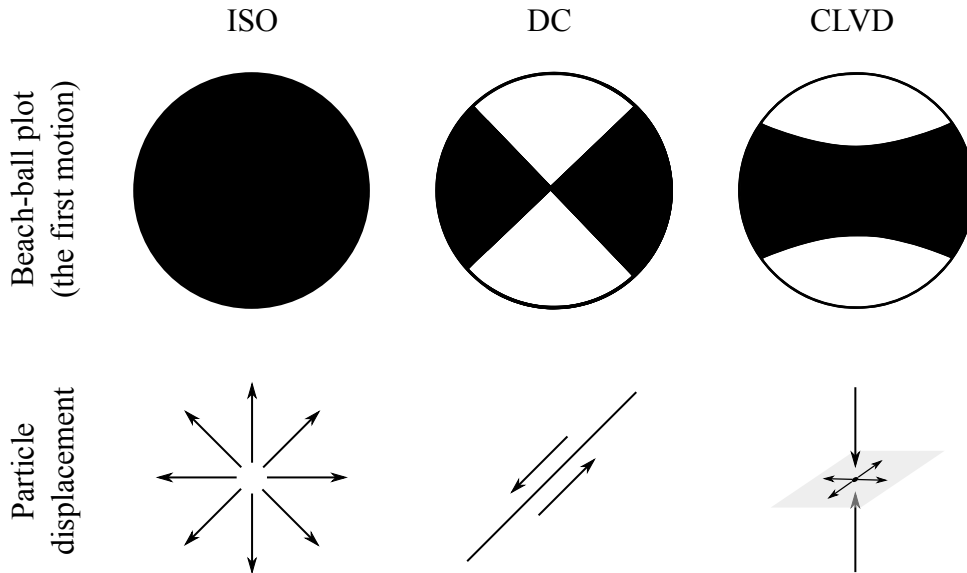


Figure 1.5: ISO, DC and CLVD elementary parts of MT, visualized by the beach-ball representations of focal mechanisms (upper row) and by the scheme of focal deformation (bottom row). The filled and blank segments in beach-ball plots distinguish directions with positive and negative P-wave polarity, respectively.

These examples demonstrate that non-DC force equivalents may be often present in the inverted MTs for all types of seismic sources. Such full MTs are usually decomposed into some elementary parts with a physical representation.

The most common decomposition by Knopoff & Randall (1970) divide a full MT into three elementary parts: ISO, DC, and compensated linear vector dipole (CLVD) (see Fig. 1.5). In the case of CLVD, the deformation along a polar axis is compensated by deformation in an equatorial band. Nevertheless, the MT decomposition can be performed in many alternative ways (see Jost & Herrmann 1989), e.g., ISO, DC₁, DC₂, and DC₃; or ISO, DC_{major}, and DC_{minor}, etc.

The MT decomposition into ISO, DC and CLVD proved to be useful for physical interpretation of earthquake sources, and became widely accepted and further developed (e.g., Jost & Herrmann 1989; Vavryčuk 2015). In order to derive its mathematical formulation, let us assume eigenvalues $\lambda_1^* \geq \lambda_2^* \geq \lambda_3^*$ of full MT (\mathbf{M}) with respective orthonormal row eigenvectors \mathbf{v}_1 , \mathbf{v}_2 and \mathbf{v}_3 . The general formula for \mathbf{M} in isotropic medium reads

$$\mathbf{M} = \lambda_1^* \mathbf{v}_1^T \mathbf{v}_1 + \lambda_2^* \mathbf{v}_2^T \mathbf{v}_2 + \lambda_3^* \mathbf{v}_3^T \mathbf{v}_3. \quad (1.21)$$

The first step is to decompose ISO and deviatoric (DEV) parts as

$$\mathbf{M} = \mathbf{M}_{\text{ISO}} + \mathbf{M}_{\text{DEV}}. \quad (1.22)$$

The ISO part of the full MT is defined as

$$\mathbf{M}_{\text{ISO}} = \frac{\lambda_1^* + \lambda_2^* + \lambda_3^*}{3} \cdot \begin{pmatrix} 1 & 0 & 0 \\ 0 & 1 & 0 \\ 0 & 0 & 1 \end{pmatrix} \quad (1.23)$$

$$= \frac{1}{3} \text{Tr}(\mathbf{M}) \mathbf{I} \quad (1.24)$$

$$= M_{\text{ISO}} \mathbf{I}, \quad (1.25)$$

where $\text{Tr}(\mathbf{M})$ is the trace of the tensor \mathbf{M} , \mathbf{I} is identity matrix and M_{ISO} is scalar seismic moment of the ISO component. Then, we assume eigenvalues $\lambda_1 \geq \lambda_2 \geq \lambda_3$ of the decomposed DEV part defined as

$$\lambda_i = \lambda_i^* - \frac{1}{3} \text{Tr}(\mathbf{M}) \quad (i = 1, 2, 3), \quad (1.26)$$

which fulfill the deviatoric condition $\lambda_1 + \lambda_2 + \lambda_3 = 0$. The formula for deviatoric moment tensor \mathbf{M}_{DEV} then reads

$$\mathbf{M}_{\text{DEV}} = \lambda_1 \mathbf{v}_1^T \mathbf{v}_1 + \lambda_2 \mathbf{v}_2^T \mathbf{v}_2 + \lambda_3 \mathbf{v}_3^T \mathbf{v}_3, \quad (1.27)$$

where eigenvectors \mathbf{v}_1 , \mathbf{v}_2 and \mathbf{v}_3 define T (tension), N (neutral), and P (pressure) axes of MT, respectively.

Eq. (1.27) is further expressed as sum of selected elementary parts of the deviatoric MT. In the case of MT decomposition into ISO, DC and CLVD parts (e.g., Vavryčuk 2015), the formula for \mathbf{M}_{DEV} reads

$$\mathbf{M}_{\text{DEV}} = \mathbf{M}_{\text{DC}} + \mathbf{M}_{\text{CLVD}} \quad (1.28)$$

$$= M_{\text{DC}} \mathbf{E}_{\text{DC}} + M_{\text{CLVD}} \mathbf{E}_{\text{CLVD}}, \quad (1.29)$$

where M_{DC} and M_{CLVD} are scalar seismic moments of respective source components, and further \mathbf{E}_{DC} and \mathbf{E}_{CLVD} are elementary (base) tensors defined as

$$\mathbf{E}_{\text{DC}} = \begin{pmatrix} 1 & 0 & 0 \\ 0 & 0 & 0 \\ 0 & 0 & -1 \end{pmatrix} \quad \mathbf{E}_{\text{CLVD}}^+ = \begin{pmatrix} 1 & 0 & 0 \\ 0 & -\frac{1}{2} & 0 \\ 0 & 0 & -\frac{1}{2} \end{pmatrix} \quad \mathbf{E}_{\text{CLVD}}^- = \begin{pmatrix} \frac{1}{2} & 0 & 0 \\ 0 & \frac{1}{2} & 0 \\ 0 & 0 & -1 \end{pmatrix}. \quad (1.30)$$

The elementary tensor for CLVD has two forms used as follows:

$$\mathbf{E}_{\text{CLVD}} = \begin{cases} \mathbf{E}_{\text{CLVD}}^+ & \text{when } \lambda_1 + \lambda_3 - 2\lambda_2 \geq 0 \\ \mathbf{E}_{\text{CLVD}}^- & \text{when } \lambda_1 + \lambda_3 - 2\lambda_2 < 0 \end{cases} \quad (1.31)$$

The CLVD is then aligned to the eigenvector respective to the largest absolute eigenvalue $|\lambda_i|$, ($i = 1, 2, 3$). This constraint arises from the deviatoric condition $\lambda_1 + \lambda_2 + \lambda_3 = 0$. Note that alternative definitions of CLVD elementary tensor are possible (e.g., Chapman & Leaney 2012). Scalar seismic moments from Eq. (1.29) are defined as

$$M_{\text{CLVD}} = \frac{2}{3}(\lambda_1 + \lambda_3 - 2\lambda_2), \quad (1.32)$$

$$M_{\text{DC}} = \frac{1}{2}(\lambda_1 - \lambda_3 - |\lambda_1 + \lambda_3 - 2\lambda_2|). \quad (1.33)$$

The total scalar seismic moment M_0 of the non-DC MT can be defined as a sum of scalar seismic moments of the respective source components defined in Eqs (1.25), (1.32), and (1.33):

$$M_0 = |M_{\text{ISO}}| + |M_{\text{CLVD}}| + M_{\text{DC}}. \quad (1.34)$$

The same value of M_0 is produced by the norm by Bowers & Hudson (1999)

$$M_0 = \|\mathbf{M}_{\text{ISO}}\| + \|\mathbf{M}_{\text{DEV}}\| \quad (1.35)$$

$$= |M_{\text{ISO}}| + \|\mathbf{M}_{\text{DEV}}\|, \quad (1.36)$$

where the spectral norm of the deviatoric moment tensor $\|\mathbf{M}_{\text{DEV}}\| = \max(|\lambda_i|)$, ($i = 1, 2, 3$). For details about definitions of the scalar seismic moment see Vavryčuk (2015). Practically, the amount of content of the ISO, DC, and CLVD components are expressed by their scale factors β_i defined as $\beta_i = M_i/M_0$, ($i = \text{ISO}, \text{DC}, \text{CLVD}$). While these scale factors satisfy

$$1 = |\beta_{\text{ISO}}| + |\beta_{\text{CLVD}}| + \beta_{\text{DC}}, \quad (1.37)$$

then decomposition in Eq. (1.29) can be expressed as

$$\mathbf{M} = M_0(\beta_{\text{ISO}}\mathbf{I} + \beta_{\text{DC}}\mathbf{E}_{\text{DC}} + \beta_{\text{CLVD}}\mathbf{E}_{\text{CLVD}}). \quad (1.38)$$

These scale factors are often expressed by percentage of the ISO, DC, or CLVD content in the non-DC MT (i.e. $\beta_i \cdot 100\%$).

The decomposition of non-DC MT is performed in order to physically interpret components of the seismic source. Nevertheless, it has to be emphasized that the source components (ISO, DC, and CLVD) cannot be understood as strictly separated focal mechanisms; the decomposition is merely mathematical description of a complex earthquake source. Still, there is an overview in Tab. 1.1 of some basic earthquake source types in terms of content of the ISO, DC, and CLVD components in isotropic media (artificial non-DC components resulting from an imprecise MT inversion are not assumed at this point). Further, please consider values of β_i in Tab. 1.1 as orientative as they may be influenced by many factors

like fault geometry (e.g., Frohlich 1994), v_P/v_S ratios of elastic medium (e.g., Vavryčuk 2015), anisotropy of the medium (e.g., Vavryčuk 2005), etc.

β_{ISO}	β_{DC}	β_{CLVD}	Source type	Phenomenon
0.0*	1.0*	0.0*	pure shear faulting	tectonic earthquakes
0.0*	0.8	0.2	shear faulting on nonplanar fault	complex tectonic earthquakes
0.2	0.0	0.8	magma intrusions	volcanic earthquakes
0.3	0.0*	0.7	pure tensile faulting	fault opening
-0.3	0.0*	-0.7	pure compressive faulting	fault closing
0.2	0.5	0.3	shear-tensile faulting	fault opening during rupturing
-0.2	0.5	-0.3	shear-tensile faulting	fault closing during rupturing
1.0*	0.0*	0.0*	underground explosion	nuclear tests

Note: *the exact β_i value by definition

Table 1.1: Overview of basic types of the seismic sources in terms of MT's content of the ISO, DC, and CLVD components in an isotropic full-space medium.

1.2 Bayesian probabilistic framework

A given description of an earthquake source from Section 1.1 can predict synthetic data for given model parameters. This problem of predicting observations is called as forward problem. The inverse problem then use observations to infer the values of parameters characterizing the earthquake source model. While the forward problem has a unique solution, the inverse problems may have multiple possible solutions in general. Here we overview Bayesian probabilistic framework for inverse problems (e.g., Tarantola & Valette 1982; Tarantola 2005), where a solution is represented by a probability.

Following Tarantola (2005) we introduce an abstract multi-dimensional vector space for an assumed choice of source parametrization, where each vector represents a model of the system. Such multi-dimensional space is called as model space \mathfrak{M} , and each model is denoted by vector \mathbf{m} . In analogy, the observed data are treated as data vector \mathbf{d} in an abstract multi-dimensional data vector space \mathfrak{D} . Note that the number of dimensions of \mathfrak{M} and \mathfrak{D} differs by definition, with meaning of total number of model parameters and total number of measured data, respectively.

The theoretical forward problem, where data \mathbf{d} for a given model \mathbf{m} are predicted by a theory (i.e. earthquake source representations), can be expressed using a forward operator $\mathbf{g}(\cdot)$ as

$$\mathbf{d} = \mathbf{g}(\mathbf{m}), \quad (1.39)$$

where the forward problem $\mathbf{g}(\cdot)$ itself can be subject of uncertainty in general. The Bayesian solution of the inverse problem (Bayes 1763) is then defined as the conditional posterior probability density function (PDF) on the model space $p(\mathbf{m}|\mathbf{d})$, expressed by Bayes theorem as

$$p(\mathbf{m}|\mathbf{d}) = \frac{p(\mathbf{m}) p(\mathbf{d}|\mathbf{m})}{p(\mathbf{d})}, \quad (1.40)$$

where

$$p(\mathbf{d}) = \int_{\mathfrak{M}} p(\mathbf{m}) p(\mathbf{d}|\mathbf{m}) d\mathbf{m}. \quad (1.41)$$

Here $p(\mathbf{m})$ is a prior PDF on the model parameters (i.e. independent on the observed data), and $p(\mathbf{d}|\mathbf{m})$ is conditional probability of data for given model \mathbf{m} , i.e. so-called likelihood function. The likelihood function contains statistical information on both the observed data and the theory uncertainty. Substituting observed data \mathbf{d}_{obs} as $\mathbf{d} = \mathbf{d}_{obs}$ in Eq. (1.40), the posterior PDF on the model space reads

$$p(\mathbf{m}|\mathbf{d}_{obs}) = const. p(\mathbf{m}) p(\mathbf{d}_{obs}|\mathbf{m}), \quad (1.42)$$

where *const.* is a normalization constant.

Let us assume that data space \mathfrak{D} is linear and that the observed data \mathbf{d}_{obs} of finite length n are characterized by Gaussian data errors with $n \times n$ covariance matrix \mathbf{C}_D (see Tarantola 2005, eq. 6.66). The likelihood function then reads

$$p(\mathbf{d}_{obs}|\mathbf{m}) = \frac{const.}{\sqrt{(2\pi)^n |\mathbf{C}_D|}} \cdot \exp\left(-\frac{1}{2} \mathcal{L}(\mathbf{m})\right) \quad (1.43)$$

where $|\mathbf{C}_D|$ is determinant of the covariance matrix and \mathcal{L} defines misfit between observed data \mathbf{d}_{obs} and synthetics calculated using the theoretical relation in Eq. (1.39). The misfit is written in matrix form as

$$\mathcal{L}(\mathbf{m}) = \left(\mathbf{d}_{obs} - \mathbf{g}(\mathbf{m})\right)^T \mathbf{C}_D^{-1} \left(\mathbf{d}_{obs} - \mathbf{g}(\mathbf{m})\right). \quad (1.44)$$

Combining Eqs (1.42) and (1.43) we get a formula for the posterior PDF on the model space assuming Gaussian data errors (Tarantola 2005, eq. 1.100) as

$$p(\mathbf{m}|\mathbf{d}_{obs}) = const. p(\mathbf{m}) \exp\left(-\frac{1}{2} \mathcal{L}(\mathbf{m})\right). \quad (1.45)$$

Note that since the uncertainty of the theory is incorporated into the uncertainty of the observed data, $\mathbf{C}_D = \mathbf{C}_{data} + \mathbf{C}_{theory}$ as in Tarantola (2005, example 1.36). This may be useful in earthquake source inversions, where the observed data are subject of uncertainty originating from imprecise measurements and also uncertainties in forward problem formulations (e.g., uncertainty of Green's functions). Then, the \mathbf{C}_D may include also uncertainty of Green's functions.

We can further assume that the model space \mathfrak{M} is linear and that the prior model parameters \mathbf{m}_{prior} of length j are characterized by Gaussian errors with $j \times j$ covariance matrix \mathbf{C}_M . The prior PDF of the model parameters then reads (Tarantola 2005, eq. 1.102)

$$p(\mathbf{m}) = \frac{1}{\sqrt{(2\pi)^j |\mathbf{C}_M|}} \cdot \exp\left(-\frac{1}{2} \mathcal{K}(\mathbf{m})\right), \quad (1.46)$$

where \mathcal{K} defines misfit between model parameters \mathbf{m} and assumed prior model parameters \mathbf{m}_{prior} , written in matrix form as

$$\mathcal{K}(\mathbf{m}) = \left(\mathbf{m} - \mathbf{m}_{prior}\right)^T \mathbf{C}_M^{-1} \left(\mathbf{m} - \mathbf{m}_{prior}\right). \quad (1.47)$$

The Gaussian prior PDF of the model parameters in Eq. (1.46) can be included in Eq. (1.45), which is then equivalently written as (see Tarantola 2005, eq. 1.104)

$$p(\mathbf{m}|\mathbf{d}_{obs}) = const. \exp\left(-\frac{1}{2} \left(\mathcal{L}(\mathbf{m}) + \mathcal{K}(\mathbf{m})\right)\right). \quad (1.48)$$

Note that posterior PDF $p(\mathbf{m}|\mathbf{d}_{obs})$ on the model space in Eq. (1.48) depends on the sum of the data misfit and prior assumptions misfit, which implies that biased prior assumptions on the model have an influence on solution even if the theory is perfect. Further, when we assume no prior information on the model parameters (i.e. infinite standard deviation in \mathbf{C}_M or equivalently constant $p(\mathbf{m})$), the posterior PDF simplifies to

$$p(\mathbf{m}|\mathbf{d}_{obs}) = const. \exp\left(-\frac{1}{2} \mathcal{L}(\mathbf{m})\right). \quad (1.49)$$

Practically speaking, the formulations of the posterior PDF by Eqs (1.48) and (1.49) can be used for Bayesian inversions of various representations of earthquake source. In our applications, the observed data \mathbf{d}_{obs} is a vector of all measured seismograms, while the forward operator $\mathbf{g}(\cdot)$ is a representation of an earthquake

source as described in Section 1.1. The latter can be CMT representation of Eq. (1.9) or finite-fault representation of Eq. (1.13), where both relate source parameters with predicted displacement (i.e. synthetic seismograms). The covariance matrix \mathbf{C}_D then characterizes expected Gaussian errors between the observed and synthetic seismograms. Finally, the solution of the inverse problem in such formulation is the posterior PDF over multi-dimensional space \mathfrak{M} . This posterior PDF can be inspected using analytical techniques (e.g., linear least-squares methods) or extensive exploration of the model space (i.e. Monte-Carlo methods).

1.2.1 Linear least-squares methods

Linear least-squares methods are popular for solving inverse problems because of undemanding computations. These methods can be applied if we assume linear vector spaces \mathfrak{D} and \mathfrak{M} , and that all prior uncertainties can be modeled using Gaussian distributions. Thereafter, when the forward problem solving the theoretical relation in Eq. (1.39) is linear, then the posterior uncertainty is Gaussian, and an analytical expression for the posterior PDF can be found. We emphasize, that even if the forward problem in Eq. (1.39) is non-linear a gradient least-squares method can be used in principle (see Tarantola 2005, pp. 68–80). Nevertheless, we overview here only the linear least-squares problem as required by this thesis.

The linear forward problem can be written in matrix form as

$$\mathbf{d} = \mathbf{G}\mathbf{m}, \quad (1.50)$$

where $n \times j$ matrix \mathbf{G} is linear forward operator (also known as design matrix), linearly relating model parameters \mathbf{m} (vector of length j) and synthetic data \mathbf{d} (vector of length n). The formula for the posterior PDF of Eq. (1.49) then reads

$$p(\mathbf{m}|\mathbf{d}_{obs}) = const. \exp\left(-\frac{1}{2}(\mathbf{d}_{obs} - \mathbf{G}\mathbf{m})^T \mathbf{C}_D^{-1}(\mathbf{d}_{obs} - \mathbf{G}\mathbf{m})\right). \quad (1.51)$$

As the data misfit is quadratic, the posterior PDF $p(\mathbf{m}|\mathbf{d}_{obs})$ is equivalently written as Gaussian PDF. After simple algebra, this Gaussian function attains its maximum for a center model $\tilde{\mathbf{m}}$ (i.e. maximum likelihood solution) and its shape is characterized by a posterior Gaussian covariance matrix $\tilde{\mathbf{C}}_M$. Such posterior PDF can be formulated as

$$p(\mathbf{m}|\mathbf{d}_{obs}) = c_\iota \exp\left(-\frac{1}{2}(\mathbf{m} - \tilde{\mathbf{m}})^T \tilde{\mathbf{C}}_M^{-1}(\mathbf{m} - \tilde{\mathbf{m}})\right), \quad (1.52)$$

with normalization constant c_ι equal to

$$c_\iota = \frac{1}{\sqrt{(2\pi)^j |\tilde{\mathbf{C}}_M|}}. \quad (1.53)$$

After some algebra the analytical solution for these posterior PDF's properties reads (see Tarantola 2005, eqs 3.40 and 3.41)

$$\tilde{\mathbf{m}} = (\mathbf{G}^T \mathbf{C}_D^{-1} \mathbf{G})^{-1} (\mathbf{G}^T \mathbf{C}_D^{-1} \mathbf{d}_{obs}), \quad (1.54)$$

$$\tilde{\mathbf{C}}_M = (\mathbf{G}^T \mathbf{C}_D^{-1} \mathbf{G})^{-1}. \quad (1.55)$$

For detailed derivation of Eqs (1.54) and (1.55) from Eqs (1.51) and (1.52) see Tarantola (2005, pp. 64–68). Evaluation of $\tilde{\mathbf{m}}$ and $\tilde{\mathbf{C}}_{\mathbf{M}}$ is then subject of the inverse problem (see example of two-dimensional PDF characterized by $\tilde{\mathbf{m}}$ and $\tilde{\mathbf{C}}_{\mathbf{M}}$ in Fig. 1.6a). The biggest advantage of such formulation is that the maximum likelihood solution $\tilde{\mathbf{m}}$, supplemented by its Gaussian uncertainty $\tilde{\mathbf{C}}_{\mathbf{M}}$, can be inferred directly from the observed data \mathbf{d}_{obs} , given linear forward operator \mathbf{G} and data covariance matrix $\mathbf{C}_{\mathbf{D}}$. Note that the maximum likelihood solution in Eq. (1.54) is strongly sensitive to outliers in the observed data \mathbf{d}_{obs} exceeding expected errors in the covariance matrix $\mathbf{C}_{\mathbf{D}}$. Also note that the estimation of the solution uncertainty by means of the posterior covariance matrix in Eq. (1.55) scales with assumed data covariance matrix $\mathbf{C}_{\mathbf{D}}$, which means that larger uncertainty of the data increases the uncertainty of the inferred model parameters.

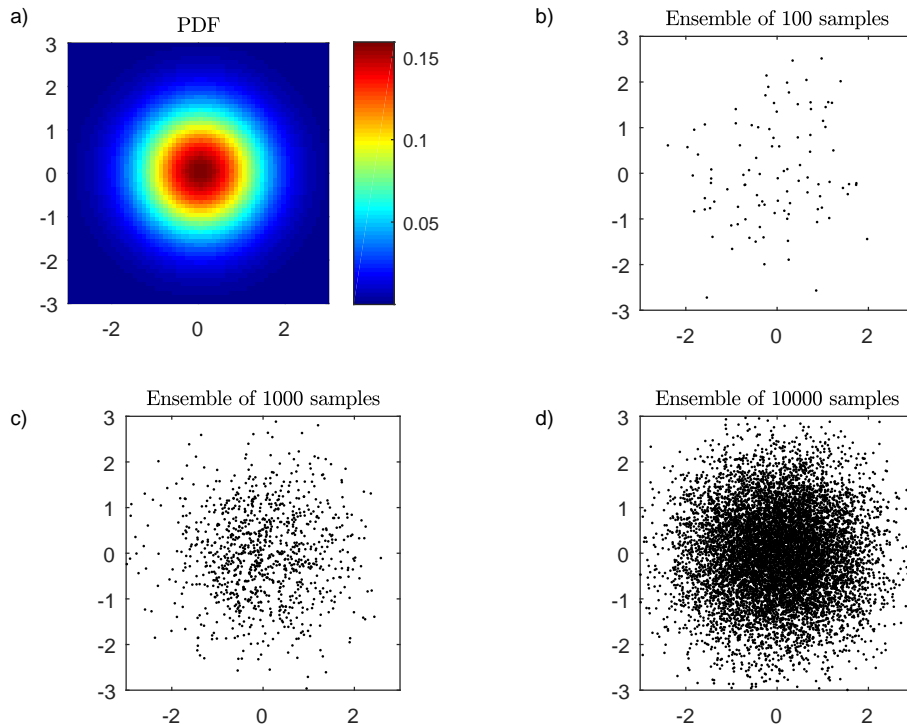


Figure 1.6: Example of Gaussian PDF and its random sampling. **a)** The Gaussian posterior PDF in two-dimensional model space \mathfrak{M} . This particular PDF is characterized by the center model $\tilde{\mathbf{m}} = (0, 0)$ and posterior covariance matrix $\tilde{\mathbf{C}}_{\mathbf{M}} = \mathbf{I}$, where \mathbf{I} is the identity matrix. Random samples drawn from this posterior PDF forming the ensemble of **b)** 100; **c)** 1000; and **d)** 10000 solutions.

A practical advantage of posterior Gaussian distributions is that it allows us to effectively generate random samples following such probability distributions. The random samples, drawn from the PDF by a random number generator algorithm, form so-called ensemble of random samples (see Fig. 1.6). Algorithms for effective generation of such ensembles are well described in literature for multi-dimensional (multivariate) Gaussian probability distributions (e.g., Genz & Bretz 2009), and they are implemented in standard numerical computational libraries (e.g., Matlab function `mvnrnd`).

1.2.2 Monte-Carlo methods

Some inverse problems require an extensive exploration of the model space \mathfrak{M} to achieve reasonable solution(s) as in the case of strongly non-linear problems and problems with complicated prior and/or posterior PDFs. Such exploration can be systematic (e.g., grid-searched) only for a small number of model parameters as the number of required tested models grows exponentially with the number of dimensions of the model space \mathfrak{M} , bringing unbearable demands on computation power. Hence, well-designed exploration algorithms need to be used.

The random samples (i.e. models \mathbf{m}) drawn from a posterior PDF form so-called ensemble of possible solutions as shown in Fig. 1.6. Here we assume rather complicated PDFs, and hence an extensive exploration algorithms has to be applied to create the ensemble. The class of computational algorithms that rely on random explorations of \mathfrak{M} are called Monte-Carlo (MC) methods (see Tarantola 2005, pp. 41–55). The problematic feature of these methods is that the sampled model space tends to be very empty at zones with lower probability density as deployed sampling algorithms have finite number of steps. This implies that a sufficient number of random samples should be drawn. Note that the measure of the “sufficient number” is rather subjective and depends on the current application. Finally, the ensemble of solutions is the inversion result, where it is possible to statistically inspect scatter or the most likely value of any model parameter. The ensemble also allows one to infer statistical properties of any derived quantities describing the solution.

Metropolis-Hastings algorithm

The Metropolis-Hastings algorithm, developed by Metropolis et al. (1953) and generalized by Hastings (1970), is a Markov chain Monte-Carlo (MCMC) method for sampling the posterior PDF by a chain of steps. The Markov chain has no memory in the sense that each step depends only on the previous step. The basic idea is to perform a “walk” through the model space as a sort of Brownian motion. Then using a probabilistic rule to modify the walk (some proposed steps are accepted and some rejected) we can obtain the ensemble of solutions drawn from posterior PDF. Such algorithms are considered as the most effective especially if the number of dimensions of \mathfrak{M} is large.

The algorithm starts from initial state \mathbf{m}_0 which should be arbitrary in general. In each step of the chain (i.e. $\mathbf{m}_0 \rightarrow \mathbf{m}_1 \rightarrow \mathbf{m}_2 \rightarrow \dots$), the model parameters \mathbf{m} are randomly perturbed with a forward step probability drawn from the proposal distribution $q(\mathbf{m}'|\mathbf{m})$ to create new (proposed) model \mathbf{m}' . The new model is accepted or rejected based on the “Metropolis choice” (Metropolis et al. 1953):

$$\mathbf{m}_{+1} = \begin{cases} \mathbf{m}', & \mathbf{m}' \text{ accepted with probability } \alpha(\mathbf{m} \rightarrow \mathbf{m}') \\ \mathbf{m}, & \mathbf{m}' \text{ rejected with probability } 1 - \alpha(\mathbf{m} \rightarrow \mathbf{m}') \end{cases} \quad (1.56)$$

Following Hastings (1970), the generalized acceptance probability of Eq. (1.56) reads

$$\alpha(\mathbf{m} \rightarrow \mathbf{m}') = \min \left(1, \frac{p(\mathbf{m}'|\mathbf{d}_{obs})}{p(\mathbf{m}|\mathbf{d}_{obs})} \frac{q(\mathbf{m}|\mathbf{m}')}{q(\mathbf{m}'|\mathbf{m})} \right), \quad (1.57)$$

where $q(\mathbf{m}|\mathbf{m}')$ is the proposal distribution used to draw probability of the reverse step ($\mathbf{m}' \rightarrow \mathbf{m}$). Substituting posterior PDFs in Eq. (1.57) by the form in Eq. (1.42), the acceptance probability leads to

$$\alpha(\mathbf{m} \rightarrow \mathbf{m}') = \min \left(1, \frac{p(\mathbf{m}')}{p(\mathbf{m})} \frac{p(\mathbf{d}_{obs}|\mathbf{m}')}{p(\mathbf{d}_{obs}|\mathbf{m})} \frac{q(\mathbf{m}|\mathbf{m}')}{q(\mathbf{m}'|\mathbf{m})} \right), \quad (1.58)$$

being independent on the normalization constant.

A generic version of Metropolis-Hastings is so-called random walk Metropolis-Hastings algorithm (or simply Metropolis algorithm; Metropolis et al. 1953), where the chain is driven by the random walk process (Pearson 1905; Einstein 1905). In such process, the forward and reverse steps are assumed to be reversible, i.e. $q(\mathbf{m}'|\mathbf{m}) = q(\mathbf{m}|\mathbf{m}')$ (see Hastings 1970, pp. 100). This condition is fulfilled for cases of a symmetric proposal distribution (i.e. probability density distribution of random perturbations) which is re-centered after each step at the value last generated by the Markov chain (e.g., Tierney 1994; Smith & Roberts 1993; Gustafson 1998). Then Eq. (1.58) reduces to

$$\alpha(\mathbf{m} \rightarrow \mathbf{m}') = \min \left(1, \frac{p(\mathbf{m}')}{p(\mathbf{m})} \frac{p(\mathbf{d}_{obs}|\mathbf{m}')}{p(\mathbf{d}_{obs}|\mathbf{m})} \right). \quad (1.59)$$

It is common to assume that the model parameters are randomly perturbed considering Gaussian proposal distribution, defined by its standard deviations in the model space \mathfrak{M} , i.e. Gaussian random walk Metropolis-Hastings algorithm. The Gaussian proposal distribution is symmetric function, hence the forward and reverse steps are reversible as shown in Fig. 1.7. The performance of such MCMC algorithm is then dependent on the choice of standard deviations of the proposal distributions governing implicitly the acceptance rates. The acceptance rates that are either “too high” or “too low” slow down the performance of the Markov chain (by means of efficiency), nevertheless the particular choice of these standard deviations does not influence the asymptotic distribution of drawn samples according to the posterior PDF. Following Roberts et al. (1997), the effective acceptance rate of the Gaussian random walk MCMC should to be close to $1/4$.

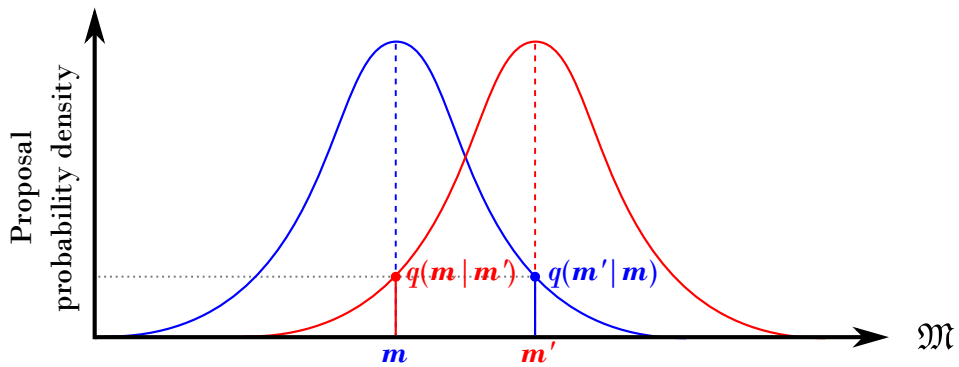


Figure 1.7: Proposal distribution in the case of the Gaussian random walk MCMC. Current model \mathbf{m} (blue) is randomly perturbed into proposed model \mathbf{m}' (red) with forward step probability drawn from the proposal distribution $q(\mathbf{m}'|\mathbf{m})$. The proposal distribution used to draw probability of reverse step $q(\mathbf{m}|\mathbf{m}')$ is assumed to be reversible $q(\mathbf{m}|\mathbf{m}') = q(\mathbf{m}'|\mathbf{m})$ as the Gaussian proposal distribution is symmetric function.

To complement, other versions of Metropolis-Hastings algorithm can be used in principal (see Tierney 1994). They differ mainly by proposal distribution q , or they are hybrids between random walk and general Metropolis-Hastings algorithm. For example, in the case of so-called guided walk Metropolis-Hastings algorithm the proposal distribution is symmetric, yet it is not re-centered after each step (Gustafson 1998). An example of hybrid Metropolis-Hastings is so-called reversible jump MCMC introduced by Green (1995, 2003). In the reversible jump MCMC, the proposed models \mathbf{m}' are allowed to be drawn from a different model space state, which can have different number of dimensions in general.

Parallel tempering

To increase the efficiency of a MCMC sampler it is possible to apply a method called parallel tempering (PT; e.g., Sambridge 2014). The PT sampling algorithm is similar to the better known simulated annealing method (Kirkpatrick et al. 1983) introducing modification of the posterior (sampled) PDF by an additional parameter called temperature γ . The modified posterior PDF from Eq. (1.42) is given by

$$p(\mathbf{m}|\mathbf{d}_{obs}, \gamma) = const. p(\mathbf{m}) \left(p(\mathbf{d}_{obs}|\mathbf{m}) \right)^{1/\gamma}. \quad (1.60)$$

The random samples are then drawn following such modified posterior PDF assuming multiple values of temperature γ . The modified posterior PDF become “smooth” for high temperatures, and as $\gamma \rightarrow \infty$ it becomes the prior PDF. For temperature $\gamma = 1$, as the other extreme, the modified posterior PDF equals to the original posterior PDF (see example in Fig. 1.8). When including the modified posterior PDF as defined in Eq. (1.60) in the acceptance probability of general Metropolis–Hastings algorithm in Eq. (1.58), the modified acceptance probability reads

$$\alpha(\mathbf{m} \rightarrow \mathbf{m}', \gamma) = \min \left(1, \frac{p(\mathbf{m}')}{p(\mathbf{m})} \left(\frac{p(\mathbf{d}_{obs}|\mathbf{m}')}{p(\mathbf{d}_{obs}|\mathbf{m})} \right)^{1/\gamma} \frac{q(\mathbf{m}|\mathbf{m}')}{q(\mathbf{m}'|\mathbf{m})} \right), \quad (1.61)$$

or alternatively the modified acceptance probability of the random walk Metropolis–Hastings algorithm in Eq. (1.59) reads

$$\alpha(\mathbf{m} \rightarrow \mathbf{m}', \gamma) = \min \left(1, \frac{p(\mathbf{m}')}{p(\mathbf{m})} \left(\frac{p(\mathbf{d}_{obs}|\mathbf{m}')}{p(\mathbf{d}_{obs}|\mathbf{m})} \right)^{1/\gamma} \right). \quad (1.62)$$

In the PT method, multiple parallel Markov chains sample the model space \mathfrak{M} simultaneously, each with different temperature. The chains with lower temperatures sample local areas of model space with PDF maxima, while chains with higher temperatures are able to escape from local maximum and sample the model space in a wider range. The temperature ladder is construct in order to have at least one chain with $\gamma_1 = 1$ and the temperatures span as $\gamma_1 \leq \gamma_2 \leq \dots \leq \gamma_{max}$. A feature of the PT method called as “exchange temperature swap” then allows two arbitrary chains to exchange the temperatures. The probability that two chains swap their temperatures is given by a balance condition for the swap proposed by Sambridge (2014, eq. 18), assuming a random walk through temperatures, as

$$\alpha(\gamma_A, \gamma_B) = \min \left(1, \left(\frac{p(\mathbf{d}_{obs}|\mathbf{m}_{\gamma_B})}{p(\mathbf{d}_{obs}|\mathbf{m}_{\gamma_A})} \right)^{1/\gamma_A} \left(\frac{p(\mathbf{d}_{obs}|\mathbf{m}_{\gamma_A})}{p(\mathbf{d}_{obs}|\mathbf{m}_{\gamma_B})} \right)^{1/\gamma_B} \right), \quad (1.63)$$

where \mathbf{m}_{γ_A} and \mathbf{m}_{γ_B} are models in two arbitrary Markov chains on temperatures γ_A and γ_B , respectively. Note that the swap balance condition in Eq. (1.63) assumes no tempering of the prior PDFs. Finally, the ensemble of solutions following the posterior PDF is formed only by random samples on temperature $\gamma_1 = 1$ sampling of the original posterior PDF $p(\mathbf{m}|\mathbf{d}_{obs})$, while chains on other temperatures work as a tool for exploration of the model space in a wider range.

For demonstration purpose, we perform MCMC sampling of a Gaussian posterior PDF (Fig. 1.8a). For this particular example we assume that the prior PDF is homogenous (Fig. 1.8b), with meaning of no available prior information on the model parameters. Eq. (1.62) then simplifies to

$$\alpha(\mathbf{m} \rightarrow \mathbf{m}', \gamma) = \min \left(1, \left(\frac{p(\mathbf{d}_{obs}|\mathbf{m}')}{p(\mathbf{d}_{obs}|\mathbf{m})} \right)^{1/\gamma} \right). \quad (1.64)$$

We have performed Gaussian random walk MCMC with the acceptance probability of Eq. (1.64) on three different temperatures ($\gamma = 1, 2, 10$). The temperature swaps are not assumed in this example to demonstrate the influence of different temperatures. Further for the demonstration purpose, the initial states \mathbf{m}_0 were the same for all three chains, while they should be random in practical applications. The walks through the model space were recorded, to illustrate the performance of MCMC in 100, 1000, and 10000 consecutive steps (see Fig. 1.8c). The chain with $\gamma = 1$ sample the original Gaussian posterior PDF (left panels in Fig. 1.8c). The chain with $\gamma = 2$ sample a modified Gaussian posterior PDF (middle panels in Fig. 1.8c), which results in more samples drawn from the “lower probability zones” on edges. Finally, the chain with $\gamma = 10$ sample a strongly modified Gaussian posterior PDF which becomes closer to a homogenous prior PDF (right panels in Fig. 1.8c). This allows MCMC sampler to explore the model space in a wider range.

The MCMC sampler can effectively sample general multi-dimensional PDFs with very complex probability distributions, while the multivariate Gaussian probability samplers (as shown in Fig. 1.6 drawn by Matlab function *mvnrnd*) are restricted to the Gaussian PDF. Further, the performance of MCMC sampler improves, while deploying temperature swaps and parallelize.

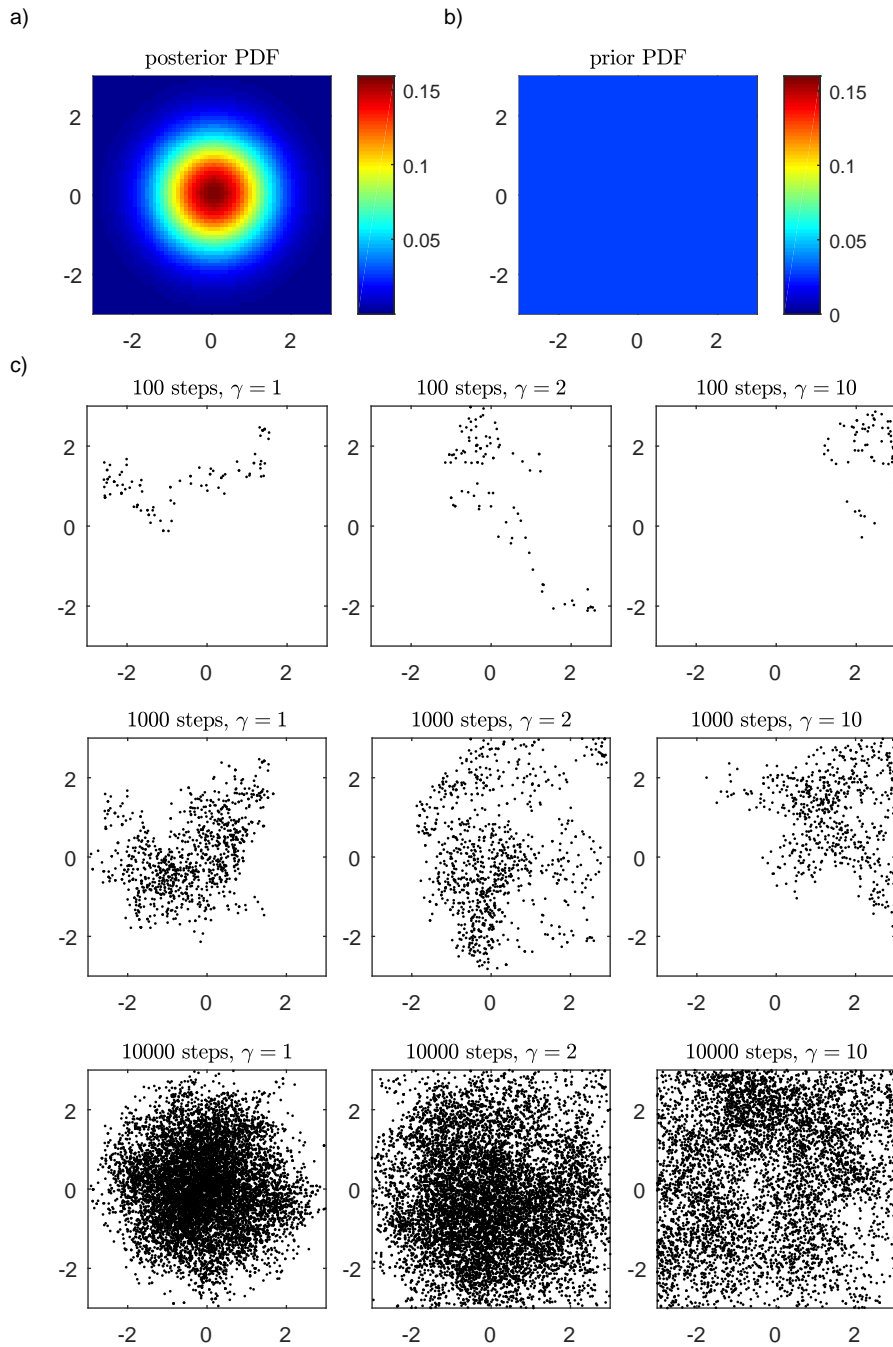


Figure 1.8: Example of sampling of Gaussian posterior PDF by three independent MCMC random walks. **a)** The original posterior PDF in two-dimensional model space \mathfrak{M} (the same PDF as in Fig. 1.6). **b)** The homogenous prior PDF of model parameters. **c)** 100, 1000, and 10000 consecutive steps of MCMC random walk (produced by Eq. (1.64)) with the initial state $\mathbf{m}_0 = (1.2, 1.8)$. The sets of samples are produced for three different temperatures $\gamma = 1, 2, 10$ (from left to right panels).

2. Fast and cheap approximation of Green's functions uncertainty for waveform-based earthquake source inversions

Published in *Geophysical Journal International*,
Volume 207, Issue 2, 1012–1029, August 2016, doi:10.1093/gji/ggw320,
text in this Chapter includes also its published supplementary material.

Miroslav Halló¹ & František Gallovič¹

Abstract: Green functions (GFs) are an essential ingredient in waveform-based earthquake source inversions. Hence, the error due to imprecise knowledge of a crustal velocity model is one of the major sources of uncertainty of the inferred earthquake source parameters. Recent strategies in Bayesian waveform inversions rely on statistical description of the GFs uncertainty by means of a Gaussian distribution characterized by a covariance matrix. Here we use Monte-Carlo approach to estimate the GF covariance considering randomly perturbed velocity models. We analyze the dependence of the covariance on various parameters (strength of velocity model perturbations, GF frequency content, source-station distance, etc.). Recognizing that the major source of the GF uncertainty is related to the random time shifts of the signal, we propose a simplified approach to obtain approximate covariances, bypassing the numerically expensive Monte-Carlo (MC) simulations. The resulting closed-form formulas for the approximate auto-covariances and cross-covariances between stations and components can be easily implemented in existing inversion techniques. We demonstrate that the approximate covariances exhibit very good agreement with the Monte-Carlo estimates, providing realistic variations of the GF waveforms. Furthermore, we show examples of implementation of the covariance matrix in a Bayesian moment tensor inversion using both synthetic and real datasets. We demonstrate that taking the GF uncertainty into account leads to improved estimates of the moment tensor parameters and their uncertainty.

Keywords: Inverse theory; Earthquake source observations; Theoretical seismology; Statistical seismology; Wave propagation.

2.1 Introduction

Inference of earthquake source parameters is an important subject in seismology. Realistic estimate of the uncertainty of earthquake source inversion results is essential for evaluation of solution quality. Strictly speaking, any geological interpretation of centroid moment tensor or rupture model requires proper assessment of their uncertainty (e.g., Sokos et al. 2015; Dettmer et al. 2014; Duputel et al.

¹Faculty of Mathematics and Physics, Charles University, Prague, Czech Republic

2015). For example, Valentine & Woodhouse (2010) also showed that imprecise source parameters negatively affect seismic tomography models.

In waveform-based earthquake source inversions two major origins of uncertainty can be recognized. The first one is related to the data error, which may be due to instrumental or ambient noise effects (Mustać & Tkalčić 2016). Typically, when dealing with larger events, the signal-to-noise ratio is rather high and data corrupted by strong disturbances (e.g., Zahradník & Plešinger 2010; Vackář et al. 2015) can be omitted. The second source of uncertainty, which is almost always neglected, is related to the uncertainty of Green’s functions (GFs) due to the inaccuracy of the crustal model considered. In practical applications, the uncertainties of the inferred source parameters due to the above-mentioned causes are typically estimated by accepting all models within a given threshold on the misfit value (e.g., Piatanesi et al. 2007; Valentine & Trampert 2012; Zahradník & Custódio 2012; Gallovič & Zahradník 2012). However, the value of such threshold is often ad-hoc or “empirical”, not based on a proper analysis of the underlying origin of the uncertainty. We point out that imprecise knowledge of the velocity model can lead to spurious non-double-couple components in moment tensor inversions (Zahradník et al. 2015) and artificial slip-rate peaks in slip inversions (Gallovič et al. 2015).

In terms of the Bayesian inference the uncertainty of source inversion results can be formulated by posterior probability density function (PDF) of the model parameters (Tarantola 2005, pp. 32–37). In such a case the two major sources of uncertainty (data error and GFs uncertainty) must be expressed by statistical models, typically by Gaussian PDFs parametrized by mean values and covariances. In particular, Yagi & Fukahata (2011) and Minson et al. (2013) also considered diagonal GF covariance matrix in their Bayesian slip inversion, treating the GF variance as an unknown parameter with uniform and log-normal prior PDF, respectively. Duputel et al. (2012) show the importance of considering the full covariance matrix of GF in the moment tensor inversion. However, in their examples they assume that the major origin of the error is due to the centroid mislocation. This study has been extended by Duputel et al. (2014, 2015), who propose to estimate the full covariance matrix approximately by considering linear relationship between the GFs and random, generally 3D, perturbations of the velocity model. However, their approach requires evaluation of sensitivity kernels, which are, in practice, very expensive to acquire (e.g., Kubo et al. 2016a). An alternative approach is represented by “empirical” estimation of the covariances from data residuals in so-called hierarchical inversions (Dettmer et al. 2007, 2014; Mustać & Tkalčić 2016). In particular, Dettmer et al. (2007, 2014) take into account the non-stationary character of the noise by scaling rows and columns of the covariance matrix by running averages of the residual waveforms.

We point out that not only the inversion procedures taking the GF uncertainty into account but even the methodology for estimation of the GF covariance matrix itself are not sufficiently developed yet. Moreover, besides exact uncertainty estimations, simple and easy-to-implement approaches have to be developed in order to efficiently involve the GF uncertainty in practical source inversions. The primary aim of this paper is to introduce such an approach by means of finding reasonable approximations for efficient evaluation of the GF covariance functions. We also address the estimation of cross-covariances between components at a

station and between stations, which have not been discussed in the literature yet despite being essential to correctly account for possible mutual dependencies of the GFs (e.g., Tarantola 2005, pp. 32–37).

In the present paper we first show by means of Monte-Carlo (MC) simulations in randomly perturbed 1D velocity models that the major source of the GF uncertainty is related to random time shifts of the GFs. This allows us to derive closed-form formulas for approximate auto- and cross-covariance functions to simplify the evaluation of the GF uncertainty avoiding any demanding computations. The proposed approximate covariances are tested on examples of moment tensor inversions using both synthetic and real data sets.

2.2 Covariance of Green’s functions

In the Bayesian framework the uncertainty of source inversions relies on statistical description of the GF uncertainty. In accordance with other authors, we assume that it can be described by a correlated multivariate Gaussian PDF characterized by a covariance matrix. To understand the relation between the uncertainty of the GFs and imprecise knowledge of the velocity model, we analyze the dependence of the covariance on velocity model perturbations using MC simulations considering stations at various distances and data in various frequency ranges. Then we propose methodologies for approximate yet simple estimation of the GF covariances.

2.2.1 Monte-Carlo estimation

We treat a GF due to randomly perturbed velocity model as a random function $x(t)$. The cross-covariance function (XCF) of two random GFs $x(t)$ and $y(t)$ is defined as

$$xcov(t, \tau) \stackrel{def}{=} E \left\{ \left[x(t) - E\{x(t)\} \right] \left[y(t + \tau) - E\{y(t + \tau)\} \right] \right\} = \quad (2.1)$$

$$= E \left\{ x(t)y(t + \tau) \right\} - E \left\{ x(t) \right\} E \left\{ y(t + \tau) \right\}, \quad (2.2)$$

where $E\{\cdot\}$ denotes expectation (mean over realizations of $x(t)$ and $y(t)$), t is time and τ is a time lag between samples (e.g., Marple 1986). Auto-covariance function (CF) can be derived from (2.2) considering $y(t) = x(t)$,

$$cov(t, \tau) = E \left\{ x(t)x(t + \tau) \right\} - E \left\{ x(t) \right\} E \left\{ x(t + \tau) \right\}. \quad (2.3)$$

A straightforward, though computationally demanding, approach to evaluate the covariances is by MC simulations (e.g., Tarantola 2005, pp. 41–55), where the expectations in (2.2) and (2.3) are directly obtained from a set of possible GFs for a particular source-receiver settings. For this purpose we consider an initial 1D layered velocity model and its 1500 random variations (Fig. 2.1a). In particular, following Tarantola (2005, pp. 164–170), we randomly vary logarithms of incompressibility modulus κ^* , shear modulus μ^* , and layer thicknesses. The parameters are changed independently to each other and also independently in all layers, assuming Gaussian distribution characterized by standard deviation σ_M expressed in percentage of the initial (mean) value.

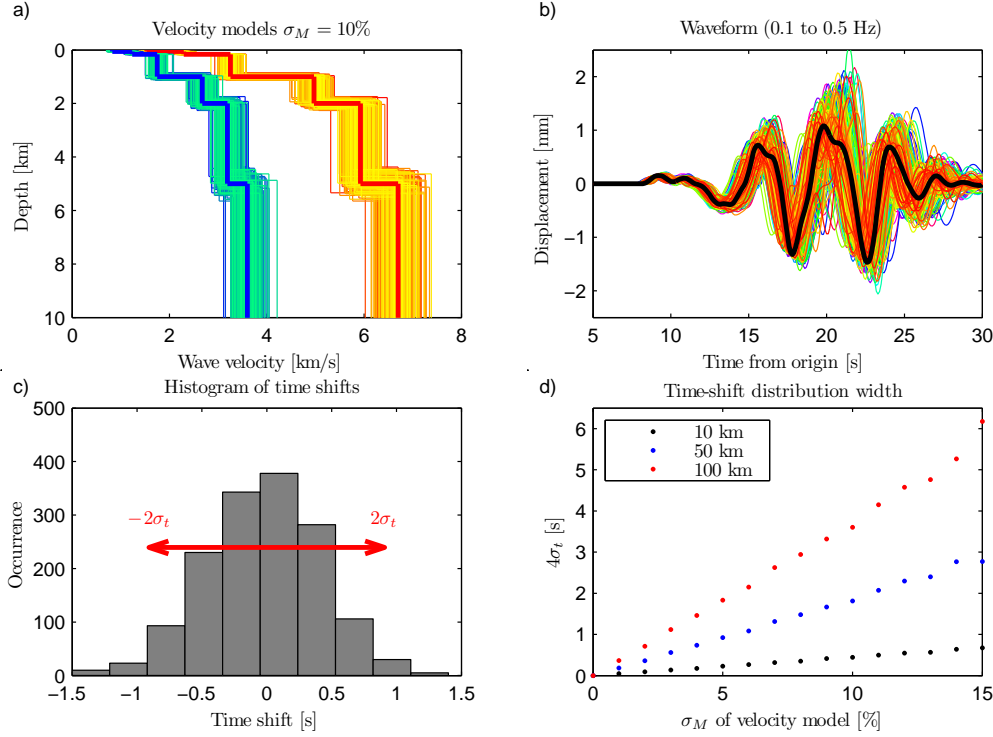


Figure 2.1: Monte-Carlo simulations. **a)** Example of the set of randomly perturbed velocity models with standard deviation $\sigma_M = 10\%$. The red/blue lines are the mean P-/S-wave velocity profiles and warm/cold colors are the P-/S-wave velocities of the perturbed models, respectively. **b)** Examples of the GFs at one component simulated by the discrete wavenumber method for the source-receiver distance of 50 km ($\sigma_M = 10\%$). The black line is the “mother” GF calculated in the mean velocity model. Other colors of waveforms have no meaning and are used only for clearer view. **c)** Distribution of time shifts of GFs from panel **b** estimated from waveforms filtered at very low frequencies (0.05–0.09 Hz) to avoid cycle skipping. The red line shows its characteristic width $4\sigma_t$. **d)** The dependence of the characteristic width of the time shift distribution ($4\sigma_t$) on the strength of the velocity model perturbations σ_M for three source-receiver distances (see legend).

We simulate GFs for source-receiver distances 10, 50, 100 km in the random realizations of the velocity models by discrete wavenumber method (Bouchon 1981), assuming a Dirac delta function as the source time function. GFs computed in the mean velocity model are referred to as the “mother” GFs. Fig. 2.1b shows example of the generated GFs for one source-receiver distance. They are similar in shape even though the velocity model perturbations are as large as 10% in the present example (maximal correlation coefficients are higher than 0.7 for all the generated GFs). A pronounced effect of the velocity model variations is represented by shifts of the generated waveforms in time. These time shifts (evaluated in this synthetic test from waveform cross-correlation lag from low-frequency waveforms to avoid cycle skipping) have approximately Gaussian distribution with standard deviation σ_t as demonstrated by the histogram in Fig. 2.1c. As illustrated in Fig. 2.1d, the characteristic width L of the time shift distribution defined as $L = 4\sigma_t$ increases approximately linearly with the velocity model perturbations σ_M with rate depending on the epicentral distance.

Solid lines in Figs 2.2a and 2.2b show examples of the CFs of a single GF

component determined from the set of simulated GFs using Eq. (2.3) for various lags τ and strengths of the velocity model perturbations σ_M . The CFs for given lag τ between samples of the GFs are clearly non-stationary, i.e. depending, generally, on time (see Figs 2.2a and 2.2b). The CFs determined this way could be used, in principle, for construction of the full covariance matrix (shown in Fig. 2.2c). However, the MC technique is very demanding on computational power as there is required an enormous set of possible GFs.

2.2.2 Approximate covariance function

Here we propose to substitute the demanding MC estimation of the GF covariance by a simplified approach, assuming that the only effect of the velocity model perturbations on the covariances is the time shift of the mother GFs. As we demonstrate later in Section 2.2.4, despite of this rather strong assumption, the approximate covariances reproduce variations of both the arrival time and the waveform amplitudes.

Let us point out that the proposed methodology is intended to deal with unknown velocity model perturbations that are close to the mean model. In particular, it is not meant to substitute (or correct for) missing velocity structures with strong effects on the waveforms, such as deep sedimentary basins. If some stations are affected by such structures, the modeling should either account for them or such stations should be omitted from the inversion. In any case, we point out that any (even 3D) velocity model is subject to uncertainty, which could be accounted for by our simplified approach.

Let us derive the approximate formulas for XCF of two, generally different, waveforms with random time shifts. We consider two “mother” waveforms $f(t)$ and $g(t)$ representing GFs in the mean velocity model. Assuming that these waveforms are randomly shifted in time, we define new (random) waveforms $x(t) = f(t - l_1)$ and $y(t) = g(t - l_1 - l_{12})$. The time shift l_1 is random but the same for both signals, while l_{12} characterizes their relative random time shift. We denote PDFs of l_1 and l_{12} as $p_1(l_1)$ and $p_{12}(l_{12})$, respectively. Expectations $E\{\cdot\}$ in Eq. (2.2) can be evaluated using “mother” waveforms and the PDFs $p_1(l_1)$ and $p_{12}(l_{12})$ as

$$E\{x(t)\} = \int_{-\infty}^{\infty} f(t - l_1) p_1(l_1) dl_1 \quad (2.4)$$

$$E\{y(t + \tau)\} = \int_{-\infty}^{\infty} \int_{-\infty}^{\infty} g(t + \tau - l_1 - l_{12}) p_{12}(l_{12}) p_1(l_1) dl_{12} dl_1 \quad (2.5)$$

$$E\{x(t)y(t + \tau)\} = \int_{-\infty}^{\infty} \int_{-\infty}^{\infty} f(t - l_1) g(t + \tau - l_1 - l_{12}) p_{12}(l_{12}) p_1(l_1) dl_{12} dl_1 \quad (2.6)$$

The XCF formula for general PDFs $p_1(l_1)$ and $p_{12}(l_{12})$ can be obtained by putting

(2.4), (2.5) and (2.6) into Eq. (2.2):

$$\begin{aligned} xcov(t, \tau) &= \int_{-\infty}^{\infty} \int_{-\infty}^{\infty} f(t - l_1) g(t + \tau - l_1 - l_{12}) p_{12}(l_{12}) p_1(l_1) dl_{12} dl_1 - \\ &- \int_{-\infty}^{\infty} f(t - l_1) p_1(l_1) dl_1 \int_{-\infty}^{\infty} \int_{-\infty}^{\infty} g(t + \tau - l_1 - l_{12}) p_{12}(l_{12}) p_1(l_1) dl_{12} dl_1, \end{aligned} \quad (2.7)$$

requiring only specification of the “mother” waveforms and PDFs of the time shifts. It is, in principle, applicable in covariance matrix estimation in this form; nevertheless, the formula can be further simplified by assuming that the time shifts are uniformly distributed,

$$p_1(l_1) = \Pi_{L_1}(l_1), \quad (2.8)$$

$$p_{12}(l_{12}) = \Pi_{L_{12}}(l_{12}), \quad (2.9)$$

where Π_L is a boxcar function of unit area centered around zero, L_1 and L_{12} are widths of the uniform probability density distributions. The time-shift l_1 is uniformly distributed in the time interval from $(-L_1)/2$ to $(+L_1)/2$. And analogically, the time-shift l_{12} is uniformly distributed from $(-L_{12})/2$ to $(+L_{12})/2$. The expectations of the random processes in (2.4), (2.5) and (2.6) then simplify to

$$E\{x(t)\} = \frac{1}{L_1} \int_{-\frac{L_1}{2}}^{\frac{L_1}{2}} f(t - l_1) dl_1 \quad (2.10)$$

$$E\{y(t + \tau)\} = \frac{1}{L_1} \int_{-\frac{L_1}{2}}^{\frac{L_1}{2}} \frac{1}{L_{12}} \int_{-\frac{L_{12}}{2}}^{\frac{L_{12}}{2}} g(t + \tau - l_1 - l_{12}) dl_{12} dl_1 \quad (2.11)$$

$$E\{x(t)y(t + \tau)\} = \frac{1}{L_1} \int_{-\frac{L_1}{2}}^{\frac{L_1}{2}} \frac{1}{L_{12}} \int_{-\frac{L_{12}}{2}}^{\frac{L_{12}}{2}} f(t - l_1) g(t + \tau - l_1 - l_{12}) dl_{12} dl_1 \quad (2.12)$$

Putting (2.10), (2.11) and (2.12) into Eq. (2.2), the final formula for approximate cross-covariance (AXCF) reads:

$$\begin{aligned} \widetilde{xcov}(t, \tau) &= \frac{1}{L_1 L_{12}} \int_{-\frac{L_1}{2}}^{\frac{L_1}{2}} \int_{-\frac{L_{12}}{2}}^{\frac{L_{12}}{2}} f(t - l_1) g(t + \tau - l_1 - l_{12}) dl_{12} dl_1 - \\ &- \frac{1}{L_1} \int_{-\frac{L_1}{2}}^{\frac{L_1}{2}} f(t - l_1) dl_1 \frac{1}{L_1 L_{12}} \int_{-\frac{L_1}{2}}^{\frac{L_1}{2}} \int_{-\frac{L_{12}}{2}}^{\frac{L_{12}}{2}} g(t + \tau - l_1 - l_{12}) dl_{12} dl_1. \end{aligned} \quad (2.13)$$

Approximate auto-covariance (ACF) can be derived analogously from (2.3), or alternatively from (2.13) considering that the “mother” waveforms are identical

$g(t) = f(t)$, and that PDF $p_{12}(l_{12})$ becomes formally a Dirac delta function. The final formula for ACF then reads:

$$\begin{aligned} \widetilde{\text{cov}}(t, \tau) &= \frac{1}{L_1} \int_{-\frac{L_1}{2}}^{\frac{L_1}{2}} f(t - l_1) f(t + \tau - l_1) dl_1 - \\ &- \frac{1}{L_1} \int_{-\frac{L_1}{2}}^{\frac{L_1}{2}} f(t - l_1) dl_1 \frac{1}{L_1} \int_{-\frac{L_1}{2}}^{\frac{L_1}{2}} f(t + \tau - l_1) dl_1. \end{aligned} \quad (2.14)$$

The ACF formula thus requires only specification of the “mother” waveform (i.e. GF in the mean velocity model) and the width of the uniform time shift distribution L_1 . Eq. (2.14) is easy to implement as the integrals normalized by $1/L_1$ operate as smoothing by a moving time window of width L_1 .

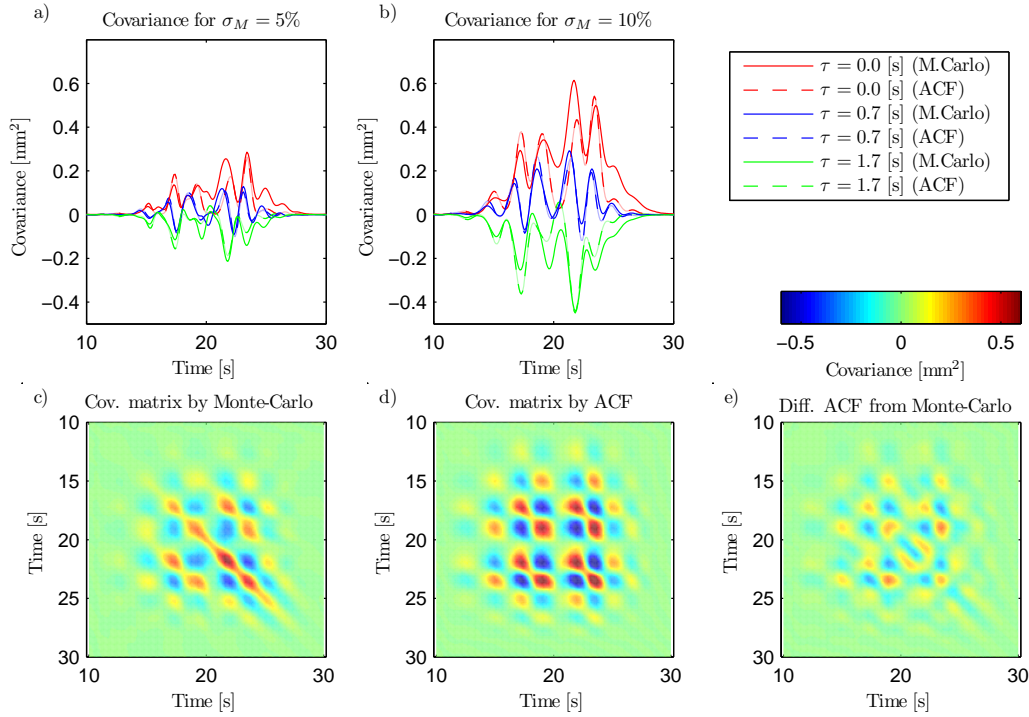


Figure 2.2: Examples of the GF auto-covariances. Panels **a)** and **b)** show time-dependence of the covariances assuming velocity model perturbations of strengths $\sigma_M = 5\%$ and $\sigma_M = 10\%$, respectively, for three selected time lags (see legend) estimated using the MC simulations (solid lines) and approximate ACF formula (2.14) (dashed lines). The GFs are calculated for source-receiver distance 50 km and filtered between 0.1–0.5 Hz. The width of the uniform PDF $L_1 = 4\sigma_t$ used in the approximate formula is adopted from the graph in Fig. 2.1d. Panels **c)** and **d)** show full covariance matrices estimated by MC simulations and using formula (2.14), respectively, assuming velocity model perturbations with $\sigma_M = 10\%$. Panel **e)** displays the differences between the latter two covariance matrices.

To illustrate the performance of the proposed simplified formulas we use “mother” GFs from the above-described MC simulations and consider uniform

$p_1(l_1)$ with width $L_1 = 4\sigma_t$, where σ_t is estimated from the MC simulations (see Fig. 2.1c). The resulting ACFs for such setting are shown in Figs 2.2a and 2.2b by dashed lines. They fit very well the main features of the CFs from the MC simulations (solid lines), confirming that in terms of the CFs the time shifts are indeed the dominant effect of the velocity model uncertainty. We note that this approximate approach is very effective because it skips the very demanding computation of thousands of GFs in the MC approach. A set of ACFs for different time lags then compose the full covariance matrix (Fig. 2.2d), which is again close to the full covariance matrix from the MC simulations (Fig. 2.2c) in terms of its pattern including signs. The rather minor differences between the two covariance matrices are shown in Fig. 2.2e and discussed in more detail in Section 2.2.4.

2.2.3 Stationarized covariance function

Here we introduce even stronger simplification of the covariance function. The motivation is as follows. Since the real elastic parameters of the Earth are rather complex (3D, anisotropic, etc.), the covariance determined by MC simulations might not reflect the reality perfectly. Nevertheless, we can assume that the overall pattern of the simulated CFs and ACFs effectively captures the main features of the GFs uncertainty. In particular, we consider that such representative of the true uncertainty for each time lag τ is just the CF's average over time, $\frac{1}{T} \int_{-\infty}^{\infty} cov(t, \tau) dt$, where T is duration of the dominant part of the signal. By calculating the mean of the (non-stationary) CF over time we obtain covariance dependent only on the time lag τ , which is property of so-called wide-sense stationary random signals (e.g., Marple 1986), and thus we denote this approach as stationarization. For example, when the stationarized covariance function (SCF) is evaluated from the ACF, we call it stationarized approximate covariance function (SACF),

$$\overline{cov}(\tau) \stackrel{def}{=} \frac{1}{T} \int_{-\infty}^{\infty} \widetilde{cov}(t, \tau) dt. \quad (2.15)$$

Note that this simplification will also help us to better understand the role of the covariance function in the source inversion (see Section 2.3.4). Since the SACFs are by definition stationary (i.e. depending only on lag τ), the respective covariance matrix has Toeplitz structure (diagonal-constant). Such property may be useful in specific (e.g., large-scale or iterative) applications because it permits very cheap calculation of the matrix's inverse, which is required when solving inverse problems (e.g., Tarantola 2005, pp. 62–68; Trench 1964). Note that the stationarized approximate cross-covariance (SAXCF) can be defined analogously

$$\overline{xcov}(\tau) \stackrel{def}{=} \frac{1}{T} \int_{-\infty}^{\infty} \widetilde{xcov}(t, \tau) dt. \quad (2.16)$$

After substitution of the AXCF in Eq. (2.13) into definition of the SAXCF

in Eq. (2.16) the formula for the SAXCF reads:

$$\begin{aligned}
\overline{xcov}(\tau) &= \frac{1}{T} \int_{-\infty}^{\infty} \frac{1}{L_1 L_{12}} \int_{-\frac{L_1}{2}}^{\frac{L_1}{2}} \int_{-\frac{L_{12}}{2}}^{\frac{L_{12}}{2}} f(t - l_1) g(t + \tau - l_1 - l_{12}) dl_{12} dl_1 dt - \\
&\quad \underbrace{\hspace{15em}}_{\text{I.}} \\
&- \frac{1}{T} \int_{-\infty}^{\infty} \frac{1}{L_1} \int_{-\frac{L_1}{2}}^{\frac{L_1}{2}} f(t - l_1) dl_1 \underbrace{\frac{1}{L_1 L_{12}} \int_{-\frac{L_1}{2}}^{\frac{L_1}{2}} \int_{-\frac{L_{12}}{2}}^{\frac{L_{12}}{2}} g(t + \tau - l_1 - l_{12}) dl_{12} dl_1 dt}_{\text{II.}}.
\end{aligned} \tag{2.17}$$

Integrals in (2.17) can be solved analytically using substitution $z = t - l_1$, and the definition of cross-correlation of real signals $r_{fg}(\tau) \stackrel{\text{def}}{=} \int_{-\infty}^{\infty} f(t)g(t + \tau)dt$. The first part (I.) of (2.17) is

$$\begin{aligned}
\text{I.} &= \frac{1}{TL_1 L_{12}} \int_{-\frac{L_1}{2}}^{\frac{L_1}{2}} \int_{-\frac{L_{12}}{2}}^{\frac{L_{12}}{2}} \int_{-\infty}^{\infty} f(z) g(z + \tau - l_{12}) dz dl_{12} dl_1 \\
&= \frac{1}{TL_1 L_{12}} \int_{-\frac{L_1}{2}}^{\frac{L_1}{2}} \int_{-\frac{L_{12}}{2}}^{\frac{L_{12}}{2}} r_{fg}(\tau - l_{12}) dl_{12} dl_1 \\
&= \frac{1}{TL_{12}} \int_{-\frac{L_{12}}{2}}^{\frac{L_{12}}{2}} r_{fg}(\tau - l_{12}) dl_{12}.
\end{aligned} \tag{2.18}$$

The second part (II.) can be written as

$$\begin{aligned}
\text{II.} &= \frac{1}{TL_1^2 L_{12}} \int_{-\frac{L_1}{2}}^{\frac{L_1}{2}} \int_{-\frac{L_1}{2}}^{\frac{L_1}{2}} \int_{-\frac{L_{12}}{2}}^{\frac{L_{12}}{2}} \int_{-\infty}^{\infty} f(z) g(z + \tau - l_{12} + l_1 - k_1) dz dl_{12} dl_1 dk_1 \\
&= \frac{1}{TL_1^2 L_{12}} \int_{-\frac{L_1}{2}}^{\frac{L_1}{2}} \int_{-\frac{L_1}{2}}^{\frac{L_1}{2}} \int_{-\frac{L_{12}}{2}}^{\frac{L_{12}}{2}} r_{fg}(\tau - l_{12} + l_1 - k_1) dl_{12} dl_1 dk_1 \\
&\dots \quad \text{after simple algebra with } s = l_1 - k_1 \\
&= \frac{1}{TL_1^2 L_{12}} \int_{-\frac{L_{12}}{2}}^{\frac{L_{12}}{2}} \int_{-L_1}^{L_1} (L_1 - |s|) r_{fg}(\tau - l_{12} + s) ds dl_{12} \\
&= \frac{1}{TL_{12}} \int_{-\frac{L_{12}}{2}}^{\frac{L_{12}}{2}} (\wedge_{2L_1}(\tau) \star r_{fg}(\tau - l_{12})) dl_{12}.
\end{aligned} \tag{2.19}$$

Equation (2.19) is an integral of correlation of the ‘‘mother’’ waveforms’ cross-correlation r_{fg} with the triangle function $\wedge_{2L_1}(\tau)$ of unit area centered around

zero with duration $2L_1$. The triangle function is symmetrical function, and hence the result of correlation operation (\star) is identical to convolution ($*$). Combining of (2.17), (2.18) and (2.19) we get simple analytical formula for the SAXCF:

$$\begin{aligned} \overline{xcov}(\tau) &= \frac{1}{TL_{12}} \left[\int_{-\frac{L_{12}}{2}}^{\frac{L_{12}}{2}} r_{fg}(\tau - l_{12}) dl_{12} - \int_{-\frac{L_{12}}{2}}^{\frac{L_{12}}{2}} (\wedge_{2L_1}(\tau) * r_{fg}(\tau - l_{12})) dl_{12} \right] = \\ &= \frac{1}{T} \Pi_{L_{12}}(\tau) * [r_{fg}(\tau) - \wedge_{2L_1}(\tau) * r_{fg}(\tau)], \end{aligned} \quad (2.20)$$

where $\Pi_{L_{12}}(\tau)$ is the time-centered boxcar function with base equal to L_{12} and with unit area. The triangle function $\wedge_{2L_1}(\tau)$ is a characteristics of the possible joint time shifts, while the boxcar function $\Pi_{L_{12}}(\tau)$ is characteristics of the possible relative time shifts.

The analytical formula for SAXCF (2.20) describes cross-covariance of two different “mother” waveforms $f(t)$ and $g(t)$ with generally different time shifts. Such settings is suitable for computing cross-covariance of signals recorded at two different seismic stations or at two components of the same station. The formula further simplifies assuming auto-covariance. The cross-correlation r_{fg} becomes auto-correlation $r_f(\tau) \stackrel{def}{=} \int_{-\infty}^{\infty} f(t)f(t+\tau)dt$ and $\Pi_{L_{12}}(\tau)$ becomes the Dirac delta function. The analytical formula for the SACF is then

$$\overline{cov}(\tau) = \frac{1}{T} [r_f(\tau) - \wedge_{2L_1}(\tau) * r_f(\tau)]. \quad (2.21)$$

Figs 2.3a and 2.3b show examples of the SACFs (red lines) obtained using Eq. (2.21). We consider the width of the uniform PDF L_1 equal to the characteristic width of the time shift distributions from the MC simulations (Fig. 2.1d), $L_1 = 4\sigma_t$. In Figs 2.3a and 2.3b we scale the covariances by the arithmetic mean of the squares of the signal f (i.e. square of the signal root-mean-square, $RMS^2(f(t))$) as it represents the maximum possible value of SACF. Indeed, by definition, the auto-correlation $r_f(\tau)$ has its maximum value at the zero time lag, and from Eq. (2.21) it follows

$$\lim_{L_1 \rightarrow \infty} (\overline{cov}(0)) = \frac{r_f(0)}{T} = RMS^2(f(t)). \quad (2.22)$$

Note that RMS^2 (i.e. “signal energy density”) is determined from the dominant part of the earthquake signal defined by the interval T .

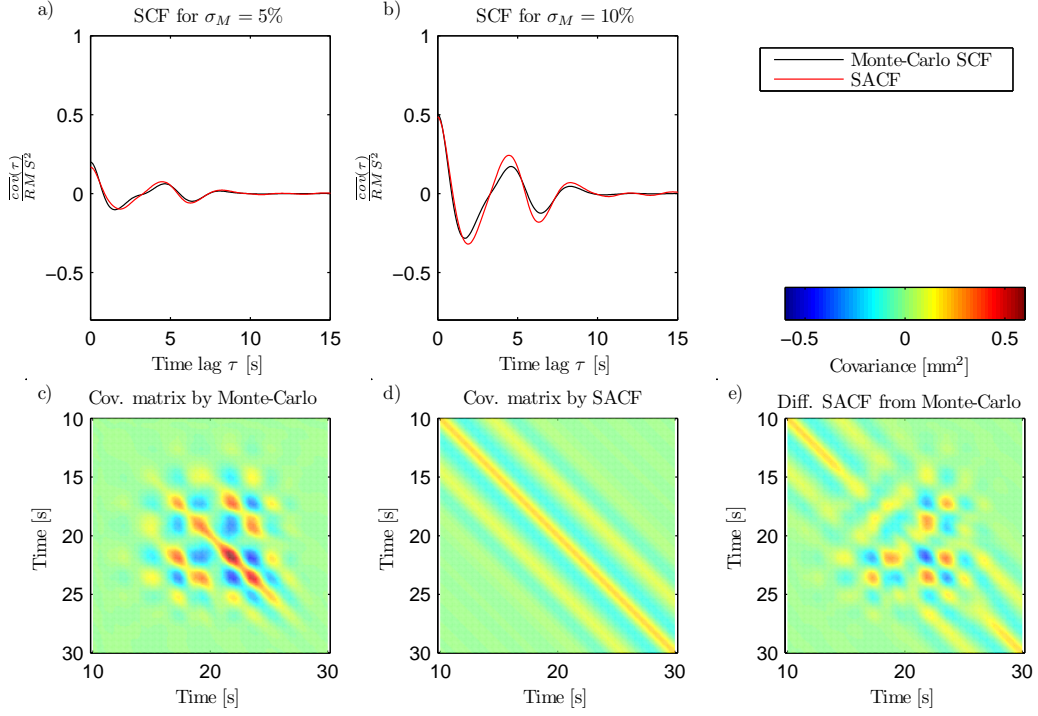


Figure 2.3: Examples of the stationarized auto-covariances (SCFs). Panels **a)** and **b)** show the SCF for two strengths of the model perturbations, $\sigma_M = 5\%$ and $\sigma_M = 10\%$, respectively, obtained by the MC simulations (black lines) and by the approximate formula Eq. (2.21) (SACF, red lines). The source-receiver distance is 50 km and the GFs are filtered in range 0.1 – 0.5 Hz. The width of the uniform PDF $L_1 = 4\sigma_t$ used in the approximate formula is adopted from the graph in Fig. 2.1d. Duration of the dominant part of the earthquake signal $T = 15$ sec. The SCF values on y-axis are scaled by the signal energy density, i.e. the mean square amplitude of the signal (RMS^2). Panels **c)** and **d)** show full covariance matrices for velocity model perturbations corresponding to $\sigma_M = 10\%$ as obtained by the non-stationarized MC approach and using SACF formula in Eq. (2.21), respectively. Panel **e)** shows the difference between the SACF and the MC non-stationarized covariance matrices.

Fig. 2.3 compares the SACFs (in red) with the SCFs estimated by the MC approach (in black). The agreement is very good even for velocity model perturbations as large as 15% in the present example despite all the simplifications made. Let us point out that, interestingly, the shape of the stationarized CFs is similar to those obtained “empirically” from waveform residuals by Dettmer et al. (2007, 2014), suggesting that their posterior estimate of the data uncertainty is dominated by the velocity model uncertainty.

Let us discuss here specifically the zero time lag of the CF, expressing variance (uncertainty) of the GF at each time sample t (Figs 2.2a and 2.2b, in red lines). In particular, after stationarization of the CF (Figs 2.3a and 2.3b, zero time lag), where the zero time lag represents mean GF variance over the waveform duration. We evaluate the dependence of the SCFs’ zero time lag on various parameters: source-receiver distances, Butterworth filtering frequencies, and strengths of velocity model perturbations σ_M . Fig. 2.4 shows these dependencies obtained by the approximate approach (dashed lines) as compared with the those obtained from the MC simulations (solid lines). The variances for absolutely correct ve-

velocity model ($\sigma_M = 0\%$) are equal to zero by definition as there is no possible variation of GFs. The variances then asymptotically increase with increasing velocity model uncertainty up to the case of variations as large as the RMS^2 . The increase of the GF variations is steeper for larger source-receiver distances (i.e. as the wave travel-time through the inaccurate velocity model increases), and also for higher considered frequencies (i.e. as the number of wavelengths along the path increases).

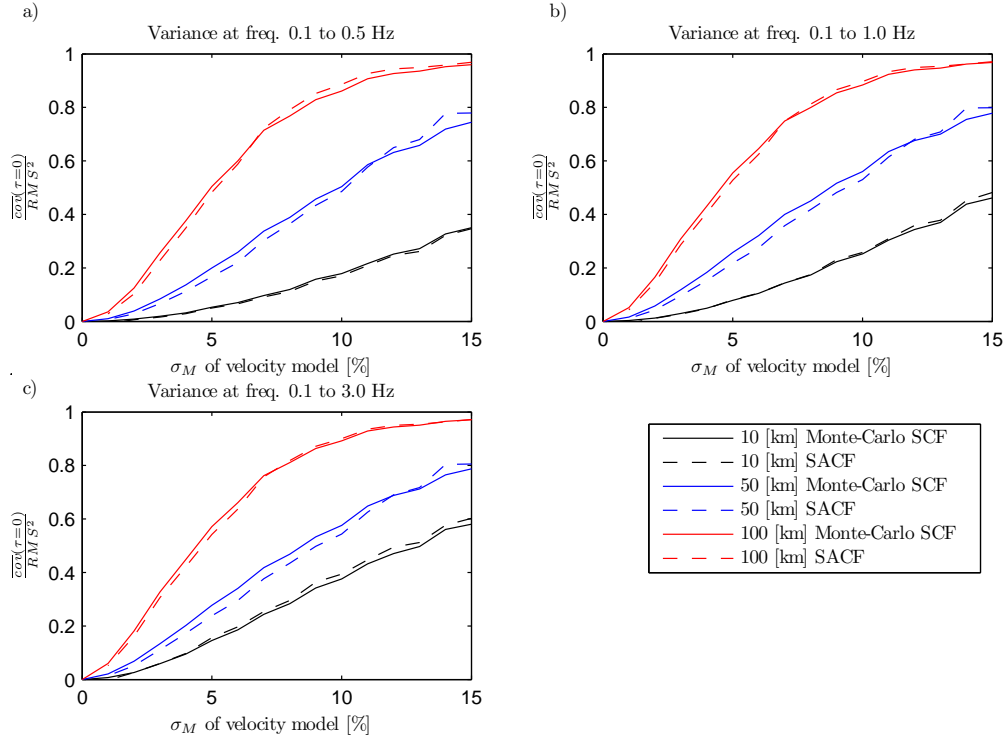


Figure 2.4: The dependence of the GF variance (SCFs at zero time lags) on various parameters estimated by the MC simulations (solid lines) and using the approximate formula for SACFs (dashed lines). The individual panels correspond to GFs filtered in various frequency ranges: **a)** 0.1 – 0.5 Hz, **b)** 0.1 – 1.0 Hz, **c)** 0.1 – 3.0 Hz. In each panel colors distinguish the source-receiver distance (see legend), the strength of the velocity model perturbations is on the x-axis and the variance scaled by RMS^2 of the mother waveform (representing maximum possible value of the variance) is on the y-axis.

We can relate our estimate of the GFs variance to an independent finding of Gallovič & Ampuero (2015), who compared results of synthetic slip inversion benchmark test SIV2a Mai et al. (2016) as obtained by several modelers. They concluded that the results were consistent up to approximately $1/10$ of the maximum singular value of the forward design matrix, which corresponds to less than 1% mean data error ($\overline{cov}/RMS^2 = 0.01$). Since very close stations and low-frequency data were considered in the benchmark, Fig. 2.4a suggests that modelers had imprecise GF in terms of velocity model perturbations $\sigma_M \leq 2\%$. Such velocity model uncertainty can be translated using Fig. 2.1d to very small error of arrival times $\sigma_t \leq 0.02$ sec, which can be related just to some minor inconsistencies among the modeler setups (including possible small shifts of the considered fault plane).

2.2.4 Performance in capturing the GF variations

Covariance matrices and their approximations are used to statistically describe the uncertainty of the GFs. However, it is not trivial to assess the quality of the proposed approximations in terms of capturing the true variability of the GFs. In other words, it is not evident what kind of GF variability is actually captured by the approximated covariances. To address this issue, we draw random GF samples from their multivariate normal distributions described by the “mother” waveforms and the auto-covariance matrices to visually inspect their effects on the GF variability. Examples of random GFs generated considering the various covariance matrices introduced herein are shown in Fig. 2.5. For drawing the random samples we use Matlab function *mvnrnd*.

Random GFs generated using the MC covariance matrix (Fig. 2.5b) may serve as a reference set. They reasonably agree with the variability of the original set of the GFs calculated for the randomly perturbed velocity models (see Fig. 2.1b). Spread of the GFs generated by the ACF matrix (Fig. 2.5d) is very similar to the reference (Fig. 2.5b), especially when taking into account the great difference in the computational demands. Indeed, the random GFs generated using the ACF matrix have similar time shifts and zero values prior and after the useful signal as the reference GFs. We note that the variations in GF amplitudes might come as a surprise because the ACF formula in Eq. (2.14) was derived assuming pure time shifts without any change of the signal shape. This is due to the fact that the Gaussian PDF is not, strictly speaking, a good statistical model for capturing such variations. In other words, the variations in amplitudes represent an artifact of using an inappropriate statistical model for the randomly shifted signal in a mathematical sense. Nevertheless, despite being an artifact, we consider it advantageous for our purpose since the ACF then captures more general variability that is closer to the reference one obtained by the expensive MC approach.

Variability of GFs for the SACF matrix (Fig. 2.5f) is similar to the reference only in the time interval where the mother GF has the strongest signal (i.e. 15 – 26 sec). Outside of this time interval, the time-independence of the SACF leads to generation of strong amplitude variations unobserved in the reference set. If needed, these variations could be suppressed by applying an additional taper on the rows and columns of the respective covariance matrix (see Fig. 2.3e), reducing values in their upper-left and bottom-right corners.

For illustration purposes we show in Fig. 2.5h also the case of a diagonal covariance matrix since it is most typically considered in practical source inversions. The resulting random samples of the GFs correspond to the mother waveform perturbed by a white (uncorrelated) Gaussian noise in the whole time window.

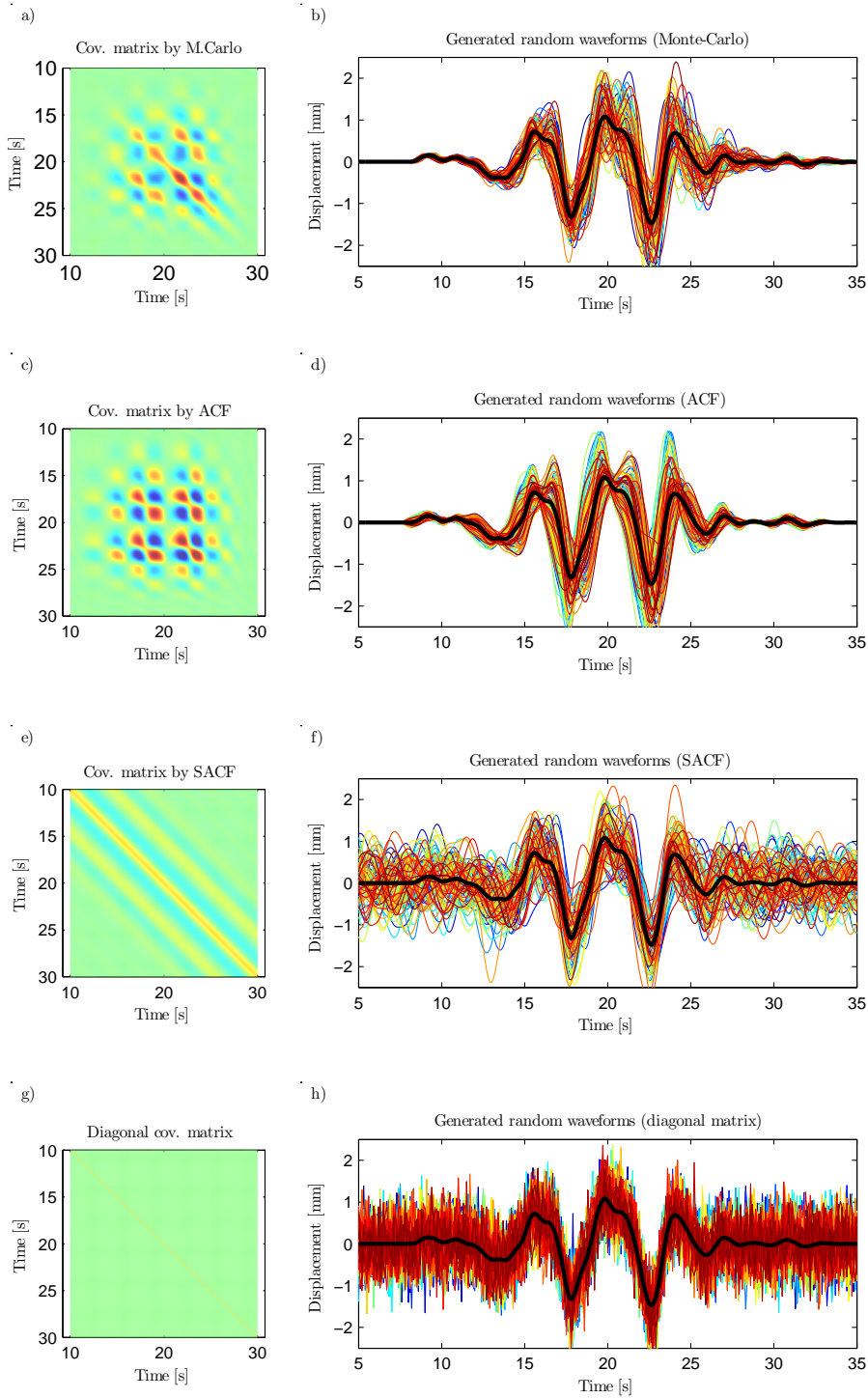


Figure 2.5: Examples of GFs (**b, d, f, h**) generated as random samples from multivariate Gaussian distributions described by a mother GFs (in bold black) and the various auto-covariance matrices shown in the respective panels (**a, c, e, g**), see legend. The color scale used for the covariance matrices is the same as in Figs 2.2 and 2.3. Waveform colors have no meaning and are used just for clearer view. The source-receiver distance for this example is 50 km, and the strength of the model perturbation $\sigma_M = 10\%$.

2.2.5 Examples of cross-covariance

We have showed examples of GFs' auto-covariances, nevertheless approximate analytical formulas were derived also for cross-covariances between generally different waveforms. Here we show two additional examples of GFs' cross-covariance to depict complete performance. In short, we firstly determine cross-covariances by MC simulations in randomly perturbed velocity models (we use the same 1500 models with $\sigma_M = 10\%$ as for auto-covariances; see Fig. 2.1a). Then we compute AXCF and SAXCF and compare them with MC simulations as the reference case.

Firstly, Figs 2.6a and 2.6b show examples of the generated synthetic waveforms at two components of a single receiver. In this case, two random signals $x(t)$ and $y(t)$ share the joint time shift distribution ($L_1 > 0 \text{ sec}$) while there is no relative random time shift between components ($L_{12} = 0 \text{ sec}$). Their cross-covariance matrix determined directly from the definition in Eq. (2.2) (i.e. using MC ensemble of the waveforms) is shown in Fig. 2.6c. Note that, contrarily to the auto-covariance, the cross-covariance matrix is not symmetrical. Fig. 2.6d displays the AXCF matrix obtained using Eq. (2.13). There is some difference between the MC and AXCF matrices, but they are close in terms of their patterns including signs. Next, simulated MC-SXCF and SAXCF, compared in Fig. 2.6f, agree well.

The second example is the cross-covariance of two nearby receivers at the source-receiver distance 50 km and 60 km from the source. Mother waveforms $f(t)$ and $g(t)$, and respective realizations in perturbed velocity models, are shown in Figs 2.7a and 2.7b. The cross-covariance matrix determined using Eq. (2.2) and the MC ensemble of the waveforms is shown in Fig. 2.7c. The perturbed realizations of $x(t)$ and $y(t)$ have generally different time shift distributions. However, in the case of nearby stations, the joint time shift distribution is assumed to have higher influence on cross-covariance than the relative time shift distribution. In other words, the inter-station differential wave travel path has smaller effect on the GFs than the shared source-receive wave travel path ($L_1 > L_{12} > 0 \text{ sec}$). The distributions of joint and relative time shifts l_1 and l_{12} determined from the ensemble of waveforms are shown in Figs 2.8a and 2.8b, respectively. Fig. 2.7d displays the AXCF matrix obtained using Eq. (2.13), there is some difference between the MC and AXCF matrices, but they are still close in terms of their patterns including signs. We note that the difference might increase with mutual distance of receivers, as the relative time shift L_{12} increases. Finally, note that the simulated MC-SXCF and SAXCF in Fig. 2.7f are not centered around zero time lag due to the different wave arrival times on two stations in different distances from the source, as captured by the cross-correlation r_{fg} .

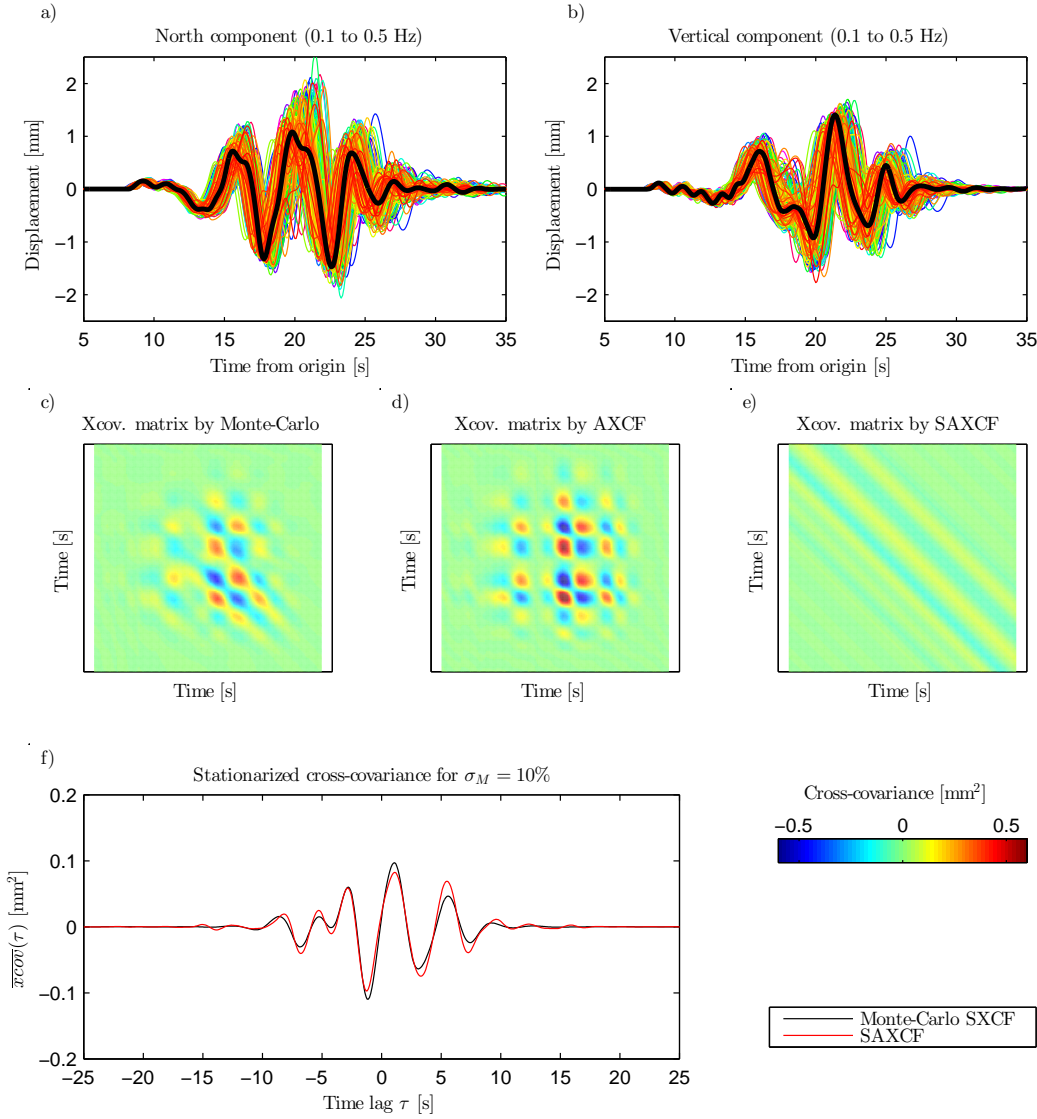


Figure 2.6: Example of the cross-covariance of two components at a single receiver. Panels **a)** and **b)** show two sets of GFs for the North and vertical component, respectively, computed by the discrete wavenumber method for the source-receiver distance of 50 km ($\sigma_M = 10\%$). The black lines are the mother GFs calculated in the mean velocity model. Other colors of waveforms have no meaning and are used only for clearer view. Panel **c)** shows cross-covariance matrix for velocity model perturbations ($\sigma_M = 10\%$) as obtained by the MC approach, while matrices in panels **d)** and **e)** were obtained by the approximate formulas in Eqs (2.13) and (2.20), respectively. The width of the uniform PDF $L_1 = 4\sigma_t$ used in the approximate formulas is adopted from graph in Fig. 2.1d; L_{12} is set to zero as the velocity model is the same for the both components. Duration of the dominant part of the earthquake signal was set $T = 15$ sec. Panel **f)** shows comparison of the stationarized MC cross-covariance function (black) and the SAXCF obtained using Eq. (2.20) (red).

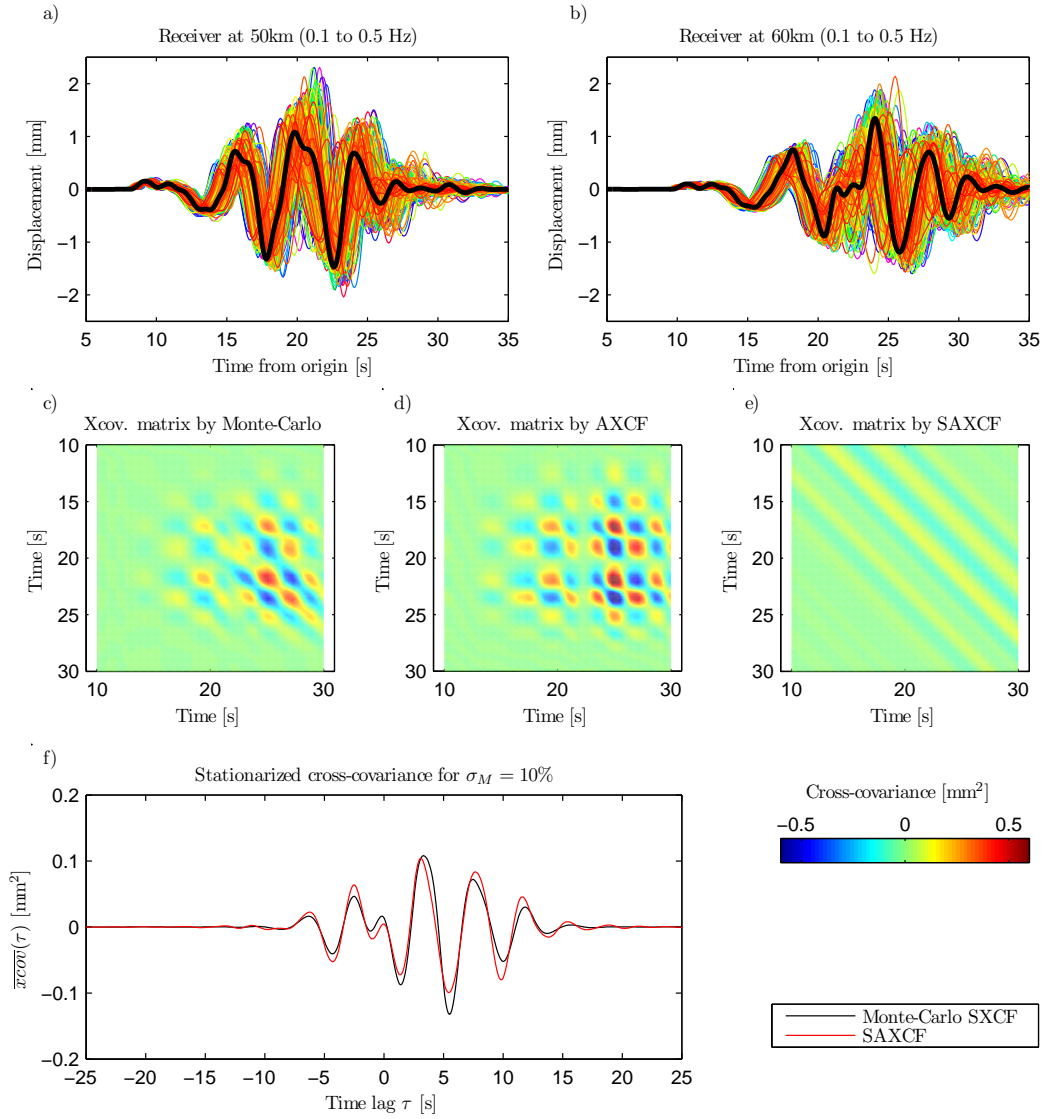


Figure 2.7: Examples of the cross-covariance of two nearby receivers. Panels **a)** and **b)** show sets of GFs for the source-receiver distances 50 km and 60 km, respectively, computed by the discrete wavenumber method ($\sigma_M = 10\%$). The black lines are the mother GFs calculated in the mean velocity model. Other colors of waveforms have no meaning and are used only for clearer view. Panel **c)** shows cross-covariance matrix for velocity model perturbations ($\sigma_M = 10\%$) as obtained by the MC approach, while matrices in panels **d)** and **e)** were obtained by the approximate formulas in Eqs (2.13) and (2.20), respectively. Widths of the uniform PDFs L_1 and L_{12} used in the approximate formulas are adopted from Fig. 2.8. Duration of the dominant part of the earthquake signal was set $T = 15$ sec. Panel **f)** shows comparison of the stationarized MC cross-covariance function (black) and the SAXCF obtained using Eq. (2.20) (red).

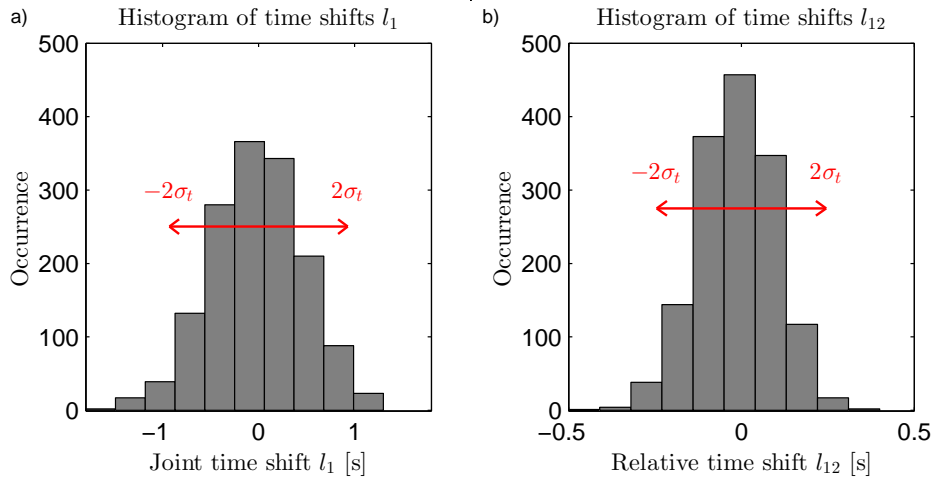


Figure 2.8: Probability distributions of time shifts of GFs due to velocity model perturbations for the example in Fig. 2.7. Time shifts are estimated from waveforms generated in perturbed velocity models, filtered at very low frequencies (0.05 – 0.09 Hz) to avoid cycle skipping. The red lines show the characteristic widths of the time shift distributions ($4\sigma_t$): **a)** Joint time shifts, $4\sigma_t = 1.86$ sec; **b)** Relative (inter-station) time shifts, $4\sigma_t = 0.49$ sec.

2.3 Example of application of the approximate covariances in moment tensor inversion

The proposed approximate covariances can be easily implemented into existing seismic source inversions based on waveform modeling including those formulated in the Bayesian framework. For example, it can be used in source inversion proposed by, e.g., Yagi & Fukahata (2011) or Duputel et al. (2012), where the covariance matrix of the modeling errors (describing the GFs uncertainty) is added to the data covariance matrix describing the seismic noise. In those approaches the covariance of the modeling error is iteratively updated every source model update. Here we show an alternative, simplified, Bayesian approach, assuming that the data error is mainly due to the velocity model uncertainty. In other words, the modeling error covariance is estimated using the approximate formulas in Eqs (2.14) and (2.21) evaluated directly from the observed waveforms. This allows us to solve the inverse problem very efficiently without any iterations.

For the present example of moment tensor (MT) inversion we consider a near-regional distribution of broadband stations in the Corinth Gulf, Greece (Fig. 2.9). Besides a synthetic example, for which the target waveforms are generated in velocity models randomly perturbed for each station, we show also a real-data inversion in the same setting.

2.3.1 Inversion method

We follow the approach of Kikuchi & Kanamori (1991), where the full seismic MT is parametrized by six elementary MTs:

$$\begin{aligned} \mathbf{M}_1 &= \begin{pmatrix} 0 & 1 & 0 \\ 1 & 0 & 0 \\ 0 & 0 & 0 \end{pmatrix} & \mathbf{M}_2 &= \begin{pmatrix} 1 & 0 & 0 \\ 0 & -1 & 0 \\ 0 & 0 & 0 \end{pmatrix} & \mathbf{M}_3 &= \begin{pmatrix} 0 & 0 & 0 \\ 0 & 0 & 1 \\ 0 & 1 & 0 \end{pmatrix} \\ \mathbf{M}_4 &= \begin{pmatrix} 0 & 0 & 1 \\ 0 & 0 & 0 \\ 1 & 0 & 0 \end{pmatrix} & \mathbf{M}_5 &= \begin{pmatrix} -1 & 0 & 0 \\ 0 & 0 & 0 \\ 0 & 0 & 1 \end{pmatrix} & \mathbf{M}_6 &= \begin{pmatrix} 1 & 0 & 0 \\ 0 & 1 & 0 \\ 0 & 0 & 1 \end{pmatrix}. \end{aligned} \quad (2.23)$$

Full MT is then composed of their linear combination described by six coefficients $(a_1 \dots a_6)$,

$$\mathbf{M} = \sum_{n=1}^6 a_n \mathbf{M}_n = \begin{pmatrix} a_2 - a_5 + a_6 & a_1 & a_4 \\ a_1 & -a_2 + a_6 & a_3 \\ a_4 & a_3 & a_5 + a_6 \end{pmatrix}. \quad (2.24)$$

For each of the elementary MT n we evaluate elementary seismogram \mathbf{E}_r^n by the discrete wavenumber method for a receiver r (vectors \mathbf{E} consists of temporal samples). Synthetic seismogram \mathbf{u}_r for a general MT in (2.24) can then be obtained by a linear combination of the six elementary seismograms,

$$\mathbf{u}_r = \sum_{n=1}^6 a_n \mathbf{E}_r^n = \mathbf{G} \mathbf{m} \quad (2.25)$$

where $\mathbf{m} = (a_1, a_2, a_3, a_4, a_5, a_6)^T$ and \mathbf{G} is linear operator of the forward problem consisting of the elementary seismograms \mathbf{E}_r^n . Generalization to more stations and components is straightforward.

The advantage of such linear formulation is the possibility to pre-compute the elementary seismograms for all receivers, and then easily find coefficients including their errors by means of the Bayesian approach (Tarantola 2005, pp. 62–68). Indeed, assuming that observed data \mathbf{d}_{obs} are characterized by Gaussian data errors with covariance matrix \mathbf{C} and considering no prior information (i.e. infinite standard deviation) on the model parameters \mathbf{m} , the posterior PDF reads

$$PDF(\mathbf{m}|\mathbf{d}_{obs}) = const. \exp\left(-\frac{1}{2}(\mathbf{d}_{obs} - \mathbf{G}\mathbf{m})^T \mathbf{C}^{-1} (\mathbf{d}_{obs} - \mathbf{G}\mathbf{m})\right) \quad (2.26)$$

where *const.* is a normalization constant. This Gaussian function attains its maximum for

$$\tilde{\mathbf{m}} = (\mathbf{G}^T \mathbf{C}^{-1} \mathbf{G})^{-1} (\mathbf{G}^T \mathbf{C}^{-1} \mathbf{d}_{obs}), \quad (2.27)$$

which is called best-fitting or maximum likelihood solution. The shape of the Gaussian PDF is characterized by the (posterior) covariance matrix $\tilde{\mathbf{C}}$ given by

$$\tilde{\mathbf{C}} = (\mathbf{G}^T \mathbf{C}^{-1} \mathbf{G})^{-1}. \quad (2.28)$$

The 6×6 elements of matrix $\tilde{\mathbf{C}}$ fully describe the uncertainty of the inverted MT solution.

Let us explain an alternative view of the role of the data covariance matrix in the Bayesian inversion. Covariance matrix is by definition positive semidefinite, and if it is, moreover, positive definite, its inverse exists and can be factorized by Cholesky decomposition,

$$\mathbf{C}^{-1} = \mathbf{R}^T \mathbf{R} \quad (2.29)$$

where \mathbf{R} is an upper triangular matrix. Putting (2.29) into (2.26), the posterior PDF can be rewritten as

$$PDF(\mathbf{m}|\mathbf{d}_{obs}) = const. \exp\left(-\frac{1}{2}(\mathbf{R}\mathbf{d}_{obs} - \mathbf{R}\mathbf{G}\mathbf{m})^T (\mathbf{R}\mathbf{d}_{obs} - \mathbf{R}\mathbf{G}\mathbf{m})\right) \quad (2.30)$$

meaning that the best-fitting solution minimizes L2-norm of so-called standardized residuals obtained as a difference between the data and synthetics after they both are multiplied by the triangular matrix \mathbf{R} from the Cholesky decomposition.

2.3.2 Source inversion of synthetic data set

We assume an earthquake from the Corinth Gulf, Greece, at depth 8 km and with moment magnitude $M_w = 5.4$. Fig. 2.9 shows the source location and the station geometry. Synthetic data for the inversion test were computed by the discrete wavenumber method (Bouchon 1981) assuming a Dirac delta function as the source time function and pure shear mechanism with strike 327° , dip 32° , and rake -45° . The waveforms were filtered by Butterworth bandpass filter with corner frequencies 0.1 – 0.2 Hz and then downsampled to 5 Hz sampling rate. In the following tests we generate “data” for the inversion assuming a realization of random variations of the wave speeds and depths of the layers (as in the MC simulations described in Section 2.2.1 for each station independently ($\sigma_M = 10\%$)). Such random variations of the reference velocity model simulate a real case when the velocity model is complex, yet well described by a mean velocity model. In all tests the inversions are performed in the reference (mean) layered velocity model.

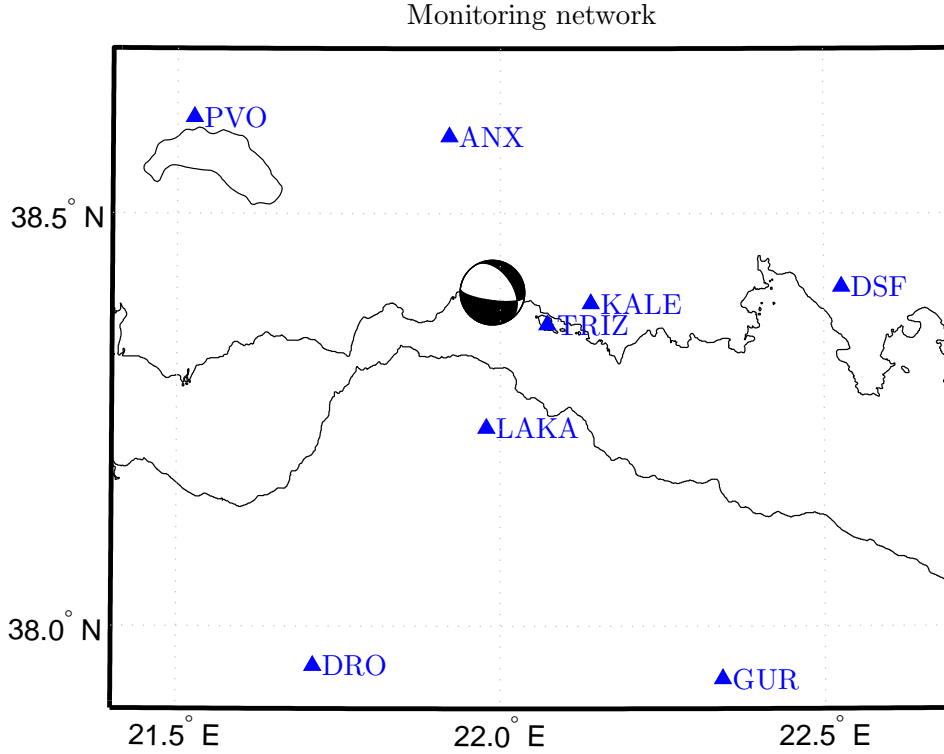


Figure 2.9: Seismic station distribution (triangles) in the Corinth Gulf used in the MT inversion tests. The beachball plotted at the event epicenter corresponds to the mechanism considered in the synthetic test (after Sokos & Zahradník 2013).

Covariance matrices describing the velocity model uncertainty

In multi-station and multi-component inversion the data covariance matrix has a block structure. Auto-covariance matrices for the individual waveforms are arranged along the diagonal, while off-diagonal blocks contain cross-covariance matrices among the individual waveforms. Here we describe six covariance matrices that are tested in the following inversions. As an example, we show here only submatrix corresponding to the synthetic 3-component waveforms DSF station (Fig. 2.10), as the complete covariance matrix is too large for the presentation purpose.

The simplest case when the crustal model uncertainty is disregarded in the inversion is represented by a diagonal covariance matrix with constant variance equal to the square of $1/50$ of the maximum signal amplitude from the entire dataset (i.e. relatively weak noise corresponding to the almost negligible ambient noise in the real-data inversion in Section 2.3.3 (see example in Fig. 2.11a). We also consider a diagonal covariance matrix consisting of diagonal values from the SACF, which implicitly weights the waveforms considered (example in Fig. 2.11b). Furthermore, we consider covariance matrices with off-diagonal components obtained using SACF and ACF (examples in Figs 2.11c and 2.11d, respec-

tively). We apply an additional taper on the rows and columns of the SACF matrix as suggested in Section 2.2.4. Finally, we show the case when even approximate cross-covariances between components of the same receiver are taken into account using the (tapered) SAXCF and AXCF (examples in Figs 2.11e and 2.11f, respectively). We add the constant weak-noise variance discussed above to all the covariance matrices considered to ensure positive definiteness of the covariance matrix.

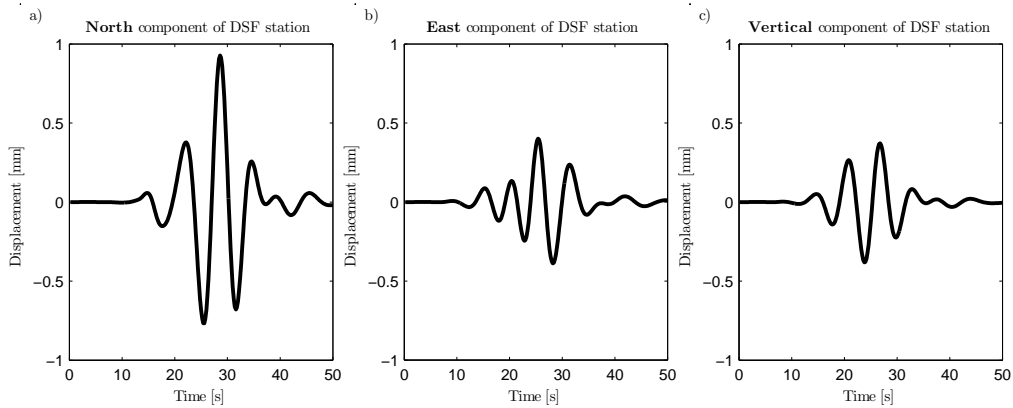


Figure 2.10: Example of synthetic waveforms on **a)** North, **b)** East and **c)** vertical component of the DSF station. Data are filtered by Butterworth bandpass filter between 0.1 – 0.2 Hz.

Formulas for the approximate covariances require definition of the width of the uniform PDF describing the time-shift distribution, L_1 . We consider a linear dependence on source-receiver distance, following values for $\sigma_M = 10\%$ in graph Fig. 2.1d. The implemented dependence reads

$$L_1[sec] = \begin{cases} 1.5 & \text{for } \frac{d}{25} \leq 1.5 \\ \frac{d}{25} & \text{for } \frac{d}{25} \geq 1.5 \end{cases} \quad (2.31)$$

where d is a source-receiver distance in kilometers.

Properties of the maximum likelihood solution

The MT inversion is performed for 1000 different target data sets computed in randomly perturbed velocity models. For each realization, we obtain best-fitting solutions in Eq. (2.27) for each type of the covariance matrix considered. Fig. 2.12 shows the ensemble of the solutions displayed in terms of DC mechanism nodal planes, and histograms of maximum difference to the true model in strike, dip, rake, DC component ratio and the inferred scalar seismic moment M_0 . We note that the spread of the differences to the reference solution (plotted in red) is caused by variations of the randomly perturbed velocity model, hence by the GFs uncertainty.

The maximum difference in the angles of the DC mechanisms reaches 10–20° depending on the covariance matrix type considered. Asymmetry of the DC mechanism angle difference (e.g., Fig. 2.12d) is related to the particular spatial settings of the monitoring network. The DC component ratios are scattered from

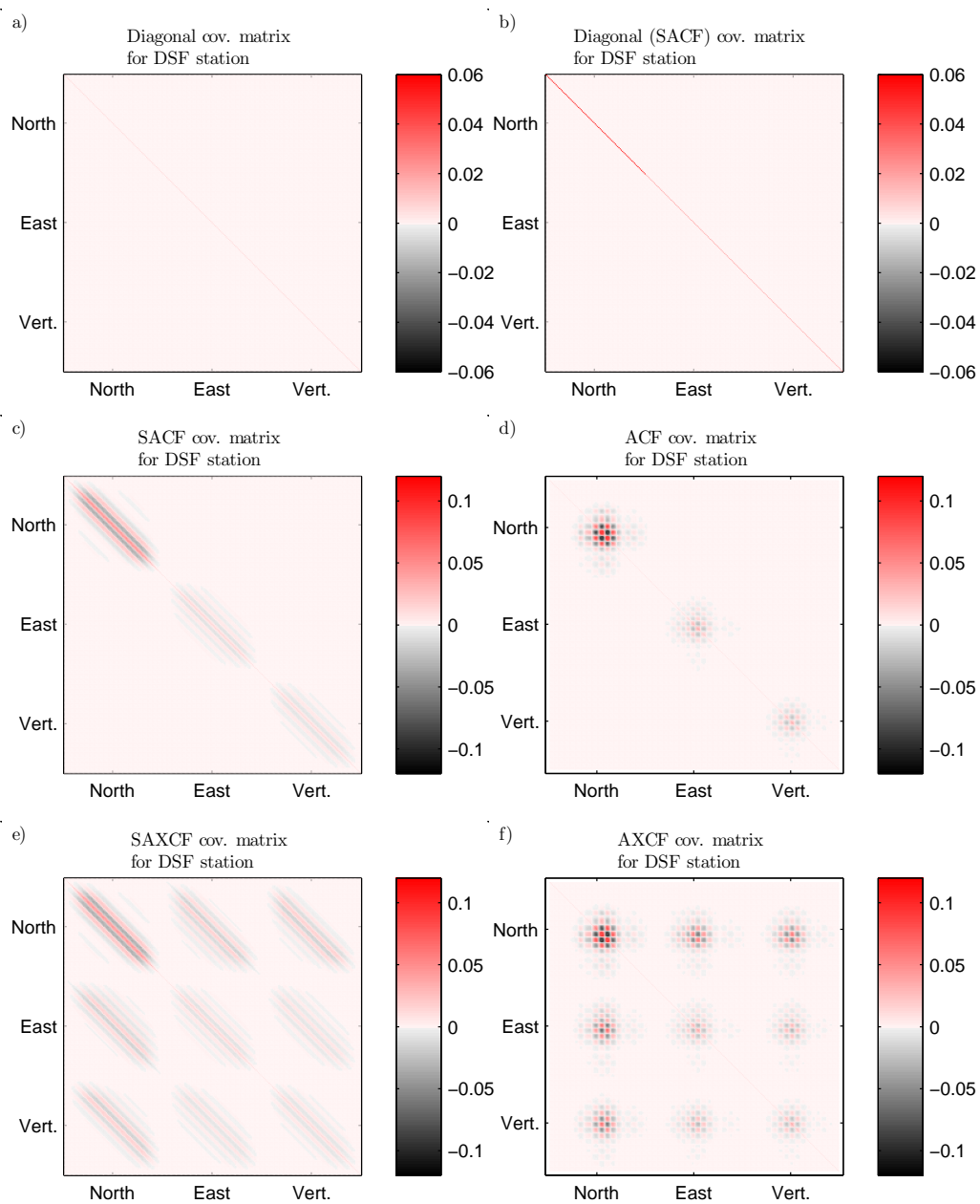


Figure 2.11: Submatrices for the six different types of covariance matrices **a)–f)** discussed in the text (see titles in figure) corresponding to the DSF station. There are shown 3 blocks of auto-covariances arranged along the diagonal and 6 blocks of cross-covariances among DSF station’s components in each submatrix. The values shown by color have units $[mm^2]$. Note especially the effect of the stronger signal on the North component.

the simulated pure shear ($DC = 1$) down to values $0.8 - 0.6$. The variability of the inferred scalar moments is similar for all the considered covariance matrix types ranging from 1.0 to $1.6 \times 10^{17} Nm$ (i.e. 5.3 to 5.4 in moment magnitude scale), except for the SAXCF case. Indeed, the latter type of the covariance matrix leads to significant underestimation of the scalar seismic moment (Fig. 2.12e). It is perhaps related to the time averaging procedure in the SAXCF definition. Although the time averaging seems to work well for the auto-correlation components in SACF, calculating temporal mean over cross-covariance components in SAXCF representing relation (correlation or even anti-correlation) between individual samples of two waveforms seems to have negative consequences on the inversion. In particular, although nodal planes solution may be similar to the reference, the scalar seismic moment is underestimated in order to reduce the effect of the time inappropriate temporal averaging of the cross-correlations. Thus if cross-covariances are required, the non-stationary type (AXCF) should be preferred.

We note that the presented statistics of the inverted best-fitting parameters can be understood as the “true” MT uncertainty caused by the velocity model uncertainty. Overall assessment of the performance of the individual covariances in Fig. 2.12 suggests that implementation of ACF (Fig. 2.12d) possibly in combination with AXCF (Fig. 2.12f) provides the lowest uncertainty of the inverted MTs. Nevertheless, even in those cases the MT uncertainty remains significant and thus should not be neglected in practical applications. Therefore, in the next section we assess the ability of the individual types of the covariances to estimate the “true” uncertainty in terms of the posterior covariance matrix.

Moment tensor uncertainty estimate

We arbitrarily selected one of the synthetic target data sets, inferred the best-fitting MT solution and estimated its uncertainty in terms of the posterior covariance matrix (Eq. (2.28)). For each type of the data covariance matrix, Fig. 2.13 shows the maximum likelihood solution together with the posterior uncertainty similarly to Fig. 2.12. However, here the ensemble of the solutions is obtained by random sampling the posterior PDF (using Matlab function *mvnrnd*). In Fig. 2.13 the true parameters are plotted by red color for comparison. We note that the best-fitting solutions are biased due to the particular velocity model perturbations considered in the target data. In the following we concentrate on the uncertainty estimation in comparison with the “true” uncertainty as revealed in Section 2.3.2.

In case of the constant diagonal covariance matrix (Fig. 2.13a) the posterior PDF is characterized by very narrow uncertainty limits in contrast to the “true” uncertainty (Fig. 2.12a). Such estimate of the MT uncertainty is clearly unacceptable. Slightly better, yet still underestimated, uncertainty is attained when including the ACF covariance matrix (Fig. 2.13d in comparison with Fig. 2.12d). It is perhaps due to the slight overestimation of inter-sample cross-covariances in the ACF, which can be visible in Figs 2.2e and 2.5d. Inversion with the SACF in Fig. 2.13c provides the largest MT uncertainty estimate, being comparable with that shown in Fig. 2.12c. The larger uncertainty estimate is linked to the time-invariance of the SACF covariance matrix allowing for more general waveform changes as can be seen in Fig. 2.5f. Finally, considering also the inter-component

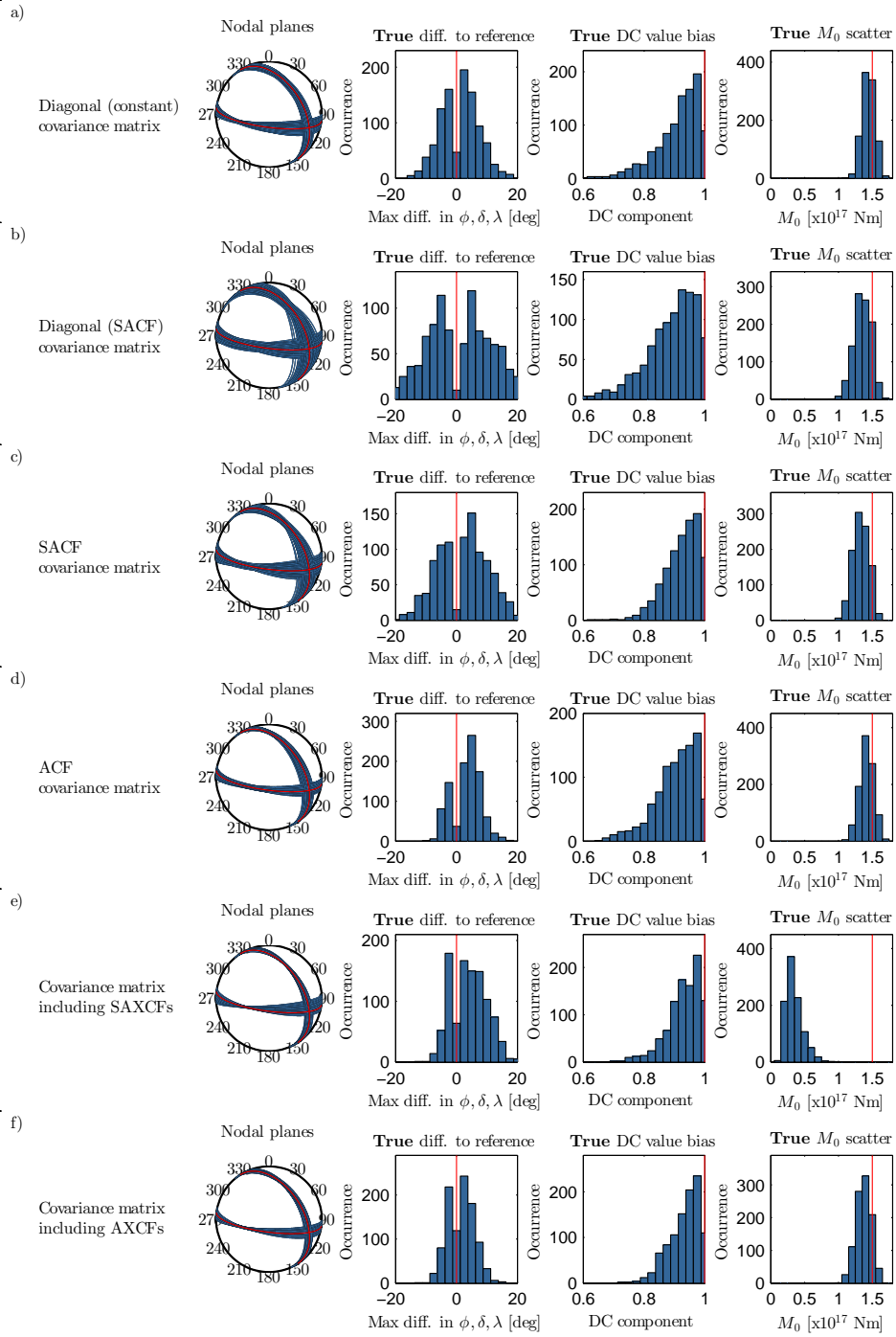


Figure 2.12: Statistical analysis of best-fitting solutions from MT inversion synthetic tests with 1000 realizations of randomly perturbed velocity models used to generate population of target data for the inversion. Panels in each row show DC mechanism nodal planes (left), maximum differences in strike, dip, rake to the reference (middle-left), DC component bias (middle-right) and M_0 scatter (right). Each row corresponds to the use of different type of the data covariance matrix (see legend). The true reference solution (in red) has a pure shear mechanism (DC = 1) with strike 327° , dip 32° , rake -45° , and scalar seismic moment $M_0 = 1.5 \times 10^{17}$ Nm.

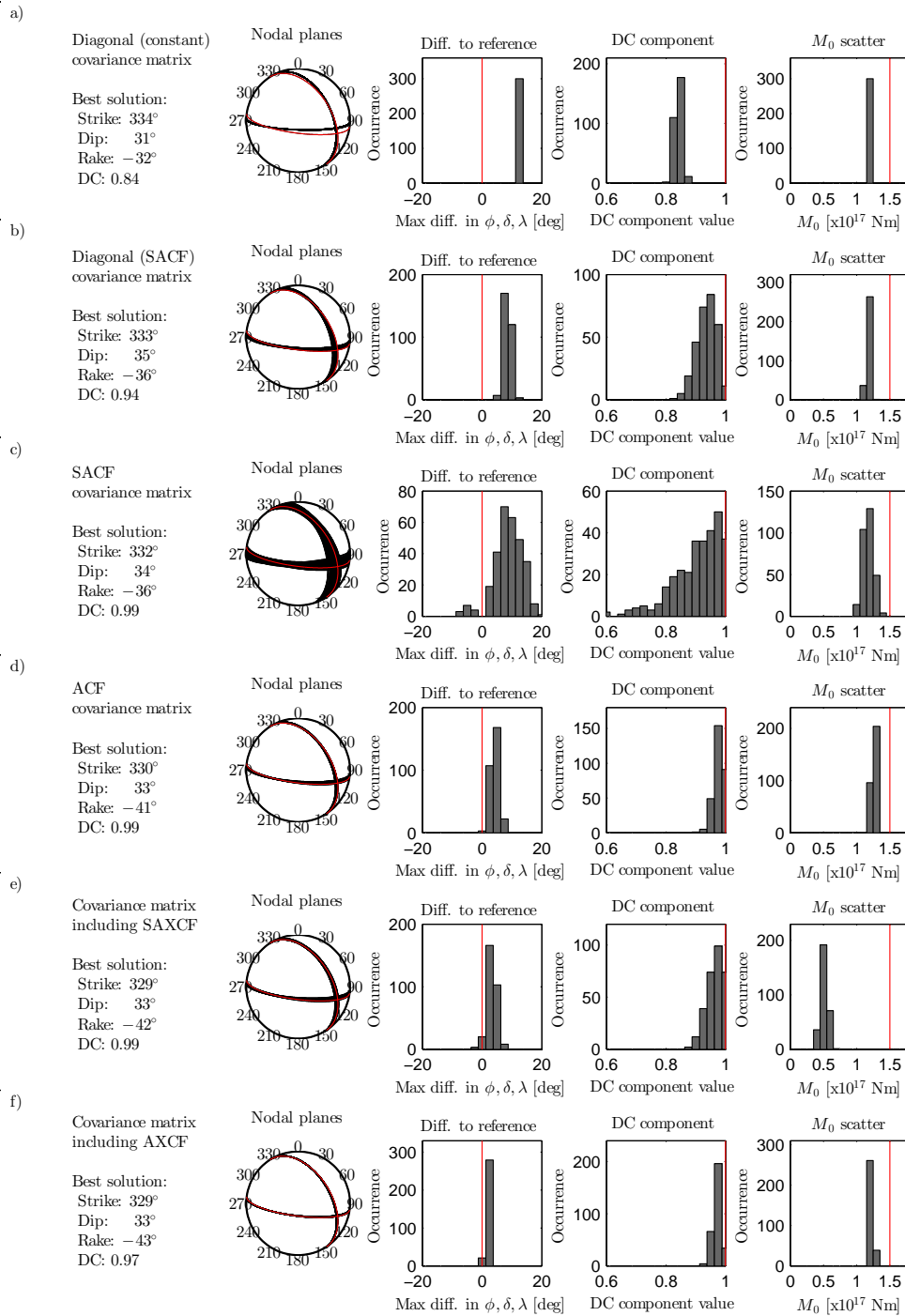


Figure 2.13: Result of a synthetic MT inversion test with a single realization of the randomly perturbed velocity models to generate the target data. Panels in a row are the maximum likelihood solutions (text), DC mechanism fault planes (left), maximum difference to reference in strike, dip, rake (middle-left), DC component (middle-right) and the M_0 scatter (right). Each row corresponds to the use of different type of the data covariance matrix (see legend). The beach balls and histograms are built from 300 random samples of the posterior PDF to visualize the estimated parameter uncertainty. The true solution (in red) is a pure shear mechanism ($DC = 1$) with strike 327°, dip 32°, rake -45°, and scalar seismic moment $M_0 = 1.5 \times 10^{17} \text{ Nm}$.

cross-covariances in the inversion reduces the posterior PDF uncertainty estimate for both the SAXCF (Fig. 2.13e) and AXCF (Fig. 2.13f). To conclude, the most reliable estimate of the uncertainty of the MT parameters is revealed when employing covariance matrix built from the SACFs.

2.3.3 Moment tensor inversion of real data set

Here, we illustrate the proposed methodology on a MT inversion using data written by a real earthquake in Greece. The test event from 25 April 2012 (10:34 UTC) with moment magnitude $M_w = 4.3$ was located in the Corinth Gulf at depth 8 km . Its centroid MT was well examined by the ISOLA full-waveform inversion software by Sokos & Zahradník (2013). The event was recorded by near-regional stations (i.e. broadband sensors supplemented by accelerograph at station TRIZ). As a reference MT solution for this event we adopt the result obtained by Sokos & Zahradník (2013) when considering the same dataset: strike 327° , dip 32° , and rake -45° with 87% of DC component. We point out that jack-knifing results of Sokos & Zahradník (2013) indicated rather large variability of the solutions with the most likely value of DC being larger than 95%.

We perform the MT inversion tests in the reference layered velocity model using only high quality records as identified by Sokos & Zahradník (2013, fig. 3). The setting of the real case test is then consistent with that of the synthetic test (Fig. 2.9). The waveforms were filtered by Butterworth bandpass filter between $0.1 - 0.2\text{ Hz}$ and then downsampled to 5 Hz sampling rate. The upper bound of the ambient noise, measured prior the useful signal, was estimated $2.8\ \mu\text{m}$ corresponding to $1/50$ of the maximum signal amplitude from the entire dataset. Square of such ambient noise level was used as variance in the diagonal data covariance matrix to show the case when the crustal model uncertainty is disregarded in the inversion. Then we perform inversion tests employing complete covariance matrices analogously to the synthetic tests performed in Section 2.3.2. The values of L_1 used in this test were adopted from (2.31).

The inversion results are summarized in Fig. 2.14. The figure shows the maximum likelihood solution together with the MT uncertainty estimate by means of posterior covariance matrix (Eq. (2.28)) for each data covariance matrix considered. The ensemble of the solutions is obtained as random samples of the posterior PDF (using Matlab function *mvrnd*). The behavior of the real-data inversion is analogous to the synthetic-data inversion described in Section 2.3.2. However, the “correct” source parameters (especially the DC parameter) are unknown in this case. The inversion with constant diagonal covariance matrix (i.e. disregarding crustal model uncertainty; Fig. 2.14a) provides clearly underestimated MT uncertainty. The ACF (Fig. 2.14d) provides good estimate in terms of the variance reduction, but the uncertainty is still underestimated as it doesn’t fully cover the reference solution. However, the maximum likelihood solution (notice especially DC component value in Fig. 2.14d) seems to be more reliable than in the case of the constant diagonal covariance matrix (Fig. 2.14a). Inversion with the SACF (Fig. 2.14c) provides the largest MT uncertainty estimate. We note that the related spread of the possible solutions is similar to that obtained by jack-knifing by Sokos & Zahradník (2013, fig. 3).

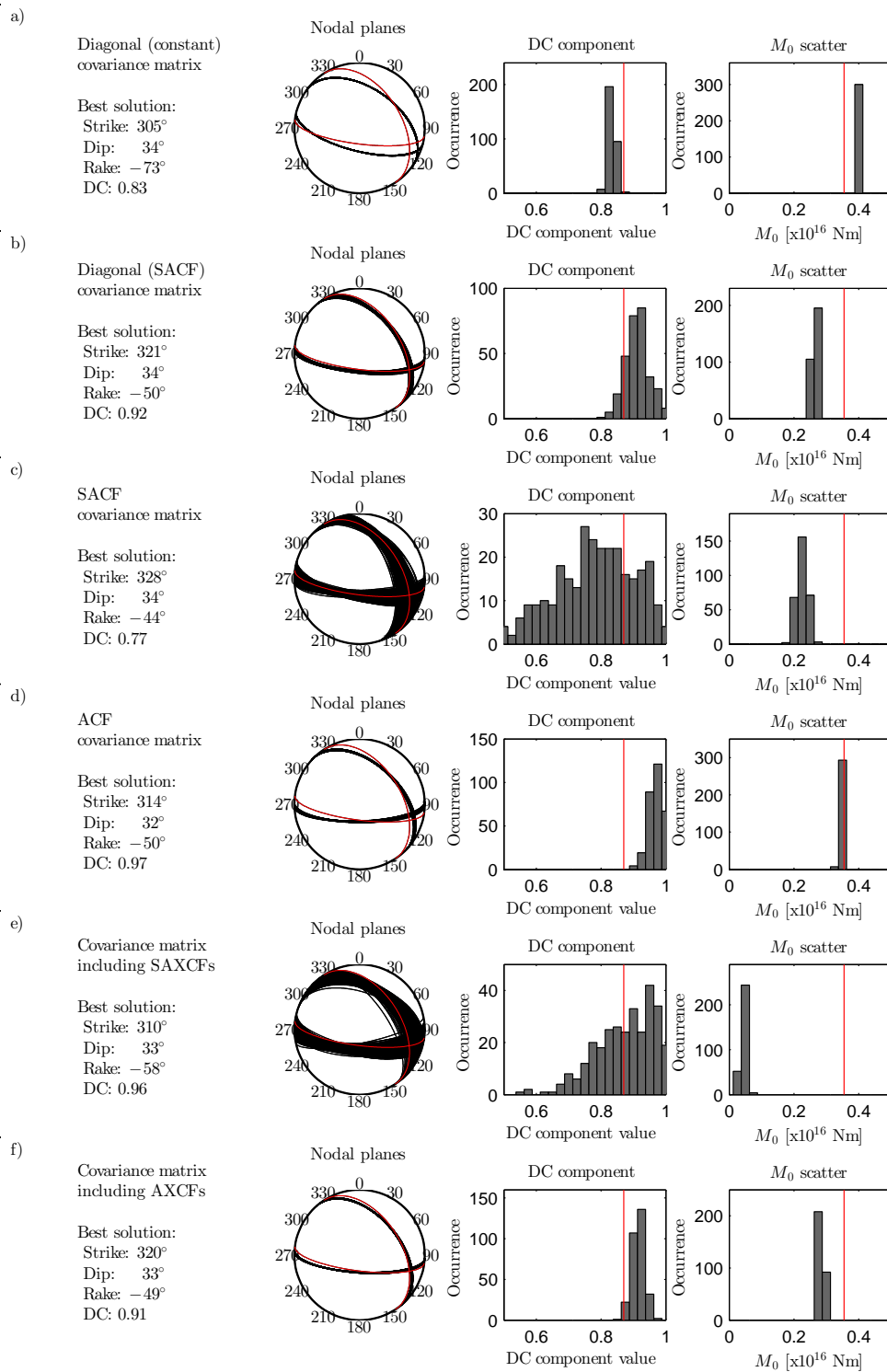


Figure 2.14: Same as Fig. 2.13 but for the real dataset of the 25 April 2012 event of moment magnitude $M_w = 4.3$ ($M_0 = 3.55 \times 10^{15}$ Nm) from the Corinth Gulf. The reference solution by Sokos & Zahradnik (2013) obtained using the same dataset has strike 327° , dip 32° , rake -45° and DC component 87% (in red).

2.3.4 Remark on the role of the covariance matrix in the inversion

As we discussed in Section 2.3.1, the MT inversion minimizes the difference (residuals) between the recorded data and synthetics in terms of L2 norm (Eq. (2.26)). Instead, if the covariance matrix with off-diagonal components is used, the inversion minimizes the standardized residuals, i.e. waveforms multiplied by the triangular matrix from the Cholesky decomposition (see Eq. (2.30)). In Fig. 2.15 we show normalized and standardized displacement fits for the real earthquake inversion. We show data only for two selected representative stations (KALE as a close station and DSF as a distant station) in Fig. 2.15, while the complete sets of for the standardized waveforms are shown in Figs 2.17, 2.18 and 2.19 for diagonal, ACF and SACF matrices, respectively.

Matrix \mathbf{R} (see Eq. (2.30)) corresponding to a diagonal covariance matrix is also diagonal, having reciprocals of square roots of the diagonal values from the \mathbf{C} matrix (i.e. reciprocals of standard deviations of the data samples). In such a case, the maximum-likelihood solution is the model that best reproduces the measured data in terms of the L2 norm of the residual seismograms weighted by the reciprocals of the data standard deviations from the \mathbf{C} matrix (see examples in Figs 2.15a, 2.15b and 2.17). If the diagonal covariance matrix is built from the variances of the SACF covariance matrix, then the station weights are proportional to the signal RMS, where the constant of proportionality depends on the signal shape and considered time shifts (as illustrated in Fig. 2.4). Multiplying by \mathbf{R} then normalizes the waveforms to a unit RMS and amplifies the near stations with respect to the distant ones.

If the covariance matrix is constructed from a time-independent (stationarized) CF, rows of matrix \mathbf{R} are composed of all-pole (minimum-phase) IIR filters with the given CF (Marple 1986). Multiplication by \mathbf{R} in Eq. (2.30) thus works approximately as a filter with Fourier spectrum equal to the reciprocal of the square root of Fourier spectrum of the original CF. Considering the SACF from Eq. (2.21), such a filter has spectrum

$$\begin{aligned} W(L_1, f) &= \mathcal{F}\left(r_f(\tau) * \left(\delta(\tau) - \wedge_{2L_1}(\tau)\right)\right)^{-1/2} \\ &= \left(r_f(\tau)\right)^{-1/2} \left(1 - \frac{\sin(\pi f L_1)}{\pi f L_1}\right)^{-1/2}. \end{aligned} \quad (2.32)$$

When applied to the data vector (see examples in Figs 2.15e, 2.15f and 2.19), the first term in Eq. (2.32) works implicitly as data pre-whitening and normalization, i.e. approximately equalizing the spectral content of the signal of all stations to a common value. The second term then implicitly amplifies the low-frequency part of the spectrum up to the reciprocal of L_1 as it is shown in Fig. 2.16 for various values of L_1 . Since L_1 generally increases with distance, the amplification at close stations reaches higher frequencies than at distant stations (see Fig. 2.16). Moreover, the closer is the station the more amplified is its spectrum in general (Fig. 2.16).

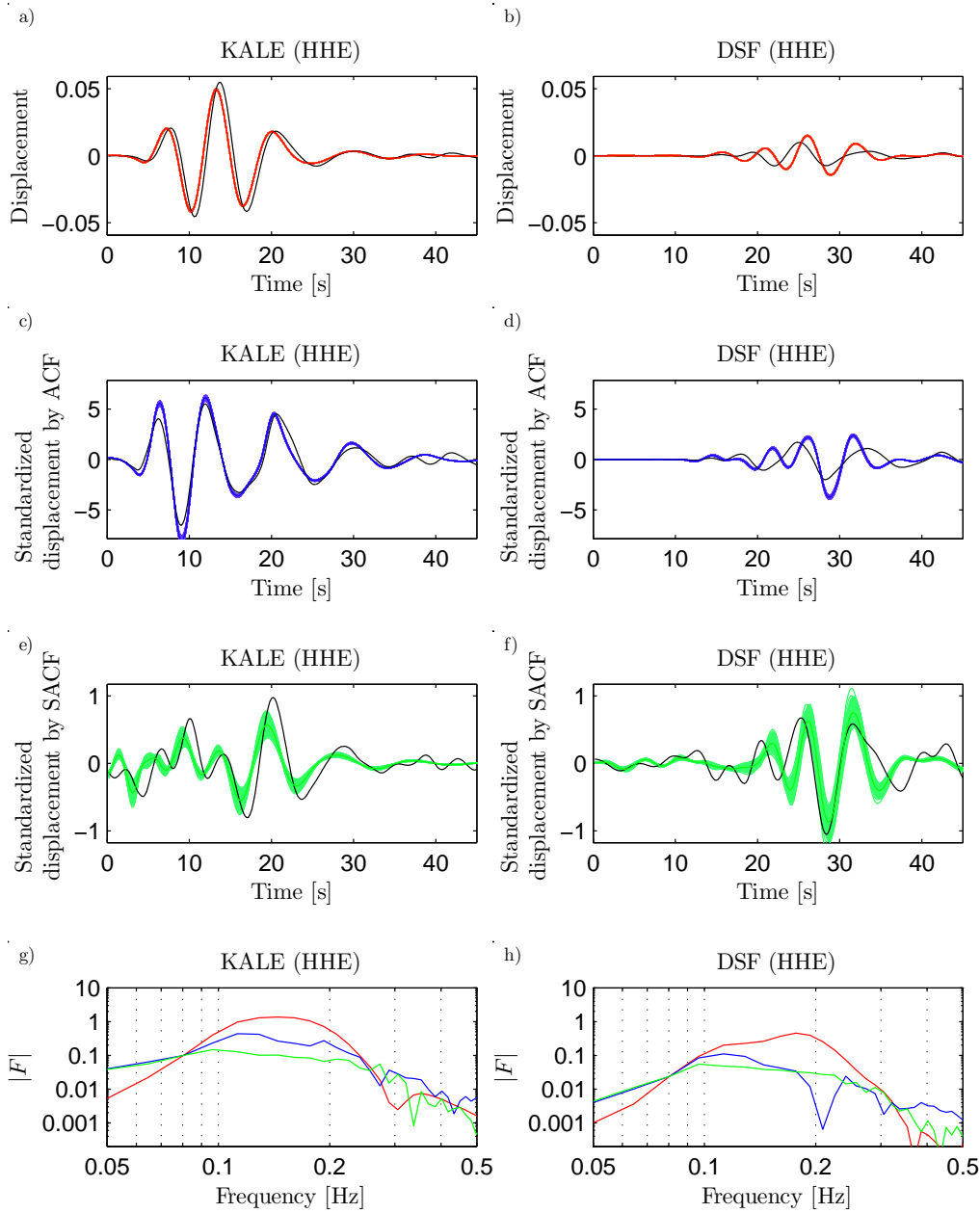


Figure 2.15: Standardized displacement data and synthetics at stations KALE (left) and DSF (right) for the real event of 25 April 2012 from the Corinth Gulf. Epicentral distances are 13 km and 47 km for the KALE and DSF stations, respectively. Black waveforms are standardized displacements and colored waveforms are 300 realizations of the standardized synthetics perturbed by the posterior covariance matrix. Data are corrected by instrument response and bandpass Butterworth filtered between 0.1–0.2 Hz. Panels **a)** and **b)** show displacements normalized by standard deviation of the ambient noise (see text). Data in panels **c)**, **d)** and **e)**, **f)** are displacements standardized by ACF and SACF covariance matrices respectively. Panels **g)** and **h)** show standardized amplitude spectra of the real data for diagonal (red), ACF (blue), and SACF (green) covariance matrices.

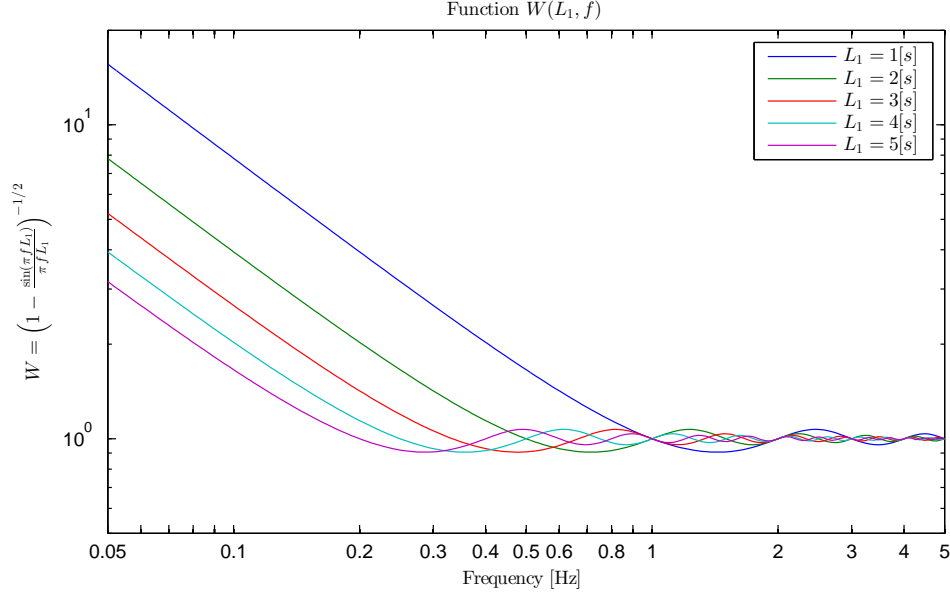


Figure 2.16: *Implicit weighting of the signal spectral components in an inversion with SACF (see the second term in Eq. (2.32)). Colors represent various widths of the time shifts window L_1 (see legend). Note that L_1 is considered to generally increase with distance, so that the graph shows also implicit relative weighting in the spectral domain between near and distant stations.*

The pre-whitening effect and the low-frequency amplification are visible in Figs 2.15g and 2.15h, comparing amplitude spectra of weighted real data waveforms (red) and seismograms standardized by SACF (green) for two selected stations. In particular, in case of the SACF the amplitude spectra are flat and increasing towards lower frequencies in the filter frequency range $0.1 - 0.2 Hz$. The closer station KALE has the low-frequency part of the spectrum amplified more than the more distant station DSF (compare green lines in Figs 2.15g and 2.15h) due to the lower value of L_1 considered for the smaller distance.

The case when the covariance matrix is constructed from the ACF (see examples in Figs 2.15c, 2.15d and 2.18) is more complex. Due to the time-dependence of the ACF, it cannot be likened as an application of a time-invariant filter. However, this time-dependence is reduced when increasing L_1 , i.e. as the integrals (i.e. expectations) in Eq. (2.14) make the ACF smoother in time. In the extreme case of $L_1 \geq T$ the ACF is nearly stationary in the period of the useful signal T , and hence almost the same as the SACF tapered over the signal duration. This means that the described features of the SACF (such as equalizing the spectral content and amplifying low-frequencies) are also present in the data standardized by ACF to an extent depending on the parameter L_1 . These effects are perceptible in Figs 2.15g and 2.15h, showing amplitude spectra of the weighted real data waveforms (red), seismograms standardized by SACF (green) and by ACF (blue), yet to lower extent than in the case of SACF. To summarize, the above interpretation of the effect of the SACF gives a hint on the implicit behavior of the inversion when the \mathbf{C} matrix is constructed using the approximate covariances proposed in the present work.

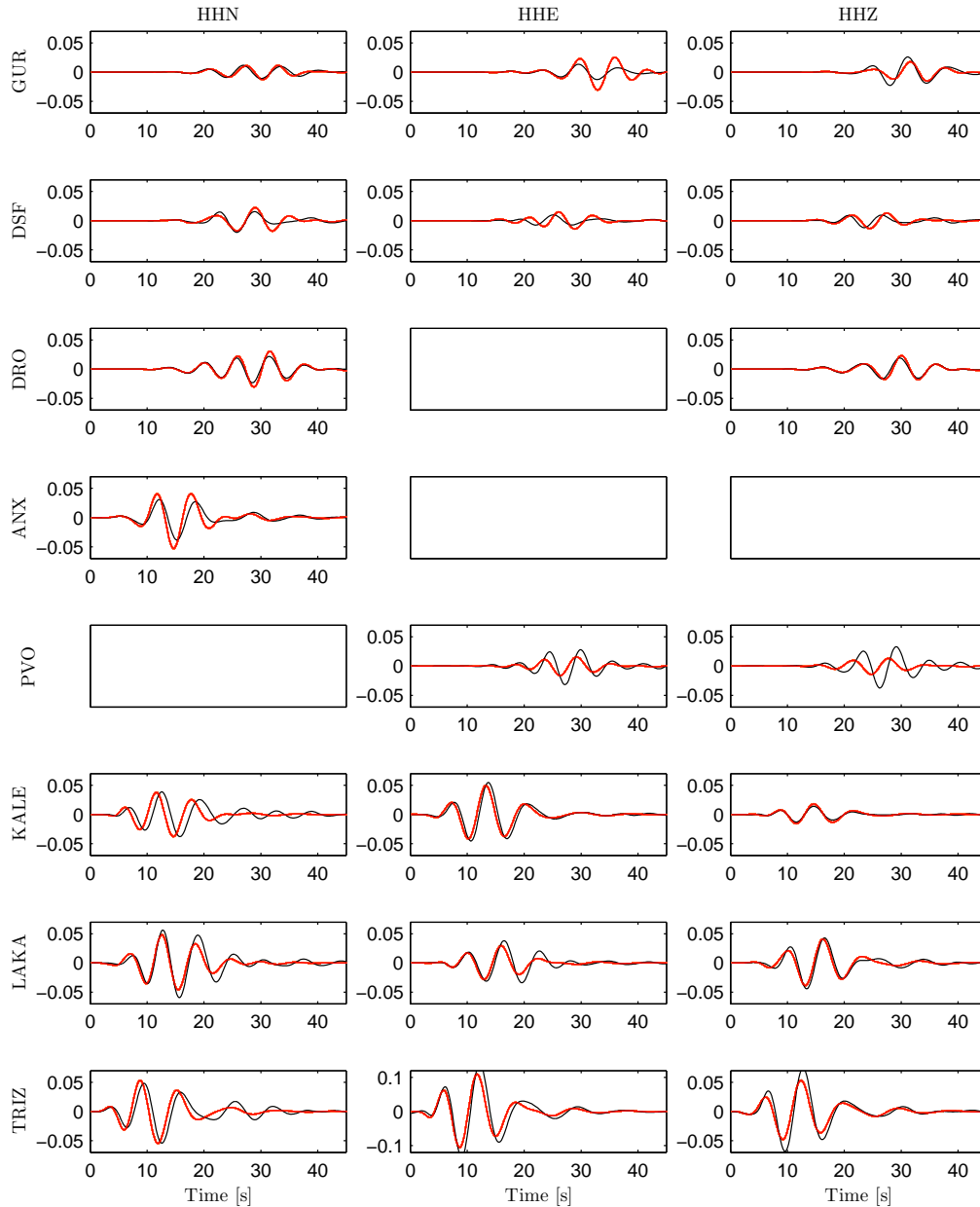


Figure 2.17: The fit of the normalized displacement (black) and synthetics (color) for the real event from 25 April 2012 from Corinth Gulf **disregarding uncertainty of GFs**. Data are corrected by instrument response and filtered by Butterworth bandpass filter between 0.1 – 0.2 Hz. Black waveforms are normalized displacement and colored waveforms are 300 synthetic realizations of normalized displacement perturbed around the best fitting solution by posteriori covariance.

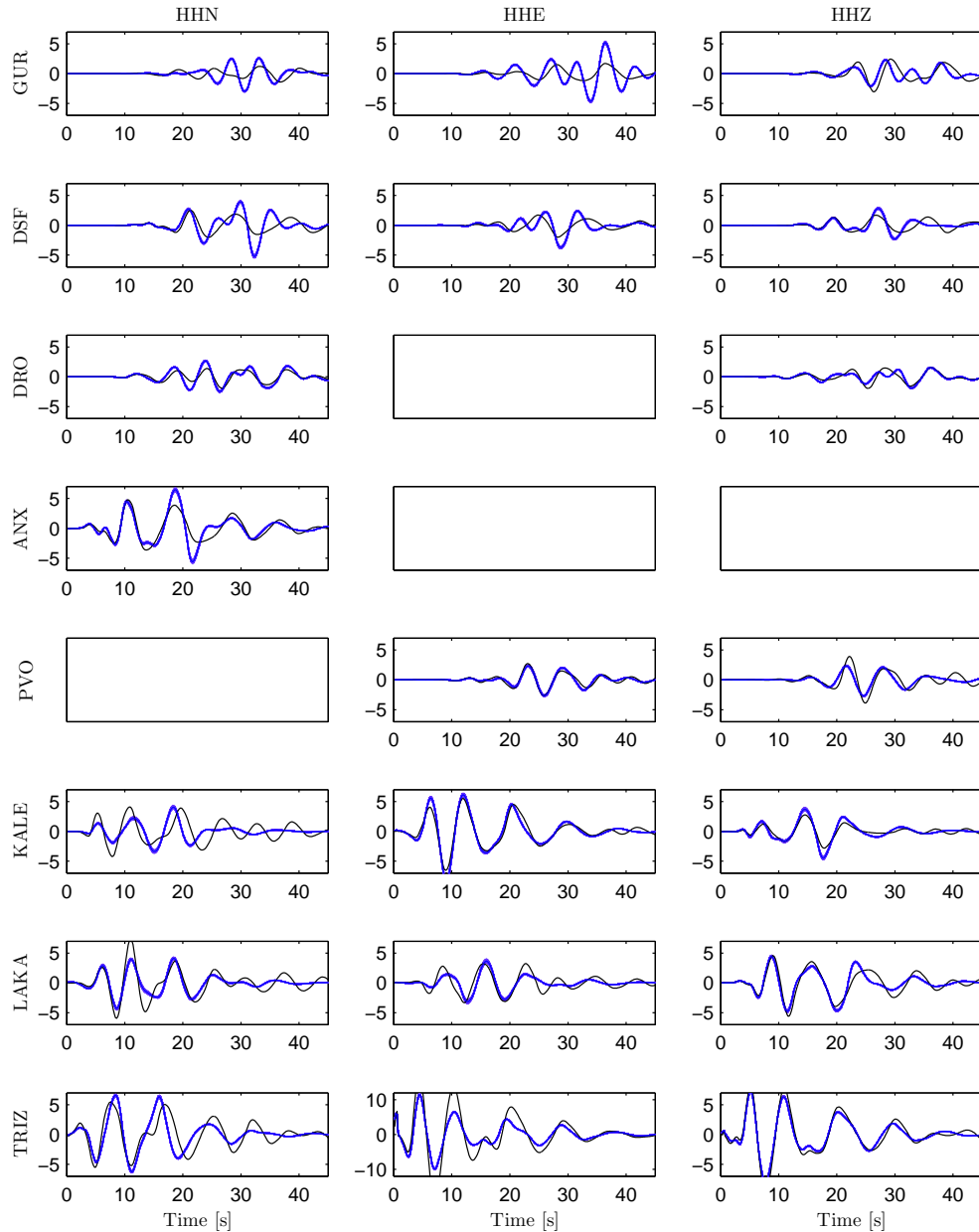


Figure 2.18: The fit of the normalized displacement (black) and synthetics (color) for the real event from 25 April 2012 from Corinth Gulf considering uncertainty of GFs by means of **ACF**. Data are corrected by instrument response and filtered by Butterworth bandpass filter between 0.1 – 0.2 Hz. Black waveforms are normalized displacement and colored waveforms are 300 synthetic realizations of normalized displacement perturbed around the best fitting solution by posteriori covariance.

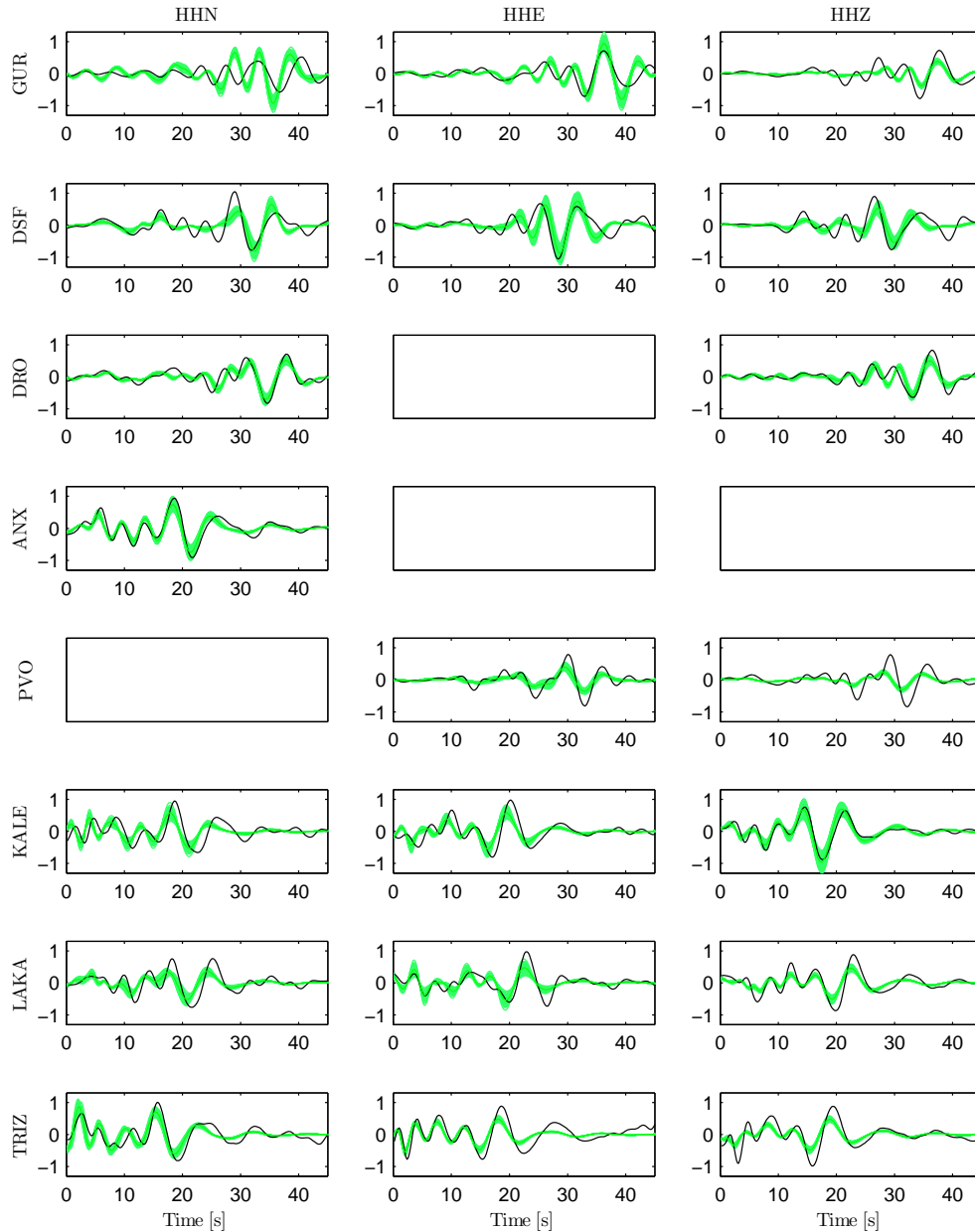


Figure 2.19: The fit of the normalized displacement (black) and synthetics (color) for the real event from 25 April 2012 from Corinth Gulf considering uncertainty of GFs by means of **SACF**. Data are corrected by instrument response and filtered by Butterworth bandpass filter between 0.1–0.2 Hz. Black waveforms are normalized displacement and colored waveforms are 300 synthetic realizations of normalized displacement perturbed around the best fitting solution by posteriori covariance.

2.4 Conclusions

The aim of this Chapter is to introduce a simple and easy-to-implement approach to efficiently involve the GF uncertainty in practical source inversions. Recent Bayesian waveform inversions rely on statistical description of the GFs uncertainty by means of a covariance matrix of a Gaussian distribution. Therefore, we introduce a fast and simple method for evaluation of the covariance matrix of GFs, incorporating uncertainty of a crustal velocity model (see Eqs (2.13), (2.14), (2.20) and (2.21)).

Our approximate approach requires a “mother” GF and statistical description of the random time shifts of the signal as an input. While the “mother” GF is calculated using a given (mean) velocity model, which is required by the source inversion anyway, the estimation of the random time shifts requires additional considerations. In particular, experiments shown in the present paper suggest that it is enough to assume a uniform PDF for the time shifts. Its width L_1 depends on the source distance and velocity model perturbations linearly (Fig. 2.1d). Alternatively, one may estimate L_1 from temporal residuals obtained during event location, but it will require future investigation and testing. We point out that despite the fact that the simplified formulas were derived assuming purely random time shifts of GFs, the proposed approach produces variations of both the arrival time and the waveform amplitudes as shown in Fig. 2.5.

An example implementation of the approach proposed in Section 2.3 was illustrated on a moment tensor inversion applied to synthetic and real datasets. Experiments with large number of synthetic target datasets obtained by randomly perturbing velocity models suggest that the lowest scatter of the maximum likelihood solutions is attained for the approximate covariance function (ACF, Eq. (2.14)), possibly in combination with the approximate cross-covariance (AXCF, Eq. (2.13)), see Fig. 2.12. Tests with a single realization of the target synthetics evaluated in the perturbed velocity models show that the posterior covariance matrix reflects the true uncertainty of the moment tensor inversion well when considering the stationarized auto-covariance function (SACF, Eq. (2.21)), see Fig 2.13c. Similarly, real-data inversion using the SACF (Fig 2.14c) provides moment tensor uncertainty estimate comparable to the result of the jack-knifing experiment by Sokos & Zahradník (2013, fig. 3).

It is clear that the performance of the proposed approach to evaluate the GF uncertainty must undergo more thorough testing in a large number of practical applications. For easier implementation in other researchers’ codes we release open source codes for computing all the types of the proposed approximate (cross-)covariance matrices including the stationarized ones. The source codes are available for downloading under GNU license on the author’s website (<http://geo.mff.cuni.cz/~hallo/>) or in Attachments A.1, A.2, A.3 and A.4.

Acknowledgments

We appreciate waveform data (same as in Sokos & Zahradník 2013) provided by the Hellenic Unified Seismic Network operated by the Geodynamic Institute of the National Observatory of Athens [doi:10.7914/SN/HL], the Aristotle University of Thessaloniki [doi:10.7914/SN/HT], the University of Patras [doi:10.7914/SN/HP], co-operating certain stations jointly with the Charles University in Prague, and the University of Athens. Data from station TRIZ of the Corinth Rift Laboratory Network are also greatly appreciated. We acknowledge financial support by the Czech Science Foundation project 14-04372S, the Grant Agency of the Charles University projects SVV-260218 and GAUK-728916, and Ministry of Education, Youth and Sports project LM2015079 CzechGeo/EPOS. We would like to thank Jakub Velínský for his comments on the Monte-Carlo simulations and Jiří Zahradník for inspiring comments. We are grateful to an anonymous reviewers and the editor for their comments that improved the original manuscript.

2.5 Unpublished supplementary material

2.5.1 Alternative estimation of parameter L

All of the functions AXCF, ACF, SAXCF and SACF in Eqs (2.13), (2.14), (2.20) and (2.21), respectively, require prescription of parameter L_1 [sec]. This parameter has meaning of the width of the uniform PDF $p_1(l_1)$ defined by Eq. (2.8), where l_1 are random (joint) time shifts of “mother” waveforms $f(t)$ (and $g(t)$) caused by the insufficient knowledge of the velocity model. Magnifying the parameter L_1 leads to larger variance of the covariance matrix, as an effect of the increase of velocity model uncertainty. In our approach, we consider $L_1 = 4\sigma_t$ where σ_t has meaning of standard deviation of Gaussian PDF of waveform time shifts generated by random velocity model perturbations (see Fig. 2.1c). Here we show comparison with an alternative approach to estimate parameter L_1 using ray theory, as the ray tracing is much faster than computing the full wavefield. In ray tracing, the standard deviation σ_t is obtained from the ensemble of P- or S-wave arrival times in randomly perturbed velocity models. We performed this procedure in the same set of perturbed velocity models as in Fig. 2.1d.

The estimated values of L_1 for direct P- or S-waves (dotted and dashed lines, respectively) are compared in Fig. 2.20 with values of L_1 estimated from the complete wavefield (solid lines). The discrepancy between P- or S-wave arrivals and complete wavefield is due to assumed wavelength, which is much shorter in the ray theory (i.e. high frequency approximation). The S-wave arrivals approximate the time shift of the complete wavefield better as we assume wavefield on the Earth’s surface composed mostly from low-frequency surface waves. To conclude, the ray tracing offers undemanding method for estimation of values of L_1 . The another alternative approach for estimation of the parameter L_1 may utilize time residuals from the earthquake hypocenter location in a velocity model.

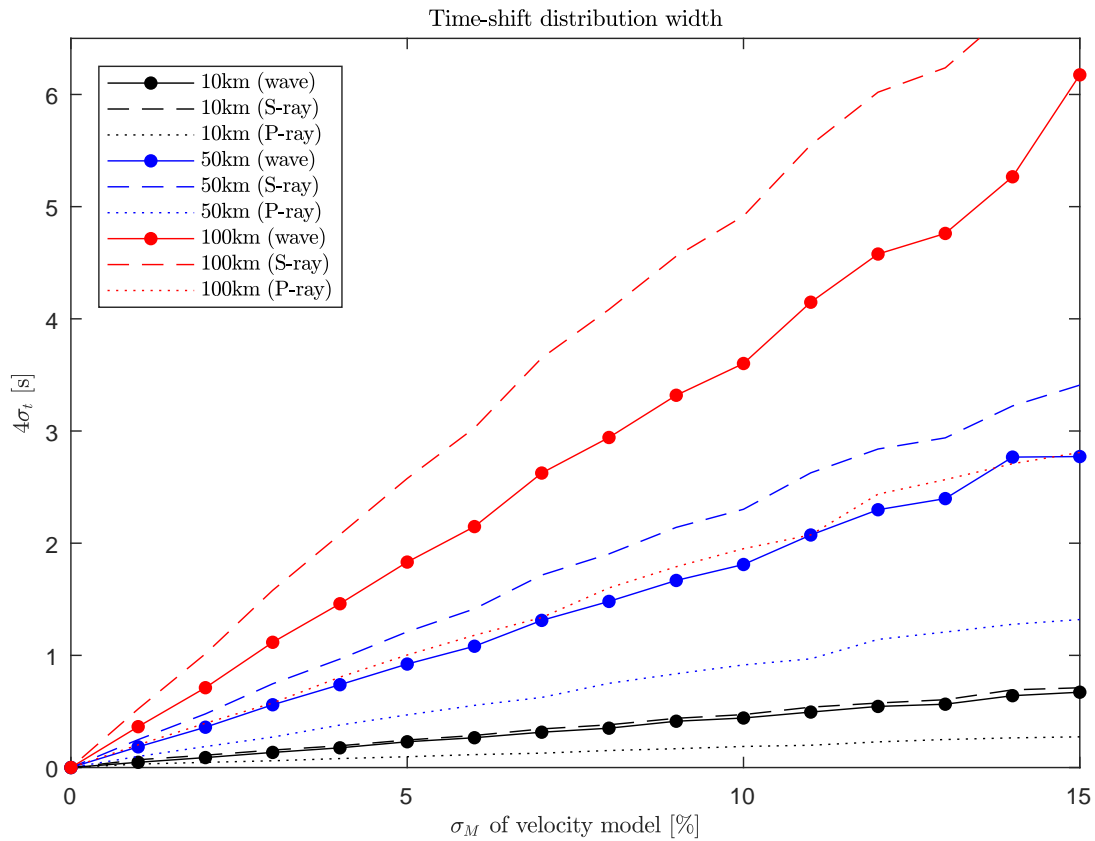


Figure 2.20: The dependence of the characteristic width of the time shift distribution ($L_1 = 4\sigma_t$) on the strength of the velocity model perturbations σ_M for three source-receiver distances. The standard deviation of Gaussian distributions of time shifts σ_t were determined from the whole wavefield generated by discrete wavenumber method, and from arrivals of direct P- and S-waves by ray tracing (see legend).

2.5.2 Inversion performance with non-DC MT

The analysis of moment tensor inversions with real and synthetic data for the test event from the Corinth Gulf, Greece, in previous Sections revealed that the DC component ratios are subject to significant uncertainty (see Figs 2.12 and 2.14c). The reliable assessment of the content of the DC component in the inverted deviatoric MTs is also an issue of our later application (see Chapter 3), hence here we perform additional synthetic tests with deviatoric MTs of various DC to CLVD ratios as the seismic sources. As the test event we assume a virtual earthquake from Kumamoto, Japan, at depth 7 km and with moment magnitude $M_w = 6.2$. Used source location and the station geometry as shown in Fig. 2.21 is consistent with the settings of the earthquake from 14 April 2016 (12:26 UTC; i.e. the largest foreshock of 2016 Kumamoto sequence).

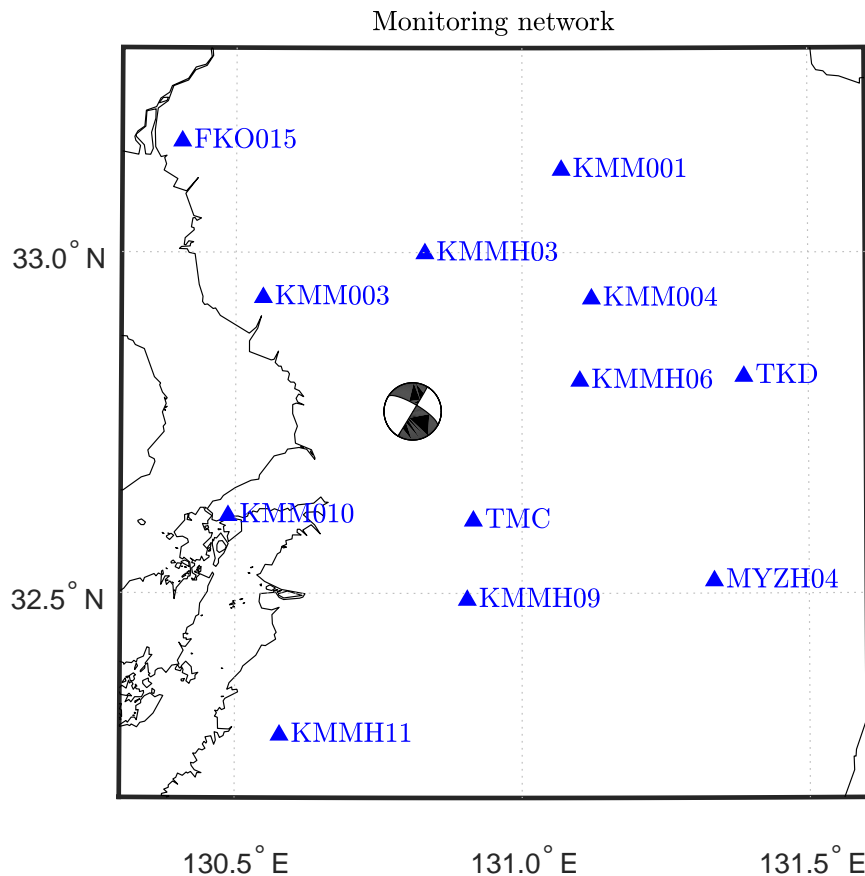


Figure 2.21: Seismic station distribution (triangles) in the Kumamoto area, Japan, used in the synthetic tests with the deviatoric MTs. The beachball plotted at the event epicenter corresponds to the pure-shear mechanism content of the source considered in the synthetic tests.

The target deviatoric MTs, as source models, were generated as the sum of DC MT with: strike 31° , dip 89° , and rake -157° and additional CLVD component of 0, 20, 40, 60, 80%, normalized to the prescribed total seismic moment. Synthetic waveforms for the inversion test were computed by the discrete wavenumber method (Bouchon 1981) assuming a Dirac delta function as the source time func-

tion, filtered by Butterworth bandpass filter with corner frequencies $0.03 - 0.1 \text{ Hz}$ and then downsampled to 2 Hz sampling rate. In the following tests we generate “data” for inversion assuming a realization of random variations of the wave speeds and depths of velocity model layers for each station independently (as in the MC simulations described in Section 2.2.1). Such random variations of the reference velocity model simulate a real case when the velocity model is not precisely known, yet well described by a mean model. In all tests the inversions are then performed in the reference (mean) layered velocity model.

Similarly as in Section 2.3.2, the deviatoric MT inversions are performed for 1000 different target data sets computed in the randomly perturbed velocity models, neglecting uncertainty of GFs in the inversion. For each realization, we obtained best-fitting solutions in Eq. (2.27) for each considered amount of CLVD component in the simulated source. Fig. 2.22 shows the ensemble of the solutions for various amount of CLVD component in the source. The ensemble is displayed in terms of DC mechanism nodal planes bias, histograms of the P-axis deviations from target source model, CLVD component bias ($1.0 = 100\%$; $0.0 = 0\%$; $-1.0 = -100\%$) and the inferred scalar seismic moment M_0 .

We note that the spread of the differences to the target solution (plotted in red) is caused by the variations of the randomly perturbed velocity model, hence by the GFs uncertainty (in analogy to Fig. 2.12). Hence, the presented statistics of the inverted best-fitting parameters can be understood as the “true” MT uncertainty caused by the velocity model uncertainty. Overall assessment of the performance of the inversions with the various amounts of CLVD content in the target source model suggests that “true” MT uncertainties are almost independent of the amount of the CLVD component in the source (compare histograms among panels **a**)–**e**). There is higher uncertainty of the inferred DC nodal planes in case of CLVD content of 80% as scalar moment of DC solution declines. The estimated CLVD uncertainties caused by the imprecise knowledge of the velocity model (of $\sigma_M = 10\%$) are up to $\pm 25\%$, and thus should not be neglected in practical applications.

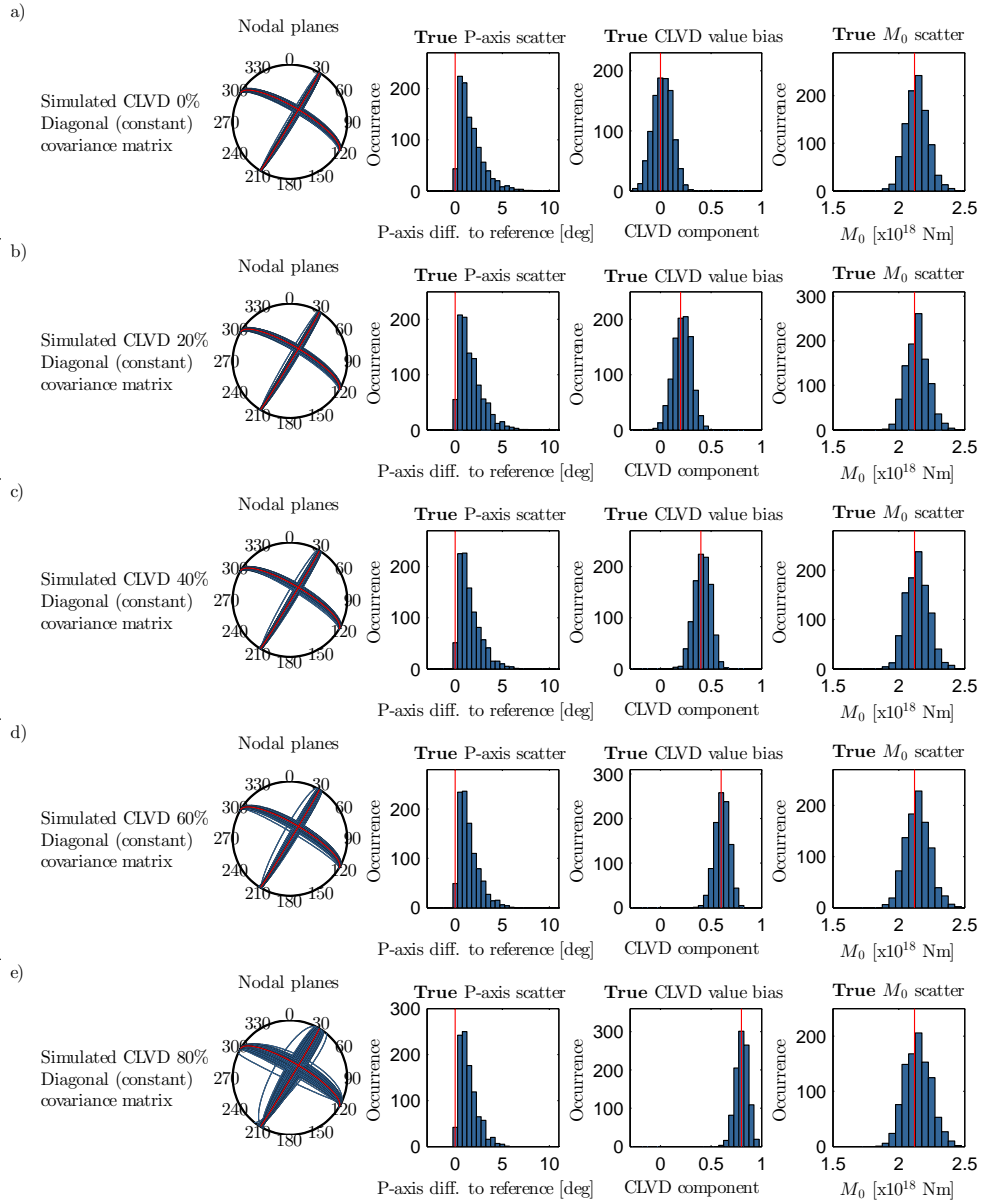


Figure 2.22: Statistical analysis of best-fitting solutions from inversion of synthetic deviatoric MT neglecting uncertainty of velocity model. 1000 realizations of randomly perturbed velocity models are used to generate population of the target data. Panels in each row show DC mechanism nodal planes (left), deviation of P-axis from the target value (middle-left), CLVD component bias (middle-right) and M_0 scatter (right). Each row **a)–e)** corresponds to the use of different amount of CLVD content in the target source of 0, 20, 40, 60, 80 %, respectively. The target solution (in red) has nodal planes with strike 31° , dip 89° , rake -157° , and scalar seismic moment $M_0 = 2.12 \times 10^{18}$ Nm.

Next, we assess the ability of the SACF and diagonal covariance matrices to estimate the “true” uncertainty of inverted deviatoric MTs. We selected three of the data sets, inferred their best-fitting MT solutions and estimated their uncertainties in terms of the posterior covariance matrix in Eq. (2.28). The synthetic data sets were selected based on the preliminary inverted best-fitting MT solution, in order to select examples with **1**) significant underestimation (*Example1*), **2**) correct estimation (*Example2*) and **3**) significant overestimation (*Example3*) of the CLVD component. Figs 2.23 and 2.24 show the maximum likelihood solutions together with their posterior uncertainties, for diagonal and SACF covariance matrices, respectively. Note that contrarily to Fig. 2.22, here the ensemble of the solutions is obtained by random sampling the posterior PDF (using Matlab function *mvnrnd*). We plot ensembles of solutions for the various amounts of CLVD content and the three selected data sets (*Example1–3*). The true values of the CLVD content are plotted by red lines.

The deviatoric MT inference assuming diagonal covariance matrix (Fig. 2.23) underestimates the CLVD uncertainty, and, in extreme case, even leads to exclusion of the true (target) solution from the confidence interval. Contrarily, the deviatoric MT inference with the SACF (Fig. 2.24) provides CLVD uncertainty estimate up to approximately $\pm 20\%$, being comparable with the true uncertainty shown in Fig. 2.22, and covering also the true (target) solution in all the investigated cases.

To conclude, using SACF covariance matrix improves the performance of the deviatoric MT inversions. The estimate of the uncertainty of the amount of CLVD component by means of posterior covariance matrix is also more reliable when employing the covariance matrix built from the SACFs.

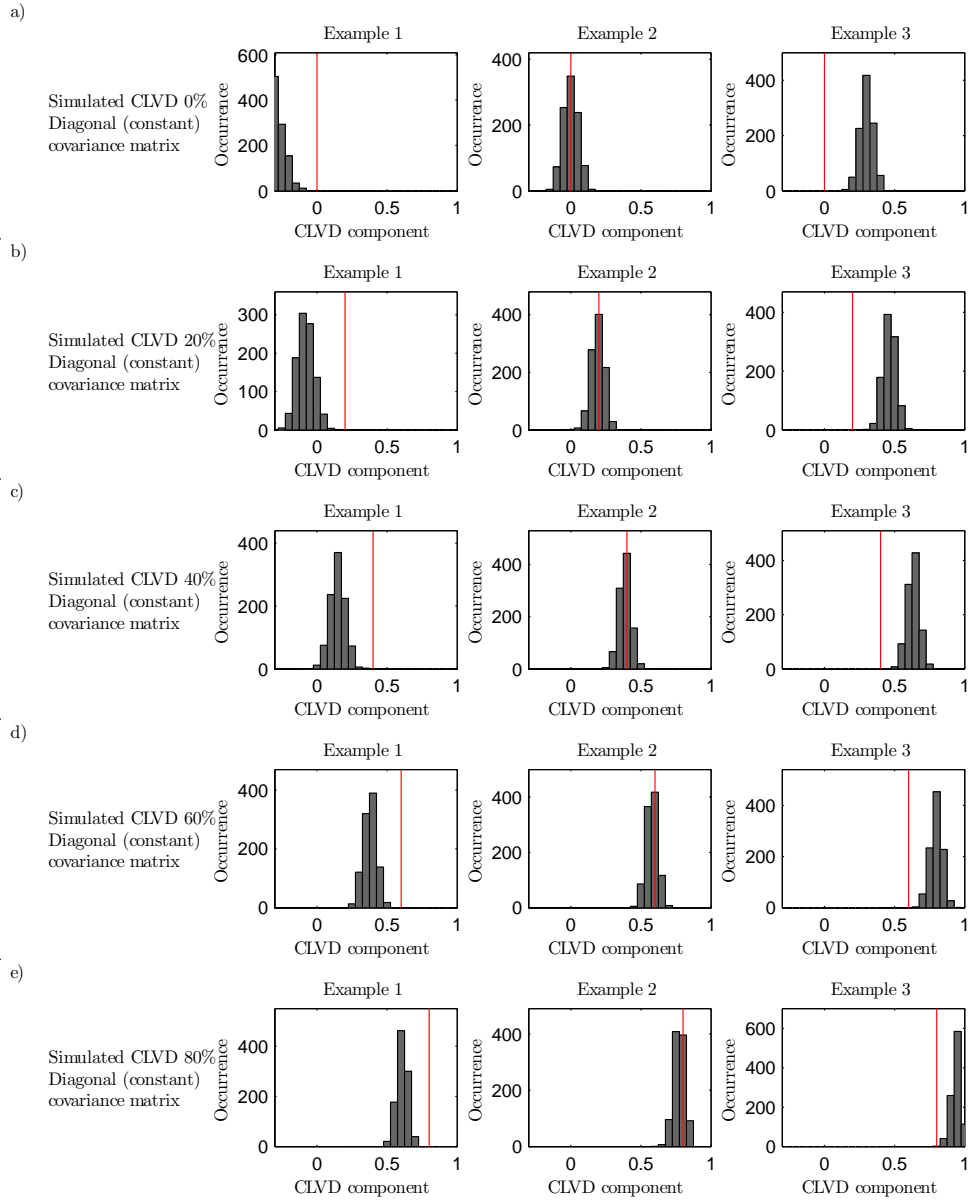


Figure 2.23: Results of an inversion of deviatoric MT with three realizations of the randomly perturbed velocity models to generate the target data, and using **diagonal** constant covariance matrix. The realization of the randomly perturbed velocity models is the same for all panels in each column (Example1–3). Panels show CLVD uncertainty estimate, where each row **a)–e)** corresponds to the use of different amount of CLVD content in the target source of 0, 20, 40, 60, 80 %, respectively. The histograms are built from 300 random samples of the posterior PDF to visualize the estimated parameter uncertainty. The true solutions of CLVD content are plotted by the red line.

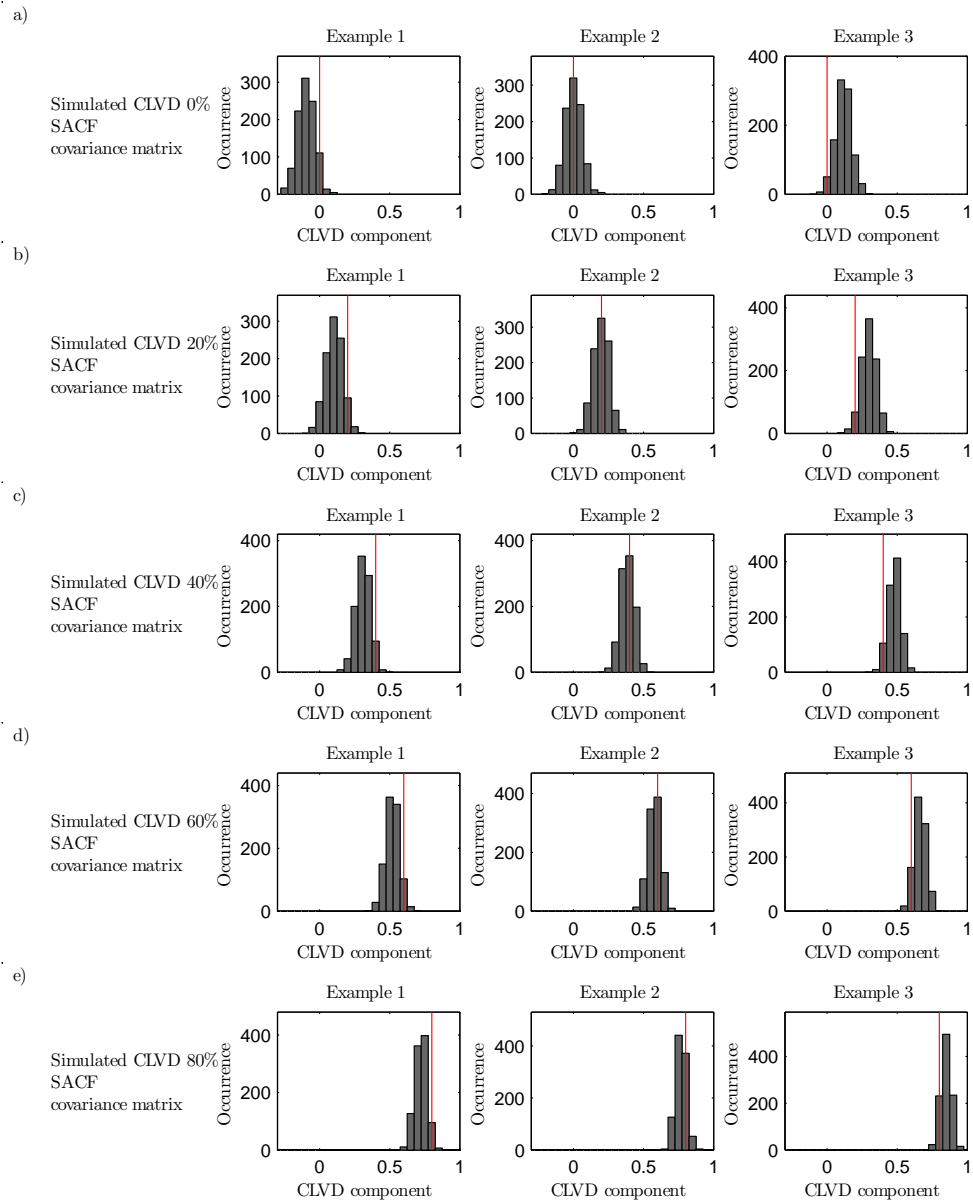


Figure 2.24: The same as Fig. 2.23 but for inversion of deviatoric MT using **SACF** covariance matrix.

3. Bayesian inference and interpretation of centroid moment tensors of the 2016 Kumamoto earthquake sequence, Japan

Published in Earth, Planets and Space,
Volume 69, Article 134, 1–19, September 2017, doi:10.1186/s40623-017-0721-4,
text in this Chapter includes also its published supplementary material.

Miroslav Halló¹, Kimiyuki Asano² & František Gallovič¹

Abstract: On April 16, 2016, Kumamoto prefecture in Kyushu region, Japan, was devastated by a shallow $M_{JMA}7.3$ earthquake. The series of foreshocks started by $M_{JMA}6.5$ foreshock 28 h before the mainshock. They have originated in Hinagu fault zone intersecting the mainshock Futagawa fault zone; hence, the tectonic background for this earthquake sequence is rather complex. Here we infer centroid moment tensors (CMTs) for 11 events with M_{JMA} between 4.8 and 6.5, using strong motion records of the K-NET, KiK-net and F-net networks. We use upgraded Bayesian full-waveform inversion code ISOLA-ObsPy, which takes into account uncertainty of the velocity model. Such an approach allows us to reliably assess uncertainty of the CMT parameters including the centroid position. The solutions show significant systematic spatial and temporal variations throughout the sequence. Foreshocks are right-lateral steeply dipping strike-slip events connected to the NE–SW shear zone. Those located close to the intersection of the Hinagu and Futagawa fault zones are dipping slightly to ESE, while those in the southern area are dipping to WNW. Contrarily, aftershocks are mostly normal dip-slip events, being related to the N–S extensional tectonic regime. Most of the deviatoric moment tensors contain only minor CLVD component, which can be attributed to the velocity model uncertainty. Nevertheless, two of the CMTs involve a significant CLVD component, which may reflect complex rupture process. Decomposition of those moment tensors into two pure shear moment tensors suggests combined right-lateral strike-slip and normal dip-slip mechanisms, consistent with the tectonic settings of the intersection of the Hinagu and Futagawa fault zones.

Keywords: Tectonics, Inverse theory, Waveform source inversion, Centroid moment tensors, Strong motion data, 2016 Kumamoto sequence, Foreshocks and aftershocks, Futagawa and Hinagu faults.

¹Faculty of Mathematics and Physics, Charles University, Prague, Czech Republic

²Disaster Prevention Research Institute, Kyoto University, Gokasho, Uji, Japan

3.1 Introduction

The 2016 Kumamoto earthquake sequence started on April 14, 2016, with an $M_{JMA}6.5$ shallow earthquake in the central part of Kyushu, Japan (see Fig. 3.1). The seismic activity continued by weaker events, including $M_{JMA}5.8$ and $M_{JMA}6.4$ earthquakes 41 *min* and 2.6 *h* after the first shock, respectively. The mainshock of the sequence of $M_{JMA}7.3$ occurred on April 16, 2016 (01:25 of Japan Standard Time), 28 *h* after the first earthquake (the yellow circle in Fig. 3.1). The mainshock generated destructive ground motions in the near-source region, causing severe damage and casualties. The following aftershocks had wide spatial distribution across the whole Kyushu with the strongest event of $M_{JMA}5.9$ that occurred 20 *min* after the mainshock. Increased seismic activity in the area was notable even 2 weeks after the first foreshock, and it was daily reported by the Japan Meteorological Agency (JMA). In the 2016 Kumamoto sequence, seven earthquakes reached or exceeded instrumental intensity 6- of the JMA intensity scale which consists of degrees 0, 1, 2, 3, 4, 5-, 5+, 6-, 6+, 7.

This earthquake sequence occurred along the Futagawa-Hinagu fault system, which is one of the major active fault zones in Kyushu. This shear zone is considered to be western extension of the Median Tectonic Line (MTL), the largest tectonic line in southwestern Japan (e.g., Okada 1980; Kamata & Kodama 1994). The MTL is an active right-lateral strike-slip fault which originates at Honshu Island and transects whole Shikoku Island. Extension of the MTL transects Kyushu at NE–SW direction, with evidence of right-lateral strike-slip and extensional movements (Kamata & Kodama 1994). An area in the central part of Kyushu, located north of the shear zone, is called the Beppu–Shimabara graben. It is characterized by many normal faults formed in the N–S extensional stress regime. According to Kamata & Kodama (1999), this extension can be related to the effect of the Ryukyu Trench and convergence of the Philippine Sea slab, where it possibly induces seafloor spreading at the Okinawa Trough. The tectonic stress in Kyushu has large spatial heterogeneities (Matsumoto et al. 2015). At Kumamoto area, the minimum principal stress σ_3 (extension) is in the N–S direction, and the maximum principal stress σ_1 has similar size as σ_2 (Matsumoto et al. 2015); therefore, strike-slip and also normal faults are expected under such stress regime (see Attachment A.5).

The mainshock created more than 30 *km* long system of co-seismic surface ruptures along the Futagawa–Hinagu fault system (e.g., Kumahara et al. 2016; Toda et al. 2016; Shirahama et al. 2016) terminating in the Aso volcano caldera (e.g., Lin et al. 2016). The surface co-seismic ruptures were dominated by right-lateral strike-slips with a secondary normal faulting component. The normal faulting was dominant especially in the northeast part of the rupture zone (e.g., Toda et al. 2016). Finite source models for the mainshock were inverted from strong motion records (e.g., Asano & Iwata 2016; Kubo et al. 2016b; Hao et al. 2017; Kobayashi et al. 2017; Yoshida et al. 2017). The inferred models suggest that the $M_{JMA}7.3$ event started near the intersection of the Futagawa and Hinagu faults by right-lateral strike-slip movement; then, the rupture propagated to the NE along the Futagawa fault as strike-slip with a normal faulting component. Finite source models and also static slip models from geodetic data (Himematsu & Furuya 2016; Fukahata & Hashimoto 2016) are consistent with field measurements

of co-seismic surface ruptures. The source models introduce two or three segments of the mainshock rupture, but their physical relation to the foreshock ruptures remains unclear because of the complex tectonic settings of the intersection of the Futagawa and Hinagu faults.

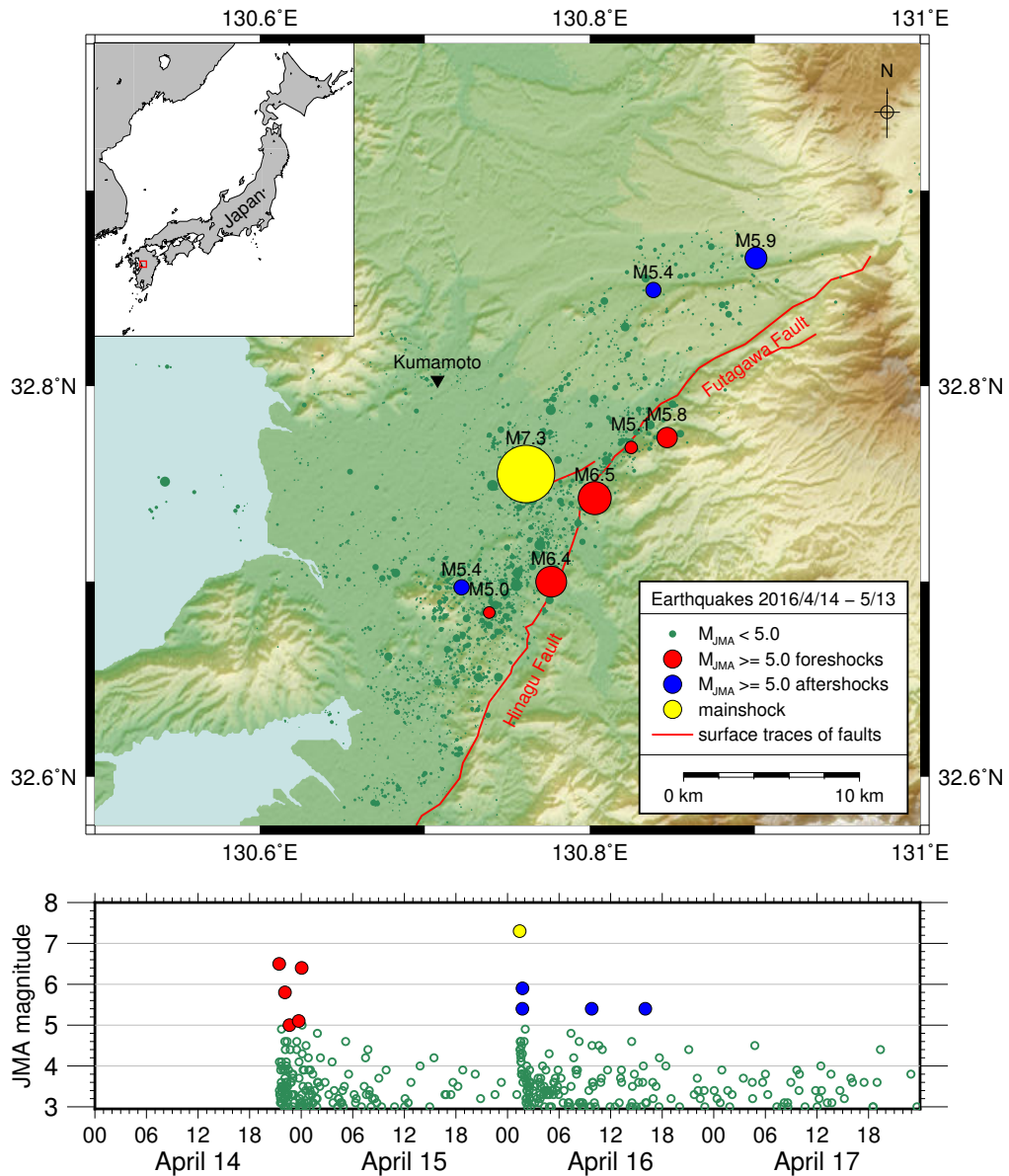


Figure 3.1: Spatial and temporal distribution of the Kumamoto earthquake sequence. **Top panel**—map of earthquake’s locations inferred by Kato et al. (2016) for period April 14–May 13, 2016. The size of circles is proportional to the JMA magnitude of the events. Earthquakes with M_{JMA} magnitude higher than or equal to 5 are distinguish by color: foreshocks (red), mainshock (yellow) and aftershocks (blue). The topography originates from the SRTM-90m digital elevation data. **Bottom panel**—temporal evolution of the earthquakes from the map in top panel is showing period from April 14–April 17, 2016, when all events with M_{JMA} magnitude higher than or equal to 5 occurred.

This study focuses on the point source models of the significant foreshocks and aftershocks of the Kumamoto sequence. The centroid moment tensors (CMTs) for

these events were inferred routinely by JMA and by National Research Institute for Earth Science and Disaster Resilience (NIED). However, these solutions are not supplemented by their uncertainty, which is required when trying to draw conclusions on the physical relations of ruptures in such case of complex tectonic settings. Here we infer CMTs of the significant foreshocks and aftershocks and their uncertainty by our novel full-waveform inversion from strong motion data. The results are then interpreted in a seismotectonic framework.

3.2 Methods

3.2.1 Problem formulation

In the low-frequency point source approximation, the source is described by the centroid moment tensor (CMT, Aki & Richards 2002, pp. 49–52). The CMT consists of ten parameters: six moment tensor elements M_{pq} , location $\boldsymbol{\xi}$ and time τ . The centroid denotes to temporal and spatial center of the moment tensor density. Ground displacement u_n at position \boldsymbol{x} and time t generated by CMT with the source time function $\boldsymbol{\Omega}(t)$ is given for the n -th component by

$$u_n(\boldsymbol{x}, t) = M_{pq}(\boldsymbol{\xi})\boldsymbol{\Omega}(t - \tau) * H_{np,q}(\boldsymbol{x}, \boldsymbol{\xi}, t), \quad (3.1)$$

where star denotes convolution and $H_{np,q}$ is the spatial derivative of Green's function (GF) representing response of the medium to a unite force. Eistein summation convention applies.

Kikuchi & Kanamori (1991) proposed to represent the moment tensor MT, for a given centroid position and time, by a linear combination of six elementary MTs defined therein (see Eqs (2.23) and (2.24)). Then, discretized Eq. (3.1) can be expressed for a given source space–time position i and a given function $\boldsymbol{\Omega}(t)$ in a matrix form (Tarantola 2005, pp. 62–68),

$$\boldsymbol{d}_i = \mathbf{G}_i \boldsymbol{m}_i, \quad (3.2)$$

where \boldsymbol{d}_i is a vector of synthetic seismograms and \boldsymbol{m}_i is a vector of six coefficients of the elementary MTs. \mathbf{G}_i is a matrix of six columns composed of elementary seismograms, representing ground displacements caused by elementary MTs placed at position i . The problem is then linear for a given source space–time position (six elementary MT coefficients), whereas it is nonlinear for the other four parameters (location $\boldsymbol{\xi}$ and time τ).

3.2.2 Bayesian inference of CMT

We apply modification of the Bayesian full-waveform CMT inversion, ISOLA-ObsPy (Vackář et al. 2017), which allows for reliable assessment of the solution uncertainty. In this method, a regular grid of four nonlinear CMT model parameters (location $\boldsymbol{\xi}$ and time τ) is considered. We assume one-column data vector \boldsymbol{d}_{obs} characterized by Gaussian data errors with covariance matrix \mathbf{C}_D (will be discussed in the next section). At a given space–time grid point i , assuming no prior information (i.e., infinite standard deviation) on the model parameters

\mathbf{m}_i , the posterior probability density function (posterior PDF) for the MT is six-dimensional Gaussian function,

$$PDF_i(\mathbf{m}_i|\mathbf{d}_{obs}) = \frac{1}{c} \exp\left(-\frac{1}{2}(\mathbf{d}_{obs} - \mathbf{G}_i\mathbf{m}_i)^T \mathbf{C}_D^{-1} (\mathbf{d}_{obs} - \mathbf{G}_i\mathbf{m}_i)\right) \quad (3.3)$$

Parameter c is a constant normalizing the total ten-dimensional PDF to unity. Note that the term including prior information on the model parameters (Tarantola 2005, eq. 1.104) is not present in Eq. (3.3) as it is equal to 1.

After simple algebra, Eq. (3.3) can be equivalently written as

$$PDF_i(\mathbf{m}_i|\mathbf{d}_{obs}) = \frac{1}{c} \exp\left(-\frac{1}{2}(\mathbf{m}_i - \tilde{\mathbf{m}}_i)^T (\tilde{\mathbf{C}}_i^M)^{-1} (\mathbf{m}_i - \tilde{\mathbf{m}}_i) - \frac{1}{2}\mathcal{L}_i\right) \quad (3.4)$$

with

$$\mathcal{L}_i = (\mathbf{d}_{obs} - \mathbf{G}_i\tilde{\mathbf{m}}_i)^T \mathbf{C}_D^{-1} (\mathbf{d}_{obs} - \mathbf{G}_i\tilde{\mathbf{m}}_i), \quad (3.5)$$

$$\tilde{\mathbf{m}}_i = (\mathbf{G}_i^T \mathbf{C}_D^{-1} \mathbf{G}_i)^{-1} (\mathbf{G}_i^T \mathbf{C}_D^{-1} \mathbf{d}_{obs}), \quad (3.6)$$

$$\tilde{\mathbf{C}}_i^M = (\mathbf{G}_i^T \mathbf{C}_D^{-1} \mathbf{G}_i)^{-1}. \quad (3.7)$$

In Eq. (3.6), $\tilde{\mathbf{m}}_i$ corresponds to the least squares solution of the six model parameters with misfit \mathcal{L}_i from Eq. (3.5) (Tarantola 2005, eq. 3.40). The associated uncertainties (of the least squares solution $\tilde{\mathbf{m}}_i$) are described by the posterior model covariance matrix $\tilde{\mathbf{C}}_i^M$ given in Eq. (3.7) (Tarantola 2005, eq. 3.41).

The role of the data covariance matrix \mathbf{C}_D in the inversion is apparent in definition of the misfit function. In MT inversion without considering \mathbf{C}_D , the misfit function is difference (residuals) between the recorded data \mathbf{d}_{obs} and synthetics \mathbf{d}_i . If the covariance matrix \mathbf{C}_D is used, the misfit function is given by so-called standardized residuals (Dettmer et al. 2014), i.e., waveforms multiplied by the triangular matrix \mathbf{W} from the Cholesky decomposition of \mathbf{C}_D

$$\mathbf{C}_D^{-1} = \mathbf{W}^T \mathbf{W}. \quad (3.8)$$

The variance reduction, a parameter evaluating solution fit to measured data in the grid point i , is then given by

$$VR_i = \left(1 - \frac{\|\mathbf{W}^T \mathbf{d}_{obs} - \mathbf{W}^T \mathbf{d}_i\|^2}{\|\mathbf{W}^T \mathbf{d}_{obs}\|^2}\right) \cdot 100 \% \quad (3.9)$$

The normalizing constant c from Eq. (3.3) can be obtained by integration over all the ten CMT parameters. In our case, we integrate over the space–time grid points (Vackář et al. 2017),

$$\begin{aligned} 1 &= \sum_i dV_i \int PDF_i(\mathbf{m}_i|\mathbf{d}_{obs}) d\mathbf{m}_i \\ &= \sum_i \frac{1}{c} \sqrt{(2\pi)^6 \det \tilde{\mathbf{C}}_i^M} \exp\left(-\frac{1}{2}\mathcal{L}_i\right) dV_i \\ &= \sum_i a_i, \end{aligned} \quad (3.10)$$

where the term dV_i is the product of grid steps of all the four nonlinear model parameters (i.e., the space and time discretization steps). The value a_i is an

integral of PDF_i at the given space–time grid point. It depends on the most likely solution misfit \mathcal{L}_i and the determinant of the posterior covariance matrix of model parameters $\tilde{\mathbf{C}}_i^{\mathbf{M}}$, in particular space–time grid point. It thus carries information about the quality of the least squares solution in particular grid point.

Vackář et al. (2017) propose to inspect posterior PDF of any CMT parameters by generating set of random possible solutions from the total ten-dimensional posterior PDF. This can be achieved by drawing a_i random samples at each space–time grid point from the multivariate normal distribution specified by $\tilde{\mathbf{m}}_i$ and $\tilde{\mathbf{C}}_i^{\mathbf{M}}$. From such ensemble, it is then possible to statistically assess uncertainty of any CMT parameter, including those that are not directly inverted for, but can be derived from the MT components (e.g., strike angle, dip angle, rake angle and DC component percentage).

3.2.3 Accounting for the uncertainty of the velocity structure

The reliability of the assessment of the solution uncertainty by this Bayesian framework depends on the assessment of the data and modeling errors. The data errors (i.e., the instrumental and ambient noise) are typically negligible when dealing with larger events, as in our present application. We avoid using data with rare instrumental artifacts (e.g., Zahradník & Plešinger 2010). The solution uncertainty is then dominated by modeling errors governed by the uncertainty of the GFs due to the inaccuracy of the crustal model considered. We include the modeling errors in covariance matrix $\mathbf{C}_{\mathbf{D}}$ following approach by Hallo & Gallovič (2016). They compose $\mathbf{C}_{\mathbf{D}}$ from so-called stationarized approximate covariance functions defined by

$$\overline{cov}(\varphi) = \frac{1}{T} \left[r(\varphi) - \Lambda_{2L}(\varphi) * r(\varphi) \right], \quad (3.11)$$

where $r(\varphi)$ is auto-correlation of the observed seismogram as a function of time lag φ , T is duration of the dominant part of the signal, star is convolution and $\Lambda_{2L}(\varphi)$ is a triangle function of unit area centered around zero with duration $2L$. Since Eq. (3.11) is stationary (i.e., depending only on time lag φ), the respective covariance matrix has Toeplitz structure (diagonal constant). Parameter L generally depends on the source–receiver distance, frequency range and considered uncertainty of the velocity model. Hallo & Gallovič (2016) tested the performance of such covariance matrices by means of numerous MT inversions with synthetic data generated in randomly perturbed velocity models. The posterior model covariance matrix from inversion using Eq. (3.11) was therein shown to reliably reflect the simulated uncertainty of the inferred MTs (see Chapter 2).

In the present multi-station and multi-component inversion, data covariance matrix $\mathbf{C}_{\mathbf{D}}$ has block structure. The covariance matrices for the individual waveforms are arranged along the diagonal, while off-diagonal blocks (cross-covariances) are neglected and hence set to zeros. A station-specific water level was added to the diagonal to preserve the covariance matrix invertible. As the water level, we use 10 % of the maximum variance from all the three station components. The parameters L from Eq. (3.11) were determined based on relation

introduced by Hallo & Gallovič (2016) in a similar inversion setting

$$L = \frac{|\mathbf{x} - \mathbf{x}_{epic}|}{25 [km/s]}, \quad (3.12)$$

where $|\mathbf{x} - \mathbf{x}_{epic}|$ denotes horizontal distance between the station and epicenter in kilometers. Such an estimate is found suitable for velocity model uncertainty of 10 %. The duration of the dominant part of the signal T was set to 15 sec for all stations and events.

3.3 Application to the Kumamoto sequence

We infer CMTs of 11 significant earthquakes with M_{JMA} magnitude in range of 4.8–6.5 (see Table 3.1 for list of the events). The set consists of all foreshocks and aftershocks with M_{JMA} magnitude higher than or equal to 5 (denoted by red and blue circles in Fig. 3.1), and two aftershocks with M_{JMA} magnitude 4.9 and 4.8. The mainshock itself was omitted from the analysis as it has rather complex earthquake source rupture process that was studied in detail in other studies (e.g., Asano & Iwata 2016; Kubo et al. 2016b; Kobayashi et al. 2017).

3.3.1 Data selection and processing

We use three-component waveforms recorded by the K-NET, KiK-net and F-net networks, operated by National Research Institute for Earth Science and Disaster Resilience (NIED), in the distances of 10 – 60 km from the epicenter (depending on the particular event). The stations are selected based on azimuthal coverage, distance and sufficient signal-to-noise ratio in the low-frequency range. Stations located too close to the epicenter are excluded to comply with the point source approximation, i.e., to avoid station distances for which GFs along the fault differ significantly. Original acceleration data (K-NET and KiK-net) and strong motion velocity data corrected for the instrument response (F-net) are filtered by a bandpass filter and integrated into displacements (the K-NET and KiK-net accelerometers have flat transfer function in our target frequency range). The filter corner frequencies are determined empirically by manual inspection and

No.	M_{JMA}	Event		Hypocentre location*			Filter corner freq. [Hz]		Number of used stations
		Date	Time*	Lat.	Lon.	Depth [km]	High pass	Low pass	
1	6.5	2016/4/14	21:26:35	32.74	130.81	11	0.03	0.07	12
2	6.4	2016/4/15	00:03:47	32.70	130.78	7	0.03	0.08	12
3	5.9	2016/4/16	01:46:56	32.86	130.90	11	0.04	0.07	11
4	5.8	2016/4/14	22:07:35	32.77	130.85	8	0.08	0.14	12
5	5.4	2016/4/16	01:44:06	32.75	130.76	15	0.15	0.20	10
6	5.4	2016/4/16	09:48:32	32.85	130.84	16	0.08	0.15	13
7	5.4	2016/4/16	16:02:01	32.70	130.72	12	0.08	0.15	11
8	5.1	2016/4/14	23:43:41	32.77	130.83	14	0.08	0.14	10
9	5.0	2016/4/14	22:38:43	32.68	130.74	11	0.09	0.15	10
10	4.9	2016/4/16	02:04:11	32.74	130.74	12	0.11	0.15	8
11	4.8	2016/4/16	07:23:55	32.79	130.77	12	0.12	0.16	9

Note: *by Japan Meteorological Agency; *Japan Standard Time

Table 3.1: List of processed earthquakes from the Kumamoto sequence.

processing of the waveforms (see Table 3.1). In general, the high-pass filter corner frequency is as low as possible in terms of signal-to-noise ratio. The low-pass filter corner frequency is limited by corner frequency of the particular earthquake. Waveform data are downsampled after the filtration and integration to the sampling frequency $0.6 - 1.3 Hz$, based on the low-pass filter corner frequency, in order to reduce computational demands.

3.3.2 Velocity model

GFs are computed by the discrete wavenumber method (Bouchon 1981) in 1D velocity model consisting of homogenous layers. The model is prepared from the 3D Japan Integrated Velocity Structure Model (Koketsu et al. 2012) as a horizontal average over area of $40 \times 40 km$ around mainshock epicenter. The horizontal average is calculated for a dense set of depths (smooth model in Fig. 3.2a) and then divided into homogenous layers preserving the vertical travel times within layers (layered model in Fig. 3.2a). Figure 3.2b shows maximal deviation of the 1D model from the original 3D model (maximal lateral heterogeneities which are not included in the 1D model). These velocity variations are less than 10% for depths larger than 1 km. The shallow layers show higher lateral heterogeneities, but they do not significantly affect the inversion using much longer wavelengths for sources at depths of Kumamoto earthquakes.

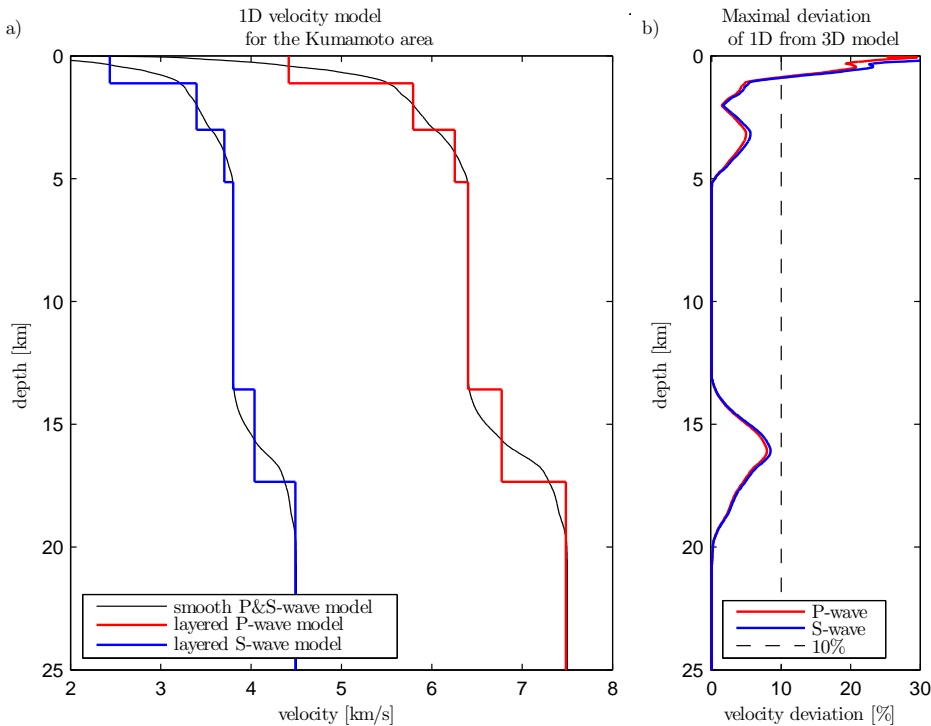


Figure 3.2: **a)** 1D velocity model of the Kumamoto area determined from the 3D Japan Integrated Velocity Structure Model (Koketsu et al. 2012). **b)** maximal horizontal deviation of the velocities of the determined 1D model from the original 3D model.

3.3.3 Application details

The CMT inversion strategy consists of the following processing steps:

1. Inference of full CMT, including isotropic component, is performed by inversion from extended set of stations without considering any model or data uncertainty. At this stage, we consider a rough grid of space-time grid points in the search of the nonlinear parameters, with regular grid steps of 1.4 km in all three coordinate directions within 16 km around the hypocenter reported by JMA. Time grid covers $0 - 4\text{ sec}$ after the hypocenter time with regular time grid steps of about $0.3 - 0.1\text{ sec}$ (depending on the particular event).
2. We manually inspect the best fit of the synthetic and measured waveforms to reveal stations with unusable signal. The proposed Bayesian inference is intended to deal with unknown velocity model perturbations which are close to the 1D velocity model, but it cannot correct for missing velocity structures or other systematical errors in the waveform data. Hence, stations with very poor fit are excluded from the next step of the processing. Mostly, it is the case of very distant stations or receivers located in the coastal area of the Ariake Sea. The final number of used stations is shown in Table 3.1.
3. We perform the Bayesian inference of CMT taking into account velocity model uncertainty of 10% . Here we consider a denser grid in the search of the nonlinear parameters with regular grid steps about $0.2 - 0.5\text{ km}$ in all three coordinate directions within $3 - 5\text{ sec}$ around the CMT location inverted in the first step. Time grid covers $0 - 4\text{ sec}$ after the hypocenter time with regular time grid steps of about 0.1 sec . Since isotropic component of MT was negligible in all cases, we conserve it at 0% .

As the ensemble of acceptable solutions, we generate 1000 random possible solutions drawn from the ten-dimensional posterior PDF. The resulting MTs are decomposed into combination of double-couple (DC) and compensated linear vector dipole (CLVD) sources. Marginal PDFs of selected CMT parameters (marginal histograms) are fitted with Gaussian function defined by its mean and standard deviation σ . We consider 2σ as the estimate of the uncertainty covering half-width of a 95% confidence interval of the normal distribution.

As examples of the application, we depict three selected CMT inversions in Figs 3.3, 3.4 and 3.5. Figure 3.3 shows the CMT inversion of the strongest $M_{JMA}6.5$ foreshock (event No. 1) in terms of the network settings, the best fit of the standardized waveforms at all stations and the best beach-ball solution with uncertainty (see the figure caption). Figure 3.4 shows the same, but for the $M_{JMA}5.8$ foreshock (event No. 4), which is performed from the same set of stations as for the previous event. The solution has a high variance reduction and high DC content. The example in Fig. 3.5 corresponds to the $M_{JMA}5.4$ aftershock (event No. 7), which is characterized by high variance reduction and high (significant) CLVD content.

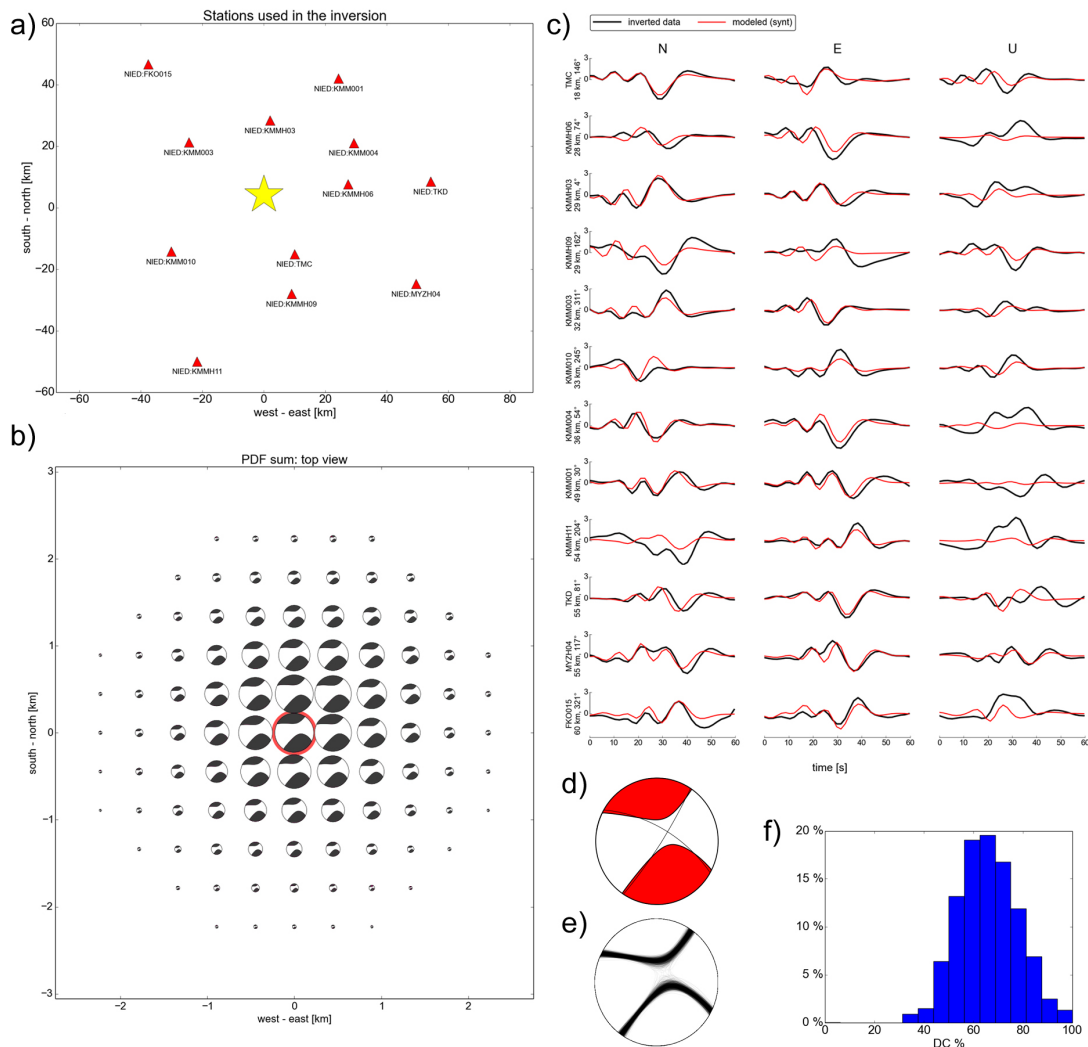


Figure 3.3: CMT inversion for the MJMA6.5 foreshock from 2016/4/14 21:26:35 JST (event No. 1). The figures are produced by modified program ISOLA-ObsPy of Vackář et al. (2017); **a)** the map of strong motion stations (red triangles) used for the CMT inference; **b)** marginal PDF of the CMT location in a horizontal slice indicated by the size of the beach-balls; the beach-balls depict inferred MTs at the individual spatial points. The beach-ball highlighted by red circle is the solution with the highest variance reduction (the best fitting solution); **c)** the comparison between measured and synthetic standardized waveforms for the best fitting solution; **d)** the beach-ball representation of the best fitting CMT; **e)** the uncertainty of the mechanism depicted by 1000 random possible solutions drawn from the ten-dimensional posterior PDF; **f)** histogram of the DC component.

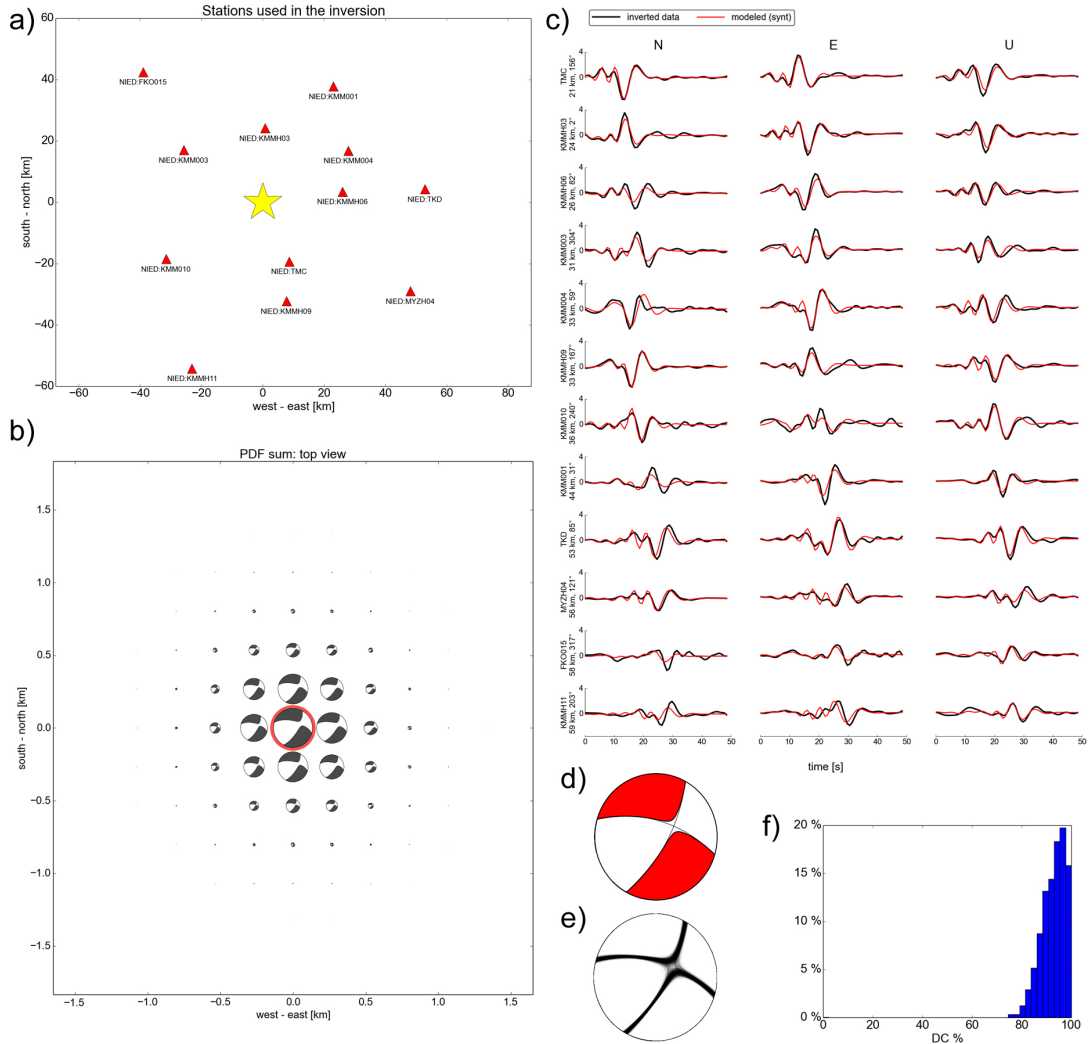


Figure 3.4: CMT inversion for the $M_{JMA}5.8$ foreshock from 2016/4/14 22:07:35 JST (event No. 4). The figures are produced by modified program ISOLA-ObsPy of Vackář et al. (2017); **a)** the map of strong motion stations (red triangles) used for the CMT inference; **b)** marginal PDF of the CMT location in a horizontal slice indicated by the size of the beach-balls; the beach-balls depict inferred MTs at the individual spatial points. The beach-ball highlighted by red circle is the solution with the highest variance reduction (the best fitting solution); **c)** the comparison between measured and synthetic standardized waveforms for the best fitting solution; **d)** the beach-ball representation of the best fitting CMT; **e)** the uncertainty of the mechanism depicted by 1000 random possible solutions drawn from the ten-dimensional posterior PDF; **f)** histogram of the DC component.

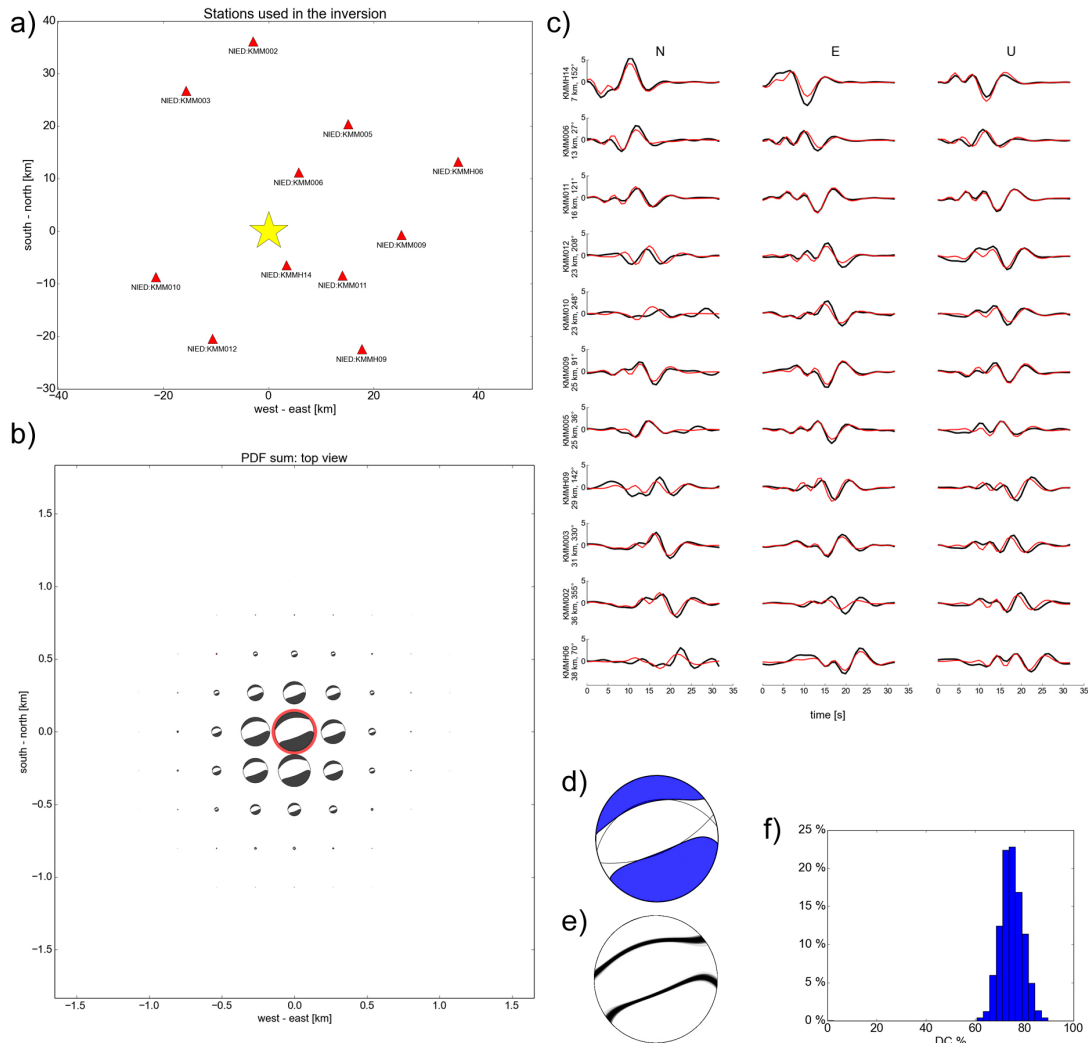


Figure 3.5: CMT inversion for the $M_{JMA}5.4$ aftershock from 2016/4/16 16:02:01 JST (event No. 7). The figures are produced by modified program ISOLA-ObsPy of Vackář et al. (2017); **a)** the map of strong motion stations (red triangles) used for the CMT inference; **b)** marginal PDF of the CMT location in a horizontal slice indicated by the size of the beach-balls; the beach-balls depict inferred MTs at the individual spatial points. The beach-ball highlighted by red circle is the solution with the highest variance reduction (the best fitting solution); **c)** the comparison between measured and synthetic standardized waveforms for the best fitting solution; **d)** the beach-ball representation of the best fitting CMT; **e)** the uncertainty of the mechanism depicted by 1000 random possible solutions drawn from the ten-dimensional posterior PDF; **f)** histogram of the DC component.

3.3.4 Solutions of the CMT inversion

Parameters of the inferred CMT solutions from the Kumamoto sequence together with their uncertainty are compiled in Tables 3.2 and 3.3. The beach-ball representations of these CMTs are shown in Fig. 3.6 together with comparison from the JMA and NIED solutions (the comparison is discussed later).

The variance reduction defined by Eq. (3.9) is high for most events; nevertheless, solutions for two events (Nos. 1 and 5) have it below 50%. In the case of event No. 5, the raw waveforms seem corrupted at very low frequencies; hence, slightly higher frequency band was used (see Table 3.1), which most likely causes the fit deterioration. The event No. 1 is the strongest foreshock which was shown to consist of two spatially separated asperities by Asano & Iwata (2016). Our inferred CMT solution is located between the asperities; nevertheless, the lower variance reduction is likely related to the fact that the distance of the nearest station is at the margin of applicability of the point source approximation (20 km CMT-to-site distance vs. 12 km length of the fault).

The uncertainties of the CMT locations are up to 1.5 km in both horizontal and vertical directions for all events. Moreover, events with high variance reduction have CMT location uncertainty as small as 0.6 km. Table 3.2 documents that the percentage of the DC source content has spans from 64 to 98%. In most cases, it is characterized by large uncertainty including also possibility of pure shear (DC 100%), and hence, the presence of CLVD component cannot be proved (but also disproved) for most of the inferred CMT solutions. The exceptions are events No. 1, 3 and 7 whose admissible DC values do not exceed 90% even taking the uncertainty into account (64 + 24, 67 + 16 and 75 + 8%, respectively; see Table 3.2). Hence, we consider these events as having a significant CLVD component. Moreover, event No. 7 has the highest variance reduction in all the events, and hence, we consider its CLVD component particularly well constrained.

No.	CMT location					DC component		DC component uncertainty	
	Lat.	Lon.	Depth [km]	M_w	VR %	S/D/R [°]	DC %	S/D/R [°]	DC %
1	32.780	130.809	8.1	6.1	44	33/82/-155	64	3/7/9	±24
2	32.696	130.768	3.8	6.0	58	212/77/178	87	2/9/12	±20
3	32.862	130.856	8.4	5.7	59	294/37/-48	67	6/4/8	±16
4	32.780	130.823	8.3	5.4	73	29/69/-149	94	2/3/4	±10
5	32.765	130.760	13.0	5.0	45	6/72/-142	79	5/7/10	±14
6	32.860	130.835	10.0	5.2	60	83/62/-71	89	3/2/3	±10
7	32.692	130.716	7.8	5.2	74	68/63/-95	75	3/2/3	±8
8	32.765	130.803	9.9	4.9	54	16/76/-163	92	2/4/4	±14
9	32.679	130.735	8.1	4.9	71	211/66/175	90	2/3/3	±8
10	32.745	130.752	5.7	4.7	53	215/81/-165	83	2/7/8	±22
11	32.800	130.788	5.7	4.6	61	79/29/-104	98	8/2/8	±12

Note: VR—variance reduction; M_w —moment magnitude; S/D/R—strike/dip/rake

Table 3.2: Parameters of the inferred CMT solutions together with their uncertainty in terms of double standard deviation of Gaussian function (2σ) fitted to the respective marginal PDF.

Event			Our CMT solution		JMA		NIED (F-net)		
No.	M_{JMA}	Date Time (JST)							
1	6.5	2016/4/14 21:26:35			DC = 64% $M_w = 6.1$		DC = 75% $M_w = 6.2$		DC = 96% $M_w = 6.1$
2	6.4	2016/4/15 00:03:47			DC = 87% $M_w = 6.0$		DC = 89% $M_w = 6.0$		DC = 49% $M_w = 6.0$
3	5.9	2016/4/16 01:46:56			DC = 67% $M_w = 5.7$		DC = 56% $M_w = 5.8$		DC = 97% $M_w = 5.7$
4	5.8	2016/4/14 22:07:35			DC = 94% $M_w = 5.4$		DC = 78% $M_w = 5.4$		DC = 16% $M_w = 5.4$
5	5.4	2016/4/16 01:44:06			DC = 79% $M_w = 5.0$	-	-	-	-
6	5.4	2016/4/16 09:48:32			DC = 89% $M_w = 5.2$		DC = 92% $M_w = 5.2$		DC = 91% $M_w = 5.2$
7	5.4	2016/4/16 16:02:01			DC = 75% $M_w = 5.2$		DC = 86% $M_w = 5.1$		DC = 92% $M_w = 5.1$
8	5.1	2016/4/14 23:43:41			DC = 92% $M_w = 4.9$		DC = 85% $M_w = 5.0$		DC = 76% $M_w = 4.9$
9	5.0	2016/4/14 22:38:43			DC = 90% $M_w = 4.9$		DC = 85% $M_w = 4.9$		DC = 86% $M_w = 4.9$
10	4.9	2016/4/16 02:04:11			DC = 83% $M_w = 4.7$	-	-	-	-
11	4.8	2016/4/16 07:23:55			DC = 98% $M_w = 4.6$		DC = 79% $M_w = 4.6$		DC = 77% $M_w = 4.6$

Figure 3.6: Beach-ball representation of the best fitting MTs for all the inferred events. Our MT solutions are supplemented by uncertainty of the mechanism depicted by 1000 random possible solutions drawn from the ten-dimensional posterior PDF. JMA and NIED solutions are adopted directly from the routine MT catalogues of these agencies accessed through Web.

No.	M_{JMA}	Event		Harvard/USGS MT [$M_{rr}M_{tt}M_{pp}M_{rt}M_{rp}M_{tp}$][Nm]	M_0 [Nm]
		Date	Time*		
1	6.5	2016/4/14	21:26:35	$[-0.42, 1.56, -1.14, -0.33, -0.53, 0.73] \times 10^{18}$	1.84×10^{18}
2	6.4	2016/4/15	00:03:47	$[-0.49, 9.49, -9.00, -2.39, 0.84, 4.56] \times 10^{17}$	1.10×10^{18}
3	5.9	2016/4/16	01:46:56	$[-3.26, 3.52, -0.26, -1.64, -2.17, -0.18] \times 10^{17}$	4.69×10^{17}
4	5.8	2016/4/14	22:07:35	$[-0.53, 1.11, -0.58, 0.11, -0.67, 0.84] \times 10^{17}$	1.47×10^{17}
5	5.4	2016/4/16	01:44:06	$[-0.96, 0.46, 0.50, 0.79, -1.67, 2.21] \times 10^{16}$	3.15×10^{16}
6	5.4	2016/4/16	09:48:32	$[-4.54, 4.37, 0.18, -3.15, 0.42, 2.33] \times 10^{16}$	6.12×10^{16}
7	5.4	2016/4/16	16:02:01	$[-4.26, 4.55, -0.29, -3.16, -1.46, 1.69] \times 10^{16}$	6.22×10^{16}
8	5.1	2016/4/14	23:43:41	$[-0.48, 1.49, -1.01, 0.41, -0.84, 2.36] \times 10^{16}$	2.91×10^{16}
9	5.0	2016/4/14	22:38:43	$[0.05, 1.74, -1.79, -0.86, 0.30, 0.86] \times 10^{16}$	2.22×10^{16}
10	4.9	2016/4/16	02:04:11	$[-0.18, 1.08, -0.90, 0.03, 0.29, 0.40] \times 10^{16}$	1.16×10^{16}
11	4.8	2016/4/16	07:23:55	$[-8.32, 8.36, -0.04, 5.59, -1.16, 0.43] \times 10^{15}$	1.02×10^{16}

Note: *Japan Standard Time

Table 3.3: MT elements of the inferred solutions for Kumamoto earthquakes in Harvard/USGS form.

3.3.5 CMTs with significant CLVD component

The inferred CMT solutions of the Kumamoto earthquakes were decomposed into combination of DC and CLVD sources. While the DC component has direct physical interpretation in terms of shear faulting, the CLVD component points to possible complexity of the faulting (e.g., Frohlich 1994). Indeed, the non-DC MT can be decomposed into a combination of two or more DC sources. Unfortunately, such decomposition is mathematically non-unique, which brings difficulties to interpretation, and requires some physical constraint.

Non-DC MT decomposition into two DC MTs

Jost & Herrmann (1989) decompose a deviatoric MT into so-called major and minor DC sources preserving directions of the three principal stress axes (P-, T- and N-axis). Note that despite the fact that the principal stress axes directions are preserved, the axes types may generally interchange. Let us assume absolute values of non-DC MT eigenvalues $|\lambda_1| \geq |\lambda_2| \geq |\lambda_3|$ with respective eigenvectors \mathbf{v}_1 , \mathbf{v}_2 and \mathbf{v}_3 (1×3 row vectors). We use definition of the major and minor DC moment tensors as

$$\mathbf{MT}_{\text{major}} = \lambda_2 \left(-\mathbf{v}_1^T \mathbf{v}_1 + \mathbf{v}_2^T \mathbf{v}_2 \right), \quad (3.13)$$

$$\mathbf{MT}_{\text{minor}} = \lambda_3 \left(-\mathbf{v}_1^T \mathbf{v}_1 + \mathbf{v}_3^T \mathbf{v}_3 \right). \quad (3.14)$$

In such formulation, the major MT is the best DC approximation of a shear seismic source, under additional assumption of preserved main principal stress axis (axis with λ_1) of the major and minor MTs.

The decomposition in Eqs (3.13) and (3.14) has one unique solution, but the assumption of fixed directions of the principal stress axes for the subsources is physically too restrictive. Therefore, we propose to weaken this assumption by systematic search among subsources with slightly deviated directions of the principal stress axes. To this, we apply a grid search for strike, dip and rake angles of the two DC sources with prescribed main axis difference being less than 20° . The optimal scalar seismic moments of each of the two tested DC sources k

and l are obtained by linear inversion

$$\tilde{\mathbf{b}}_{kl} = (\mathbf{B}_{kl}^T \mathbf{B}_{kl})^{-1} (\mathbf{B}_{kl}^T \mathbf{n}), \quad (3.15)$$

where \mathbf{n} is vectorized non-DC MT (9×1 column vector), \mathbf{B}_{kl} is 9×2 matrix composed of two tested vectorized DC MTs with unit scalar seismic moments and $\tilde{\mathbf{b}}_{kl}$ is vector of the optimal scalar seismic moments. The fit of the summed DC MTs with the target non-DC MT \mathbf{n} is measured by misfit (normalized variance)

$$\ell_{kl} = \frac{\|\mathbf{n} - \mathbf{B}_{kl} \tilde{\mathbf{b}}_{kl}\|^2}{\|\mathbf{n}\|^2} \cdot 100 \% \quad (3.16)$$

Note that the scalar seismic moments obtained by (3.15) may also have negative values; such solutions are considered unphysical and are thus excluded. Then, we accept solutions with misfit (3.16) lower than 1 %. The result of this approach is a set of possible decompositions of non-DC MT into two DC MTs with prescribed main axis difference being less than 20° .

Application of the non-DC MT decomposition

The decomposition methodologies (Eqs (3.13), (3.14), (3.15) and (3.16)) are based on preserving main principal stress axis with the largest absolute eigenvalue $|\lambda_1|$; it may be either P-axis or T-axis of MTs. In the Kumamoto area, the stress field has σ_3 as the main principal stress in the NNW–SSE direction, while σ_1 and σ_2 in WSW–ENE and vertical directions, respectively, have similar size (Matsumoto et al. 2015, Fig. 3.7e). Hence, the decomposition of the selected non-DC MTs was performed to preserve T-axis (related to the stable σ_3 direction).

Three of the inferred MTs of the Kumamoto earthquakes (events No. 1, 3 and 7) have significant CLVD component. Two of them (events No. 1 and 7) have T-axis as the main principal stress axis; hence, we analyzed those two in detail. The first analyzed earthquake is the strongest $M_{JMA}6.5$ strike-slip foreshock, and the second event is $M_{JMA}5.4$ normal faulting aftershock. The decomposition of these non-DC MTs into major and minor DC sources is depicted in Fig. 3.7a, b. The summed MTs in Fig. 3.7 are in perfect agreement with our original non-DC MTs in Fig. 3.6. In the decomposition with preserved T-axis (Fig. 3.7a, b, and Tables 3.4 and 3.5), the major MT is the best DC approximation of the shear seismic source, while minor MT represents complexity of the faulting (secondary faulting mechanism). It has to be emphasized that the major and minor DC sources cannot be understood as two asperities of an activated fault system; the decomposition is merely mathematical description of a complex earthquake source.

	Mechanism	S/D/R [$^\circ$]	DC %	M_0 [Nm]	$(M_0/M_0^{sum}) \cdot 100\%$
Original non-DC MT	Strike-slip	33/82/-155	64	1.84×10^{18}	100
MT _{major}	Strike-slip	33/82/-155	100	1.51×10^{18}	82
MT _{minor}	Normal	93/60/-63	100	0.33×10^{18}	18
MT _{sum}	Strike-slip	33/82/-155	64	1.84×10^{18}	100

Note: Decomposed major and minor MTs and their sum $\mathbf{MT}_{major} + \mathbf{MT}_{minor} = \mathbf{MT}_{sum}$; S/D/R–strike/dip/rake

Table 3.4: Decomposition of non-DC MT of the $M_{JMA}6.5$ foreshock from 2016/4/14 21:26:35 JST (event No. 1) and the decomposition by Eqs (3.13) and (3.14) preserving MT T-axis.

Better understanding can be gained from the examples of possible decomposition provided by the grid search approach (Fig. 3.7c, d), documenting the non-uniqueness of the decomposition. Nevertheless, all the selected examples are, generally, a combination of a strike-slip and a normal dip-slip mechanism (as shown in Fig. 3.7), which is consistent with the tectonic settings of the intersection of the Hinagu and Futagawa fault zones.

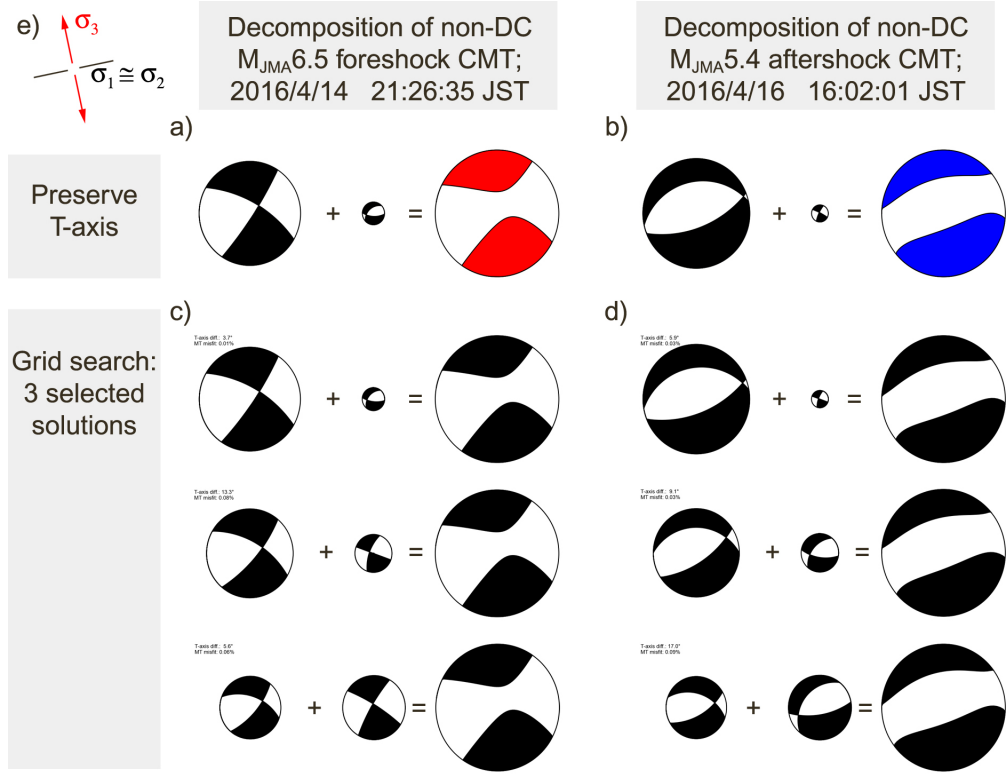


Figure 3.7: Decomposition of non-DC MTs of the $M_{JMA}6.5$ foreshock (left column) and the $M_{JMA}5.4$ aftershock (right column) into combination of two DC MTs; DC MTs are shown together with their sum $\mathbf{MT}_1 + \mathbf{MT}_2 = \mathbf{MT}_{sum}$ by trinity of beach-balls; radius of beach-balls is proportional to scalar seismic moment. **a)** and **b)** are unique solutions of the MT decomposition preserving main (T -)axis (Eqs (3.13) and (3.14)). **c)** and **d)** are selected representative solutions of the non-unique MT decomposition by the grid search approach, where the scalar moments were obtained by a linear inversion (3.15). **e)** the regional stress field indicated by directions of σ_1 , σ_2 and σ_3 , dopted from Matsumoto et al. (2015).

	Mechanism	S/D/R [°]	DC %	M_0 [Nm]	$(M_0/M_0^{sum}) \cdot 100\%$
Original non-DC MT	Normal	68/63/-95	75	6.22×10^{16}	100
\mathbf{MT}_{major}	Normal	68/63/-95	100	5.44×10^{16}	87
\mathbf{MT}_{minor}	Strike-slip	297/81/16	100	0.79×10^{16}	13
\mathbf{MT}_{sum}	Normal	68/63/-95	75	6.22×10^{16}	100

Note: Decomposed major and minor MTs and their sum $\mathbf{MT}_{major} + \mathbf{MT}_{minor} = \mathbf{MT}_{sum}$; S/D/R—strike/dip/rake

Table 3.5: Decomposition of non-DC MT of the $M_{JMA}5.4$ aftershock from 2016/4/16 16:02:01 JST (event No. 7) and the decomposition by Eqs (3.13) and (3.14) preserving MT T -axis.

3.4 Geometry of the activated ruptures

The inferred CMTs of the analyzed events exhibit significant systematic spatial variations throughout the source region (Fig. 3.8). Analyzed CMTs of foreshocks are strike-slip events located near the surface traces of the Hinagu and Futagawa faults (red DC beach-balls in Fig. 3.8). Contrarily, aftershocks have various mechanisms with majority of normal dip-slips (blue DC beach-balls in Fig. 3.8). We estimate that more than 99% of the total scalar seismic moment of the Kumamoto sequence in studied area was released by the analyzed events together with the $M_{JMA}7.3$ mainshock. Hence, we aim to construct the network of major faults and ruptures, which were activated within the analyzed sequence, from the CMT solutions.

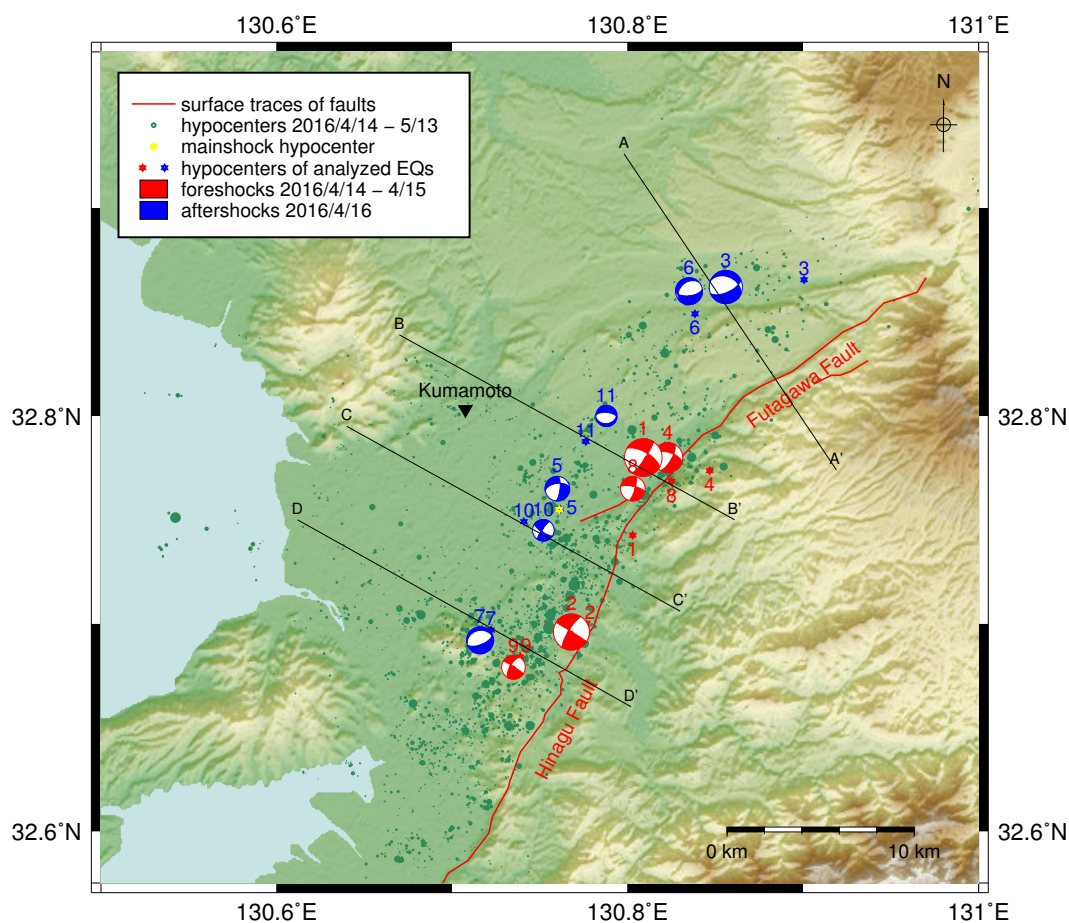


Figure 3.8: Map of inferred CMTs of the Kumamoto earthquake sequence. CMTs are shown by beach-ball representation of the best DC source. The background seismicity is adopted from Kato et al. (2016). The sizes of the circles are proportional to the JMA magnitude of the events. Events are numbered according to Table 3.2. Black lines are traces of vertical cross sections shown in Fig. 3.9. The topography originates from the SRTM-90m digital elevation data. For details, see legend.

Firstly, we determine the preferred fault planes out of the two MT nodal planes based on the (a) orientation of surface traces of the faults; (b) geometry of clusters of the relocated hypocenters; and (c) by the mutual co-location of the hypocenter and centroid (so-called H-C method, Zahradník et al. 2008). In the latter method, the fault plane is identified as that one from two nodal planes of

CMT that encompasses the hypocenter location in 3D. The assumption is that ruptures propagate from the hypocenter along a fault plane described by the CMT solution. Major surface traces of the Hinagu and Futagawa faults are oriented in the NE–SW direction, which is indicative for the strike-slip fault planes. The strike-slip fault planes of Hinagu fault zone are noticeable also in the vertical cross sections in Fig. 3.9 showing hypocenters of the Kumamoto earthquakes as inferred by Kato et al. (2016). The H–C method is useful, especially for the normal dip-slip aftershocks with unclear evidence of surface traces of faults; moreover, it supports also assumed orientation of strike-slip fault planes. Hence, the strike-slip fault planes are identified with higher certainty than the dip-slip fault planes. Determined preferable nodal planes of the sources are listed in Table 3.2 by means of their strike, dip and rake angles.

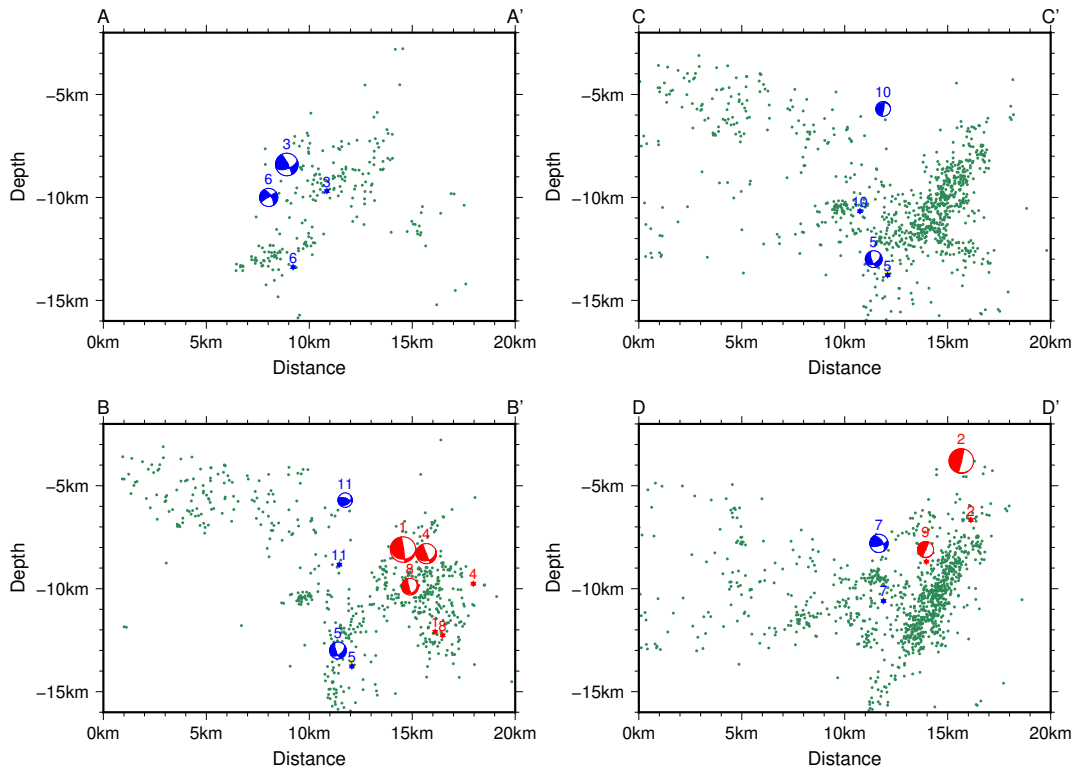


Figure 3.9: Vertical cross sections with inferred CMTs (beach-balls) and relative locations (green dots) of earthquakes adopted from Kato et al. (2016). For events coloring and cross-sectional placement, see Fig. 3.8. Events shown in the cross sections are taken from volume spreading 5 km on each side of the cross-sectional plane. Events are numbered according to Table 3.2

Secondly, we estimate the rupture area of the analyzed earthquakes from their scalar seismic moments. The adopted empirical relationship from Somerville et al. (1999) is based on the self-similar scaling of the large to midsize crustal earthquakes. The rupture area A in square kilometers is given by

$$A = 2.23 \cdot 10^{-15} \cdot M_0^{2/3}, \quad (3.17)$$

where the scalar seismic moment M_0 is in *dyne – cm*. The estimated rupture areas supplemented by rupture lengths L , assuming square geometry of the fault

planes, are listed in Table 3.6. The rupture area and geometry of the $M_{JMA}7.3$ mainshock are adopted from the slip inversion by Asano & Iwata (2016), having area of 756 km^2 .

No.	Event			$A [\text{km}^2]$	$L [\text{km}]$	$R [\text{km}]$
	M_{JMA}	Date	Time*			
1	6.5	2016/4/14	21:26:35	155.4	12.5	1.3
2	6.4	2016/4/15	00:03:47	110.3	10.5	1.1
3	5.9	2016/4/16	01:46:56	62.5	7.9	0.2
4	5.8	2016/4/14	22:07:35	28.8	5.4	1.6
5	5.4	2016/4/16	01:44:06	10.3	3.2	0.0
6	5.4	2016/4/16	09:48:32	16.1	4.0	1.7
7	5.4	2016/4/16	16:02:01	16.2	4.0	1.6
8	5.1	2016/4/14	23:43:41	9.8	3.1	1.7
9	5.0	2016/4/14	22:38:43	8.2	2.9	0.3
10	4.9	2016/4/16	02:04:11	5.3	2.3	3.9
11	4.8	2016/4/16	07:23:55	4.9	2.2	2.6

*Japan Standard Time; A —total rupture area; L —rupture length assuming square geometry of the fault plane; R —minimum distance in 3D between the hypocenter and the respective fault plane

Table 3.6: Rupture area of the analyzed Kumamoto earthquakes estimated from empirical relation by Somerville et al. (1999) in Eq. (3.17)

We have centered the assumed rupture planes defined by their spatial orientation (Table 3.2) and rupture size (Table 3.6) in their respective CMT locations (Table 3.2) and plotted them in 3D visualization program ParaView (Fig. 3.10). As locations of the inferred CMTs and also hypocenters are subjects of uncertainty (estimated to be up to 1.5 km for CMTs), the assumed fault planes do not necessarily cross perfectly the hypocenter. The minimum distance of the hypocenters from the respective fault planes is shown in Table 3.6 as parameter R . Foreshocks' major ruptures (red squares in Fig. 3.10) continuously cover the northernmost part of the Hinagu fault zone, having length of approximately 20 km . They span from the surface to the depth of approximately 14 km . The aftershocks' major ruptures (blue squares in Fig. 3.10) spread NW along the adopted fault plane of the $M_{JMA}7.3$ mainshock (yellow rectangles in Fig. 3.10). Moreover, three of the inferred aftershock's ruptures (events No. 3, 5 and 7) intersect the mainshock fault plane.

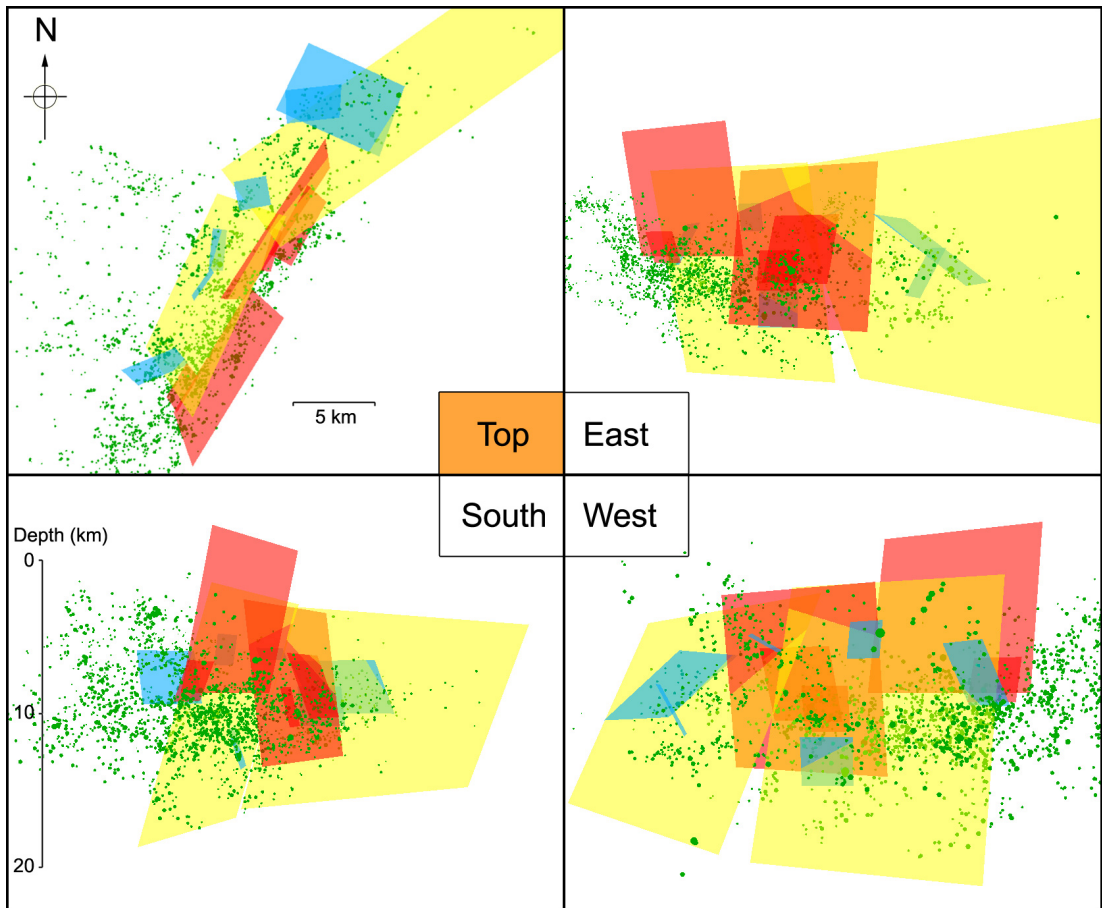


Figure 3.10: Visualization of the assumed activated fault planes in top, south-side, east-side and west-side view; red squares = foreshocks' ruptures; blue squares = aftershocks' ruptures; yellow rectangles = mainshock's rupture adopted from Asano & Iwata (2016); green dots = relative locations of earthquakes inferred by Kato et al. (2016) for period April 14–May 13, 2016. The scale in figure is only orientative, because of used perspective projection.

3.5 Discussion

3.5.1 Solutions in seismotectonic framework

The relationship between the earthquakes, active tectonics and faults may play role in the local seismic hazard assessment. The constructed network of activated ruptures (Fig. 3.10) represents such seismotectonic description of the intersection of the Hinagu and Futagawa fault zones. Foreshocks (red beach-balls in Fig. 3.8) imply right-lateral strike-slip movements in the NE–SW direction in the Hinagu fault zone. Those ruptures located close to the intersection of the Hinagu and Futagawa fault zones are dipping slightly to ESE, while those in the southern area are dipping to WNW. The activated ruptures span from surface to depth of approximately 14 km. Contrarily, aftershocks are mostly normal dip-slip events (blue beach-balls in Fig. 3.8) and spread NW along the assumed fault plane of the $M_{JMA}7.3$ mainshock (see Fig. 10), where the surface subsidence occurred as documented by InSAR (Himematsu & Furuya 2016). Aftershock’s ruptures are situated at depths greater than 5 km, close to the assumed fault plane of the mainshock (adopted from Asano & Iwata 2016), and three of them intersect the mainshock fault plane. These findings imply that foreshocks and partially also mainshock are driven by stresses of the NE–SW shear zone (western extension of the MTL), while aftershocks are mostly related to the N–S extensional stress regime of Beppu–Shimabara graben (Kamata & Kodama 1994), being triggered by the mainshock. This is confirmed by principal stress axes analysis performed by code of Vavryčuk (2014), see Fig. 3.11, showing that the N–S extensional stress σ_3 is stable (blue dots in Fig. 3.11a, b), while main principal stress σ_1 is oriented NE–SW and vertically for foreshocks and aftershocks, respectively (red dots in Fig. 3.11a, b).

Co-activation of the right-lateral strike-slips with normal faulting ruptures through the sequence was introduced also by static slip model from geodetic data (Himematsu & Furuya 2016; Kobayashi 2017). Field investigation by Toda et al. (2016) shows that surface displacements along the previously mapped active fault traces of the Hinagu–Futagawa fault zone are dominated by right-lateral strike-slip surface displacement up to 2 m. A normal surface rupture zone of about 10 km in length dipping to northwest, which is parallel to the Futagawa fault outside the Aso caldera, was also reported by Toda et al. (2016), and its maximum co-seismic displacement is also up to 2 m. The normal dip-slip aftershocks that occurred along the NW edge of the mainshock rupture had no clear relationship with co-seismic surface ruptures; however, minor surface ruptures in downtown of Kumamoto City have been mapped by InSAR (Himematsu & Furuya 2016) and field survey (Goto et al. 2017). The field investigations imply the complex surface phenomena and tectonic settings in this region. Further surveys on imaging causative source faults beneath the surface are necessary to investigate the relationship between the surface ruptures and the geometry of earthquake source faults.

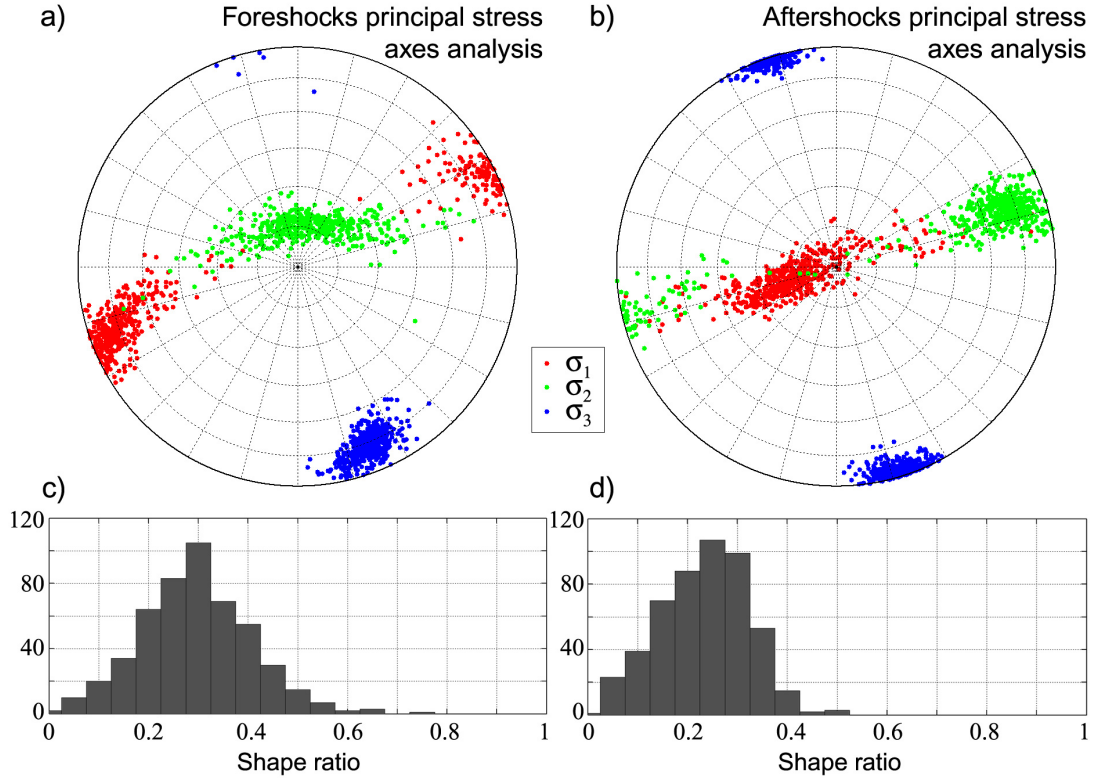


Figure 3.11: Principal stress axes analysis for foreshocks (left) and aftershocks (right) by method of Michael (1984) with uncertainty estimate coded by Vavryčuk (2014). **a)** and **b)** show confidence limits of principal stress axes visualized by 500 randomly perturbed pure shear solutions by the approach of Vavryčuk (2014) for foreshocks and aftershocks, respectively. In panels **c)** and **d)** are histograms of their respective shape ratios defined as $= \frac{\sigma_1 - \sigma_2}{\sigma_1 - \sigma_3}$. Note that the relatively low shape ratios imply $\sigma_1 \approx \sigma_2$.

Finally, here we summarize the temporal seismotectonic evolution of the Kuramamoto sequence:

- Activity started on April 14th by the $M_{JMA}6.5$ foreshock close to the intersection of the Hinagu and Futagawa fault zones as right-lateral strike-slip shear movement in the NE–SW direction on fault plane(s) dipping slightly to the ESE (events No. 1 and 4).
- Right-lateral strike-slip shear movements continued by simultaneous activity in the northern (dipping to the ESE) and southern (dipping to the WNW) segments of the Hinagu fault zone (events No. 8 and 9).
- On April 15th, activity migrated to the southern (dipping to the WNW) segment of the Hinagu fault zone. The activity comprised the second largest foreshock $M_{JMA}6.4$ (event No. 2).
- This was followed by the mainshock on April 16th as right-lateral shear slips complemented by normal dip-slip in the Futagawa fault segment in the later phase of the rupture propagation.
- Aftershocks in the area of interest were mostly dip-slip events, spreading along the NW edge of the mainshock rupture (events No. 3, 6, 7 and 11).

3.5.2 Complexity of activated ruptures

The local stress field conditions (e.g., Matsumoto et al. 2015) and seismotectonic settings of the intersection of the Hinagu and Futagawa fault zones imply combination of a strike-slip and a normal dip-slip shearing mechanism. Indeed, the source models for the mainshock (e.g., Asano & Iwata 2016; Kubo et al. 2016b) suggest simultaneous right-lateral strike-slip shear movement complemented by normal dip-slip movement of the Futagawa fault segment. The rupture of the mainshock then has to be complex and segmented to two or more fault planes (as suggested by the mainshock source models).

The analyzed foreshocks and aftershocks are mostly right-lateral strike-slip and a normal dip-slip shearing event with insignificant CLVD component and hence may be assumed as single fault plane ruptures. The exceptions are the $M_{JMA}6.5$ foreshock (event No. 1) and the $M_{JMA}5.4$ aftershock (event No. 7) with significant CLVD component and T-axis as the main principal stress axis. These two events can be interpreted as a result of complex ruptures composed of right-lateral strike-slip and a normal dip-slip fault plane with preserved T-axis (Fig. 3.7). The assumption of preserved T-axis is in accord the inferred principal stress in Fig. 3.11, where σ_3 is stable in N-S direction. Such interpretation of non-DC component is supported by the static slip model for the $M_{JMA}6.5$ foreshock inferred from InSAR data (Kobayashi 2017), being composed of right-lateral strike-slip displacement on the Hinagu fault segment and normal dip-slip displacement on the Futagawa fault segment.

3.5.3 Comparison with routine MT catalogues

The MTs for most of the processed events were also inferred routinely by JMA and NIED institutions. Our and JMA approaches infer CMTs by searching the centroid location in both horizontal and vertical directions. Contrarily, NIED fixes the horizontal centroid location at the (revised) JMA epicenter and searches for the centroid depth only.

Our MTs are compared with solutions from JMA and NIED catalogues in Fig. 3.6. Our solutions generally agree with both agency MTs in terms of nodal planes angles, while non-DC components agree better with JMA (e.g., see the DC component percentage for the $M_{JMA}6.4$ foreshock, No. 2 in Fig. 3.6). This can be related to the use of higher number of records from shorter epicenter distances and searching CMT in both horizontal and vertical directions in our and JMA approaches. Moreover, uncertainty estimate by our approach allows the assessment of reliability of the inferred non-DC component. For example, in cases of events No. 2 and 11 (Fig. 3.6), the JMA and our solutions exhibit opposite signs of the CLVD component, but this difference is within the estimated uncertainty.

3.6 Conclusions

We have presented application of the innovative Bayesian full-waveform CMT inversion method, which takes into account uncertainty of the velocity model. The approach allows us to reliably assess the uncertainty of the source parameters, which proved to be beneficial in terms of interpretation of the results (statistical significance of selected source parameters). Additionally, we have implemented decomposition of MT with significant CLVD component into two shear MTs with preserved T-axis as a physical constraint.

The methodology has been applied to significant earthquakes from the Kumamoto sequence of April 2016 with M_{JMA} magnitude in range of 4.8–6.5. The quality of the inferred solutions is mostly high as we have used dense network of local to regional receivers. The inferred CMT solutions show systematic spatial and temporal variations. Hence, we have estimated geometry of the major activated ruptures and interpreted them in the seismotectonic framework. Foreshocks imply right-lateral NE–SW strike-slip movements in the Hinagu fault zone. Aftershocks are mostly normal dip-slip events spreading along the NW edge of the assumed mainshock fault plane. Moreover, the inferred CMTs with significant CLVD component may suggest a complex source process. These events can be interpreted as a result of complex ruptures composed of right-lateral strike-slip and a normal dip-slip fault plane. Our model of major activated ruptures inferred from seismic data is consistent with the local tectonic settings, stress field conditions and geodetic data.

Acknowledgments

The authors thank all operators involved in station maintenance at K-NET, KiK-net and F-net networks. We appreciate relative locations of hypocenters (same as in Kato et al. 2016) provided by A. Kato from Earthquake Research Institute, University of Tokyo, Japan. Generic Mapping Tools (Wessel & Smith 1998) was used to draw the figures. This paper is based on achievements of the collaborative research program (28S-02) of the Disaster Prevention Research Institute of Kyoto University. We acknowledge financial support by the Grant Agency of the Charles University project GAUK-728916 and Charles University Grant SVV 260447/2017. We are grateful to two anonymous reviewers for their comments that improved the original manuscript.

3.7 Unpublished supplementary material

3.7.1 ISO component

A full MT can be generally decomposed into DC, CLVD and ISO components. As the volumetric ISO component is mostly negligible in the particular case of tectonic earthquakes, MT inversion is often performed as deviatoric inversion to increase stability of the inverse problem (suitable for shear tectonic earthquakes). In the case of 2016 Kumamoto sequence, we first inferred full CMTs in a rough space-time grid, then excluded stations with very poor fit, and finally performed Bayesian deviatoric CMT inversion in a dense grid (see Section 3.3.3). However, we should test whether the possible content of the ISO component could have an influence on the inferred deviatoric solution and the uncertainty of the DC to CLVD ratios. Therefore, we present here additional inference and analysis of full CMTs and its comparison with inference of deviatoric CMTs. The aim is to investigate the possible influence of neglecting ISO in the inversion.

For this analysis we selected the three largest foreshocks with $M_{JMA}6.5$, $M_{JMA}6.4$, $M_{JMA}5.8$ (events No. 1, 2 and 4) and the $M_{JMA}5.4$ aftershock (event No. 7) with the significant CLVD component (see Tabs 3.1 and 3.2). The inferred full MT solutions for these events are compared with deviatoric MTs in Fig. 3.12. The figure shows the best fitting MT solutions and their uncertainties depicted by an ensemble of 1000 random possible solutions drawn from the ten-dimensional posterior PDF. Particularly, we show in Fig. 3.12 marginal PDFs by means of beach-ball representation, DC, CLVD and ISO components of the inferred full MT in comparison with the deviatoric ones.

MTs from full and deviatoric inferences are generally in almost perfect agreement in terms of the best fitting MT solutions. There is also very good conformity in the assessed uncertainty of the DC and CLVD components. The ISO components decomposed from full MT solutions have very low values with narrow uncertainty interval around 0%.

To conclude, neglecting the ISO component does not play an important role in the particular case of the 2016 Kumamoto CMTs and their interpretation. However, we acknowledge, that in specific cases the deviatoric MT may be generally insufficient and the full MT should be preferred.

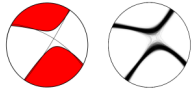
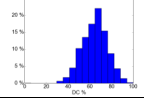
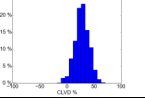
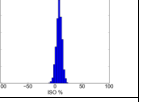
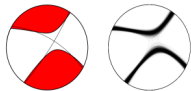
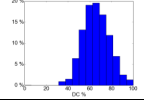
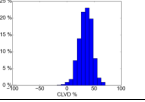
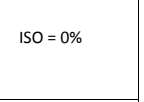
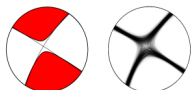
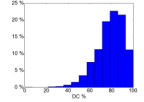
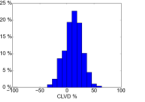
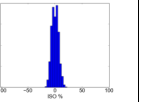
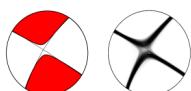
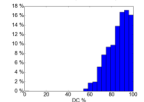
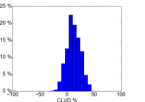
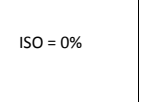

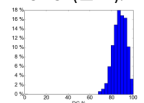
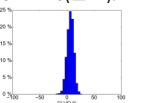
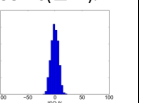

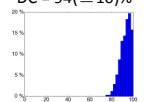
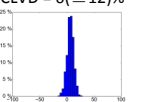
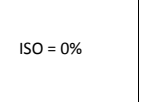

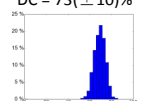
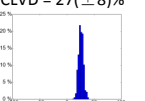
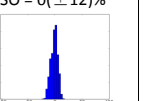

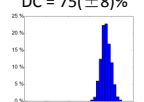
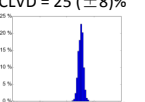
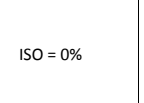
Event			CMT solution	DC	CLVD	ISO
No.	M _{JMA}	Date Time (JST)				
1	6.5	2016/4/14 21:26:35	Full CMT inversion 	DC = 65(± 22)% 	CLVD = 29(± 26)% 	ISO = 7(± 10)% 
			Deviatoric CMT inversion 	DC = 64(± 24)% 	CLVD = 36(± 24)% 	ISO = 0% 
2	6.4	2016/4/15 00:03:47	Full CMT inversion 	DC = 86(± 26)% 	CLVD = 14(± 32)% 	ISO = -1(± 12)% 
			Deviatoric CMT inversion 	DC = 87(± 20)% 	CLVD = 13(± 26)% 	ISO = 0% 
4	5.8	2016/4/14 22:07:35	Full CMT inversion 	DC = 94(± 12)% 	CLVD = 6(± 12)% 	ISO = 0(± 14)% 
			Deviatoric CMT inversion 	DC = 94(± 10)% 	CLVD = 6(± 12)% 	ISO = 0% 
7	5.4	2016/4/16 16:02:01	Full CMT inversion 	DC = 73(± 10)% 	CLVD = 27(± 8)% 	ISO = 0(± 12)% 
			Deviatoric CMT inversion 	DC = 75(± 8)% 	CLVD = 25(± 8)% 	ISO = 0% 

Figure 3.12: Comparison of inferred full and deviatoric CMTs for selected events. The best fitting MT solutions are supplemented by uncertainty of the mechanism depicted by 1000 random possible solutions drawn from the ten-dimensional posterior PDF. We show beach-ball representation and histograms of the DC, CLVD and ISO values from this ensemble.

4. Bayesian self-adapting fault slip inversion with Green's functions uncertainty

Abstract: Kinematic finite-extent source models of earthquakes are inferred by inverse modeling of observed seismic waveforms and/or geodetic data. The solutions are subject of significant uncertainty as a result of inaccurate observations and imperfect physical description of the complex properties of the Earth's crust. In the case of waveform-based earthquake source inversions the major source of uncertainty is related to the uncertainty of Green's function (GF) due to the inaccuracy of the crustal model considered, and subjectively selected parametrization of the finite-extent source model. Recently, Bayesian inversions of the fault slip distribution taking into account the GFs' uncertainty have been introduced by several studies. We develop a Bayesian parametric slip inversion method with self-adapting parametrization of slip functions and with an analytical representation of the GF uncertainty. Our finite fault inversion consists of four major components: 1) convenient parametrization of the model space to limit its number of dimensions, 2) fast direct solver, which provides synthetics for a given set of parameters, 3) trans-dimensional Markov chain Monte Carlo algorithm on sampling the posterior Bayesian probability density in the self-adapting model space, and 4) statistical processing of the ensemble of solutions to evaluate the result uncertainty. The performance of our method is demonstrated on the case study of the destructive M_w 7.1 mainshock of the 2016 Kumamoto, Japan, earthquake sequence. We infer ensemble of more than 590k possible finite source models, representing samples of the posterior probability density function, and inspect which features of the finite source model are reliable and which are rather artifacts.

4.1 Introduction

Earthquake ground motions originate from rupture processes on faults in Earth. Constraints on earthquake source models are important for better understanding of earthquake physics and for seismic hazard analysis (e.g., Hutchings et al. 2017), which is particularly significant for construction engineering and disaster mitigation planning. In addition, earthquake source models serve as input for studies like analysis of the earthquake energy budget (e.g., Kanamori & Rivera 2006), dynamic stress drop analysis (e.g., Day et al. 1998), Coulomb stress modeling (e.g., King & Devès 2015), etc.

Kinematics of tectonic earthquake sources can be described by finite-extent source models with heterogeneous distribution of slip functions on a fault (see Section 1.1.2). Such models are inferred by inverse modeling of observed seismic waveforms and/or geodetic data. Nevertheless, the inverse solutions are subject to significant uncertainty (e.g., Mai et al. 2016). Consideration of the solution uncertainty is hence important for assessment of source model reliability, which improves physical interpretation of the results, re-evaluation of seismic hazard, and anti-seismic construction design.

Approaches to the inference of fault slip models differ mainly by chosen parametrization of the source model (e.g., Ide 2007, and references therein). The inverse problem can be linear when a dense spatial and temporal discretization of the slip rates over the assumed fault is considered (e.g., Olson & Apsel 1982; Hartzell & Heaton 1983; Sekiguchi et al. 2000; Gallovič & Zahradník 2010), as commonly used to infer kinematic sources of large crustal earthquakes (e.g., Wald & Heaton 1994; Asano et al. 2005; Asano & Iwata 2016; Gallovič et al. 2015; Pizzi et al. 2017). Linear inversions (also known as multiple-time window methods) are typically overparametrized and hence extremely unstable, requiring a regularization by positivity of the slip rates and spatial-temporal smoothing. Such regularization has to be specified a priori for the whole model and it has been shown to produce artifacts (e.g., Zahradník & Gallovič 2010). The issue of ill-posedness of the linear rupture inversions was tackled by exploring the eigenstructure of the inverse problem by Gallovič & Ampuero (2015). They decomposed the linear forward operator by singular value decomposition, providing set of singular vectors in the model space. Differencing large and small singular values then points on the correctly resolved features of such inversion.

Non-linear fault slip inversions rely on spatial-temporal parametrization of the slip-rate function (SRF). Such approach reduces the number of unknown parameters and revoke requirements on a regularization (e.g., Archuleta 1984; Ji et al. 2002; Bouchon et al. 2002; Liu & Archuleta 2004; Piatanesi et al. 2007; Monelli et al. 2009; Minson et al. 2013; Minson et al. 2014; Dettmer et al. 2014). However, these inversions require additional demands on computational power as the strongly non-linear inverse problem should be solved by a Monte-Carlo (MC) method.

Each particular selection of the parametrization represents an assumption on the slip distribution and can lead to different inverse solutions (e.g., Clévéde et al. 2004). This brings concerns about the reliability of the inferred source models due to the non-uniqueness of the inverse problem (e.g., Hartzell et al. 2007; Mai et al. 2016). In particular, Beresnev (2003) critically illustrated that the choice of a particular inversion scheme, parametrization of the SRF, spatial parametrization of the slip on the fault, and geometry of the monitoring array have big influence on the inferred solution. It is rather complicated to distinguish between artificial and real features of the finite-extent source models, and hence the importance of the consideration of the solution uncertainty arises again.

The finite-extent source model inversions with the assessment of the solution uncertainty are usually performed in the Bayesian probabilistic framework (see Section 1.2). In the Bayesian framework a prior information on the physical model is specified, which is then updated to a conditional posterior probability of model parameters affected by the observed data. In such scheme, the assumptions on the uncertainty of the observed data and theory needs to be incorporated (e.g., Tarantola & Valette 1982). Yagi & Fukahata (2011) and Hallo & Gallovič (2016) emphasize that the major source of such uncertainty is related to the uncertainty of Green's function (GFs) due to the inaccuracy of the crustal model considered. The Bayesian slip inversions have been introduced by several recent studies. For example, Minson et al. (2013, 2014) and Kubo et al. (2016a) take into account the GF variance, treating it as an unknown parameter with uniform and log-normal probability distributions, respectively. Duputel et al. (2014, 2015)

show the importance of considering the full covariance matrix in inversions, and propose to estimate the full covariance matrices by considering linear relationship between the GFs and random perturbations of the velocity model. Further, Hallo & Gallovič (2016) introduced so-called approximate (analytical) covariance functions inferred from observed seismograms, and have shown that these functions can reliably represent GFs uncertainties (see Chapter 2).

Bayesian inversions estimate the solution uncertainty for the particular choice of parametrization. The choice of parametrization may have big influence on the inferred solution (e.g., Beresnev 2003), and hence also on the estimated uncertainty of the solution. Therefore, it is advisable to choose the source model parametrization considering the resolution power of the observed data (e.g., Custódio & Archuleta 2007). Over-parametrization is associated with over-fitting the observed data (i.e. noise fitting), while under-parametrization is associated with too simple models. This issue can be overcome by so-called trans-dimensional (trans-D) Bayesian inversion method developed by Green (1995, 2003), where the number of model parameters is subject to inversion itself (e.g., Sambridge et al. 2006; Bodin et al. 2012; Dettmer et al. 2014). A non-linear hierarchical Bayesian fault slip inversion with trans-D parametrization was introduced by Dettmer et al. (2014). This approach does not include uncertainty of the GFs, yet it takes into account the non-stationary character of the noise in the residual waveforms (following Dettmer et al. (2007)).

Our work introduces a non-linear Bayesian fault slip inversion with effective trans-D parametrization of the SRFs and implemented uncertainty of GFs (following Hallo & Gallovič 2016). The SRFs' parametrization relies on the regularized Yoffe function (Tinti et al. 2005), which was shown to be compatible with rupture dynamics (e.g., Bizzarri 2012), and hence, it may interlink kinematic and dynamic rupture parameters. The slip on the fault is modeled using biharmonic spline interpolation from variable number of spline points (Sandwell 1987; Causse et al. 2017). This parametrization permits the use of the trans-D Markov chain Monte Carlo (MCMC) method (e.g., Sambridge et al. 2006), leading to a self-adapting model space parameterization driven by the observed data.

The performance of our parametric slip inversion method is demonstrated on the inversion of the destructive M_w 7.1 mainshock of the 2016 Kumamoto, Japan, earthquake sequence (see Chapter 3). We use strong motion records of the K-NET, KiK-net and F-net networks (Okada et al. 2004) and infer an ensemble of more than 590k possible finite-source models, representing samples of the posterior probability density function. Such massive ensemble of solutions is then statistically processed to reveal which features of the finite source model of the 2016 Kumamoto mainshock are reliable and which are rather artifacts.

4.2 Method

4.2.1 Rupture parametrization

Let us assume a planar generally oriented finite-extent fault Σ in solid medium. The displacement wavefield $\mathbf{u} = (u_E, u_N, u_Z)$ measured at receiver position $\boldsymbol{\zeta}$ and time t is related to the slip-rate function $\Delta\dot{u}(\boldsymbol{\xi}, t)$ distributed along the fault by the representation theorem (see Section 1.1.2). Assuming that the shear slip direction does not change in time, the representation theorem reads

$$\mathbf{u}(\boldsymbol{\zeta}, t) = \iint_{\Sigma} \Delta\dot{u}(\boldsymbol{\xi}, t) * \mathbf{G}(\boldsymbol{\zeta}, t; \boldsymbol{\xi}) \, d\Sigma(\boldsymbol{\xi}), \quad (4.1)$$

where $*$ denotes temporal convolution. \mathbf{G} represents the displacement response of the medium at location $\boldsymbol{\zeta}$ to double-couple force acting at source position $\boldsymbol{\xi}$ with Heaviside step time function. Note that here we denote \mathbf{G} as the GFs while their definition by Aki & Richards (2002) (Section 1.1) is more general.

The fault plane is spatially discretized into N_{Σ} uniform rectangular subfaults of area $\Delta\Sigma$. These subfaults are assumed to be small enough to be treated as point sources with respect to the used wavelengths and source-receiver distances. Then, formula for the n -th displacement component reads

$$u_n(t) = \Delta\Sigma \sum_{i=1}^{N_{\Sigma}} \Delta\dot{u}_i(t) * G_{ni}(t), \quad (4.2)$$

where $G_{ni}(t)$ is n -th component of the GFs for the subfault i . The fault geometry is fixed and expected to be given a priori (e.g., from geological mapping or as result of a centroid moment tensor inversion). Then, the subfaults are characterized by their strike and dip angles (see Aki & Richards 2002, fig. 4.13), while rake angles ϑ_i (i.e. slip direction on the fault) are subject to the inversion. The GFs for given subfault i can be expressed by a linear combination of two GFs, $\hat{G}_{ni}(t)$ and $\check{G}_{ni}(t)$, for two given perpendicular rake angles $\hat{\vartheta}$ and $\check{\vartheta}$ as

$$G_{ni}(t) = \hat{G}_{ni}(t) \cos(\vartheta_i - \hat{\vartheta}) + \check{G}_{ni}(t) \cos(\check{\vartheta} - \vartheta_i), \quad (4.3)$$

where $\check{\vartheta} - \hat{\vartheta} = 90^\circ$. The advantage of such formulation is possibility to pre-compute GFs for all receivers and subfaults prior to the inversion (e.g., by discrete wavenumber method, Bouchon 1981) for arbitrarily rake angle.

Slip-rate function (SRF)

In our approach, we utilize a temporal parametrization of $\Delta\dot{u}_i(t)$, and solve the problem as non-linear. The time dependence of SRF is modeled by the regularized Yoffe function $\Upsilon(t; \tau_R, \tau_P)$ introduced by Tinti et al. (2005) (see Supplement 4.5.1), and the formula for SRF then reads

$$\Delta\dot{u}_i(t) = A_i \Upsilon\left(t - t_i^0; \tau_i^R, \tau_i^P\right), \quad (4.4)$$

where t_i^0 is rupture time, A_i is slip, τ_i^R is rise time, and τ_i^P is so-called peak time (i.e. duration of positive slip acceleration of SRF), respective to subfault i . Note

that the regularized Yoffe function is non-negative function of unit area, i.e.

$$1 = \int_0^{\tau_i^R} \Upsilon(t - t_i^0; \tau_i^R, \tau_i^P) dt. \quad (4.5)$$

The regularized Yoffe function can be expressed analytically (Supplement 4.5.1) and it is dynamically compatible with processes of sub-shear ruptures (Bizzarri 2012), therefore it is suitable as shape of SRF for fast forward problem computations. To summarize, the SRF of a given subfault i is in our formulation fully parametrized by four parameters $A_i, t_i^0, \tau_i^R, \tau_i^P$ (i.e. slip, rupture time, rise time and peak time).

Rupture propagation

Initiation of the rupture process in the subfaults distributed on the fault surface is defined by rupture times t_i^0 (see Eq. (4.4)). We assume that the rupture propagates from a hypocenter

$$\mathbf{h} = (x_H, y_H, t_H), \quad (4.6)$$

where $(x_H, y_H) \in \Sigma$ denote coordinates of the hypocenter on the fault and t_H is the hypocenter time. The rupture propagates with rupture-front velocity $v^0(\Sigma)$ which is function of position on the fault plane. The rupture times are then formally solution of two-dimensional eikonal equation, describing propagation of the rupture-front along the fault. The eikonal equation can be numerically solved on dense grid by a method relying on a systematic application of Huygens' principle in the finite difference approximation (e.g., Podvin & Lecomte 1991). Nevertheless, the selection of the particular rupture-front propagation solver is not bounded to our inversion method.

Then, we treat the hypocenter \mathbf{h} and rupture-front velocity function $v^0(\Sigma)$ as model parameters instead of arbitrary rupture times t_i^0 . Such parametrization is not too restrictive because of the assumption of spatially variable rupture-front velocity. It forbids nucleation of the rupture from multiple spatially separated areas and enforces causality.

Spatial parametrization

Parameters $\vartheta_i, A_i, \tau_i^R$ and τ_i^P are assigned to positions of subfaults' centers $(x_i, y_i) \in \Sigma$ on the fault. In our approach, these parameters are interpolated to the subfaults' centers from a sparse net of so-called control points on the fault (e.g., Eiseman 1992; Mortenson 2006). Advantage of such approach are: lower number of parameters and possibility of an irregular spatial parametrization.

We define two independent systems of spatial control points differing in their spatial positioning and the interpolation method. Firstly, we use a regular grid of control points distributed over the whole fault (see Fig 4.1a), with their total count of N_Γ . Assigned parameters in the position of the r -th control point $(x_r, y_r) \in \Sigma$ can be expressed by vector $\mathbf{\Gamma}_r$ as

$$\mathbf{\Gamma}_r = (\vartheta_r, v_r^0, \tau_r^R, \tau_r^P), \quad \text{where } (\mathbf{\Gamma}_r)_{r=1}^{N_\Gamma}, \quad (4.7)$$

then $N_\Gamma \times 4$ matrix $\mathbf{\Gamma}$ parametrizes the earthquake source in terms of spatial distribution of rake, rupture-front velocity, rise time and peak time. The value of any parameter in i -th subfaults' positions (x_i, y_i) is obtained by bilinear interpolation (e.g., Jain 1989) from the regularly distributed control points with assigned values stored in matrix $\mathbf{\Gamma}$. In case of rupture-front velocity $v^0(\Sigma)$, the values in control points are interpolated by the bilinear interpolation into the dense finite-difference grid used by the rupture-front propagation solver (e.g., Podvin & Lecomte 1991), and then resampled to the given (x_i, y_i) .

For the spatial parametrization of the slip A_i we use different system of control points. We utilize self-adapting parametrization with varying number of control points where the density of control points can vary spatially (Causse et al. 2017). Such parametrization can effectively adapt to heterogeneity of slip such as, e.g., to the case of multiple asperity source model (Lay et al. 1982). The used system of control points consists of a varying number of points N_Φ (called as ‘‘spline points’’) arbitrarily distributed over the fault plane (see Fig 4.1b). These spline points are allowed to move over the whole fault surface during the inversion (Moreau et al. 2014; Causse et al. 2017). Then, assigned parameters of the s -th spline point can be expressed by vector $\mathbf{\Phi}_s$ as

$$\mathbf{\Phi}_s = (x_s, y_s, A_s), \quad \text{where } (\mathbf{\Phi}_s)_{s=1}^{N_\Phi}, \quad (4.8)$$

where $(x_s, y_s) \in \Sigma$ are coordinates of the s -th spline point on the fault. Then $N_\Phi \times 3$ matrix $\mathbf{\Phi}$ parametrizes the spatial distribution of the magnitude of slip on the fault. In such formulation, positions of spline points are also parameters of the earthquake source model. The slip magnitude at the i -th subfaults' positions (x_i, y_i) is then evaluated using biharmonic spline interpolation (Sandwell 1987). The interpolation is performed with enforced zero slip at the fault edges; this is achieved by adding fixed auxiliary spline points regularly distributed on the fault edges with assigned zero slip magnitude (see Fig 4.1b). Then, utilizing biharmonic spline interpolation by Sandwell (1987), magnitude of slip A_i at position (x_i, y_i) is given by

$$A_i(x_i, y_i) = \sum_{s=1}^{N_\Phi} \epsilon_s |\mathbf{z}|^2 (\ln |\mathbf{z}| - 1) \quad (4.9)$$

$$|\mathbf{z}| = \sqrt{(x_i - x_s)^2 + (y_i - y_s)^2},$$

where ‘‘strenght’’ of each spline point $\epsilon_s = \epsilon_{s'}$ is found by solving the following linear system of equations:

$$A_s(x_s, y_s) = \sum_{s'=1}^{N_\Phi} \epsilon_{s'} |\mathbf{z}'|^2 (\ln |\mathbf{z}'| - 1) \quad (4.10)$$

$$|\mathbf{z}'| = \sqrt{(x_s - x_{s'})^2 + (y_s - y_{s'})^2}, \quad \text{with } (A_s)_{s=1}^{N_\Phi}.$$

As the system in Eq. (4.10) is linear, the values of $\epsilon_{s'}$ can be calculated very efficiently. Further, we allow slip magnitude A_s at each spline control point s vary arbitrarily, i.e. $A_s \in (-\infty, \infty)$. Subsequently, the interpolated slip magnitudes lower than zero are annulled as negative slip values are not expected, i.e. $A_i \geq 0$. Such approach permits to generate even sharp spatial slip distributions.

In such system of spline points, the density of control points vary spatially, and then the parametrization can effectively adapt to heterogeneity of slip (see Fig. 4.1b). Furthermore, the varying number of spline points N_Φ controls the spatial complexity of the resolved slip on the fault in the inversion, which permits the use of trans-D MCMC method (e.g., Sambridge et al. 2006). In this sense, it leads to the self-adapting model space parametrization driven by the observed data (trans-D Bayesian inversion).

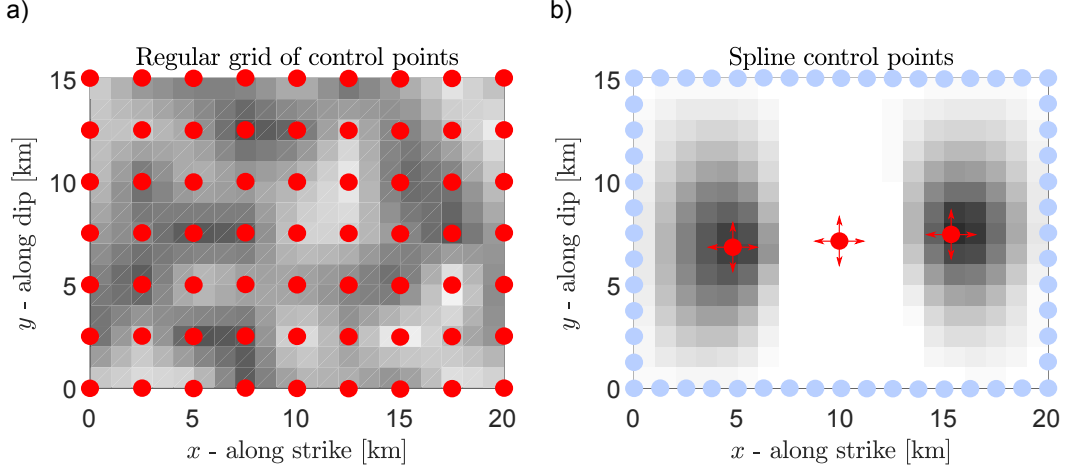


Figure 4.1: Schemes of two systems of control points used for the spatial parametrization of the rupture. Shaded gray rectangles represent subfaults with parameter values coded by the shade scale (τ_i^R and A_i in panels **a** and **b**, respectively). Positions of control points on the fault are shown by red circles for **a**) regular grid, and **b**) system of spline points. The blue circles show auxiliary control points setting slip magnitude on the fault edges to zero. The total number of control points in this example is $N_\Gamma = 63$ (panel **a**) and $N_\Phi = 3$ (panel **b**).

4.2.2 Forward problem

The representation theorem in Eq. (4.2) shows straightforward relation among the synthetic displacement, GFs and the shear slip on the assumed fault. For the sake of the numerical computations, the forward expression in Eq. (4.2) with Eq. (4.3) included is rewritten in the discrete time samples form as

$$u_n^k = \Delta\Sigma \Delta t \sum_{i=1}^{N_\Sigma} \sum_{l=1}^{N_T} \Delta\dot{u}_i^l \left(\hat{G}_{ni}^{k-l} \cos(\vartheta_i - \hat{\vartheta}) + \check{G}_{ni}^{k-l} \cos(\check{\vartheta} - \vartheta_i) \right), \quad (4.11)$$

where Δt is temporal sampling interval of SRFs with N_T samples in total (indexes k and l denote temporal samples of waveforms and SRFs, respectively). The GFs for two perpendicular rakes ($\hat{\vartheta}$ and $\check{\vartheta}$) are pre-computed prior to the inversion for all receivers and subfaults. Then, the n -th synthetic component can be directly computed for a given set of SRFs, i.e. time series $(\Delta\dot{u}_i^l)_{l=1}^{N_T}$, and respective rakes ϑ_i . Note that for practical reasons, the temporal sampling interval Δt is assumed to be the same for the SRFs, GFs and synthetics.

The forward problem of Eq. (4.11) is solved many times for various sets of model parameters (or simply “models”), defined in our approach as

$$\mathbf{m} = (\mathbf{h}, \text{vec}(\mathbf{\Gamma}), \text{vec}(\mathbf{\Phi}), N_{\Phi}), \quad (4.12)$$

where $\text{vec}(\cdot)$ denote vectorization of a matrix. Vectors \mathbf{h} and $\text{vec}(\mathbf{\Gamma})$ (see Eqs (4.6) and (4.7)) have a fixed size, while $\text{vec}(\mathbf{\Phi})$ (see Eq. (4.8)) is vector of varying length N_{Φ} . Such model \mathbf{m} fully parametrizes the spatial-temporal rupture propagation on the fault plane, where the vector’s length has meaning of the number of model parameters.

The forward problem, where synthetic waveforms on all receivers for a given model \mathbf{m} are predicted by Eq. (4.11), can be expressed using a forward operator $\mathbf{g}(\cdot)$ as

$$\mathbf{d} = \mathbf{g}(\mathbf{m}), \quad (4.13)$$

where vector \mathbf{d} contain all synthetic waveforms predicted on all three-component receivers.

To summarize, the forward computation consists of the following steps:

- Interpolate parameters ϑ_r , τ_r^R and τ_r^P assigned to N_{Γ} control points from the regular grid (i.e. $(\mathbf{\Gamma}_r)_{r=1}^{N_{\Gamma}}$) into all subfaults’ positions (x_i, y_i) by bilinear interpolation.
- Interpolate parameter v_r^0 assigned to N_{Γ} control points from the regular grid (i.e. $(\mathbf{\Gamma}_r)_{r=1}^{N_{\Gamma}}$) into a dense finite-difference grid used by the rupture-front propagation solver (e.g., Podvin & Lecomte 1991).
- Evaluate rupture times t_i^0 in all subfaults by the eikonal solver, assuming rupture-front propagation from the hypocenter \mathbf{h} .
- Interpolate the slip magnitude prescribed by N_{Φ} spline points (i.e. $(\mathbf{\Phi}_s)_{s=1}^{N_{\Phi}}$) and additional invariable auxiliary spline points distributed on the fault edges into all the subfaults by biharmonic spline interpolation, Eq. (4.9).
- Compute SRFs for all the subfaults by Eq. (4.4).
- Perform the temporal discrete convolution of the computed SRFs and GFs following Eq. (4.11) to acquire synthetic waveforms.

4.2.3 Bayesian inference

Lets us assume, for a moment, a constant number of spline control points, i.e. fixed number of model parameters. In the Bayesian framework (see Section 1.2; Tarantola & Valette 1982; Tarantola 2005) a prior assumption on the model is specified, which is then updated to a conditional posterior probability on model parameters affected by the observed data. The Bayesian solution of the inverse problem is then defined as the conditional posterior probability density function (PDF) on the model parameters $p(\mathbf{m}|\mathbf{d}_{obs})$, where \mathbf{d}_{obs} denote one-column vector of all observed data (i.e. vectorized measured seismograms).

The Bayes' theorem (Bayes 1763) is utilized to combine prior probability with the observed data to acquire the posterior PDF by

$$p(\mathbf{m}|\mathbf{d}_{obs}) = \frac{p(\mathbf{m}) p(\mathbf{d}_{obs}|\mathbf{m})}{\int p(\mathbf{m}) p(\mathbf{d}_{obs}|\mathbf{m}) d\mathbf{m}}, \quad (4.14)$$

where $p(\mathbf{m})$ is a prior PDF on the model parameters, and $p(\mathbf{d}_{obs}|\mathbf{m})$ is conditional probability of data for given model \mathbf{m} , i.e. so-called likelihood function. Note that if the likelihood function is a constant function, with meaning of no information carried by the observed data, then the posterior PDF is the same as the prior PDF.

The likelihood function $p(\mathbf{d}_{obs}|\mathbf{m})$ evaluates how well given model \mathbf{m} describes the observed waveforms \mathbf{d}_{obs} by means of misfit with synthetic waveforms calculated using the theoretical relation in Eq. (4.13) (i.e. misfit function). The likelihood function $p(\mathbf{d}_{obs}|\mathbf{m})$ can be expressed for Gaussian errors (Tarantola 2005, eq. 1.100) as

$$p(\mathbf{d}_{obs}|\mathbf{m}) = const. \exp\left(-\frac{1}{2} \mathcal{L}(\mathbf{m})\right), \quad (4.15)$$

with the misfit function $\mathcal{L}(\mathbf{m})$ expressed in matrix form as

$$\mathcal{L}(\mathbf{m}) = \left(\mathbf{d}_{obs} - \mathbf{g}(\mathbf{m})\right)^T \mathbf{C}_D^{-1} \left(\mathbf{d}_{obs} - \mathbf{g}(\mathbf{m})\right). \quad (4.16)$$

Gaussian covariance matrix \mathbf{C}_D characterizes cross-covariances of misfits, which can be explained by the expected errors of observed data or the theory. The covariance matrix \mathbf{C}_D can be decomposed by Cholesky decomposition as

$$\mathbf{C}_D^{-1} = \mathbf{W}^T \mathbf{W}, \quad (4.17)$$

where \mathbf{W} is an upper triangular matrix. Substituting Eq. (4.17) into Eq. (4.16), the misfit function reads

$$\mathcal{L}(\mathbf{m}) = \left(\mathbf{W}\mathbf{d}_{obs} - \mathbf{W}\mathbf{g}(\mathbf{m})\right)^T \left(\mathbf{W}\mathbf{d}_{obs} - \mathbf{W}\mathbf{g}(\mathbf{m})\right) \quad (4.18)$$

$$= \left(\mathbf{d}_{obs}^* - \mathbf{g}^*(\mathbf{m})\right)^T \left(\mathbf{d}_{obs}^* - \mathbf{g}^*(\mathbf{m})\right), \quad (4.19)$$

where \mathbf{d}_{obs}^* and $\mathbf{g}^*(\mathbf{m})$ are so-called standardized waveforms (Dettmer et al. 2014; Hallo & Gallovič 2016), i.e. waveforms multiplied by the upper triangular matrix \mathbf{W} from the Cholesky decomposition of \mathbf{C}_D .

If the estimate of data and theory uncertainties by means of the data covariance matrix \mathbf{C}_D is given, then the standardized observed waveforms \mathbf{d}_{obs}^* can be pre-computed prior to the inversion. The standardized synthetic waveforms $\mathbf{g}^*(\mathbf{m})$ can be evaluated utilizing Eq. (4.11) substituting GFs by so-called standardized GFs, $\hat{\mathbf{G}}^*$ and $\check{\mathbf{G}}^*$. Such standardized GFs are pre-computed prior to the inversion for the two perpendicular rakes as

$$\text{vec}(\hat{\mathbf{G}}_i^*) = \mathbf{W} \cdot \text{vec}(\hat{\mathbf{G}}_i), \quad \text{where } (\hat{\mathbf{G}}_i)_{i=1}^{N_\Sigma} \quad (4.20)$$

$$\text{vec}(\check{\mathbf{G}}_i^*) = \mathbf{W} \cdot \text{vec}(\check{\mathbf{G}}_i), \quad \text{where } (\check{\mathbf{G}}_i)_{i=1}^{N_\Sigma} \quad (4.21)$$

where $\text{vec}(\cdot)$ denote here one-column vector of GFs for all receivers with the source at i -th subfault position. The advantage of the formulation with standardized residuals in Eq. (4.19) is avoiding repetition of numerically demanding multiplication by the large covariance matrix \mathbf{C}_D^{-1} in Eq. (4.15). Such approach significantly increases the efficiency of the numerical evaluation of the likelihood function.

Data covariance matrix

The reliability of the assessment of the solution uncertainty by such Bayesian framework depends on the assessment of data and modeling errors. As, the instrumental and ambient noise errors are typically negligible when dealing with larger events, the covariance matrix \mathbf{C}_D is dominated by modeling errors governed by the uncertainty of the GFs due to the inaccuracy of the velocity structure considered (e.g., Yagi & Fukahata 2011; Duputel et al. 2014, 2015; Hallo et al. 2017). We include the modeling errors in covariance matrix \mathbf{C}_D following the approach by Hallo & Gallovič (2016). They compose \mathbf{C}_D from discrete time samples from approximate covariance functions (ACF or SACF). The formula for ACF dependent on time t and time lag φ reads

$$\begin{aligned} ACF_n(t, \varphi) = & \frac{1}{L} \int_{-\frac{L}{2}}^{\frac{L}{2}} u_n^{obs}(t-l) u_n^{obs}(t+\varphi-l) dl - \\ & - \frac{1}{L} \int_{-\frac{L}{2}}^{\frac{L}{2}} u_n^{obs}(t-l) dl - \frac{1}{L} \int_{-\frac{L}{2}}^{\frac{L}{2}} u_n^{obs}(t+\varphi-l) dl, \end{aligned} \quad (4.22)$$

where $u_n^{obs}(t)$ is the n -th observed displacement component, and L [sec] is the width of the uniform PDF of random perturbation defined in Eq. (2.8). The second approximate function, the SACF, depends only on time lag φ as

$$SACF_n(\varphi) = \frac{1}{T} \left(r_n^{obs}(\varphi) - \wedge_{2L}(\varphi) * r_n^{obs}(\varphi) \right), \quad (4.23)$$

where T is duration of the dominant part of the signal, $*$ denotes convolution, $\wedge_{2L}(\varphi)$ is the triangle function of unit area centered around zero with duration $2L$, and $r_n^{obs}(\varphi)$ is auto-correlation of the n -th observed waveform $u_n^{obs}(t)$.

In the multi-station and multi-component inversions, data covariance matrix \mathbf{C}_D has block-diagonal structure. The covariance matrices for each n -th waveform are arranged along the diagonal, while the off-diagonal blocks are inter-component and inter-station cross-covariances. Hallo & Gallovič (2016) successfully tested the performance of these covariance matrices (created from ACF and SACF) in capturing the GFs uncertainty (Chapter 2) in the moment tensor inversion tests, and further Hallo et al. (2017) applied SACF in the Bayesian inference of centroid moment tensors of foreshocks and aftershocks of the 2016 Kumamoto, Japan, earthquake sequence (Chapter 3).

In this first test we deploy the time-dependent ACF covariance matrix, with a station-specific water level added to the diagonal. As the water level we use 25% of the maximum variance from all the three station components, which preserves the covariance matrix invertible and also increases possible variations of the waveforms.

Trans-dimensional MCMC

“Everything should be as simple as it can be, but not simpler.” — Albert Einstein

“With four parameters I can fit an elephant, and with five I can make him wiggle his trunk.” — John von Neumann

The forward problem is solved as non-linear problem by random exploration of the model space (Monte Carlo method; see Section 1.2.2). As we assume a varying number of spline points N_{Φ} , the dimension of the model space may vary. This leads to trans-D inverse problem, where the number of dimensions of model space is treated as an unknown parameter (e.g., Green 1995, 2003; Richardson & Green 1997; Sambridge et al. 2006; Fan & Sisson 2011).

Let us assume that we have a countable collection of model states \mathcal{K} indexed by parameter $k \in \mathcal{K}$. Each model state has respective n_k -dimensional model vector \mathbf{w}_k in its own model space, $\mathbf{w}_k \in \mathcal{R}^{n_k}$. We define state space Ξ for across-model simulations (Green 2003, pp. 2) as

$$\Xi = \bigcup_{k \in \mathcal{K}} (\{k\} \times \mathcal{R}^{n_k}), \quad (4.24)$$

which is the target of a Monte Carlo sampler (see example in Table 4.1). The stationary posterior PDF of model $\mathbf{m} = (k, \mathbf{w}_k)$, where $\mathbf{m} \in \Xi$, then following Green (2003, pp. 2) reads

$$p(\mathbf{m}|\mathbf{d}_{obs}) = p(k, \mathbf{w}_k|\mathbf{d}_{obs}) = \frac{p(k) p(\mathbf{w}_k|k) p(\mathbf{d}_{obs}|k, \mathbf{w}_k)}{\sum_{k' \in \mathcal{K}} \int_{\mathcal{R}^{n_{k'}}} p(k') p(\mathbf{w}'_{k'}|k') p(\mathbf{d}_{obs}|k', \mathbf{w}'_{k'}) d\mathbf{w}'_{k'}}, \quad (4.25)$$

where $p(k)$ is a prior PDF on model state, $p(\mathbf{w}_k|k)$ is prior PDF on model parameters under state k , and $p(\mathbf{d}_{obs}|k, \mathbf{w}_k) = p(\mathbf{d}_{obs}|\mathbf{m})$ is conditional probability of data for given model (k, \mathbf{w}_k) , i.e. so-called likelihood function.

To draw random samples from the multiple-state posterior PDF $p(\mathbf{m}|\mathbf{d}_{obs})$, we utilize the reversible jump MCMC algorithm by Green (1995, 2003). The algorithm is based on Metropolis-Hastings algorithm, developed by Metropolis et al. (1953) and generalized by Hastings (1970), as a Markov chain Monte-Carlo method for sampling posterior PDF by a chain of steps. The used algorithm extends the Metropolis-Hastings to cases when the model change the state between iterates of the Markov chain. By such MCMC approach, model $\mathbf{m} = (k, \mathbf{w}_k)$ is perturbed in each step of the Markov chain to create a new (proposed) model $\mathbf{m}' = (k', \mathbf{w}'_{k'})$ with a forward step probability drawn from the proposal distribution $q(\mathbf{m}'|\mathbf{m})$ within the whole state space Ξ . The proposed model \mathbf{m}' is then accepted or rejected based on the “Metropolis choice” (Metropolis et al. 1953):

$$\mathbf{m}_{+1} = \begin{cases} \mathbf{m}', & \mathbf{m}' \text{ accepted with probability } \alpha(\mathbf{m} \rightarrow \mathbf{m}') \\ \mathbf{m}, & \mathbf{m}' \text{ rejected with probability } 1 - \alpha(\mathbf{m} \rightarrow \mathbf{m}') \end{cases} \quad (4.26)$$

Following Green (2003), the acceptance probability $\alpha(\mathbf{m} \rightarrow \mathbf{m}')$ as mechanism of balance condition for construction of Markov chain in state space Ξ reads

$$\alpha(\mathbf{m} \rightarrow \mathbf{m}') = \min \left(1, \frac{p(k')}{p(k)} \frac{p(\mathbf{w}'_{k'}|k')}{p(\mathbf{w}_k|k)} \frac{p(\mathbf{d}_{obs}|\mathbf{m}')}{p(\mathbf{d}_{obs}|\mathbf{m})} \frac{q(\mathbf{m}|\mathbf{m}')}{q(\mathbf{m}'|\mathbf{m})} \right), \quad (4.27)$$

where $q(\mathbf{m}|\mathbf{m}')$ is the proposal distribution used to draw probability of the reverse step ($\mathbf{m}' \rightarrow \mathbf{m}$). It resembles the standard Metropolis-Hastings acceptance probability (Hastings 1970), and it includes it as a special case when $\dim(\mathcal{K}) = 1$. This form of reversible jump MCMC is rather general as the model states \mathcal{K} may have generally different properties and/or dimensions.

A special case of the reversible jump MCMC algorithm is the trans-D MCMC, where the proposal moves between model states may be achieved by the “dimension matching” (e.g., Green 2003; Fan & Sisson 2011). Let us assume that the Markov chain is in the state k and we wish to propose a move to model state k' with a higher dimension, i.e. $n_{k'} > n_k$. In order to “match dimensions”, a random vector \mathbf{z} of length $(n_{k'} - n_k)$ is generated from a prescribed joint density $q(\mathbf{z})$. The model vector \mathbf{w}_k and random vector \mathbf{z} are then mapped to the proposed model vector $\mathbf{w}'_{k'}$ by diffeomorphism (i.e. the transformation and its inverse are differentiable). Assuming such mechanism of “dimension matching”, the acceptance probability from Eq. (4.27) becomes (Green 2003, pp. 5)

$$\alpha(\mathbf{m} \rightarrow \mathbf{m}') = \min \left(1, \frac{p(k')}{p(k)} \frac{p(\mathbf{w}'_{k'}|k')}{p(\mathbf{w}_k|k)} \frac{p(\mathbf{d}_{obs}|\mathbf{m}')}{p(\mathbf{d}_{obs}|\mathbf{m})} \frac{j_{k' \rightarrow k}}{j_{k \rightarrow k'}} \frac{q(\mathbf{z}')}{q(\mathbf{z})} |J| \right), \quad (4.28)$$

where $j_{k \rightarrow k'}$ denotes the probability of proposing move from model state k to k' , and vice versa. $|J| = \left| \frac{\partial(\mathbf{w}'_{k'}, \mathbf{z}')}{\partial(\mathbf{w}_k, \mathbf{z})} \right|$ is the determinant of the Jacobian for the diffeomorphism from \mathbf{m} to \mathbf{m}' . Green (1995) shows, that samples of such Markov chain are asymptotically distributed according the posterior PDF. For details see Green (1995, 2003), Sambridge et al. (2006), Fan & Sisson (2011). The trans-D MCMC algorithm with applications in geoscience is described also in previous studies conducted by, e.g., Malinverno (2002), Gallagher et al. (2009), Bodin et al. (2012), Dettmer et al. (2014) and Dettmer et al. (2016).

In our particular case (see Table 4.1), each model state consists of different number of spline points, i.e. index k has meaning of number of spline points N_Φ in model \mathbf{m} . The difference in number of dimensions of two neighboring model spaces \mathcal{R}^{n_k} and $\mathcal{R}^{n_{k+1}}$ is $(n_{k+1} - n_k) = 3$, as we define every spline point by three parameters (see Eq. (4.8)). Further, let us assume the model states' transitions are considered in one Markov chain step only between neighboring model states. It can be either model state with one extra or one less spline point (e.g., chain steps as $\mathcal{R}^{n_1} \rightarrow \mathcal{R}^{n_2} \rightarrow \mathcal{R}^{n_2} \rightarrow \mathcal{R}^{n_1} \rightarrow \mathcal{R}^{n_2} \rightarrow \mathcal{R}^{n_3} \rightarrow \mathcal{R}^{n_3} \rightarrow \dots$). This is so-called birth-death MCMC, and it consists of three move types which occur with probabilities j_P , j_B and j_D such that

$$1 = j_P + j_B + j_D, \quad (4.29)$$

where j_P is probability of “perturb” move with no change in dimensions $\mathcal{R}^{n_k} \rightarrow \mathcal{R}^{n_k}$, j_B is probability of “birth” of new dimensions $\mathcal{R}^{n_k} \rightarrow \mathcal{R}^{n_{k+1}}$ (creation of one arbitrarily spline point), and j_D is probability of “death”, i.e. reducing dimensions $\mathcal{R}^{n_k} \rightarrow \mathcal{R}^{n_{k-1}}$ (deleting one arbitrarily spline point). The probabilities of birth and death moves are equal, i.e. $j_B = j_D$, so as not to prefer either birth or death proposals. On the other hand, the probability of perturb move may be higher, i.e. $j_P > (j_B + j_D)$, in order to let the MCMC sampler explore various parameters' combinations of the model with temporarily fixed model state k . The common values of moves' probabilities are $j_P = 0.9$, $j_B = 0.05$, $j_D = 0.05$. Note that the term $\frac{j_{k' \rightarrow k}}{j_{k \rightarrow k'}}$ in Eq. (4.28) is then unity for all possible moves.

model	model state	model vector \mathbf{w}_k	model space
$\mathbf{m} = (k, \mathbf{w}_k)$	k_{max} N_Φ	$\mathbf{h}, \text{vec}(\Gamma)$ $x_1, y_1, A_1 \cdots x_{k_{max}}, y_{k_{max}}, A_{k_{max}}$	$\mathcal{R}^{n_{k_{max}}}$

	$k = 3$ N_Φ	$\mathbf{h}, \text{vec}(\Gamma)$ x_1, y_1, A_1 x_2, y_2, A_2 x_3, y_3, A_3	\mathcal{R}^{n_3}
	$k = 2$ N_Φ	$\mathbf{h}, \text{vec}(\Gamma)$ x_1, y_1, A_1 x_2, y_2, A_2	\mathcal{R}^{n_2}
	$k = 1$ N_Φ	$\mathbf{h}, \text{vec}(\Gamma)$ x_1, y_1, A_1	\mathcal{R}^{n_1}

Table 4.1: Structure of model $\mathbf{m} \in \Xi$ as appears in Eq. (4.12). Model state k has meaning of varying number of spline points N_Φ . MCMC then inspects posterior PDF Eq. (4.25) by a chain of moves between (and within) the model states.

We utilize Gaussian proposal distribution for random perturbations of the existing model parameters, which is re-centered after each step at the value last generated by the Markov chain. In the case of “perturb” move, the Jacobian is unity, and the trans-D MCMC behaves as Gaussian random walk MCMC (see Section 1.2.2). The acceptance probability $\alpha_P(\mathbf{m} \rightarrow \mathbf{m}')$ for this scenario then reads

$$\alpha_P(\mathbf{m} \rightarrow \mathbf{m}') = \min \left(1, \frac{p(\mathbf{w}'_k|k) p(\mathbf{d}_{obs}|\mathbf{m}')}{p(\mathbf{w}_k|k) p(\mathbf{d}_{obs}|\mathbf{m})} \right). \quad (4.30)$$

Sambridge et al. (2006) show that for the case of birth-dead MCMC the Jacobian in Eq. (4.28) is unity as well. Furthermore, the acceptance probabilities for “birth” and “death” moves $\alpha_B(\mathbf{m} \rightarrow \mathbf{m}')$ and $\alpha_D(\mathbf{m} \rightarrow \mathbf{m}')$, are given respectively by (Sambridge et al. 2006, eqs 40 and 41)

$$\alpha_B(\mathbf{m} \rightarrow \mathbf{m}') = \min \left(1, \frac{p(k+1) p(\mathbf{w}'_{k+1}|k+1) p(\mathbf{d}_{obs}|\mathbf{m}') q_{k+1}^D}{p(k) p(\mathbf{w}_k|k) p(\mathbf{d}_{obs}|\mathbf{m}) q_k^B} \right), \quad (4.31)$$

$$\alpha_D(\mathbf{m} \rightarrow \mathbf{m}') = \min \left(1, \frac{p(k-1) p(\mathbf{w}'_{k-1}|k-1) p(\mathbf{d}_{obs}|\mathbf{m}') q_{k-1}^B}{p(k) p(\mathbf{w}_k|k) p(\mathbf{d}_{obs}|\mathbf{m}) q_k^D} \right). \quad (4.32)$$

Here q_k^B and q_k^D are probability densities of birth or death of a spline point, respectively, assuming equally weighted spline points. Further, we assume homogenous prior PDF on number of spline points in model, i.e. $p(k+1) = p(k)$, then the prior PDF on model parameters under state $k+1$ can be expressed by

$$p(k+1) p(\mathbf{w}'_{k+1}|k+1) = p(k) p(\mathbf{w}'_k|k) c_\Phi, \quad (4.33)$$

where c_Φ is a constant with meaning of the prior PDF of one spline point arbitrarily located on the fault. Further, assuming homogenous prior PDF on the model parameters, i.e. constant $p(\mathbf{w}_k|k)$ for a given model state k , and utilizing probability densities of birth or death of a spline point in the same sense as in, e.g., Bodin et al. (2012), the acceptance probabilities for “perturb”, “birth” and “death” moves in Eqs (4.30), (4.31) and (4.32) simplify to

$$\alpha_P(\mathbf{m} \rightarrow \mathbf{m}') = \min \left(1, \frac{p(\mathbf{d}_{obs}|\mathbf{m}')}{p(\mathbf{d}_{obs}|\mathbf{m})} \right), \quad (4.34)$$

$$\alpha_B(\mathbf{m} \rightarrow \mathbf{m}') = \min \left(1, \frac{p(\mathbf{d}_{obs}|\mathbf{m}')}{p(\mathbf{d}_{obs}|\mathbf{m})} \frac{1}{N_\Phi + 1} \right), \quad (4.35)$$

$$\alpha_D(\mathbf{m} \rightarrow \mathbf{m}') = \min \left(1, \frac{p(\mathbf{d}_{obs}|\mathbf{m}')}{p(\mathbf{d}_{obs}|\mathbf{m})} N_\Phi \right), \quad (4.36)$$

where N_Φ is the present number of spline points. The “birth” move is thus penalized with increasing number of spline points, while the “death” move acceptance probability increases with the number of spline points. Hence, a better misfit function of data and synthetics is required to increase the number of spline points in the ensemble of solutions.

To increase the efficiency of the trans-D MCMC sampler, we apply the Parallel tempering (PT) method introduced by Sambridge (2014) (see Section 1.2.2). The PT sampling algorithm is similar to the simulated annealing method (Kirkpatrick et al. 1983) introducing modification of the posterior PDF by an additional parameter called temperature $\gamma \geq 1$. The random samples are then drawn following such modified posterior PDF assuming multiple values of temperature γ (multiple trans-D Markov chains), while at least one chain has $\gamma = 1$, i.e. so-called “sampling” chain. The acceptance probabilities in Eqs (4.34), (4.35) and (4.36), are modified as follows

$$\alpha_P(\mathbf{m} \rightarrow \mathbf{m}', \gamma) = \min \left(1, \left(\frac{p(\mathbf{d}_{obs}|\mathbf{m}')}{p(\mathbf{d}_{obs}|\mathbf{m})} \right)^{1/\gamma} \right), \quad (4.37)$$

$$\alpha_B(\mathbf{m} \rightarrow \mathbf{m}', \gamma) = \min \left(1, \left(\frac{p(\mathbf{d}_{obs}|\mathbf{m}')}{p(\mathbf{d}_{obs}|\mathbf{m})} \right)^{1/\gamma} \frac{1}{N_\Phi + 1} \right), \quad (4.38)$$

$$\alpha_D(\mathbf{m} \rightarrow \mathbf{m}', \gamma) = \min \left(1, \left(\frac{p(\mathbf{d}_{obs}|\mathbf{m}')}{p(\mathbf{d}_{obs}|\mathbf{m})} \right)^{1/\gamma} N_\Phi \right). \quad (4.39)$$

Arbitrary trans-D chains are allowed to exchange the temperatures with a probability given by a balance condition for the swap (e.g., Sambridge 2014). Finally, the ensemble of solutions following the posterior PDF is formed only by random samples on temperature $\gamma = 1$ sampling of the original posterior PDF.

To summarize, the utilized trans-D MCMC algorithm with PT in each Markov chain step:

1. Randomly selects the move type (driven by probabilities j_P , j_B and j_D).
2. Randomly perturbs the current model to create a new (proposed) model.
3. Creates a new spline point or deletes an existing spline point (only in trans-D moves).
4. Accepts or rejects the new model based on the respective acceptance probability of Eqs (4.37), (4.38), or (4.39).
5. Tries to exchange the temperature γ with another Markov chain.

4.3 Application to the mainshock of the 2016 Kumamoto sequence

The mainshock of the 2016 Kumamoto earthquake sequence of $M_{JMA}7.3$ ($M_w7.1$) occurred in the central part of Kyushu, Japan on April 16, 2016 (01:25 of Japan Standard Time). It generated destructive ground motions in the near-source region, causing severe damage and casualties. The mainshock occurred 28 hours after the first recognized foreshock of $M_{JMA}6.5$, and it has been followed by a series of aftershocks (see Chapter 3 and references therein).

Finite-extent source models for the mainshock were inverted from strong motion records (e.g., Asano & Iwata 2016; Kubo et al. 2016b; Hao et al. 2017; Kobayashi et al. 2017; Yoshida et al. 2017). Moreover, the static slip models were inverted from geodetic data (e.g., Himematsu & Furuya 2016; Fukahata & Hashimoto 2016). The inferred models suggest that the rupture started near the intersection of the Futagawa and Hinagu faults by right-lateral strike-slip movement, with subsequent propagation to the NE along the Futagawa fault as strike-slip with a normal faulting component.

4.3.1 Inversion settings

Fault geometry

Following Asano & Iwata (2016), we assume a fault plane model consisting of two planar fault segments based on surface traces of known active faults and the aftershock distribution (e.g., Kato et al. 2016). The first fault segment #1 is set along the Hinagu fault intersecting the hypocenter of the $M_w7.1$ mainshock. The second (larger) fault segment #2 is set along the Futagawa fault spreading to NE from the intersection of both faults (see Fig. 4.2). The Hinagu and Futagawa fault segments are assumed to have rectangular shape of dimension larger than assumed by Asano & Iwata (2016) to not restrain the distance of the rupture propagation. For detailed settings of the assumed fault planes and their spatial parametrization see Table 4.2.

	Hinagu segment #1	Futagawa segment #2
Origin time*	April 16 2016 / 01:25:06 [†]	April 16 2016 / 01:25:07 [†]
Hypocenter*	32.75°N / 130.76°E / 12 km	32.79°N / 130.75°E / 12 km
Fault strike/dip	205° / 72°	235° / 65°
Fault length/width	18 km / 18 km	34 km / 18 km
Rake angle*	-160°	-142°
Subfault size	2 km × 2 km	2 km × 2 km
Num. of subfaults	81	153
Regular control points	7 along strike × 7 along dip	13 along strike × 7 along dip
Num. of control points	49	63

Note: *initial model parameters, not fixed during inversion; [†]Japan Standard Time

Table 4.2: Geometry of the Hinagu and Futagawa fault segments considered in the slip inversion (following Asano & Iwata 2016). The rupture process is assumed to initiate formally at each fault segment separately, hence they have separate hypocenters and origin times. Note that the hypocenter/origin time of segment #1 represents also the mainshock hypocenter/origin time taken from the JMA unified earthquake catalog.

In Section 4.2.1 we describe parametrization of the slip on a single fault segment. In the case of two fault segments, we consider parametrization of the slip on each fault segment separately. The augmented model vector \mathbf{m} , as originally formulated in Eq. (4.12) for a single segment, then reads

$$\mathbf{m} = (\mathbf{h}^{\#1}, \mathbf{h}^{\#2}, \text{vec}(\mathbf{\Gamma}^{\#1}), \text{vec}(\mathbf{\Gamma}^{\#2}), \text{vec}(\mathbf{\Phi}^{\#1}), \text{vec}(\mathbf{\Phi}^{\#2}), N_{\Phi}^{\#1}, N_{\Phi}^{\#2}), \quad (4.40)$$

where $\mathbf{h}^{\#}$ are hypocenters, $\mathbf{\Gamma}^{\#}$ are matrices of parameters assigned in the regularly distributed control points, $\mathbf{\Phi}^{\#}$ are matrices of slip spline control points, and $N_{\Phi}^{\#}$ are numbers of the spline points.

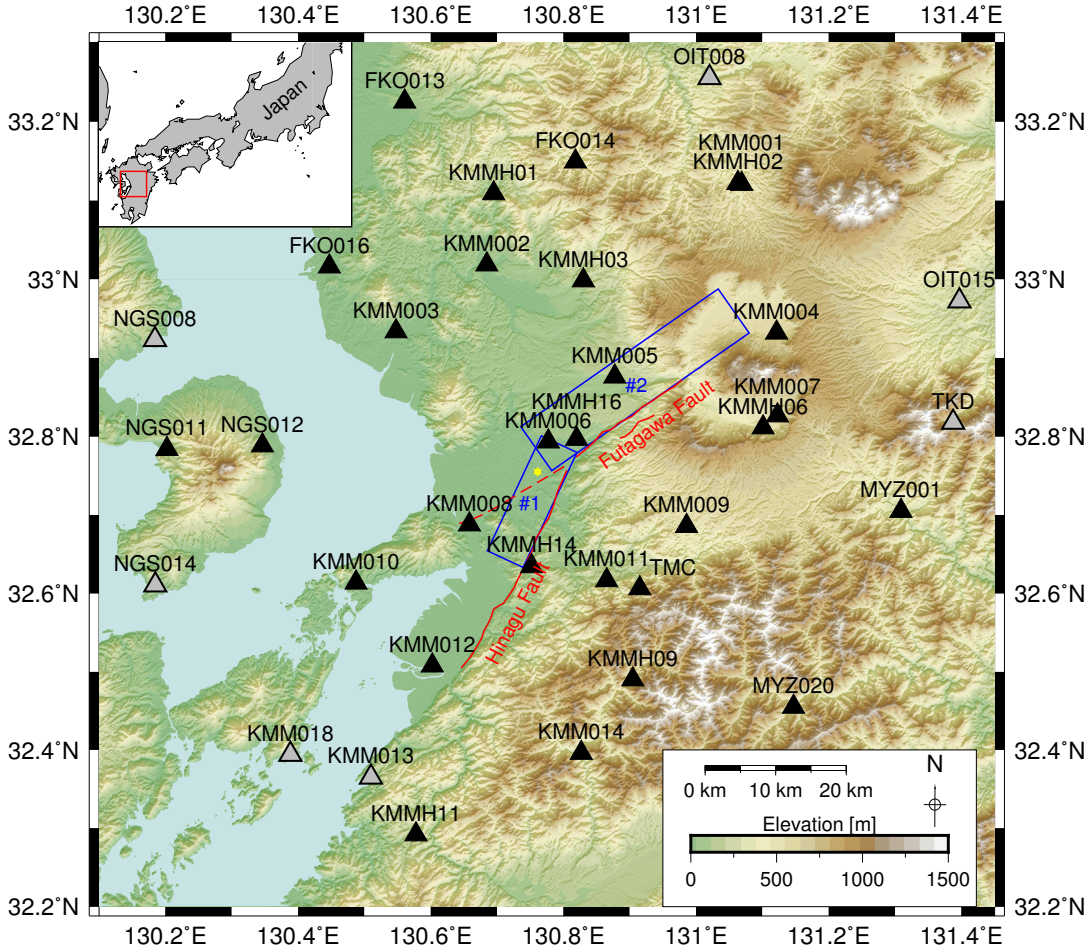


Figure 4.2: Map of the Kumamoto area, Japan, with the settings of the mainshock inversion (the M_w 7.1 earthquake from April 16, 2016). Blue rectangles denote projection of the assumed Hinagu (#1) and Futagawa (#2) fault segments, and the yellow star is the epicenter of the mainshock (from the JMA earthquake catalog). Black triangles show positions of strong motion stations of the K-NET, KiK-net and F-net networks used in the inversion. The gray triangles are stations excluded from the inversion (see text). Red lines denote surface traces of the main known active faults. The topography is created from the SRTM-90m digital elevation data.

Data selection and processing

We use three-component waveforms recorded at 29 stations of the K-NET, KiK-net and F-net strong motion networks (e.g., Okada et al. 2004), operated by

National Research Institute for Earth Science and Disaster Resilience (NIED), up to the distance of 55 km from the mainshock epicenter (see Fig. 4.2). The stations are selected based on distance and sufficient signal-to-noise ratio. Few regional stations were excluded from the selection, as their waveforms contain complex oscillations probably caused by shallow sedimentary layers. Nevertheless, these stations are located on the edge of the area of interest (see gray triangles in Fig. 4.2).

Original acceleration data (K-NET and KiK-net) and strong motion velocity data corrected for the instrument response (F-net) are filtered by a bandpass filter in the range of $0.05 - 0.5 \text{ Hz}$ and then integrated into displacements. The processed waveforms are downsampled to the sampling frequency of 2.5 Hz in order to reduce computational demands. The observed data time window used in the inversion spans $0 - 40 \text{ sec}$ after the adopted origin time of the mainshock (Tab. 4.2).

Velocity models

GFs for all of the assumed subfaults are pre-computed by the discrete wavenumber method (Bouchon 1981) considering one-dimensional station dependent velocity models consisting of homogenous layers (Fig. 4.3). As the uppermost sedimentary layers may affect the amplitude and shape of the strong motion waveforms at frequencies $0.05 - 0.5 \text{ Hz}$ (e.g., Asano & Iwata 2009), we considered different one-dimensional velocity model for each station.

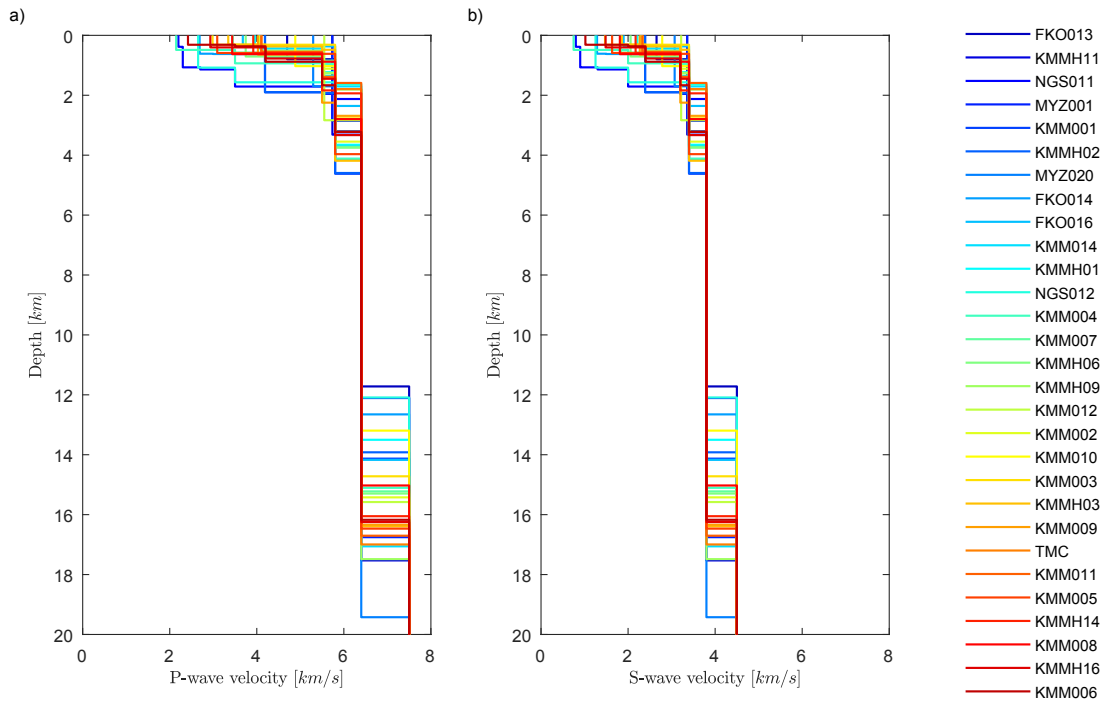


Figure 4.3: One-dimensional velocity models for all stations used in the mainshock inversion. **a)** P-wave and **b)** S-wave velocities are extracted from the three-dimensional Japan Integrated Velocity Structure Model (Koketsu et al. 2012). The stations are sorted by distance from the furthestmost (blue) to the nearest (red) to the mainshock epicenter.

One-dimensional velocity models were extracted from the three-dimensional Japan Integrated Velocity Structure Model (Koketsu et al. 2012) as the velocity depth profiles below the receivers. The models are shown in Fig. 4.3 in terms of P-wave and S-wave velocities.

4.3.2 Application details

Prior PDF

The Bayesian framework enables to account for prior knowledge provided as a prior PDF. Such prior PDF of the model parameters can be very subjective, which may be targeted as the weak feature of the Bayesian framework. We assume prior PDF for each model parameter z to have separate uniform distribution over the interval $Z = [z_{min}, z_{max}]$. The prior PDF then reads

$$p(z) = \begin{cases} \frac{1}{z_{max} - z_{min}} & \text{if } z \in Z \\ 0 & \text{otherwise.} \end{cases} \quad (4.41)$$

In such formulation of prior PDF the only subjective information are range limits z_{min} and z_{max} . The ranges of the uniform prior PDFs considered in the mainshock inversion are shown in Table 4.3. The prior PDFs of hypocenter, origin time and rake angle are assumed to have uniform distribution centered in the initial values z_0 as listed in Table 4.2. To complete, we assume homogenous prior PDF of the slip spline control point locations over the whole fault plane of length X and width Y . The prior PDF of occurrence of any spline point on the fault then reads

$$p(z) = \frac{1}{XY}, \quad \text{where } z \in \Sigma. \quad (4.42)$$

Model parameter z	Low limit z_{min}	High limit z_{max}
Rupture velocity	1500 m/s	5000 m/s
Rise time	2.0 s	6.5 s
Peak time	0.8 s	2.4 s
Origin time*	$z_0 - 1.0 s$	$z_0 + 1.0 s$
Hypocenter (along strike distance)*	$z_0 - 6000 m$	$z_0 + 6000 m$
Hypocenter (along dip distance)*	$z_0 - 6000 m$	$z_0 + 6000 m$
Rake angle*	$z_0 - 45^\circ$	$z_0 + 45^\circ$

Note: *prior PDFs defined around the initial model parameters z_0 from Table 4.2.

Table 4.3: Range limits z_{min} and z_{max} of homogenous prior PDFs for various model parameters as utilized in the $M_{JMA} 7.3$ mainshock inversion.

Processing steps

The posterior PDF of source model parameters is sampled by the trans-D MCMC algorithm with PT as described in Section 4.2.3. The sampling strategy consists of the following processing steps:

1. Pre-compute GFs and ACF covariance matrices. Then, compute standardized waveforms (\mathbf{d}_{obs}^*) and standardized GFs ($\hat{\mathbf{G}}^*$ and $\check{\mathbf{G}}^*$). This step has big impact on the efficiency of the method as the standardized GFs do not require to be re-computed in each Markov chain step.
2. Create 30 initial source models per each CPU. These initial source models are random, yet model parameters are confined by their assumed prior ranges. The slip distribution is initiated by one spline point ($N_{\Phi} = 1$) randomly generated on each fault segment. These initial models are initial states of the Markov chains of the PT algorithm. One “sampling” chain per CPU has temperature $\gamma = 1$, while the other “exploration” chains have assigned random temperatures $\gamma > 1$ as described in Section 1.2.2 (e.g., Sambridge 2014).
3. Start the “burning” phase of PT on all the deployed CPUs. In this phase, various models are explored by the Markov chains, but the model samples are excluded from the ensemble of solutions (i.e. no model is saved). The “burning” phase takes approximately 3k chain steps in our case.
4. Start the “production” phase, providing model samples drawn from the posterior PDF. The samples are recorded by the “sampling” chains with temperature $\gamma = 1$. This phase lasts as many chain steps as necessary to create a sufficiently large ensemble of solutions. We performed approximately 24k chain steps on deployed 24 CPUs in total, which took 48 hours on the IT4I Salomon supercomputing cluster, i.e. 1152 CPU hours. The produced samples then compose an ensemble of more than 590k possible finite source models following the posterior PDF.
5. Process statistically the ensemble of solutions to find the maximum likelihood solution and inspect uncertainties of the model parameters.

4.3.3 Solution of the fault slip inversion

The maximum likelihood solution

The maximum likelihood solution for the $M_{JMA}7.3$ mainshock fault slip inversion is shown in Figs 4.4 and 4.5. The inferred source model has seismic moment of $6.74 \times 10^{19} Nm$ ($M_w = 7.2$). The maximum and average slip values are 6.29 and 1.29 m , respectively. The variance reduction is 78.5%, which indicates good fit of observed and synthetic standardized waveforms (Fig. 4.7).

In Fig. 4.4 we show inferred SRFs for all subfaults on both the Hinagu (#1) and the Futagawa (#2) fault segments. The slip values with denoted rake angles (slip direction) are illustrated for all the subfaults in Figs 4.5a and 4.5b. In Figs 4.5c and 4.5d we show rupture times on the both the fault segments.

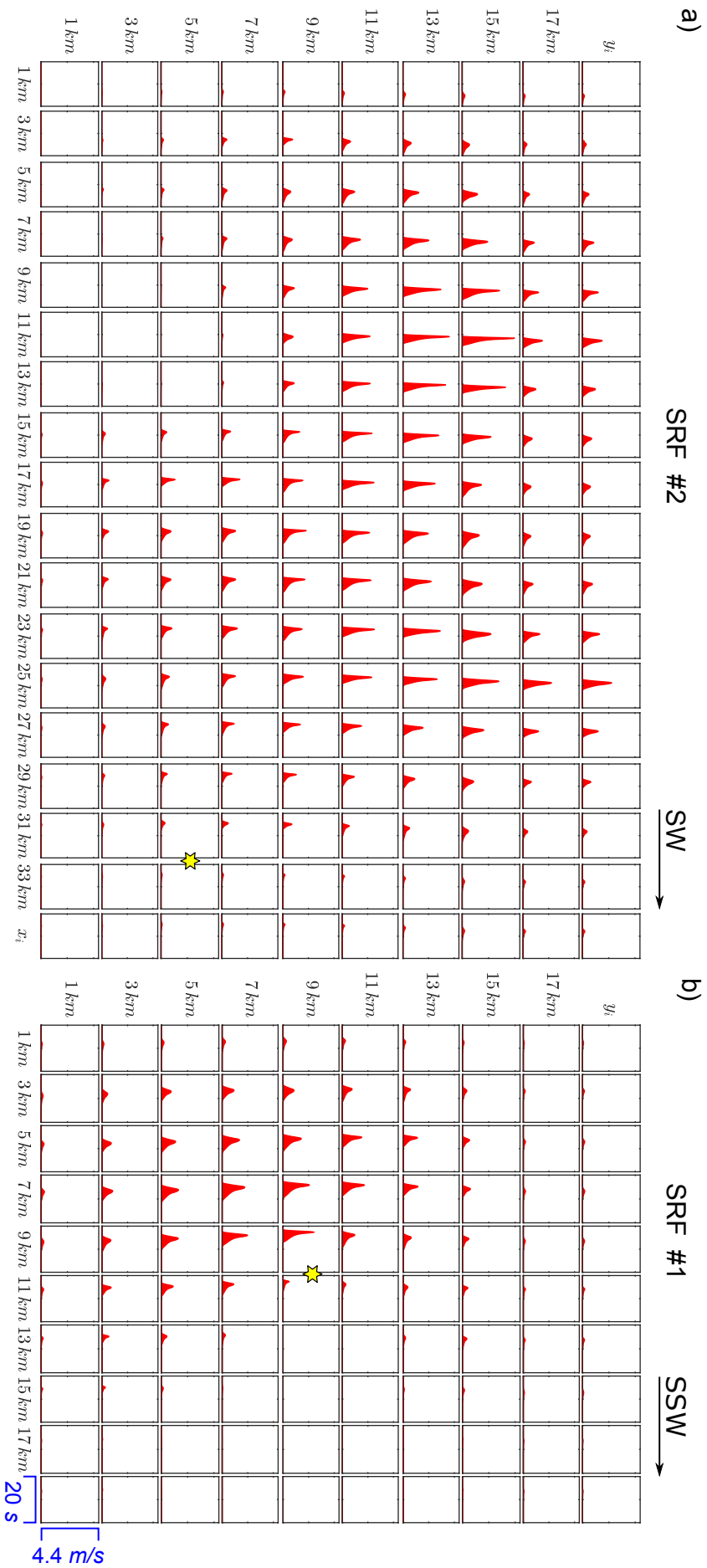


Figure 4.4: SRFs of the maximum likelihood solution of the $M_{jMA7.3}$ mainshock inversion on the **a)** Futagawa (#2) and **b)** Hinagu (#1) fault segments. Separate subfaults are spatially distributed along the strike x and along dip y directions, where $(0, 0) \in \Sigma$ is the bottom-left corner of the fault footwall. Red functions are the inferred SRFs in the time window $0 - 20$ sec after the mainshock origin time. The axis of the SRFs span the range of $0 - 4.4$ m/s. The yellow stars denote the inferred position of hypocenters on their respective fault segments.

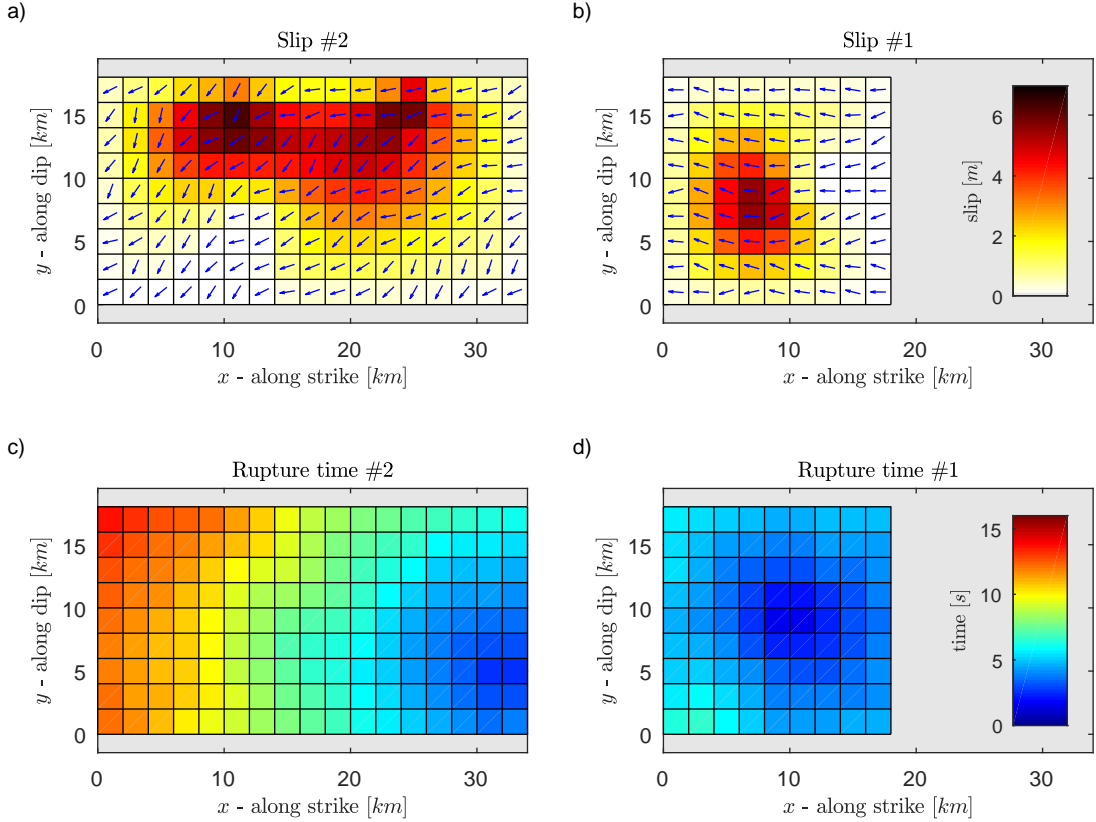


Figure 4.5: Slip **a, b)** and rupture times **c, d)** of the maximum likelihood solution of the MJMA 7.3 mainshock inversion on the **a, c)** Futagawa (#2) and **b, d)** Hinagu (#1) fault segments. The squares represent 2×2 km subfaults spatially distributed along strike x and along dip y directions, where $(0, 0)$ is the bottom-left corner of the fault footwall. The final slip values and the rupture times are shown by color (see colorbars). The rake angles (slip directions) are shown by blue arrows.

The maximum likelihood solution has hypocenter located at the Hinagu segment (#1) at the depth of 9 km (yellow star in Fig. 4.4b). The rupture propagates by the average rupture velocity of 2.5 km/s along segment #1, terminating at the intersection of the both fault segments. A large slip on fault segment #1 is concentrated in the zone between the hypocenter and intersection with the fault segment #2 at the depth of approximately $6 - 14$ km. The inferred origin time in the Futagawa segment (#2) is delayed by 1.2 sec after the origin in segment #1. The hypocenter on segment #2 is located approximately at depth of 13 km at the intersection of the fault segments (yellow star in Fig. 4.4a). The rupture then continuous upward and to NE along segment #2 by the average rupture velocity of 2.7 km/s (see Fig. 4.5c). The largest slip on fault segment #2 is concentrated at shallower parts at depths of approximately $1 - 8$ km. The rupture terminates at the shallow depths inside the Aso volcano caldera. The inferred rake angles in the segment #1 are close to pure right-lateral strike-slip movement. Contrarily, the slip directions on segment #2 have significant normal-slip component.

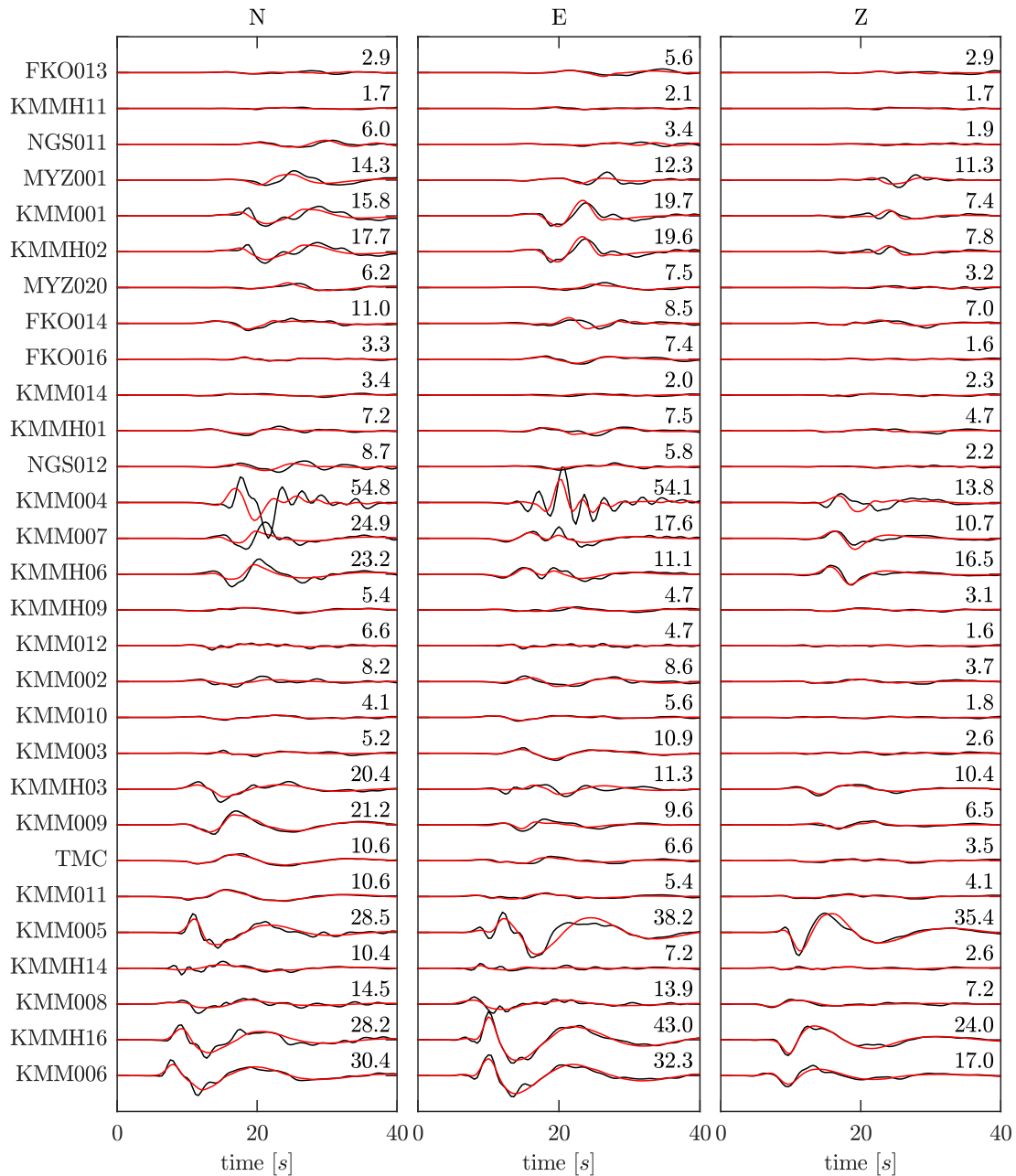


Figure 4.6: The fit of observed (black) and synthetic (red) **displacement waveforms** for the *M_{JMA}7.3* mainshock (16 April 2016). The synthetics correspond to the maximum likelihood solution inferred considering the ACF covariance matrix. Stations are sorted by epicentral distance. Data are corrected by instrument response and both data and synthetics are bandpass Butterworth filtered between 0.05 – 0.5 Hz. The displacement waveforms are normalized to the largest value of all stations and components. The values shown next to the waveforms denote their maximum displacements in cm. Note that these maximum absolute displacements are measured on the filtered and integrated data, and hence do not include static displacements which were significant (almost 200 cm) for stations close to the activated fault.

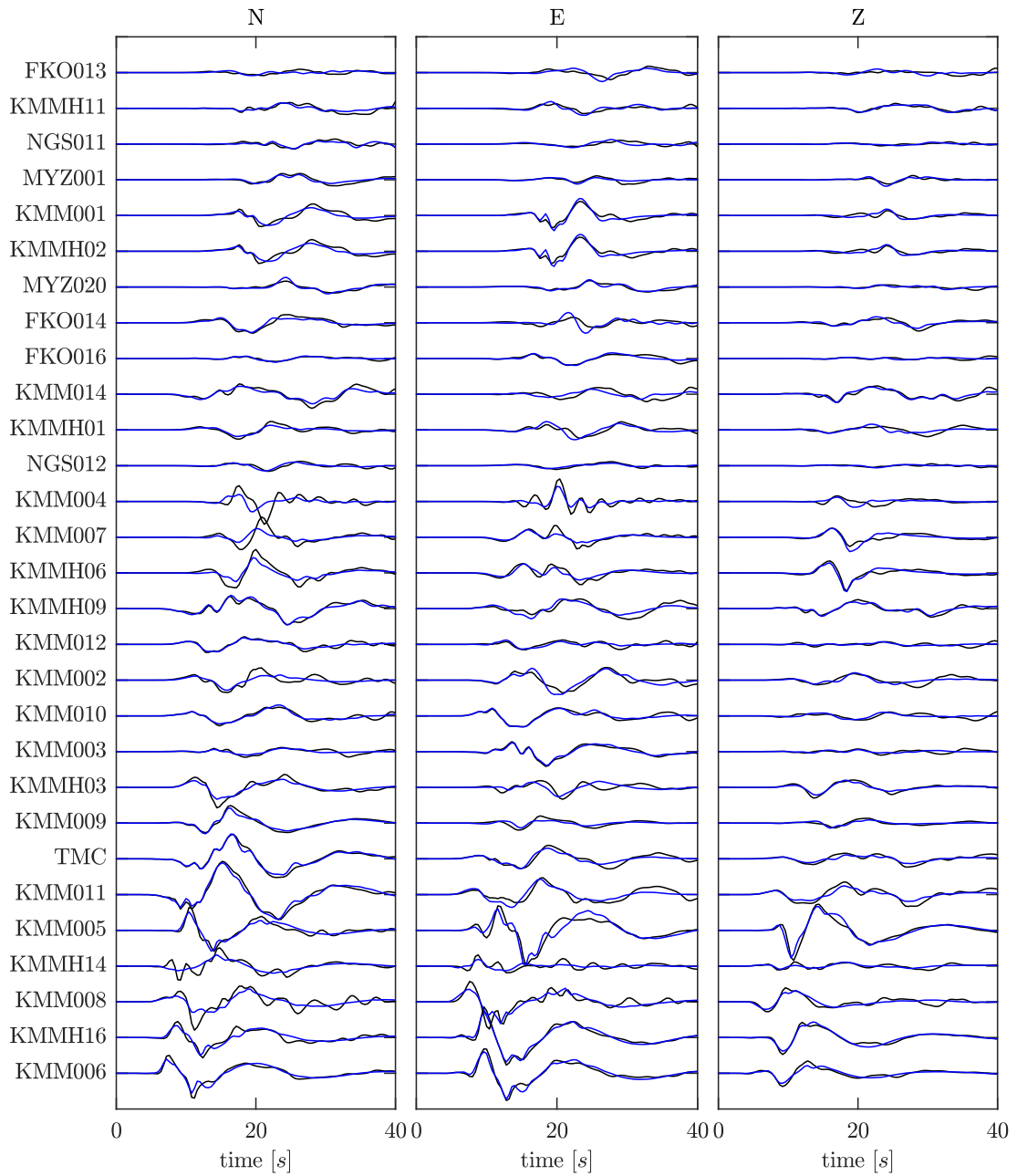


Figure 4.7: The fit of the *standardized* data (black) and synthetics (blue) for the $M_{JMA}7.3$ mainshock (16 April 2016). The standardized synthetics correspond to the maximum likelihood solution inferred considering the ACF covariance matrix. Stations are sorted by epicentral distance. Data are corrected by instrument response and both data and synthetics are bandpass Butterworth filtered between 0.05 – 0.5 Hz prior the standardization by triangular matrix from the Cholesky decomposition of the ACF covariance matrix. The standardized waveforms are normalized to the largest value of all stations and components.

The maximum likelihood solution of our Bayesian inversion minimizes the difference between the recorded data and synthetics. Since the ACF covariance matrix is deployed the solution minimizes the standardized residuals, i.e. waveforms multiplied by the triangular matrix from the Cholesky decomposition of the ACF covariance matrix (see Section 4.2.3). In Figs 4.6 and 4.7 we show displacement and standardized waveform fits, respectively, for the maximum likelihood solution. Note that the fit of the displacement waveforms (Fig. 4.6) is shown for illustration purpose as the inversion itself minimizes the difference between the standardized waveforms shown in Fig. 4.7.

Waveforms in Figs 4.6 and 4.7 can be used for inspection of the effects of the ACF covariance matrix in the inversion. The standardized waveforms tend to have equalized spectral content with amplified low-frequency part of the spectrum as described in Section 2.3.4. For example, the standardized waveforms of station KMM004 (located inside the Aso caldera) have the high-frequency content suppressed. At the same time the stations in intermediate distances have amplified the low-frequency part of the spectrum, which increases their weight in the inversion. Generally, the overall fits are very good for the both displacement and standardized displacement waveforms. The variance reduction of the standardized displacement waveforms shown in Fig. 4.7 is 78.5 %.

Ensemble of source models - uncertainty estimate

The maximum likelihood solution is not a unique solution, it is rather one of many possible source models that fit the data well. The ensemble of the total of 590 264 possible finite fault source models allows statistical evaluation of the inferred source parameters and an assessment of the model uncertainty.

Fig. 4.8a shows histogram of the variance reduction of the standardized waveforms from the complete ensemble of the possible source models. It spans the range of 74 – 78.5 %, which means that all the models fit the observed data well. Therefore, we should look critically on the maximum likelihood solution as merely a single representation of the plausible source models. To complete, we show histograms for inferred seismic moment M_0 and moment magnitude M_w in Figs 4.8b and 4.8c, respectively.

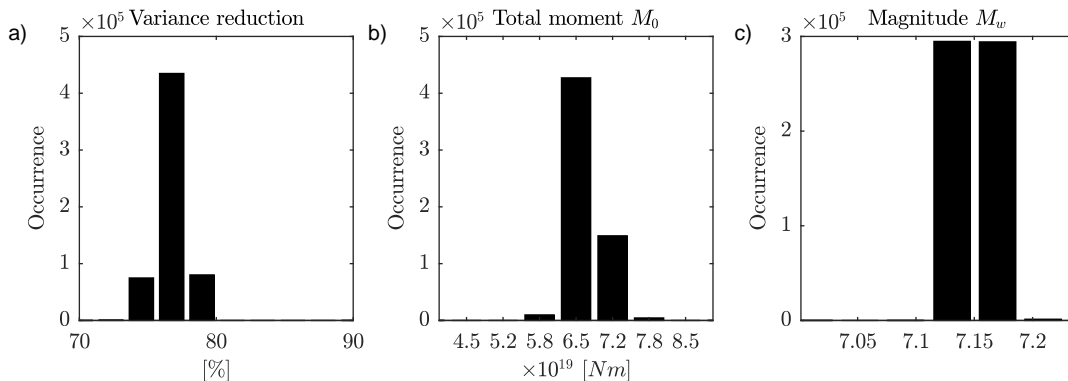


Figure 4.8: Ensemble statistics for the $M_{JMA} 7.3$ mainshock inversion. Histograms show occurrences of **a)** variance reduction, **b)** total seismic moment M_0 , and **c)** moment magnitude M_w .

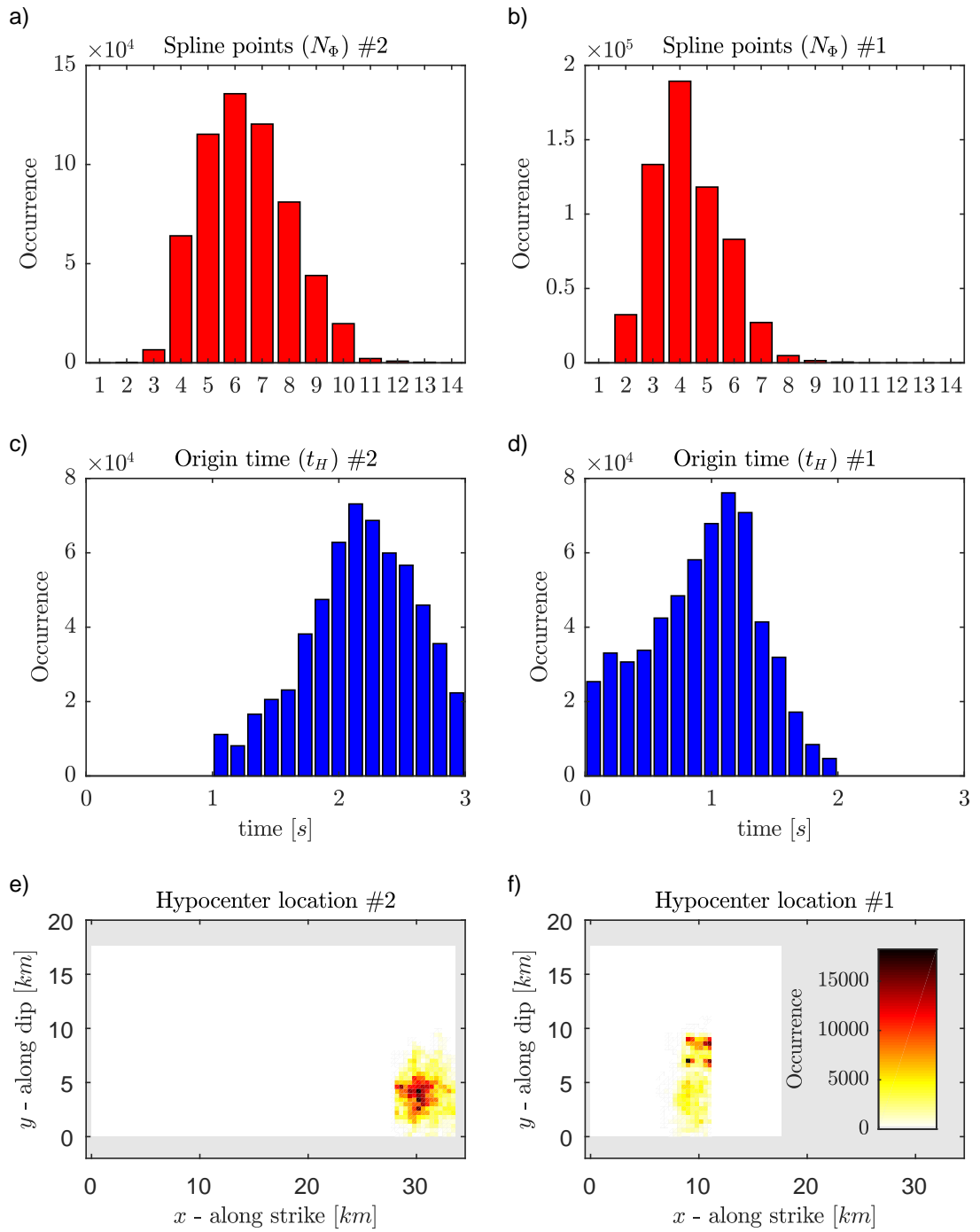


Figure 4.9: Ensemble statistics for the $M_{JMA} 7.3$ mainshock inversion. The statistics are shown for the Hinagu (#1) and Futagawa (#2) fault segments separately. **a)** and **b)** are histograms of the number of slip spline control points, **c)** and **d)** show the scatter of the hypocenter origin times (relatively to the mainshock JMA origin time in Table 4.2), and **e)** and **f)** show spatial scatter of the hypocenter locations on the fault segments.

Let us now inspect features of the finite source models on the Hinagu (#1) and Futagawa (#2) fault segments. The slip distribution is controlled by the spline control points, where their increasing number increases the possible spatial complexity of the resolved slip. On the other hand, the number of spline points is penalized by the birth-death probabilities of the trans-D MCMC sampler (see Section 4.2.3). The statistics of the number of slip spline control points of the inferred source models are shown in Fig. 4.9 (panels a and b).

The statistic from the inferred hypocenter origin times and locations on segments #1 and #2 are shown in Fig. 4.9 (panels c-f). The statistics show that the origin times have scatter of about ± 1 sec. It may be explained by possible trade-offs among rupture velocity, rise times and/or peak times. Nevertheless, the hypocenter locations are well resolved on both the fault segments, where the uncertainty is higher in the along dip direction (especially for segment #1).

To show statistics of the slip distribution we introduce a modified polar histogram plot called slip disc histogram (SDH). It shows the occurrence of the slip values on individual subfaults as captured by the ensemble of all the finite model solutions. An example of SDH is shown in Fig. 4.10, which may serve as a legend for the full SDH plot of the mainshock inversion in Fig 4.11. The radial coordinate of SDH has the meaning of inferred slip value on the subfault, which spans from zero up to 7.5 m. The angular coordinate has no meaning, and hence SDH is radially symmetric. The radial coordinate of SDH is divided into several slip value histogram bins, so that the SDH is composed of several concentric hoops (with meaning of the histogram bins). If the occurrence of the slip value exceeds in any bin the threshold of 10%, then the hoop is colored by red color. The red disc composed of the colored hoops then shows, by its inner and outer edge, the range of possible slip values as captured by the whole ensemble of solutions. The width of the SDH disc shows the estimate of the slip value uncertainty. Wider disc represents wider histogram of the slip value occurrence with meaning of higher uncertainty of the slip. If the center of the SDH is filled, the plausible slip values from the inversion include also zero slip.

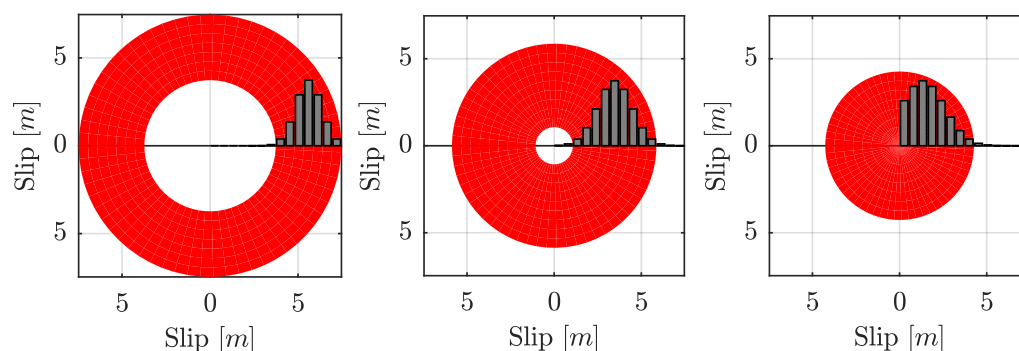


Figure 4.10: Example of slip disc histogram (SDH) plot which may serve as the legend for the full SDH plot of the $M_{JMA}7.3$ mainshock inversion in Fig 4.11. The gray histograms indicate a source statistical data, which are displayed by the SDH plot as the red discs. For further explanation see the text.

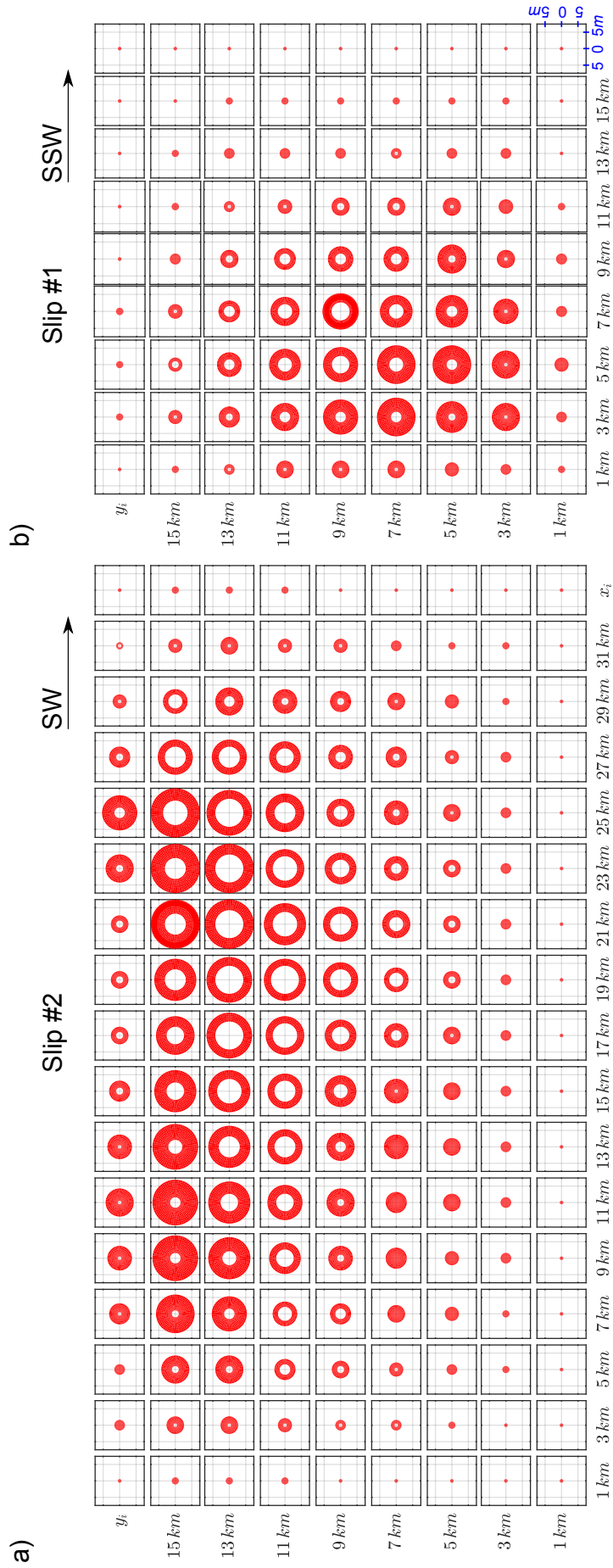


Figure 4.11: The slip disc histogram (SDH) plot of the solution ensemble from the MJMA 7.3 mainshock inversion. The SDH plots are shown for the **a)** Futagawa (#2) and **b)** Himagu (#1) fault segments. SDHs for the individual subfaults are spatially distributed along strike x and along dip y directions, where $(0, 0) \in \Sigma$ is the bottom-left corner of the fault footwall. For the explanation of the SDHs see Fig. 4.10 and the text.

The SDH plot for the ensemble of solutions of the $M_{JMA}7.3$ mainshock inversion is shown in Fig 4.11. The large slip on fault segment #1 (Fig. 4.11b) at the depths of approximately $6 - 14 \text{ km}$ exhibits high uncertainty, especially in the deepest part. The slip value in this zone can be smaller than suggested by the maximum likelihood solution, i.e. the maximum slip is in the range of $2.6 - 5.7 \text{ m}$. On the other hand, the low slip value in the southernmost part of segment #1 is a feature supported by the whole ensemble. The SDH plot for segment #2 in Fig. 4.11a suggests that the maximum slip is in the range of $4.2 - 7.5 \text{ m}$. The slip value is well resolved in the southwestern part, while it has large uncertainty in the shallow northeastern zone, i.e. in the Aso volcano caldera.

The parameters rise time, peak time and rake angle vary significantly at the subfaults of the inferred models due to their spatial trade-offs. Hence, we present only the statistical evaluation of their spatially weighted arithmetic means. The weights are represented by the spatial distribution of the slip values. In such spatially weighted averages the variability at the individual subfaults with relatively low influence on the synthetic waveforms is suppressed. Histograms of these spatially weighted averages of rise times, peak times and rake angles for the Hinagu (#1) and Futagawa (#2) fault segments are shown in Fig. 4.12. The statistics reveals that segment #1 has average rise time $4.2 - 5.8 \text{ sec}$, average peak time $1.5 - 1.9 \text{ sec}$ and average rake angle $-145^\circ \pm 10^\circ$. Segment #2 has then average rise time $3.6 - 5.2 \text{ sec}$, average peak time $1.3 - 1.7 \text{ sec}$ and average rake angle $-180^\circ \pm 10^\circ$. This highlights the significance of the inferred pure right-lateral strike-slip movement on segment #1 and significant normal-slip component on segment #2 as observed also in the maximum likelihood solution.

To complete, Fig. 4.13 shows histograms of spatially weighted averages of rupture velocities for the Hinagu (#1) and Futagawa (#2) fault segments. The statistics reveals that segment #1 has average rupture velocity in the range of $2.2 - 3.6 \text{ km/s}$, while segment #2 has it in the range of $2.2 - 3.2 \text{ km/s}$. Note that these rupture front velocities suggest the sub-shear rupture propagation pattern.

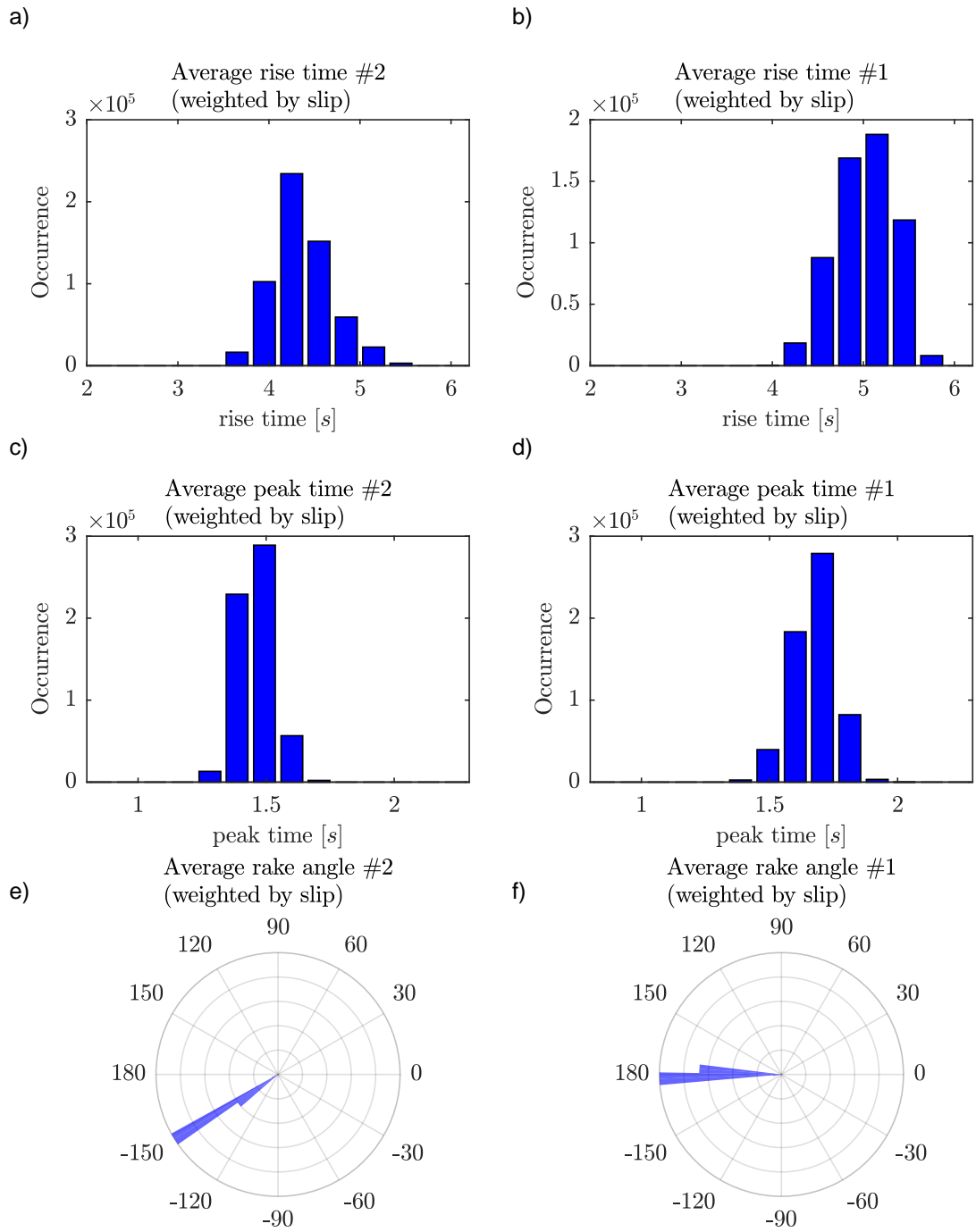


Figure 4.12: Ensemble statistics for the $M_{JMA}7.3$ mainshock inversion, showing histograms of weighted averages of rise times (a, b), peak times (c, d), and rake angles (e, f). These statistics are created from spatially weighted averages for the Hinagu (#1) and Futagawa (#2) fault segments. The weights are given by the spatial distribution of the slip values.

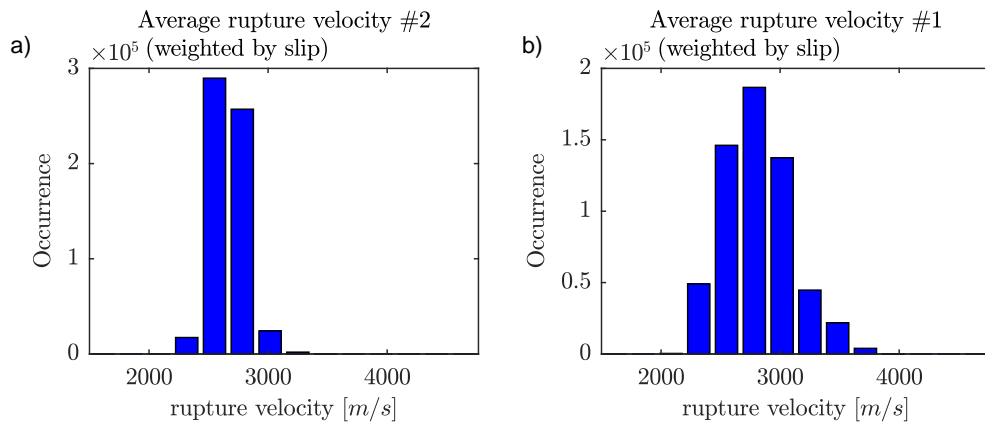


Figure 4.13: Ensemble statistics for the $M_{JMA7.3}$ mainshock inversion. These histograms are created from spatially weighted averages of rupture front velocities for the **a)** Futagawa (#2) and **b)** Hinagu (#1) fault segments. The weights are given by the spatial distribution of the slip values.

4.4 Discussion and Conclusions

We have developed and applied a kinematic Bayesian non-linear finite fault slip inversion method, which accounts for uncertainty of Greens' functions by means of the approximate covariance functions introduced by Hallo & Gallovič (2016). This inversion is applied to the $M_{JMA}7.3$ mainshock of the 2016 Kumamoto, Japan, earthquake sequence of April 16th, 2016 (01:25 of JST). The resultant ensemble of the 590 264 plausible finite fault source models with the variance reduction in the range of 74 – 78.5% allows to perform an assessment of the source model uncertainty.

Major characteristics of our solutions are in accord with previous studies (e.g., Asano & Iwata 2016; Kubo et al. 2016b; Yoshida et al. 2017; Himematsu & Furuya 2016). The mainshock rupture process started on the Hinagu fault segment (#1) as a right-lateral pure strike-slip movement. The rupture propagated by the average rupture velocity of 2.2 – 3.6 km/s along the Hinagu fault reaching the intersection of the Hinagu and Futagawa fault segments. The rupture origin at the Futagawa fault segment (#2) was located at the intersection of both faults at the depth of approximately 11 – 16 km. Then the rupture extended upward and to NE along the Futagawa fault segment by the average rupture velocity of 2.2 – 3.2 km/s as a strike-slip with a normal faulting component. The largest slip of 4.2 – 7.5 m took place on the Futagawa fault segment approximately 9 sec after the mainshock origin time. Duration of the whole rupture processes was in the range of 16 – 19 sec.

The inferred scalar seismic moment of the mainshock is in the range of 5.5 – 8.0 × 10¹⁹ Nm. This value is larger than obtained by Asano & Iwata (2016), i.e. 4.50 × 10¹⁹ Nm (M_w 7.0), or by Yoshida et al. (2017), i.e. 4.70 × 10¹⁹ Nm (M_w 7.1). Nevertheless, the lower limit of our estimate agrees with the scalar seismic moment obtained by Kubo et al. (2016b), i.e. 5.50 × 10¹⁹ Nm (M_w 7.1). The rather larger seismic moment of our solution may be caused by the larger fault plane assumed in the inversion. Note that Yoshida et al. (2017) obtained seismic moment 6.7 × 10¹⁹ Nm (M_w 7.2) prior trimming the fault plane, which is similar to the value obtained by our maximum likelihood solution.

Ensemble statistics show that the pure right-lateral strike-slip movement in the Hinagu fault segment and the strike-slip with significant normal-slip component in the Futagawa fault segment are the well resolved features. Indeed such slip directions are present in other authors' solutions by Asano & Iwata (2016), Kubo et al. (2016b), and Yoshida et al. (2017)). The so-called slip disc histogram (SDH) plot representing the uncertainty of the final slip in Fig. 4.11 shows that:

- The southernmost area of Hinagu fault segment (#1) is characterized by low slip values as inferred also by the other studies.
- There is high uncertainty in the large slip zone on the Hinagu fault segment (#1). This is in accord with the variability of solutions of the other authors. Indeed, Asano & Iwata (2016) located this zone at shallow depth, while models by Kubo et al. (2016b) and Yoshida et al. (2017) have this zone less pronounced and at slightly different position both along dip and along strike.
- The large slip in the southwest and in the central part of the Futagawa

fault segment (#2), inferred with rather low uncertainties in our inversion, can be considered as well resolved feature, being also consistently imaged by the other studies.

- The slip at shallow depth inside the Aso caldera, i.e. northeast on the Futagawa fault segment (#2), is considered as an uncertain feature as shown by the SDH plot. Indeed, Asano & Iwata (2016) and Yoshida et al. (2017) inferred only insignificant slip, while Kubo et al. (2016b) inferred slip value $> 2 m$ for this shallow zone.

Finally, we emphasize that this is the first application of the developed inversion method. It may require more thorough long-term testing in order to be routinely used. Nevertheless, the acquired results have already a significance in terms of the evaluation of the finite source models quality as demonstrated on the $M_{JMA}7.3$ mainshock of the 2016 Kumamoto earthquake sequence. The ensemble statistics in comparison with the other authors' solutions point on the well or poorly resolved features of the mainshock model. The inferred source model of the mainshock supplemented by its uncertainty completes the analysis of the evolution of the Kumamoto sequence in the seismotectonic framework described in Section 3.5.1.

4.5 Supplementary material

4.5.1 Regularized Yoffe function

The regularized Yoffe function $\Upsilon(t; \tau_R, \tau_P)$ has been introduced by Tinti et al. (2005) as a parametric SRF useful for non-linear earthquake source inversions. The function is defined as convolution of Yoffe function (Yoffe 1951) and a triangle of duration τ_S (i.e. temporal smoothing of the Yoffe function). Following Tinti et al. (2005) τ_S can be approximately linearly related to the duration of positive slip acceleration τ_P of SRF as

$$\tau_S \approx \frac{\tau_P}{1.27}. \quad (4.43)$$

Further, rise time τ_R of the regularized Yoffe function reads

$$\tau_R = \tau_Y + 2\tau_S, \quad (4.44)$$

where τ_Y is rise time of the Yoffe function (Yoffe 1951). Longer effective duration of the regularized Yoffe function results from the temporal smoothing by the triangle function of duration τ_S . The regularized Yoffe function is then parametrized by two parameters τ_R and τ_P , and it is analytically expressed (Tinti et al. 2005) as follows:

$$\Upsilon(t; \tau_Y, \tau_S) = \frac{2}{\pi\tau_Y\tau_S^2} \cdot \begin{cases} 0 & \text{for } t < 0 \\ (C1 + C2) & \text{for } 0 \leq t < \tau_S \\ (C1 - C2 + C3) & \text{for } \tau_S \leq t < 2\tau_S \\ (C1 + C3 + C4) & \text{for } 2\tau_S \leq t < \tau_Y \\ (C3 + C4 + C5) & \text{for } \tau_Y \leq t < \tau_Y + \tau_S \\ (C4 + C6) & \text{for } \tau_Y + \tau_S \leq t < \tau_Y + 2\tau_S \\ 0 & \text{for } \tau_Y + 2\tau_S \leq t \end{cases} \quad (4.45)$$

where

$$C1 = \left(\frac{t}{2} + \frac{\tau_Y}{4}\right) \sqrt{t(\tau_Y - t)} + (t\tau_Y - \tau_Y^2) \cdot \arcsin \sqrt{\frac{t}{\tau_Y}} - \frac{3}{4}\tau_Y^2 \cdot \arctan \sqrt{\frac{\tau_Y - t}{t}} \quad (4.46)$$

$$C2 = \frac{3}{8}\pi\tau_Y^2 \quad (4.47)$$

$$C3 = \left(\tau_S - t - \frac{\tau_Y}{2}\right) \sqrt{(t - \tau_S)(\tau_Y - t + \tau_S)} + \tau_Y(2\tau_Y - 2t + 2\tau_S) \cdot \arcsin \sqrt{\frac{t - \tau_S}{\tau_Y}} + \frac{3}{2}\tau_Y^2 \cdot \arctan \sqrt{\frac{\tau_Y - t + \tau_S}{t - \tau_S}} \quad (4.48)$$

$$C4 = \left(-\tau_S + \frac{t}{2} + \frac{\tau_Y}{4}\right) \sqrt{(t - 2\tau_S)(\tau_Y - t + 2\tau_S)} - \tau_Y(\tau_Y - t + 2\tau_S) \cdot \arcsin \sqrt{\frac{t - 2\tau_S}{\tau_Y}} - \frac{3}{4}\tau_Y^2 \cdot \arctan \sqrt{\frac{\tau_Y - t + 2\tau_S}{t - 2\tau_S}} \quad (4.49)$$

$$C5 = \frac{\pi}{2} \tau_Y (t - \tau_Y) \quad (4.50)$$

$$C6 = \frac{\pi}{2} \tau_Y (2\tau_S - t + \tau_Y). \quad (4.51)$$

Note that $C4$ in Eq. (4.49) is corrected following Bizzarri (2012), as there is a typographic error in corresponding equation in Tinti et al. (2005).

Bizzarri (2012) shows that the regularized Yoffe function appropriately describes the shape of SRFs for sub-shear ruptures. This function is especially advantageous for pulse-like ruptures, however Bizzarri (2012) concludes that it may also capture features of crack-like ruptures. Its versatility is demonstrated in Fig. 4.14. In examples in Fig. 4.14a τ_P is fixed while τ_R varies. It leads to frequency shifts of the source spectra with reciprocal of τ_R (Fig. 4.14c). In Fig. 4.14b τ_R is fixed while τ_P varies, resulting in a change in the amplitude spectra fall off (Fig. 4.14d). Note that kinematic parameters of the regularized Yoffe function can be related to dynamic rupture parameters (e.g., Tinti et al. 2005; Bizzarri 2012).

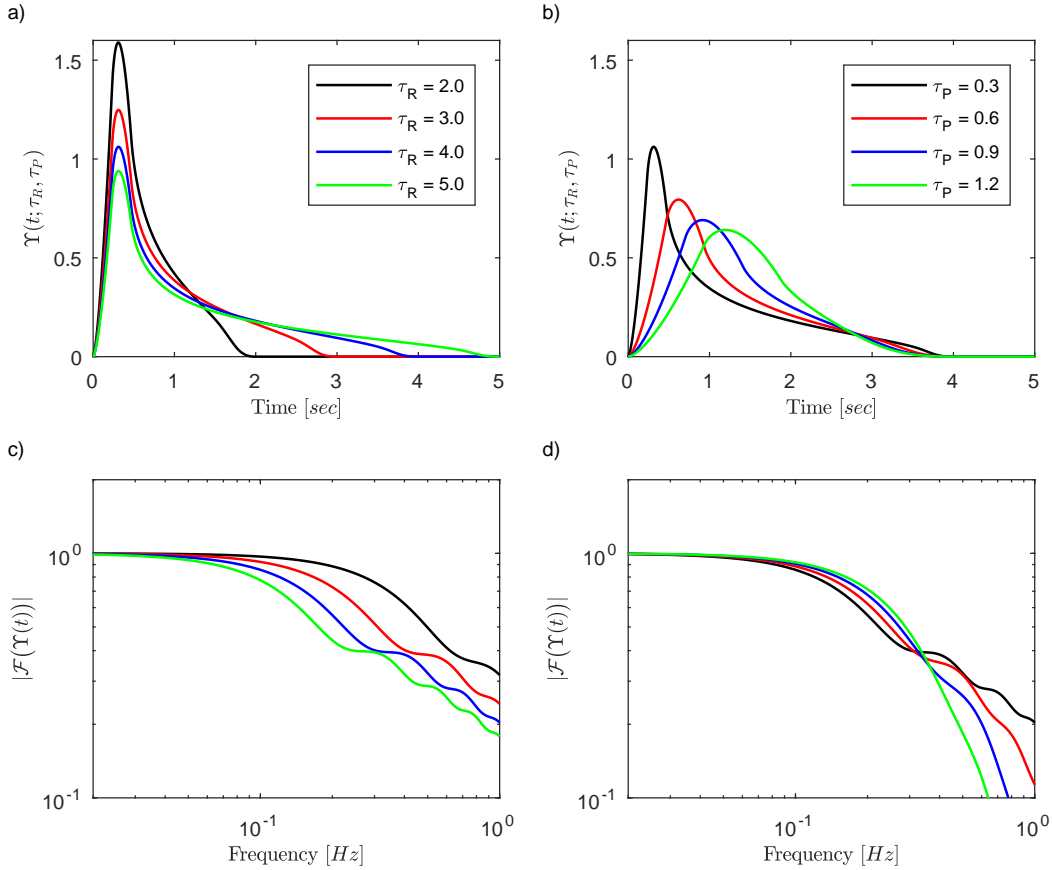


Figure 4.14: Regularized Yoffe functions $\Upsilon(t; \tau_R, \tau_P)$ for various combinations of rise time τ_R [sec] and peak time τ_P [sec]. Examples are shown for **a)** fixed peak time $\tau_P = 0.3$ [sec], and **b)** fixed rise time $\tau_R = 4.0$ [sec]. For the variable parameter see legend. **c)** and **d)** show Fourier amplitude spectra of the functions in **a** and **b**, respectively.

Conclusion

This research is focused on the influence of crustal velocity model uncertainty on inferred earthquake source parameters. Chapter 1 overviews the fundamental theoretical background and probabilistic techniques as used in this Thesis. It is followed in Chapter 2 by introducing a simple approach to efficiently involve the uncertainty of a crustal velocity model in earthquake source inversions. Such approach is applied in Chapter 3 on the Bayesian full-waveform centroid moment tensor inversion of foreshocks and aftershocks of the 2016 Kumamoto, Japan, earthquake sequence. Finally, in Chapter 4, we propose new Bayesian parametric fault slip inversion which accounts for velocity model’s uncertainty. The fault slip inversion method is applied on the mainshock of the 2016 Kumamoto sequence.

In particular, in Chapter 2 (also published as Hallo & Gallovič 2016), we perform Monte-Carlo simulations of GFs in randomly perturbed velocity models to reveal the effects of the imprecise velocity model on the synthetic waveforms. Based on the learned knowledge, we derive closed-form formulas for approximate covariance functions to obtain fast and effective characterization of the GFs’ uncertainty (see AXCF in (2.13); ACF in (2.14); SAXCF in (2.20); and SACF in (2.21)). These approximate covariance functions require a GF calculated using a given (mean) velocity model and statistical description of the assumed random time shifts of the signal as an input. Experiments indicate that it is enough to assume a uniform PDF for the time shifts of GFs. The width of the uniform PDF denoted as L_1 depends on the source distance and velocity model perturbations linearly, and can be implemented by a simple formula (Eq. (2.31)). Alternatively, the parameter L_1 may be estimated by ray tracing, as shown in supplementary Section 2.5.1. Further, we point out that despite the fact that the simplified formulas were derived assuming purely random time shifts of GFs, the proposed approach produces variations of both the arrival time and the waveform amplitudes as shown in Fig. 2.5.

The proposed approximate covariance functions are tested on Bayesian moment tensor inversions of synthetic and real data sets (Section 2.3). Experiments with the large number of synthetic target datasets obtained by randomly perturbing velocity models reveal that the lowest scatter of the maximum likelihood solutions is attained for the approximate covariance function (ACF and AXCF). Tests also show that the posterior covariance matrix of model parameters reflects the true uncertainty of the MT solution well when considering the stationarized auto-covariance function (SACF), see Fig. 2.13c. Similarly, real-data inversion using the SACF (Fig. 2.14c) provides MT uncertainty estimate comparable to the result of the jack-knifing experiment by Sokos & Zahradník (2013, fig. 3). Finally, additional synthetic tests imply that using SACF in Bayesian inversion allows reliable assessment of the CLVD component uncertainty (supplementary Section 2.5.2). For easier implementation in other researchers’ codes we release open source codes for computing all the types of the proposed ACFs and SACFs. The source codes in “Fortran90” and “Matlab” programming languages are available under GNU license on the author’s website (<http://geo.mff.cuni.cz/~hallo/>) or in Attachments A.1, A.2, A.3 and A.4.

We have extended the Bayesian full-waveform CMT inversion code package ISOLA-ObsPy (Vackář et al. 2017) with the source code for assessment of GFs' uncertainties by ACFs and SACFs. The modified ISOLA-ObsPy is successfully applied on selected earthquakes from the Kumamoto, Kyushu, Japan, earthquake sequence of April 2016 with M_{JMA} magnitude in range of 4.8–6.5 (Chapter 3 also published as Hallo et al. 2017). The use of SACF covariance matrices in the Bayesian inversion allow us to perform realistic assessment of the uncertainties of the CMTs (Table 3.2 and Fig. 3.6). The inferred CMT solutions show systematic spatial and temporal variations (Fig. 3.8). We estimate geometry of the major activated ruptures and interpret them in the seismotectonic framework (Section 3.5). Foreshocks imply right-lateral NE–SW strike-slip movements in the Hinagu fault zone. Aftershocks are mostly normal dip-slip events spreading along the NW edge of the assumed mainshock fault plane (see Fig. 3.10). The inferred CMTs with significant CLVD component may suggest a complex source processes, however this issue is still open because of non-uniqueness of the non-DC MTs' decomposition. Therefore, the realistic assessment of the uncertainties of the inferred CMTs proved to be useful in terms of interpretation.

In Chapter 4 we develop a new Bayesian non-linear fault slip inversion which accounts for the GFs' uncertainty by means of the approximate covariance functions (ACF and SACF). The utilized self-adapting parametrization of slip function (by varying number of unattached spline control points) captures features of the slip functions discernible by the observed waveforms.

The Bayesian fault slip inversion is applied in Section 4.3 on the destructive $M_{JMA}7.3$ mainshock of the 2016 Kumamoto, Japan, earthquake sequence of April 16th, 2016 (01:25 of JST). According to our solution the mainshock started on the Hinagu fault segment as right-lateral pure strike-slip movement. The rupture propagated along the Hinagu fault reaching the intersection of the Hinagu and Futagawa fault segments. Then, the rupture extended upward and to NE along the Futagawa fault segment as a strike-slip with a normal faulting component. The largest slip of 4.2–7.5 m took place on the Futagawa fault segment. Statistics from the ensemble of possible solutions then show that the above features are well constrained, being also consistent with other researchers' models (e.g., Asano & Iwata 2016; Kubo et al. 2016b; Yoshida et al. 2017; Himematsu & Furuya 2016). Contrarily, the uncertainty analysis reveals that the zone of the largest slip on the Hinagu fault segment and the slip at the shallow depth inside the Aso caldera are less constrained. The latter is in agreement with the fact that these features are not consistently imaged in the other published source models. The inferred source model of the mainshock supplemented by its uncertainty completes the analysis of the evolution of the Kumamoto sequence in the seismotectonic framework described in Section 3.5.1.

Bibliography

- Aki, K. & Richards, P. G., 2002. *Quantitative seismology, 2nd Ed.*, University Science Books, Sausalito.
- Anderson, E. M., 1951. *The Dynamics of Faulting and Dyke Formation With Applications to Britain*, Oliver and Boyd, Edinburgh.
- Angelier, J., 2002. Inversion of earthquake focal mechanisms to obtain the seismotectonic stress IV—a new method free of choice among nodal lines, *Geophysical Journal International*, **150**, 588–609.
- Archuleta, R. J., 1984. A faulting model for the 1979 Imperial Valley earthquake, *Journal of Geophysical Research*, **89**, 4559–4585.
- Asano, K. & Iwata, T., 2009. Source rupture process of the 2004 Chuetsu, Mid-Niigata prefecture, Japan, earthquake inferred from waveform inversion with dense strong-motion data, *Bulletin of the Seismological Society of America*, **99**(1), 123–140.
- Asano, K. & Iwata, T., 2016. Source rupture processes of the foreshock and mainshock in the 2016 Kumamoto earthquake sequence estimated from the kinematic waveform inversion of strong data, *Earth, Planets and Space*, **68:147**, 1–11.
- Asano, K., Iwata, T., & Irikura, K., 2005. Estimation of source rupture process and strong ground motion simulation of the 2002 Denali, Alaska, earthquake, *Bulletin of the Seismological Society of America*, **95**(5), 1701–1715.
- Bayes, T., 1763. An essay towards solving a problem in the doctrine of chances, *Philosophical Transactions of the Royal Society of London*, **53**, 370–418.
- Beresnev, I. A., 2003. Uncertainties in finite-fault slip inversions: To what extent to believe? (A critical review), *Bulletin of the Seismological Society of America*, **93**(6), 2445–2458.
- Bizzarri, A., 2012. Analytical representation of the fault slip velocity from spontaneous dynamic earthquake models, *Journal of Geophysical Research*, **117**, B06309.
- Bodin, T., Sambridge, M., Tkalčić, H., Arroucau, P., Gallagher, K., & Rawlinson, N., 2012. Transdimensional inversion of receiver functions and surface wave dispersion, *Journal of Geophysical Research*, **117**, B02301.
- Bouchon, M., 1981. A simple method to calculate Green's functions for elastic layered media, *Bulletin of the Seismological Society of America*, **71**, 959–971.
- Bouchon, M., Toksoz, M. N., Karabulut, H., Bouin, M., Dietrich, M., Aktar, M., & Edie, M., 2002. Space and time evolution of rupture and faulting during the 1999 Izmit (Turkey) earthquake, *Bulletin of the Seismological Society of America*, **92**(1), 256–266.

- Bowers, D. & Hudson, J. A., 1999. Defining the scalar moment of a seismic source with a general moment tensor, *Bulletin of the Seismological Society of America*, **89**(5), 1390–1394.
- Brune, J. N., 1970. Tectonic stress and the spectra of seismic shear waves from earthquakes, *Journal of Geophysical Research*, **75**, 4997–5009.
- Causse, M., Cultrera, G., Moreau, L., Herrero, A., Schiappapietra, E., & Courboux, F., 2017. Bayesian rupture imaging in a complex medium: The 29 May 2012 Emilia, Northern Italy, earthquake, *Geophysical Research Letters*, **44**(15), 7783–7792.
- Chapman, C. H. & Leaney, W. S., 2012. A new moment-tensor decomposition for seismic events in anisotropic media, *Geophysical Journal International*, **188**(1), 343–370.
- Clévéde, E., Bouin, M. P., Bukchin, B., Mostinskiy, A., & Patau, G., 2004. New constraints on the rupture process of the 1999 August 17 Izmit earthquake deduced from estimates of stress glut rate moments, *Geophysical Journal International*, **159**(3), 931–942.
- Custódio, S. & Archuleta, R. J., 2007. Parkfield earthquakes: Characteristic or complementary?, *Journal of Geophysical Research*, **112**, B05310.
- Day, S. M., Yu, G., & Wald, D. J., 1998. Dynamic stress changes during earthquake rupture, *Bulletin of the Seismological Society of America*, **88**(2), 512–522.
- Dettmer, J., Dosso, S. E., & Holland, C. W., 2007. Uncertainty estimation in seismo-acoustic reflection travel-time inversion, *The Journal of the Acoustical Society of America*, **122**, 161–176.
- Dettmer, J., Benavente, R., Cummins, P. R., & Sambridge, M., 2014. Transdimensional finite-fault inversion, *Geophysical Journal International*, **199**, 735–751.
- Dettmer, J., Hawkins, R., Cummins, P. R., Hossen, J., Sambridge, M., Hino, R., & Inazu, D., 2016. Tsunami source uncertainty estimation: The 2011 Japan tsunami, *Journal of Geophysical Research*, **121**, 4483–4505.
- Duputel, Z., Rivera, L., Fukahata, Y., & Kanamori, H., 2012. Uncertainty estimations for seismic source inversions, *Geophysical Journal International*, **190**(2), 1243–1256.
- Duputel, Z., Agram, P. S., Simons, M., Minson, S. E., & Beck, J. L., 2014. Accounting for prediction uncertainty when inferring subsurface fault slip, *Geophysical Journal International*, **197**(1), 464–482.
- Duputel, Z., Jiang, J., Jolivet, R., Simons, M., Rivera, L., Ampuero, J.-P., Riel, B., Owen, S. E., Moore, A. W., Samsonov, S. V., Ortega Culaciati, F., & Minson, S. E., 2015. The Iquique earthquake sequence of April 2014: Bayesian modeling accounting for prediction uncertainty, *Geophysical Research Letters*, **42**(19), 7949–7957.

- Einstein, A., 1905. Investigation on the theory of the Brownian movement (A. D. Cowper Trans.), *Annalen der Physik*, **17**(8), 549–560.
- Eiseman, P. R., 1992. Control point grid generation, *Computers and Mathematics with Applications*, **24**(5/6), 57–67.
- Fan, Y. & Sisson, S. A., 2011. *Reversible jump Markov chain Monte Carlo*, In: *Handbook of Markov Chain Monte Carlo*, Chapman and Hall/CRC.
- Frohlich, C., 1994. Earthquakes with non-double-couple mechanisms, *Science*, **264**, 804–809.
- Fukahata, Y. & Hashimoto, M., 2016. Simultaneous estimation of the dip angles and slip distribution on the faults of the 2016 Kumamoto earthquake through a weak nonlinear inversion of InSAR data, *Earth, Planets and Space*, **68:204**, 1–10.
- Gallagher, K., Charvin, K., Nielsen, S., Sambridge, M., & Stephenson, J., 2009. Markov chain Monte Carlo (McMC) sampling methods to determine optimal models, model resolution and model choice for earth science problems, *Marine and Petroleum Geology*, **26**, 525–535.
- Gallovič, F. & Ampuero, J.-P., 2015. A new strategy to compare inverted rupture models exploiting the eigen-structure of the inverse problem, *Seismological Research Letters*, **86**, 1679–1689.
- Gallovič, F. & Zahradník, J., 2010. Toward understanding slip inversion uncertainty and artifacts: 2. Singular value analysis, *Journal of Geophysical Research*, **116**, B02309.
- Gallovič, F. & Zahradník, J., 2012. Complexity of the M_w 6.3 2009 L’Aquila (central Italy) earthquake: 1. Multiple finite-extent source inversion, *Journal of Geophysical Research*, **117**, B04307.
- Gallovič, F., Imperatori, W., & Mai, P. M., 2015. Effects of three-dimensional crustal structure and smoothing constraint on earthquake slip inversions: case study of the M_w 6.3 2009 L’Aquila earthquake, *Journal of Geophysical Research*, **120**, 428–449.
- Genz, A. & Bretz, F., 2009. *Computation of Multivariate Normal and t Probabilities*, Springer, Berlin.
- Gephart, J. W. & Forsyth, D. W., 1984. An improved method for determining the regional stress tensor using earthquake focal mechanism data: application to the San Fernando earthquake sequence, *Journal of Geophysical Research*, **89**, 9305–9320.
- Goto, H., Tsutsumi, H., Toda, S., & Kumahara, Y., 2017. Geomorphic features of surface ruptures associated with the 2016 Kumamoto earthquake in and around the downtown of Kumamoto City, and implications on triggered slip along active faults, *Earth, Planets and Space*, **69:26**, 1–12.

- Graves, R. W. & Wald, D. J., 2001. Resolution analysis of finite fault source inversion using one- and three-dimensional Green’s functions 1. Strong motions, *Journal of Geophysical Research*, **106**(B5), 8745–8766.
- Green, P. J., 1995. Reversible jump Markov chain Monte Carlo computation and Bayesian model determination, *Biometrika*, **82**(4), 711–732.
- Green, P. J., 2003. *Trans-dimensional Markov chain Monte Carlo*, In: *Highly Structured Stochastic Systems*, Oxford University Press, Oxford Statistical Science Series edn.
- Gustafson, P., 1998. A guided walk Metropolis algorithm, *Statistics and Computing*, **8**(4), 357–364.
- Hallo, M. & Gallovič, F., 2016. Fast and cheap approximation of Green functions uncertainty for waveform-based earthquake source inversions, *Geophysical Journal International*, **207**(2), 1012–1029.
- Hallo, M., Asano, K., & Gallovič, F., 2017. Bayesian inference and interpretation of centroid moment tensors of the 2016 Kumamoto earthquake sequence, Kyushu, Japan, *Earth, Planets and Space*, **69:134**, 1–19.
- Hao, J., Ji, C., & Yao, Z., 2017. Slip history of the 2016 M_w 7.0 Kumamoto earthquake: intraplate rupture in complex environment, *Geophysical Research Letters*, **44**, 743–750.
- Hartzell, S., Liu, P., Mendoza, C., Ji, C., & Larson, K. M., 2007. Stability and uncertainty of finite-fault slip inversions: Application to the 2004 Parkfield, California, earthquake, *Bulletin of the Seismological Society of America*, **97**(6), 1911–1934.
- Hartzell, S. H. & Heaton, T. H., 1983. Inversion of strong ground motion and teleseismic waveform data for the fault rupture history of the 1979 Imperial Valley, California earthquake, *Bulletin of the Seismological Society of America*, **73**(6), 1553–1583.
- Hastings, W. K., 1970. Monte Carlo sampling methods using Markov Chains and their applications, *Biometrika*, **57**, 97–109.
- Himematsu, Y. & Furuya, M., 2016. Fault source model for the 2016 Kumamoto earthquake sequence based on ALOS-2/PALSAR-2 pixel-offset data: evidence for dynamic slip partitioning, *Earth, Planets and Space*, **68:169**, 1–10.
- Hutchings, L., Mert, A., Fahjan, Y., Novikova, T., Golar, A., Miah, M., Fergany, E., & Foxall, W., 2017. Physics-based hazard assessment for critical structures near large earthquake sources, *Pure and Applied Geophysics*, **174**(9), 3635–3662.
- Ide, S., 2007. *Slip inversion*, In: *Treatise on Geophysics*, Elsevier, Amsterdam, vol. 4 edn.
- Jain, A. K., 1989. *Fundamentals of Digital Image Processing*, Prentice-Hall, Upper Saddle River, USA.

- Ji, C., Wald, D. J., & Helmberger, D. V., 2002. Source description of the 1999 Hector Mine, California, earthquake, Part I: Wavelet domain inversion theory and resolution analysis, *Bulletin of the Seismological Society of America*, **92**(4), 1192–1207.
- Jost, M. L. & Herrmann, R. B., 1989. A student's guide to and review of moment tensors, *Seismological Research Letters*, **60**(2), 37–57.
- Kamata, H. & Kodama, K., 1994. Tectonics of an arc-arc junction: an example from Kyushu Island at the junction of the Southwest Japan Arc and the Ryukyu Arc, *Tectonophysics*, **233**(1-2), 69–81.
- Kamata, H. & Kodama, K., 1999. Volcanic history and tectonics of the Southwest Japan Arc, *Isl Arc*, **8**(3), 393–403.
- Kanamori, H. & Brodsky, E. E., 2004. The physics of earthquakes, *Reports on Progress in Physics*, **67**, 1429–1496.
- Kanamori, H. & Rivera, L., 2006. *Energy partitioning during an earthquake*, In: *Radiated Energy and the Physics of Faulting*, American Geophysical Union, geophysical monograph series edn.
- Kato, A., Fukuda, J., Nakagawa, S., & Kazushige, O., 2016. Foreshock migration preceding the 2016 M_w 7.0 Kumamoto earthquake, *Jpn Geophysical Research Letters*, **43**(17), 8945–8953.
- Kikuchi, M. & Kanamori, H., 1991. Inversion of complex body waves—III, *Bulletin of the Seismological Society of America*, **81**(6), 2335–2350.
- King, G. C. P. & Devès, M., 2015. *Fault Interaction, Earthquake Stress Changes, and the Evolution of Seismicity*, In: *Treatise on Geophysics, 2nd Ed.*, Elsevier B.V., Oxford.
- Kirkpatrick, S., Gelatt, C. D. J., & Vecchi, M. P., 1983. Optimization by simulated annealing, *Science*, **220**, 671–680.
- Knopoff, L. & Randall, M. J., 1970. The compensated linear-vector dipole: A possible mechanism for deep earthquakes, *Journal of Geophysical Research*, **75**(26), 4957–4963.
- Kobayashi, H., Koketsu, K., & Miyake, H., 2017. Rupture processes of the 2016 Kumamoto earthquake sequence: Causes for extreme ground motions, *Geophysical Research Letters*, **44**(12), 6002–6010.
- Kobayashi, T., 2017. Earthquake rupture properties of the 2016 Kumamoto earthquake foreshocks (M_j 6.5 and M_j 6.4) revealed by conventional and multiple-aperture InSAR, *Earth, Planets and Space*, **69**:7, 1–12.
- Koketsu, K., Miyake, H., & Suzuki, H., 2012. Japan integrated velocity structure model version 1., In: *Proceedings of the 15th world conference on earthquake engineering*, Lisbon, 24–28 Sept 2012.

- Kubo, H., Asano, K., Iwata, T., & Aoi, S., 2016a. Development of fully Bayesian multiple-time-window source inversion, *Geophysical Journal International*, **204**(3), 1601–1619.
- Kubo, H., Suzuki, W., Aoi, S., & Sekiguchi, H., 2016b. Source rupture processes of the 2016 Kumamoto, Japan, earthquakes estimated from strong-motion waveforms, *Earth, Planets and Space*, **68**:161, 1–13.
- Kumahara, Y., Goto, H., Nakata, T., Ishiguro, S., Ishimura, D., Ishiyama, T., Okada, S., Kagohara, K., Kashihara, S., Kaneda, H., Sugito, N., Suzuki, Y., Takenami, D., Tanaka, K., Tanaka, T., Tsutsumi, H., Toda, S., Hirouchi, D., Matsuta, N., Moriki, H., Yoshida, H., & Watanabe, M., 2016. Distribution of surface rupture associated with the 2016 Kumamoto earthquake and its significance, Japan Geoscience Union Meeting 2016, MIS34-05.
- Lay, T., Kanamori, H., & Ruff, L., 1982. The asperity model and the nature of large subduction zone earthquakes, *Earthquake Prediction Research*, **1**(1), 3–71.
- Lin, A., Satsukawa, T., Wang, M., Mohammadi, A. Z., Fueta, R., & Nakajima, F., 2016. Coseismic rupturing stopped by Aso volcano during the 2016 M_w 7.1 Kumamoto earthquakes, *Science*, **354**(6314), 869–874.
- Liu, J., Li, L., Zahradník, J., Sokos, E., Liu, C., & T, X., 2018. North Korea’s 2017 test and its non-tectonic aftershock, *Geophysical Research Letters*, **45**(7), 3017–3025.
- Liu, P. & Archuleta, R. J., 2004. A new nonlinear finite fault inversion with three-dimensional Green’s functions: Application to the 1989 Loma Prieta, California, earthquake, *Journal of Geophysical Research*, **109**(B02318), 1–15.
- Mai, P. M., Schorlemmer, D., Page, M., Ampuero, J., Asano, K., Causse, M., Custodio, S., Fan, W., Festa, G., Galis, M., Gallovic, F., Imperatori, W., Käser, M., Malytskyy, D., Okuwaki, R., Pollitz, F., Passone, L., Razafindrakoto, H. N. T., Sekiguchi, H., Song, S. G., Somala, S. N., Thingbaijam, K. K. S., Twardzik, C., van Driel, M., Vyas, J. C., Wang, R., Yagi, Y., & Zielke, O., 2016. The earthquake-source inversion validation (SIV) project, *Seismological Research Letters*, **87**(3), 690–708.
- Malinverno, A., 2002. Parsimonious Bayesian Markov chain Monte Carlo inversion in a non linear geophysical problem, *Geophysical Journal International*, **151**, 675–688.
- Marple, S. L., 1986. *Digital Spectral Analysis: With Applications*, Prentice-Hall, Inc., Upper Saddle River, NJ, USA.
- Matsumoto, S., Nakao, S., Ohkura, T., Miyazaki, M., Shimizu, H., Abe, Y., Inoue, H., Nakamoto, M., Yoshikawa, S., & Yamashita, Y., 2015. Spatial heterogeneities in tectonic stress in Kyushu, Japan and their relation to a major shear zone, *Earth, Planets and Space*, **67**:172, 1–9.

- Metropolis, N., Rosenbluth, A., Rosenbluth, M., Teller, A., & Teller, E., 1953. Equation of state calculations by fast computing machines, *The Journal of Chemical Physics*, **21**, 1081–1092.
- Michael, A. J., 1984. Determination of stress from slip data: faults and folds, *Journal of Geophysical Research*, **89**(B13), 11517–11526.
- Miller, A. D., Foulger, G. R., & Julian, B. R., 1998. Non-double-couple earthquakes 2: observations, *Reviews of Geophysics*, **36**(4), 551–568.
- Minson, S. E., Simons, M., & Beck, J. L., 2013. Bayesian inversion for finite fault earthquake source models. I—Theory and algorithm, *Geophysical Journal International*, **194**(3), 1701–1726.
- Minson, S. E., Simons, M., Beck, J. L., Ortega, F., Jiang, J., Owen, S. E., Moore, A. W., Inbal, A., & Sladen, A., 2014. Bayesian inversion for finite fault earthquake source models – II: the 2011 great Tohoku-oki, Japan earthquake, *Geophysical Journal International*, **198**, 922–940.
- Monelli, D., Mai, P. M., Jónsson, S., & Giardini, D., 2009. Bayesian imaging of the 2000 Western Tottori (Japan) earthquake through fitting of strong motion and GPS data, *Geophysical Journal International*, **176**(1), 135–150.
- Moreau, L., Hunter, A. J., Velichko, A., & Wilcox, P. D., 2014. 3-D reconstruction of sub-wavelength scatterers from the measurement of scattered fields in elastic waveguides, *IEEE Transactions on Ultrasonics, Ferroelectrics and Frequency Control*, **61**(11), 1864–1879.
- Mortenson, M. E., 2006. *Geometric Modeling, 3rd Ed.*, Industrial Press, New York City.
- Mustać, M. & Tkalčić, H., 2016. Point source moment tensor inversion through a Bayesian hierarchical model, *Geophysical Journal International*, **204**(1), 311–323.
- Nettles, M. & Ekström, G., 1998. Faulting mechanism of anomalous earthquakes near Bárðarbunga volcano, Iceland, *Journal of Geophysical Research*, **103**(B8), 17973–17983.
- Okada, A., 1980. Quaternary faulting along the median tectonic line of southwest Japan; In: Median Tectonic Line of Southwest Japan; Ed: Ichikawa, K., *Memoir of Geol. Soc. Japan*, **18**, 187–210.
- Okada, Y., Kasahara, K., Hori, S., Obara, K., Sekiguchi, S., Fujiwara, H., & Yamamoto, A., 2004. Recent progress of seismic observation networks in Japan – Hi-net, F-net, K-NET and KiK-net –, *Earth, Planets and Space*, **56**, xv–xxviii.
- Olson, A. H. & Apsel, R. J., 1982. Finite faults and inverse theory with applications to the 1979 Imperial Valley earthquake, *Bulletin of the Seismological Society of America*, **72**(6A), 1969–2001.
- Pearson, K., 1905. The problem of the Random Walk, *Nature*, **72**, 294.

- Piatanesi, A., Cirella, A., Spudich, P., & Cocco, M., 2007. A global search inversion for earthquake kinematic rupture history: application to the 2000 western Tottori, Japan earthquake, *Journal of Geophysical Research*, **112**, B07314.
- Pizzi, A., Di Domenica, A., Gallovič, F., Luzi, L., & Puglia, R., 2017. Fault segmentation as constraint to the occurrence of the main shocks of the 2016 Central Italy seismic sequence., *Tectonics*, **36**, 2370–2387.
- Podvin, P. & Lecomte, I., 1991. Finite difference computation of traveltimes in very contrasted velocity models: a massively parallel approach and its associated tools, *Geophysical Journal International*, **105**(1), 271–284.
- Richardson, S. & Green, P. J., 1997. On Bayesian analysis of mixtures with an unknown number of components, *Journal of the Royal Statistical Society. Series B (Methodological)*, **59**(4), 731–792.
- Roberts, G., Gelman, A., & Gilks, W., 1997. Weak convergence and optimal scaling of random walk Metropolis algorithms, *Annals of Applied Probability*, **7**, 110–120.
- Rudajev, V. & Šílený, J., 1985. Seismic events with non-shear components, II. Rockbursts with implosive source component, *Pure and Applied Geophysics*, **123**, 17–25.
- Sambridge, M., 2014. A Parallel Tempering algorithm for probabilistic sampling and multimodal optimization, *Geophysical Journal International*, **196**(1), 357–374.
- Sambridge, M., Gallagher, K., Jackson, A., & Rickwood, P., 2006. Transdimensional inverse problems, model comparison and the evidence, *Geophysical Journal International*, **167**, 528–542.
- Sandwell, D. T., 1987. Biharmonic splines interpolation of GEOS-3 and SEASAT altimeter data, *Geophysical Research Letters*, **14**(2), 139–142.
- Sekiguchi, H., Irikura, K., & Iwata, T., 2000. Fault geometry in the rupture termination of the 1995 Hyogo-ken Nanbu earthquake, *Bulletin of the Seismological Society of America*, **90**(1), 117–133.
- Shirahama, Y., Yoshimi, M., Awata, Y., Maruyama, T., Azuma, T., Miyashita, Y., Mori, H., Imanishi, K., Takeda, N., Ochi, T., Otusbo, M., Asahina, D., & Miyakawa, A., 2016. Characteristics of the surface ruptures associated with the 2016 Kumamoto earthquake sequence, central Kyushu, Japan, *Earth, Planets and Space*, **68:191**, 1–12.
- Smith, A. F. M. & Roberts, G. O., 1993. Bayesian computation via the gibbs sampler and related markov chain monte carlo methods, *Journal of the Royal Statistical Society*, **55**(1), 3–23.
- Sokos, E. & Zahradník, J., 2013. Evaluating centroid-moment-tensor uncertainty in the new version of ISOLA software, *Seismological Research Letters*, **84**(4), 656–665.

- Sokos, E., Kiratzi, A., Gallovič, F., Zahradník, J., Serpetsidaki, A., Plicka, V., Janský, J., Kostelecký, J., & Tselentis, G.-A., 2015. Rupture process of the 2014 Cephalonia, Greece, earthquake doublet (M_w 6) as inferred from regional and local seismic data, *Tectonophysics*, **656**, 131–141.
- Somerville, P., Irikura, K., Graves, R., Sawada, S., Wald, D., Abrahamson, N., Iwasaki, Y., Kagawa, T., Smith, N., & Kowada, A., 1999. Characterizing crustal earthquake slip models for the prediction of strong ground motion, *Seismological Research Letters*, **70**(1), 59–80.
- Tarantola, A., 2005. *Inverse Problem Theory and Methods for Model Parameter Estimation*, Society for Industrial and Applied Mathematics, Philadelphia.
- Tarantola, A. & Valette, B., 1982. Inverse problems = quest for information, *Journal of Geophysics*, **50**(3), 159–170.
- Tierney, L., 1994. Markov chains for exploring posterior distributions, *The Annals of Statistics*, **22**(4), 1701–1762.
- Tinti, E., Fukuyama, E., Piatanesi, A., & Cocco, M., 2005. A kinematic source-time function compatible with earthquake dynamics, *Bulletin of the Seismological Society of America*, **95**(4), 1211–1223.
- Toda, S., Kaneda, H., Okada, S., Ishimura, D., & Mildon, Z. K., 2016. Slip-partitioned surface ruptures for the M_w 7.0 16 April 2016 Kumamoto, Japan, earthquake, *Earth, Planets and Space*, **68:188**, 1–11.
- Trench, W. F., 1964. An algorithm for the inversion of finite toeplitz matrices, *Journal of the Society for Industrial and Applied Mathematics*, **12**(3), 515–522.
- Vackář, J., Burjánek, J., & Zahradník, J., 2015. Automated detection of disturbances in seismic records; MouseTrap code, *Seismological Research Letters*, **86**(2A), 442–450.
- Vackář, J., Gallovič, F., Burjánek, J., Zahradník, J., & Clinton, J., 2017. Bayesian ISOLA: new tool for automated centroid moment tensor inversion, *Geophysical Journal International*, **210**(2), 693–705.
- Valentine, A. P. & Trampert, J., 2012. Assessing the uncertainties on seismic source parameters: towards realistic error estimates for centroid-moment-tensor determinations, *Physics of the Earth and Planetary Interiors*, **210–211**, 36–49.
- Valentine, A. P. & Woodhouse, J. H., 2010. Approaches to automated data selection for global seismic tomography, *Geophysical Journal International*, **182**(2), 1001–1012.
- Vavryčuk, V., 2005. Focal mechanisms in anisotropic media, *Geophysical Journal International*, **161**(2), 334–346.
- Vavryčuk, V., 2011. Tensile earthquakes: Theory, modeling, and inversion, *Journal of Geophysical Research*, **116**(B12320), 1–14.

- Vavryčuk, V., 2014. Iterative joint inversion for stress and fault orientations from focal mechanisms, *Geophysical Journal International*, **199**(1), 69–77.
- Vavryčuk, V., 2015. Moment tensor decompositions revisited, *Geophysical Journal International*, **19**(1), 231–252.
- Wald, D. J. & Heaton, T. H., 1994. Spatial and temporal distribution of slip for the 1992 Landers, California, earthquake, *Bulletin of the Seismological Society of America*, **84**, 668–691.
- Wessel, P. & Smith, W. H. F., 1998. New, improved version of generic mapping tools released, *EOS Transactions American Geophysical Union*, **79**(47), 579.
- Yagi, Y. & Fukahata, Y., 2011. Introduction of uncertainty of Green’s function into waveform inversion for seismic source processes, *Geophysical Journal International*, **186**(2), 711–720.
- Yoffe, E., 1951. The moving Griffith crack, *Philosophical Magazine*, **42**, 739–750.
- Yoshida, K., Miyakoshi, K., Somei, K., & Irikura, K., 2017. Source process of the 2016 Kumamoto earthquake ($M_j7.3$) inferred from kinematic inversion of strong-motion records, *Earth, Planets and Space*, **69:64**, 1–13.
- Zahradník, J. & Custódio, S., 2012. Moment tensor resolvability: application to Southwest Iberia, *Bulletin of the Seismological Society of America*, **102**(3), 1235–1254.
- Zahradník, J. & Gallovič, F., 2010. Toward understanding slip-inversion uncertainty and artifacts, *Journal of Geophysical Research*, **115**(B09310), 1–16.
- Zahradník, J. & Plešinger, A., 2010. Toward understanding subtle instrumentation effects associated with weak seismic events in the near field, *Bulletin of the Seismological Society of America*, **100**(1), 59–73.
- Zahradník, J. & Sokos, E., 2018. *ISOLA code for multiple-point source modeling – review*, In: *Moment Tensor Solutions - A Useful Tool for Seismotectonics*, Ed: Sebastiano D’Amico, Springer International Publishing.
- Zahradník, J., Gallovič, F., Sokos, E., Serpetsidaki, A., & Tselentis, G. A., 2008. Quick fault-plane identification by a geometrical method: application to the M_w 6.2 Leonidio Earthquake, 6 January 2008, Greece, *Seismological Research Letters*, **79**(5), 653–662.
- Zahradník, J., Fojtíková, L., Carvalho, J., Barros, L. V., Sokos, E., & Janský, J., 2015. Compromising polarity and waveform constraints in focal-mechanism solutions; the Mara Rosa 2010 M_w 4 central Brazil earthquake revisited, *Journal of South American Earth Sciences*, **63**, 323–333.

List of Abbreviations

ACF – approximate covariance function – Eq. (2.14)
AXCF – approximate cross-covariance function – Eq. (2.13)
CF – covariance function – Eq. (2.3)
CLVD – compensated linear vector dipole
CMT – centroid moment tensor
CPU – central processing unit
DC – double-couple component
DEV – deviatoric
GF – Green’s function
ISO – isotropic component
JMA – Japan Meteorological Agency
JST – Japan Standard Time
MC – Monte-Carlo
MCMC – Markov chain Monte-Carlo
MT – moment tensor
MTL – Median Tectonic Line
NASA – National Aeronautics and Space Administration
NIED – National Research Institute for Earth Science and Disaster Resilience
PDF – probability density function
PT – parallel tempering
RMS – root-mean-square
SACF – stationarized approximate covariance function – Eq. (2.21)
SAXCF – stationarized approximate cross-covariance function – Eq. (2.20)
SCF – stationarized covariance function
SDH – slip disk histogram
SRF – slip rate function
SRTM – NASA Shuttle Radar Topographic Mission
STF – source time function
SXCF – stationarized cross-covariance function
trans-D – trans-dimensional
UTC – Universal Time Coordinated
XCF – cross-covariance function – Eq. (2.2)

List of included publications

Hallo, M. & Gallovič, F., 2016. Fast and cheap approximation of Green functions uncertainty for waveform-based earthquake source inversions, *Geophysical Journal International*, **207**(2), 1012–1029.

Hallo, M., Asano, K. & Gallovič, F., 2017. Bayesian inference and interpretation of centroid moment tensors of the 2016 Kumamoto earthquake sequence, Kyushu, Japan, *Earth, Planets and Space*, **69**:134, 1–19.

A. Attachments

A.1 Fortran code for ACF (AXCF)

```
!-----
! Fortran f90 subroutines for determining the (cross-)covariance
! matrix by approximate (cross-)covariance functions (AXCF or ACF)
! (Hallo and Gallovic, 2016).
! Hallo,M., Gallovic,F. (2016): Fast and cheap approximation of Green
! functions uncertainty for waveform-based earthquake source inversions,
! Geophysical Journal Int., 207, 1012-1029.
!
! Authors: Miroslav Hallo and Frantisek Gallovic (8/2017)
! Charles University, Faculty of Mathematics and Physics
! Revision 1/2018: Corrected and tested for real signals
!
! This code is published under the GNU General Public License. To any
! licensee is given permission to modify the work, as well as to copy
! and redistribute the work or any derivative version. Still we would
! like to kindly ask you to acknowledge the authors and don't remove
! their names from the code. This code is distributed in the hope
! that it will be useful, but WITHOUT ANY WARRANTY.
!-----

SUBROUTINE axcf(N, f1, f2, L1, L12, C)
!-----
! Compute AXCF of functions f1 and f2 of samples N
! L1 and L12 are time-shift windows in samples
! -> Output into covariance matrix C
!-----

implicit none
integer, intent(in):: N, L1, L12
real(8), intent(in):: f1(N), f2(N)
real(8), intent(out):: C(N,N)
complex(8), allocatable:: smooth1(:), smooth12(:), s1(:), s2(:), XC(:, :)
complex(8), allocatable:: s1smooth1(:), s2smooth1(:), s2smooth12(:)
integer:: i, j, FFT, Lzeros

! Check the length of smoothing window L1
if(L1<2)then
write(*,*) 'Warning! L1 is too short'
endif

! Allocation and init of variables
FFT = 2**((int(log(dble(2*N)))/log(2.d0)+0.99999999d0)+1)
allocate(smooth1(FFT), s1(FFT), s2(FFT), s1smooth1(FFT))
allocate(s2smooth1(FFT), s2smooth12(FFT), XC(FFT, FFT))
C=0.d0
s1=0.
s2=0.
s1(1:N) = f1(1:N)
s2(1:N) = f2(1:N)

! Put zeros (values) before and after the signal
Lzeros = max(L1, L12);
s1(N+1:N+Lzeros) = f1(N)
s2(N+1:N+Lzeros) = f2(N)
s1(FFT-Lzeros+1:FFT) = f1(1)
s2(FFT-Lzeros+1:FFT) = f2(1)

! f2 smoothing by L12 window
if(L12>1)then
allocate(smooth12(FFT))
smooth12=0.
smooth12(1:int(dble(L12)/2.+ .51))=1.d0/dble(L12*FFT)
smooth12(FFT:FFT-L12/2+1:-1)=1.d0/dble(L12*FFT)
call four1(smooth12, FFT, 1)
call four1(s2, FFT, 1)
s2smooth12=s2*smooth12
```

```

        call four1(s2smooth12,FFT,-1)
        deallocate(smooth12)
    else
        s2smooth12=s2
    endif

! smoothing window L1
smooth1=0.
smooth1(1:int(dble(L1)/2+.51))=1.d0/dble(L1*FFT)
smooth1(FFT:FFT-L1/2+1:-1)=1.d0/dble(L1*FFT)
call four1(smooth1,FFT,1)

! compute XCF
do i=1,FFT
    XC(:,i)=s1(:)*cshift(s2smooth12(:),SHIFT=(FFT/2+1)-i)
    call four1(XC(:,i),FFT,1)
    XC(:,i)=XC(:,i)*smooth1(:)
    call four1(XC(:,i),FFT,-1)
enddo

call four1(s1,FFT,1)
s1smooth1=s1*smooth1
call four1(s1smooth1,FFT,-1)
call four1(s2smooth12,FFT,1)
s2smooth1=s2smooth12*smooth1
call four1(s2smooth1,FFT,-1)

do i=1,FFT
    XC(:,i)=XC(:,i)-s1smooth1(:)*cshift(s2smooth1(:),SHIFT=(FFT/2+1)-i)
enddo

! Fill the covariance matrix by AXCF
do i=1,N
    do j=1,N
        C(i,j)=dble(XC(i,FFT/2+1-(j-i)))
    enddo
enddo

deallocate(smooth1,s1,s2,s2smooth12,s1smooth1,s2smooth1,XC)
END SUBROUTINE

```

A.2 Fortran code for SACF (SAXCF)

```

|-----|
! Fortran f90 subroutines for determining the (cross-)covariance
! matrix by approximate (cross-)covariance functions (SAXCF and SACF)
! (Hallo and Gallovic, 2016).
! Hallo, M., Gallovic, F. (2016): Fast and cheap approximation of Green
! functions uncertainty for waveform-based earthquake source inversions,
! Geophysical Journal Int., 207, 1012–1029.
!
! Authors: Miroslav Hallo and Frantisek Gallovic (8/2017)
! Charles University, Faculty of Mathematics and Physics
! Revision 1/2018: Corrected and tested for real signals
!
! This code is published under the GNU General Public License. To any
! licensee is given permission to modify the work, as well as to copy
! and redistribute the work or any derivative version. Still we would
! like to kindly ask you to acknowledge the authors and don't remove
! their names from the code. This code is distributed in the hope
! that it will be useful, but WITHOUT ANY WARRANTY.
!-----|

SUBROUTINE saxcf(N, f1, f2, L1, L12, T, C)
|-----|
!   Compute SAXCF of functions f1 and f2 of samples N
!   L1 and L12 are time-shift windows in samples
!   T is characteristic length of the signal in samples
!   -> Output into covariance matrix C
|-----|

  implicit none
  real(8), parameter :: PI=3.1415926535d0
  integer, intent(in) :: N, L1, L12, T
  real(8), intent(in) :: f1(N), f2(N)
  real(8), intent(out) :: C(N,N)
  complex(8), allocatable :: s1(:), s2(:), Rfg(:), fSACF(:)
  complex(8), allocatable :: smooth1(:), smooth12(:)
  real(8), allocatable :: SACF(:), tw(:)
  real(8) :: taper, r
  integer :: i, j, FFT

! Check the length of smoothing window L1
  if(L1<2)then
    write(*,*) 'Warning! L1 is too short'
  endif

! Allocation and init of variables
  FFT = 2**((int(log(dble(2*N))/log(2.d0))+0.99999999d0)+1)
  allocate(s1(FFT), s2(FFT), Rfg(FFT), fSACF(FFT), smooth1(FFT))
  allocate(SACF(2*N-1), tw(2*N-1))
  C=0.d0
  s1=0.
  s2=0.
  s1(1:N) = f1(1:N)
  s2(1:N) = f2(1:N)

! FFT of the f and g functions
  call four1(s1, FFT, 1)
  call four1(s2, FFT, 1)

! Prepare smoothing functions in freq. domain
  smooth1=0.
  smooth1(1:int(dble(L1)/2+.51))=1.d0/dble(L1)
  smooth1(FFT-FFT-L1/2+1:-1)=1.d0/dble(L1)
  call four1(smooth1, FFT, 1)

! Cross-correlation of signals in freq. domain
  Rfg = conjg(s1)*s2

! Convolution of triangle function (width 2*L1) and cross-corr
  fSACF = Rfg - smooth1*conjg(smooth1)*Rfg

! Smoothing by joint shift (width L12) in freq. domain

```

```

if (L12>1)then
  allocate (smooth12(FFT))
  smooth12=0.
  smooth12(1:int(dble(L12)/2.+ .51))=1.d0/dble(L12)
  smooth12(FFT:FFT-L12/2+1:-1)=1.d0/dble(L12)
  call four1(smooth12,FFT,1)
  fSACF = smooth12*fSACF
  deallocate (smooth12)
endif

! Norm by the effective signal length
fSACF = fSACF/dble(T)

! Back to time domain
call four1(fSACF,FFT,-1)
fSACF = fSACF/FFT
SACF(1:N-1) = dble(fSACF(FFT-N+2:FFT))
SACF(N:2*N-1) = dble(fSACF(1:N))

! Tapered cosine window (SACF)
taper = 0.666d0
tw=1.d0
do i=1,2*N-1
  r = dble(i-1)/dble(2*N-2)
  if(r.le.(taper/2.d0))then
    tw(i) = 0.5d0*( 1 + cos((2.d0*PI/taper)*(r-taper/2.d0)))
  elseif(r.ge.(1.d0-taper/2.d0))then
    tw(i) = 0.5d0*( 1 + cos((2.d0*PI/taper)*(r-1+taper/2.d0)))
  endif
enddo
tw = tw**3 ! cube for bigger effect
SACF = SACF * tw ! Taper cosine window

! Fill the covariance matrix by SACF
do i=0,N-1
  C(i+1,1:N) = SACF(N-i:2*N-i-1)
enddo

deallocate (s1 , s2 , Rfg , fSACF , SACF , tw , smooth1)
END SUBROUTINE

```


A.3 Matlab code for ACF (AXCF)

```
function C = axcf(varargin)
% -----
% Matlab function for determining the (cross-)covariance matrix by
% approximate (cross-)covariance function (AXCF or ACF)
% (Hallo and Gallovic, 2016).
% Hallo, M., Gallovic, F. (2016): Fast and cheap approximation of Green
% functions uncertainty for waveform-based earthquake source inversions,
% Geophysical Journal Int., 207, 1012–1029.
%
% Authors: Miroslav Hallo and Frantisek Gallovic (1/2016)
% Charles University, Faculty of Mathematics and Physics
% Revision 1/2018: Corrected and tested for real signals
%
% This code is published under the GNU General Public License. To any
% licensee is given permission to modify the work, as well as to copy
% and redistribute the work or any derivative version. Still we would
% like to kindly ask you to acknowledge the authors and don't remove
% their names from the code. This code is distributed in the hope
% that it will be useful, but WITHOUT ANY WARRANTY.
% -----
% INPUT:
% f – First input signal (vector)
% g – Second input signal (vector)
% L1 – Width of the joint uniform distribution of time-shifts [sec]
% L12 – Width of the relative unif. distribution of time-shifts [sec]
% dt – Signal sampling [sec] (scalar)
% -----
% OUTPUT:
% C – (cross-)covariance matrix (2D matrix)
% -----
% EXAMPLES:
% axcf(f,L1,dt) – Compute auto-covariance matrix of f
% axcf(f,g,L1,L12,dt) – Compute cross-covariance matrix of f and g
% -----
% REQUIREMENTS:
% smooth (Matlab Curve Fitting Toolbox)
% -----

% Manage input arguments
if nargin == 5 % cross-covariance
    f = varargin{1};
    g = varargin{2};
    L1 = varargin{3};
    L12 = varargin{4};
    dt = varargin{5};
else
    if nargin == 3 % auto-covariance
        f = varargin{1};
        g = f;
        L1 = varargin{2};
        L12 = 0;
        dt = varargin{3};
    else
        error('axcf: Incorrect number of input arguments');
    end
end

% The number of samples in f
nsampl = length(f);

% Check the size of the final covariance matrix
if nsampl > 22360
    display('axcf: The covariance matrix require more than 4GB of memory');
elseif nsampl > 11180
    display('axcf: The covariance matrix require more than 1GB of memory');
elseif nsampl > 5590
    display('axcf: The covariance matrix require more than 250MB of memory');
end

% Check the length and preallocate output C matrix
```

```

if nsampl ~= length(g)
    error('axcf: Signals f ang g have to have the same length');
else
    C = zeros(nsampl);
end

% Prepare smoothing windows
L1s = ceil(L1/dt);
if L1s < 3
    L1s = 3;
    display(['axcf: L1 changed to ', num2str(L1s*dt), ' [s]'])
end
L12s = max(ceil(L12/dt), 1);

% Put zeros (values) before and after the signal
Lzeros = max(L1s, L12s);
f = [zeros(Lzeros,1)+f(1); f(:); zeros(Lzeros,1)+f(end)];
g = [zeros(Lzeros,1)+g(1); g(:); zeros(Lzeros,1)+g(end)];

% New number of samples
nsamplN = nsampl + 2*Lzeros;

% Smooth f and g signals
fSmooth = smooth(f, L1s, 'moving');
gSmooth = smooth(g, L12s, 'moving');

% Compute ACF for time-lags
ACF = zeros(nsamplN, nsamplN*2);
for tshift = 1 : nsamplN*2 % loop for time-lags (nsamplN+1 is zero time-lag)
    gShift = circshift(gSmooth, tshift -(nsamplN+1));
    ACF(:, tshift) = smooth( f.*gShift, L1s, 'moving' ) ...
        - (fSmooth.*smooth( gShift, L1s, 'moving' ) );
end

% Fill the covariance matrix by ACF
for i=1:nsampl % loop for rows
    for j=1:nsampl % loop for columns
        C(i, j) = ACF(i+Lzeros, nsamplN+1-(j-i));
    end
end

% Check if covariance matrix is symmetric (in case any numerical issues)
if isequal(f,g) % only auto-covariance
    issym = @(x) all(all(x==x.'));
    if ~issym(C)
        % Symmetrize it
        Cm = triu(ones(nsampl));
        C = C.*Cm;
        C = C + tril(C.', -1);
        %display('axcf: The covariance matrix was symmetrized')
    end
end

return

```

A.4 Matlab code for SACF (SAXCF)

```
function C = saxcf(varargin)
% -----
% Matlab function for determining the (cross-)covariance matrix by
% stationarized approximate (cross-)covariance function (SAXCF or SACF)
% (Hallo and Gallovic, 2016).
% Hallo,M., Gallovic,F. (2016): Fast and cheap approximation of Green
% functions uncertainty for waveform-based earthquake source inversions,
% Geophysical Journal Int., 207, 1012–1029.
%
% Authors: Miroslav Hallo and Frantisek Gallovic (1/2016)
% Charles University, Faculty of Mathematics and Physics
% Revision 1/2018: Corrected and tested for real signals
%
% This code is published under the GNU General Public License. To any
% licensee is given permission to modify the work, as well as to copy
% and redistribute the work or any derivative version. Still we would
% like to kindly ask you to acknowledge the authors and don't remove
% their names from the code. This code is distributed in the hope
% that it will be useful, but WITHOUT ANY WARRANTY.
% -----
% INPUT:
% f – First input signal (vector)
% g – Second input signal (vector)
% L1 – Width of the joint uniform distribution of time-shifts [sec]
% L12 – Width of the relative unif. distribution of time-shifts [sec]
% dt – Signal sampling [sec] (scalar)
% T – Dominant signal length [sec] (scalar)
% -----
% OUTPUT:
% C – stationarized (cross-)covariance matrix (2D matrix)
% -----
% EXAMPLES:
% saxcf(f,L1,dt,T) – Compute auto-covariance matrix of f
% saxcf(f,g,L1,L12,dt,T) – Compute cross-covariance matrix of f and g
% -----
% REQUIREMENTS:
% smooth (Matlab Curve Fitting Toolbox)
% filtfilt (Matlab Signal Processing Toolbox)
% -----

% Manage input arguments
if nargin == 6 % cross-covariance
    f = varargin{1};
    g = varargin{2};
    L1 = varargin{3};
    L12 = varargin{4};
    dt = varargin{5};
    T = varargin{6};
else
    if nargin == 4 % auto-covariance
        f = varargin{1};
        g = f;
        L1 = varargin{2};
        L12 = 0;
        dt = varargin{3};
        T = varargin{4};
    else
        error('saxcf: Incorrect number of input arguments');
    end
end

% The number of samples in f
nsampl = length(f);

% Check the size of the final covariance matrix
if nsampl > 22360
    display('saxcf: The covariance matrix require more than 4GB of memory');
elseif nsampl > 11180
    display('saxcf: The covariance matrix require more than 1GB of memory');
elseif nsampl > 5590
```

```

    display('saxcf: The covariance matrix require more than 250MB of memory');
end

% Check the length and preallocate output C matrix
if nsampl ~= length(g)
    error('saxcf: Signals f and g have to have the same length');
else
    C = zeros(nsampl);
end

% Check the triangle function base
L1s = round(L1/dt);
if L1s < 2
    L1s = 2;
    display(['saxcf: L1 changed to ', num2str(L1s*dt), ' [s]'])
end

% Cross-correlation of signals
RfgP = zeros(1, nsampl);
RfgN = zeros(1, nsampl);
for tshift=0:nsampl-1 % loop for time-lags
    RfgN(tshift+1) = sum(g(1:nsampl-tshift).*f(1+tshift:nsampl))*dt; % negative
    RfgP(tshift+1) = sum(f(1:nsampl-tshift).*g(1+tshift:nsampl))*dt; % positive
end
Rfg = [RfgN(nsampl:-1:2), RfgP(1:nsampl)];

% Convolution of triangle function (width 2*L1) and cross-correlation
b = ones(L1s,1)/L1s;
SCF = Rfg - filtfilt(b,1,Rfg);

% Smoothing by joint shift (width L12)
if ceil(L12/dt)>2
    SCF = smooth(SCF, ceil(L12/dt), 'moving');
end

% Norm by the effective signal length
SCF = SCF/T;

% Taper of C matrix
taper = 0.666;
tw = tukeywin(length(SCF), taper);
tw = tw.^3;
SCF = SCF(:) .* tw(:);

% Fill the covariance matrix by SCF
for tshift=0:nsampl-1 % loop for rows
    C(tshift+1,:) = SCF(nsampl-tshift : 2*nsampl-tshift-1);
end

% Check if covariance matrix is symmetric (in case any numerical issues)
if isequal(f,g) % only auto-covariance
    issym = @(x) all(all(x==x.'));
    if ~issym(C)
        % Symmetrize it
        Cm = triu(ones(nsampl));
        C = C.*Cm;
        C = C + tril(C.', -1);
        %display('saxcf: The covariance matrix was symmetrized')
    end
end

return

```

A.5 Tectonic cube - Earth's stress regimes

The stress field in the solid Earth is not the issue of this thesis, however it is an important topic connected to the interpretation of inferred earthquake source models. While, the interpretation in the tectonic framework is tackled in the case study of 2016 Kumamoto earthquakes in Chapter 3, I present here a brief attachment related to the interpretation of earthquake sources in the tectonic framework. For detailed information about Earth's stress field and methods for its estimation see Michael (1984), Gephart & Forsyth (1984), Angelier (2002), and Vavryčuk (2014).

Briefly, the tectonic earthquakes are associated with ruptures exposed to a stress field in the solid Earth. If the stress overcome the critical value of the strength of a fault, fast slip occurs. The stress can have a non-tectonic or tectonic origin. The stress field may be regionally very heterogeneous because it is affected, among others, by regional topography, pore pressure and heterogeneity of the Earth's crust.

The stress field can be mathematically represented by a symmetric tensor of second order τ , where the coordinate system can be always rotated in the way that the stress tensor diagonalizes:

$$\tau = \begin{pmatrix} \sigma_1 & 0 & 0 \\ 0 & \sigma_2 & 0 \\ 0 & 0 & \sigma_3 \end{pmatrix}, \quad (\text{A.1})$$

where σ_1 , σ_2 , and σ_3 are called the maximum, intermediate and minimum principal stresses with

$$\sigma_1 \geq \sigma_2 \geq \sigma_3, \quad (\text{A.2})$$

while the orthonormal vectors of such coordinate system define so-called principal stress directions. Following Anderson (1951), it is possible to distinguish three basic stress regimes in the solid Earth with typical mechanisms of faulting: **1**) the “normal faulting” regime having σ_1 vertical; **2**) the “strike-slip faulting” regime having σ_2 vertical; and **3**) the “reverse faulting” regime having σ_3 vertical. The activated faults are then spatially oriented with respects to the stress regime. By the Coulomb shear failure criteria, the slip vector is close to direction of σ_1 tilted by a shear angle θ defined as

$$\tan(2\theta) = \frac{1}{\mu}, \quad (\text{A.3})$$

where μ is coefficient of internal friction of the medium.

In Fig. A.1, I present a tool called “tectonic cube” useful for intuitive earthquake source interpretations and educational purpose. It is based on empirical experiences from geology, and comply with the Coulomb shear failure criteria. The tectonic cube shows spatial orientation of critically oriented (principal) faults for the given orientation of principal stress directions. The coefficient of internal friction is taken as $\mu = 0.75$ corresponding to the shear angle $\theta \approx 27^\circ$ (practical choice with $\tan(\theta) = 0.5$). Two conjugate principal faults are shown by red and blue lines as projected fault-planes into the rotated coordinate system. The red and blue arrows denote shear slip vectors on the principal faults as tangential to

the cube plane. Further, \oplus and \ominus signs denote forward and backward slip vectors tilted by θ from the cube normals. Moreover, the orange dashed line denotes orientation of the fault plane of possible pure tensile cracks (i.e. $\mu \rightarrow \infty$).

As a demonstration of the cube usage, let's assume the stress field settings of the Kumamoto area (Fig. 3.7e), i.e. fix σ_3 in NNW-SSE direction and rotate the cube along this axis to observe possible principal faults, and compare with inferred CMT solutions in Fig. 3.8. This tool is presented with the hope that it will be useful, keeping in mind that it is only a simplified model.

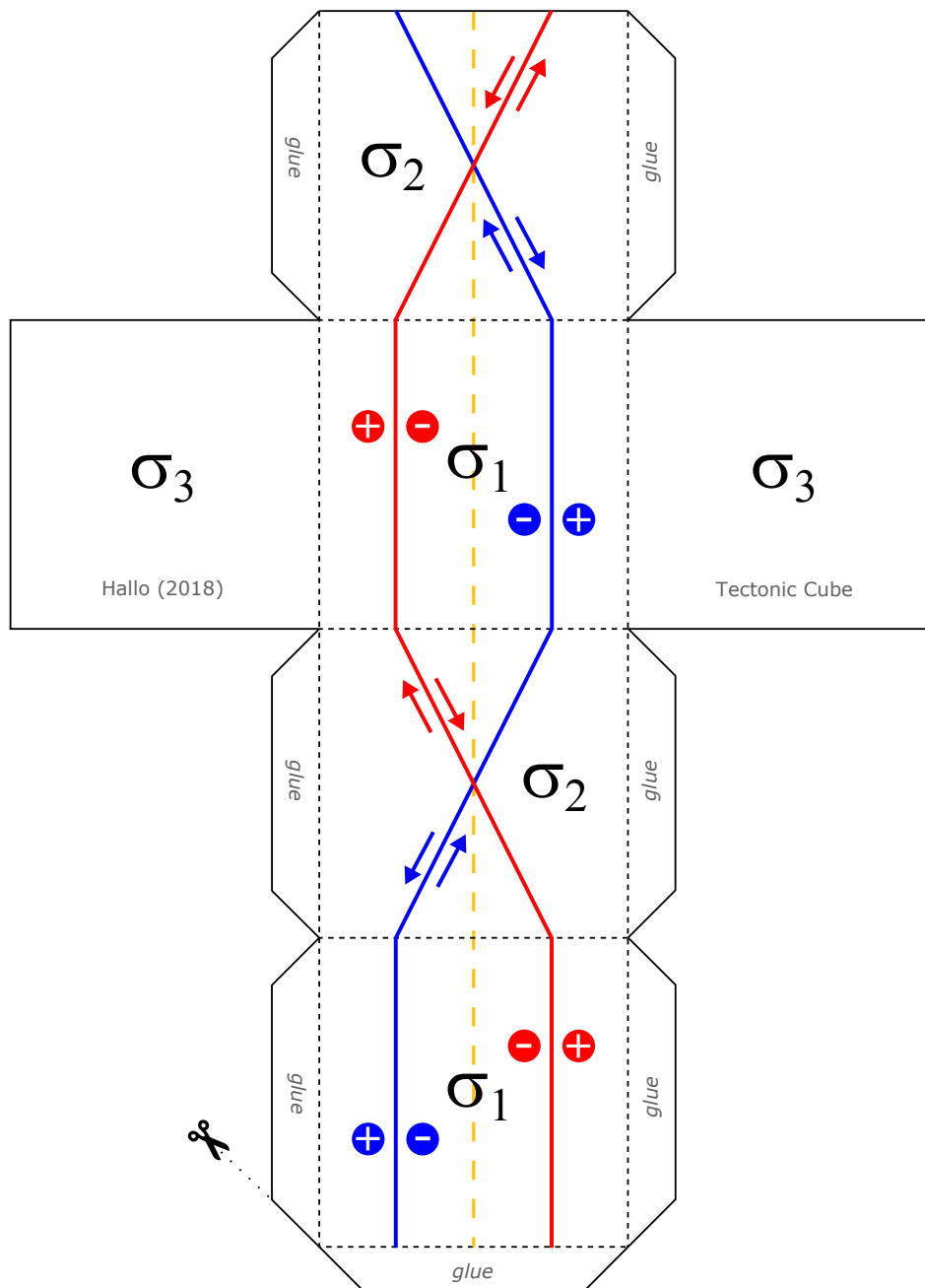


Figure A.1: The tectonic cube as a tool for interpretations of earthquake sources in tectonic framework. To construct the cube: **1)** print or copy this page to a white cardboard; **2)** cut the cube according to solid black lines; **3)** bend along dashed black lines; **4)** stick all folds by a glue.